Theoretical and Laboratory Studies of Aminomethanol Chemistry

by

Colton R. Moore

A dissertation submitted in partial fulfillment
of the requirements for the degree of

Doctoral of Philosophy

(Chemistry)

at the

UNIVERSITY OF WISCONSIN – MADISON

2026

Date of Final Oral Exam: 04/24/2026

The dissertation is approved by the following members of the Final Oral Committee:

Susanna Widicus Weaver, Professor, Chemistry and Astronomy (Advisor)
Robert McMahon, Professor, Chemistry
Yang Yang, Professor, Chemistry
Timothy Bertram, Professor, Chemistry, Atmospheric and Oceanic Sciences

Acknowledgments

Pursuing my PhD over the past several years has been both an immense challenge and an incredible privilege. I have truly immeasurable gratitude for everyone who has lifted me up and supported me in this journey. This process has been full of personal, professional, and scientific trials and victories. I do not know where I would be without everyone who has stood by me, but it certainly would not be here.

First, I would like to express my deepest gratitude to my advisor, Prof. Susanna Widicus Weaver. Your positivity and enthusiasm is infectious. No matter how terrible it felt like things were going, you always believed in my potential, even when I didn't yet. You have met me with kindness, empathy, and patience every step of my PhD. And you've always been willing to roll with ideas I've had, even when they're a bit crazy. Few people are so lucky to have someone so strongly in their corner, let alone as their advisor. From the bottom of my heart, thank you so much for everything.

I have numerous mentors to thank for their guidance in much of this work. First, I would like to thank my committee, for providing caring and constructive feedback throughout my PhD. You've challenged me throughout this process and made yourselves available when I've reached out for help, and I am eternally grateful. Next, I would like to thank the many people who have made time to answer my questions about some of the work in this dissertation. Thank you to Brian Esselman for many informative discussions about both theory and experiments over the years, including how to set up CFOUR calculations and different perspectives to consider when my experiments were not working. Thank you to Desiree Bates for so many informative conversations about theory best practices, including walking through job submissions with me when I needed it. Thank you to Prof. Yang Yang, Dr. Zehua Chen, Prof. Ryan Fortenberry, and Prof. David Woon for helpful and informative discussions on DFT methods, kinetics computations, and more. Thank you to Anna

Gerosolina for an introduction to high level transition state theory calculations with Polyrate and help with structuring files for such calculations. Thank you to Paul McGuire for troubleshooting assistance with running Polyrate on the Kestrel computational cluster. Thank you to the many, many people who have helped behind the scenes with our laboratory instruments including Steve Myers, Nick Devries, Blaise Thompson, and Amber Bartz.

There are so many labmates, past and present, to thank for their help with the works contained in this dissertation. First, I would like to thank Hayley Bunn and Chase Schultz for their mentorship in the early years of my PhD studies. Hayley, thank you for constructing the O_3 models in Chapter 4, involving me in the N_2O models, and showing me the ropes of just about everything in grad school. Chase, thank you involving me with setting up the spectrometer and helping me make the leap to become a more independent researcher. I was so lucky to begin my journey with both of you and I will always be grateful for your mentorship and encouragement as I was just getting my sea legs. I would also like to thank Will Thompson and Jonathan Rebelsky, who I joined the group with, for their friendship over the years.

Next, I like to thank the current and previous iterations of the $O(^1D)$ team, including Riana Smith, Marissa Panethiere, Ashley Peter, Carter Brown, and Katelynn Doehrmann for their help in constructing, reconstructing, testing, and documenting just about everything as we got the experiment up and running (multiple times). An especially big thanks to Ashley for sticking with me through more boring parts of rewriting the scanning routine and to Marissa for enthusiastically taking the reigns on the project, including helping with nightmarish purchasing problems. I couldn't be leaving the project in better hands and I so am excited to see what you do with it. Thank you to the ions team, Haocheng Liang, Alex Sandquist, and Annika Goldstein for letting me jump in on your project. Thank you to Hao, Alex, Annika, Marissa, and Ashley for helping me collect spectra used in Section 4.3. Additionally, thank you to the ice queens, Catherine Walker, Collette Sarver, Ruby Neisser, and Alejandra Lopez for being wonderful coworkers and always making time to chat when I have ideas to bug you with. Especially Ruby, who I bugged quite often. I have learned so much from each and every member of this group and you all have been such a pleasure to work with.

Thank you to the many people throughout my life who have encouraged me as a young chemist. Thank you to my high school chemistry teachers, Rhonda Reist and Amy Clement, who showed me that chemistry was as much magic as it was a science. Thank you to my brothers in Alpha

Chi Sigma - Beta Rho, especially Courtney Johnson and Dahlia Denton, for binding, striving, and aiding throughout my undergraduate career. Thank you to my first research mentor, Prof. Takashi Ito, for teaching me the fundamentals of research and instilling in me laboratory best practices that I use to this day. When the going gets tough, I remember the joys I have shared with all of you and that is an indescribable gift.

Lastly, I would like to thank my friends and family that have stood behind me with unwavering support. Especially those of you who had absolutely no idea what I was talking about most of the time but met me with excitement nonetheless. Thank you to my mother and father, Diane and Barry, for your support throughout, well, everything. You've always been excited for me, listened to my struggles, and loved me no matter what. Also, the care packages you sent me always seemed to arrive at the times I most needed it. Thank you to my brother, Nolan, for your support. I know we don't talk very often but I know you're in my corner cheering me on. Also, thank you for fighting with me so much when we were young, it makes a PhD look like nothing! Thank you to my pups, Kepler and Maxwell, for so often distracting me from all the difficult parts of a PhD with your doggy weirdness.

Finally, words cannot express how thankful I am for my beautiful fianceé, Sophie. Throughout this journey, you have been my rock. You took the leap of moving from Kansas to Wisconsin with me in the middle of COVID, including sleeping in our car with the dogs on our laps after a derecho kept us from checking into our hotel. You supported me through every victory and hardship of this PhD, every personal victory and hardship. You have supported me unconditionally in everything that I do. You have grounded me when everything seemed impossible. Being with you has been such a gift, and I cannot wait to continue onto our next chapter with you. Thank you for every single moment, there's no one else I would rather have done this with.

Contents

List of Tables

List of Figures

Abstract

This dissertation examines both experimental and chemical contexts for understanding and improving the laboratory synthesis of transient species of astrochemical interest, with an emphasis on aminomethanol (NH_2CH_2OH). The first portion of this work describes efforts to improve the spectrometer and experimental configuration of two rotational spectrometers used to characterize novel terrestrially unstable species. These efforts include examination of an alternative source for electronically excited atomic oxygen, $O(^1D)$, for use in insertion reactions to generate novel species; implementation of a new optical cavity to increase sensitivity of the spectrometer; improvements to a specialized data collection program; and systematic benchmarking of high voltage discharge source to determine the best operating conditions for radical production. The next portion describes detailed kinetic study of the decomposition of a key predicted intermediate in the Strecker synthesis of amino acids, aminomethanol (NH_2CH_2OH) and its protonated analog ($^+NH_3CH_2OH$). In this study, the feasibility of protonation by common proton carriers in the interstellar medium (ISM) is examined. Then, a detailed study of the decomposition of both aminomethanol and its protonated analog, using variational transition state (VTST) with highly accurate tunneling corrections is presented. Finally, a spectral prediction of N-protonated aminomethanol is presented. In the final portion, a wide breadth of catalytic microclusters with catalysts in various orientations about aminomethanol were examined to determine the effects on decomposition. These catalysts were chosen for their relevance to laboratory synthesis efforts and presence in the ISM. Catalysts were examined in both active and passive roles, and the effects on reaction barrier height, shape, and reaction rate constants were examined using density functional theory (DFT) methods combined with transition state theory (TST) and one dimensional tunneling corrections. These results are discussed with an emphasis on the impact of the detectability of aminomethanol in laboratory experiments and in the ISM.

Chapter 1

Introduction

1.1 Motivation

In the field of astrochemistry, the disciplines of observational astronomy, theoretical chemistry, and laboratory chemistry come together seeking to unravel the chemical complexity of space. The chemical environment of space is often at temperature extremes from as low as 10 K in the case of ices in dense clouds [1] to hotter than 100,000 K in the case of hot white dwarf stars[2]. Moreover, there is often an incredibly low number density of molecules and harsh radiation across the entire electromagnetic spectrum, including X-rays. Suffice it to say, the chemistry in space can get complicated.

Major areas of study in astrochemistry are how life may have formed and the search for prebiotic molecules. A prebiotic molecule is any molecule that can chemically react to form biomolecules such as sugars, amino acids, nucleobases, and lipids. Within the category of prebiotic molecules, complex organic molecules are of particular interest. Complex organic molecules (COMs) in an astronomical context refer to species made up of six or more atoms which are most commonly carbon, hydrogen, oxygen, nitrogen, phosphorous, and sulfur [3–5].

COMs form in space as stars and planets form. Atoms necessary for the synthesis of biologically relevant COMs are generated in stars and flow out into the interstellar medium, or ISM[5]. Complex chemistry can then occur in dense regions of the ISM. The extreme cold and low density environments found within the ISM lend well to ion-neutral reactions, ion-electron dissociative recombination reactions, radiative recombination reactions, and neutral-neutral reac-

tions[6, 7]. These reactions take place in two distinct regions in dense clouds: in the gas phase of warm regions, and on the icy surfaces of dust grains in the cold regions. In warm regions, gas phase chemistry converts atoms to simple molecular species such as OH, CO, N_2, NH_3, and SO [6]. As these simple species travel to cold regions, dust grains made of silicate cores covered with an ice mantle consisting of H_2O, CO, and/or CO_2 form. These dust grain surfaces facilitate the generation of even more complex species via adsorption of and subsequent reaction between simple molecules. Complex molecules such as methanol, ethanol, formaldehyde, acetaldehyde, and ammonia have been detected in interstellar ices[8]. Both laboratory experiments and theoretical calculations have shown that even more complex species, including amino acids such as glycine, can be generated on the surface of these ices[9, 10].

A favored pathway for the interstellar synthesis of the simplest α-amino acid, glycine, is through Strecker synthesis starting from NH_3 and H_2CO. A key step in this process is the generation of the simplest aminoalcohol, aminomethanol (NH_2CH_2OH). Aminomethanol is predicted to be generated in high abundance within interstellar ice mantles with nearly barrierless formation pathways[11–15]. Despite the facile nature of formation and detection of the next most complex aminoalcohol, aminoethanol ($NH_2CH_2CH_2OH$), in the ISM[16, 17], aminomethanol remains undetected, largely due to the difficulty of laboratory gas phase isolation and characterization. Characterization in the gas phase using rotational spectroscopy is necessary to provide a basis for radio astronomical observations, which is the main technique in observational astronomy to identify COMs in space. Our research group has previously attempted synthesis of this key aminoalcohol but thus far attempts have been unsuccessful[18]. This work combines experimental and theoretical chemical methods to explore potential causes of nondetection in previous works with the aim of successful laboratory detection and characterization in future experiments.

1.2 Outline of Chapters

This dissertation contains a total of 7 chapters, organized as follows:

- Chapter 2 contains an explanation of how rotational spectroscopy works as well as a detailed description of the spectrometers used in Chapter 4.
- Chapter 3 contains detailed explanations of the theory methods used in Chapters 5 and 6.

- Chapter 4 describes exploration of an alternate O(^{1}D) source for generation of terrestrially unstable molecules, improvements made to the rotational spectrometer, and benchmarking of a similar spectrometer to inform laboratory genreation of radical species.
- Chapter 5 describes theoretical characterization of a decomposition pathway of aminomethanol and its protonated analog using density functional theory methods, variational transition state theory with multidimensional tunneling methods, and normal mode analysis.
- Chapter 6 explores the effect of astrochemically relevant catalytic microclusters on the decomposition pathway of aminomethanol using density functional theory and transition state theory, as well as discusses implications for both laboratory and interstellar detection of aminomethanol.
- Chapter 7 summarizes the results of Chapters 4-6 and discusses the implication of these results on future work.

Chapter 2

Experimental Methods

2.1 Introduction

This chapter focuses on the experimental methods used in Chapter 4. This section will briefly discuss rotational spectroscopy, the type of spectroscopy used for the experiments described. It will then discuss key aspects of our specific laboratory setup, including the chamber configuration used and the concepts underlying our in-house data collection program. Finally, it will briefly discuss the merits of this experimental configuration and why this is the most appropriate choice for the types of experiments performed.

2.2 Rotational Spectroscopy

Millimeter/submillimeter spectroscopy is an ideal method for studying complex organic molecules important to the origins of life because of its structural specificity, high resolution, and direct applicability to observations of molecules in the interstellar medium. In this wavelength regime, pure rotation, low frequency vibration, and fluxional behavior of molecules can be observed with Doppler-limited accuracy [19, 20]. This is in contrast to the broader vibrational bands observed in the infrared region that may provide structural insight but not necessarily identification, or mass spectral data which only provide mass specificity. With rotational spectroscopy, the collected spectra are highly resolved and structrually specific such that separate conformers or even rotamers may be uniquely identified. Additionally, the atmosphere and ionosphere of the Earth are opaque to

many regions of the electromagnetic spectrum but most transparent in the microwave, millimeter, and submillimeter regions from 1 MHz to 1 THz allowing for ground based observations using telescopes such as the Atacama Large Millimeter/submillimeter Array (ALMA) or the Northern Extended Millimeter Array (NOEMA). Moreover, dense clouds in the interstellar medium tend to be opaque in the visible and infrared region of the electromagnetic spectrum but readily observable using the millimeter/submillimeter range.

Rotational spectroscopy begins with the assumption that a molecule can be treated as a rigid body. The components of angular momentum of the molecule in terms of moments of inertia can be represented by Equation 2.1 [19].

$$\begin{pmatrix} J_x \\ J_y \\ J_z \end{pmatrix} = \begin{pmatrix} I_{xx} - I & I_{xy} & I_{xz} \\ I_{yx} & I_{yy} - I & I_{yz} \\ I_{zx} & I_{zy} & I_{zz} - I \end{pmatrix} \begin{pmatrix} \omega_x \\ \omega_y \\ \omega_z \end{pmatrix} \tag{2.1}$$

Where J is angular momentum, I is moment of inertia, ω is angular velocity, and x, y, and z denote the cartesian coordinates of the system. Diagonalizing this moment of inertia tensor simplifies this to Equation 2.2.

$$\begin{pmatrix} J_x \\ J_y \\ J_z \end{pmatrix} = \begin{pmatrix} I_x & 0 & 0 \\ 0 & I_y & 0 \\ 0 & 0 & I_z \end{pmatrix} \begin{pmatrix} \omega_x \\ \omega_y \\ \omega_z \end{pmatrix} \tag{2.2}$$

These diagonal moment of inertia values are three perpendicular vectors that can be used to represent a coordinate system for the molecule with an origin at its center of mass. In rotational spectroscopy, these axes are labeled A, B, and C such that $I_A \leq I_B \leq I_C$ [21]. These moment of inertia values can then be used to categorize the symmetry of molecules as linear ($I_B = I_C$, $I_A = 0$), spherical top ($I_A = I_B = I_C$), symmetric top ($I_A < I_B = I_C$ or $I_A = I_B < I_C$), or asymmetric top ($I_A < I_B < I_C$). Most complex organics of interest to origins of life research are asymmetric tops, which tend to have more complex spectra than their more symmetric counterparts.

The diagonalized moment of inertia values can then be used to describe the total rotational kinetic energy Hamiltonian as in Equation 2.3.

$$\hat{H} = A\hat{J}_A^2 + B\hat{J}_B^2 + C\hat{J}_C^2 \tag{2.3}$$

Solving the Schrödinger equation for the case of a symmetric top yields the rotational constants $A = \frac{\hbar^2}{2I_A}, B = \frac{\hbar^2}{2I_B}, C = \frac{\hbar^2}{2I_C}$[21]. Solving the Schrödinger equation for the case of an asymmetric top is a more complicated endeavor with no general analytical solution and must be solved numerically with a computer starting from the basis of a symmetric top. Once the A, B, and C rotational constants are determined, rough energy levels can be calculated. However, additional terms can be included to account for centrifugal distortion resulting from a breakdown of the rigid rotor approximation as the molecule rotates, hyperfine splitting due to nuclear spin, Coriolis coupling of states, vibration-rotation coupling, and internal rotations. Each molecule has three dipole moments, μ_a, μ_b, and μ_c, along the principal axes that determine the intensity of the transitions along with temperature according to the rotational partition function. These dipole moments also determine allowed transitions for ΔK_a and ΔK_c (the projections of the total angular momentum, J, along the a and c axes, respectively) transitions depending upon which dipole moments are nonzero.

These principles are used to generate predicted spectra for molecules of interest with the spectral fitting programs SPFIT and SPCAT [22]. These predicted spectra provide a "first guess" for where lines may be in an experimental spectrum. Transitions in collected spectra are then assigned to predicted transitions, new rotational constants are generated and the prediction is updated, and new transitions are assigned. This process is repeated until the error between predicted and observed transitions is minimized to the extent that the data allow. This iterative fitting process incorporating theoretical and laboratory data insures that details that alter the observed transitions, such as differences between observed and predicted geometries, large amplitude motions, spectral splitting, or chemical effects such as dimers or clusters, are not missed and that the most accurate information possible is available to guide astronomical observation.

2.3 Experimental Setup

Experiments in this dissertation, in particular those in Chapter 4 Sections 4.1 and 4.2, were conducted in a vacuum chamber as shown in Figure 2.1. This chamber is made of stainless steel and operated under vacuum using a roots blower (Leybold RUVAC WH2500), achieving a base pressure of 10 mTorr. When operating, gases (backing gases and chemical precursors) are balanced using mass flow controllers (MKS 1179A). Typically argon was used as a backing gas. When in-

vestigating $O(^1D)$ chemistry, O_3 or N_2O were used as precursors. When O_3 was used as an $O(^1D)$ precursor, it was generated continuously using the Pacific Ozone L11 Ozone Generator, with an O_2 (Airgas, 99.994%) feed gas. The gases in use were mixed in stainless steel gas lines beneath the chamber and introduced using a pulsed valve (Parker Hannifin Series 9 general valve with 1 mm pinhole aperature). The pulsed valve was run with a repetition rate of 25 Hz and driven by a pulsed driver (Parker Hannifin Iota One).

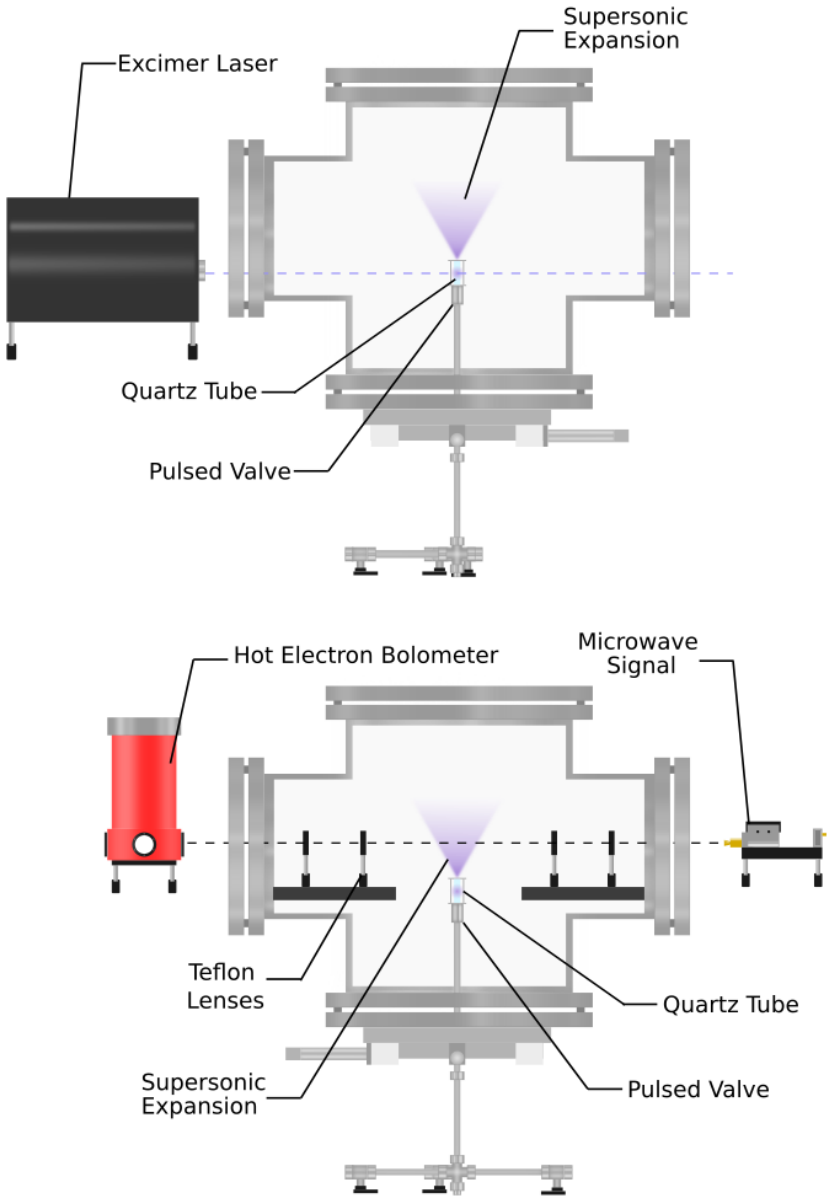

Figure 2.1: Side views showing the optical path of the excimer laser (top) and of the millimeter/submillimeter signal (right). The UV irradiation from the laser initiates chemistry in the quartz photolysis tube. The millimeter/submillimeter signal probes the supersonic expansion.

In the exerpiment described in Chapter 4, Sections 4.1 and 4.2, chemistry was initiated by an ultraviolet excimer laser (Coherent Excistar 1000) in order to photolyze O_3 or N_2O and generate electronically excited atomic oxygen in the form of $O(^1D)$, which then barrierlessly inserts into bonds to synthesize terrestrially unstable species. In these experiments, a quartz photolysis tube

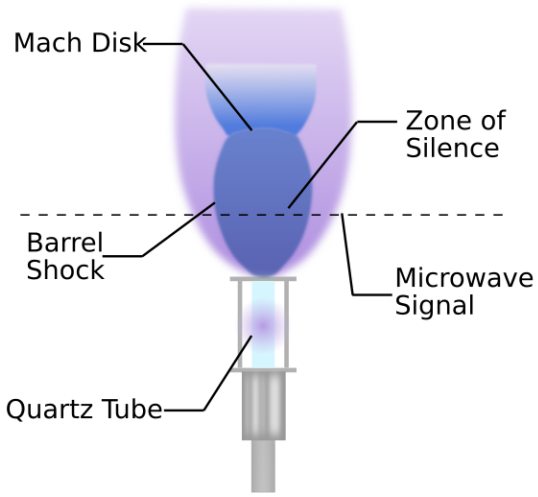

Figure 2.2: Anatomy of the supersonic expansion. The supersonic expansion, consists of a zone of silence in the center, differentiated from the surrounding turbulent gas by a barrel shock region. The edge of the zone of silence is terminated by the mach disk shock.

3 cm long with an OD of 5.00 mm and an ID of 1.00 mm (wall thickness = 2.00 mm) was affixed to the pulsed valve faceplate. This experimental configuration is shown in Figures 2.1 and 2.2. As described in Chapter 4 Section 4.3, a high voltage ring electrode source was used to strike a plasma and generate radical species. These electrodes were made of stainless steel and had an inner diameter of 2 mm to match the pulsed valve pinhole aperture. Voltage was applied across the electrode source using a high voltage power supply (Spellman SL2PN2000) run through a ballast resistor with resistance of 2.5 kΩ. This configuration is depicted in Figure 2.3.

The pressure differential between the high pressure gas lines and the low pressure vacuum chamber generates a supersonic expansion, as shown in Figures 2.2 and 2.3. From these two figures, the nature of the supersonic expansion should maintain similar characteristics regardless of the presence of a photolysis tube or ring electrode source. Supersonic expansions consist of a turbulent outer shell (depicted in purple), a barrel shock region which separates the turbulent shell from the quiescent core called the zone of silence. At the leading edge of the zone of silence is the mach disk, which occurs when the mach number of the exiting gas goes from from $M > 1$ to $M < 1$. The zone of silence is of the greatest interest for on-the-fly synthesis of terrestrially unstable products due to its greater adiabatic cooling and quiescent nature.

The products exiting the photolysis tube were characterized using the multiplier chain system and the Fast Sweep scanning method developed by Hays[23] and optimized by Zou[24]. Briefly,

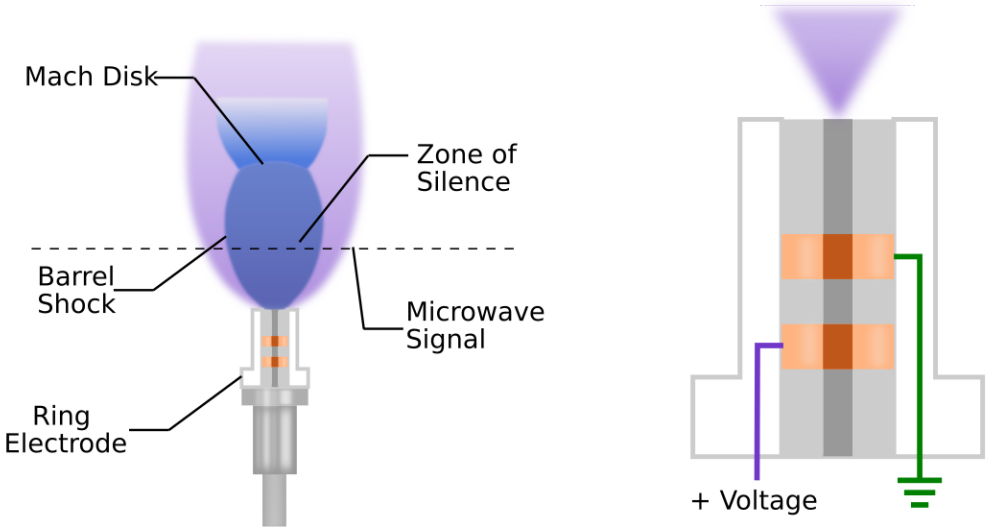

Figure 2.3: The pulsed valve configuration with a high voltage ring discharge source. An enlarged cross sectional view of the ring electrode source is shown to the right. The outer housing is made of teflon. The inside of the ring source consists of teflon spacers and stainless steel electrodes which have an applied voltage to initiate plasma generation.

a microwave synthesizer (Agilent Technologies E8257D PSG) produces a 0-50 GHz signal that is then multiplied by a Virginia Diodes Inc. GaAs Schottky diode multiplier chain (AMC-268,-166) to achieve higher frequencies. In the case of these experiments, the frequency range probed was 140-225 GHz, which was achieved using the WR1.5 doubler and triplers. The resultant signal was then passed through teflon lenses and focused on the supersonic expansion produced by the pulsed valve apparatus. The signal through the expansion was then focused onto the window of a cryogenically cooled InSb hot electron bolometer (QMC Ltd. QFIXBI/PTC) detector, which is a semiconductor whose resistivity changes as a result of incident radiation. The voltage output from the bolometer was processed using an oscilloscope.

2.3.1 Fast Sweep

Data collected on the spectrometers described in Section 2.3 were acquired using an in-house program called Fast Sweep[25]. In the Fast Sweep acquisition scheme, a triangular frequency modulated signal centered on a particular frequency is passed from the microwave synthesizer and multiplier chain system, through the sample in the supersonic expansion where radiation is absorbed by molecules according to their rotational transitions, and finally detected by the bolometer. This triangular wave is aligned in time with the event that initiates the chemistry,

whether that is the laser pulse or the high voltage discharge, so that products of interest are present in the beginning of the data collection at sweep 1 but not sweep 5. The resultant data then contains both time and frequency dependent spectral signatures over the collected waveform as in Figure 2.4. The frequency range covered by the triangular wave is dependent upon the degree of deviation in the frequency modulation as well as the degree of frequency multiplication. The total bandwidth is given by 2 x (FM Deviation) x (Frequency Multiplication).

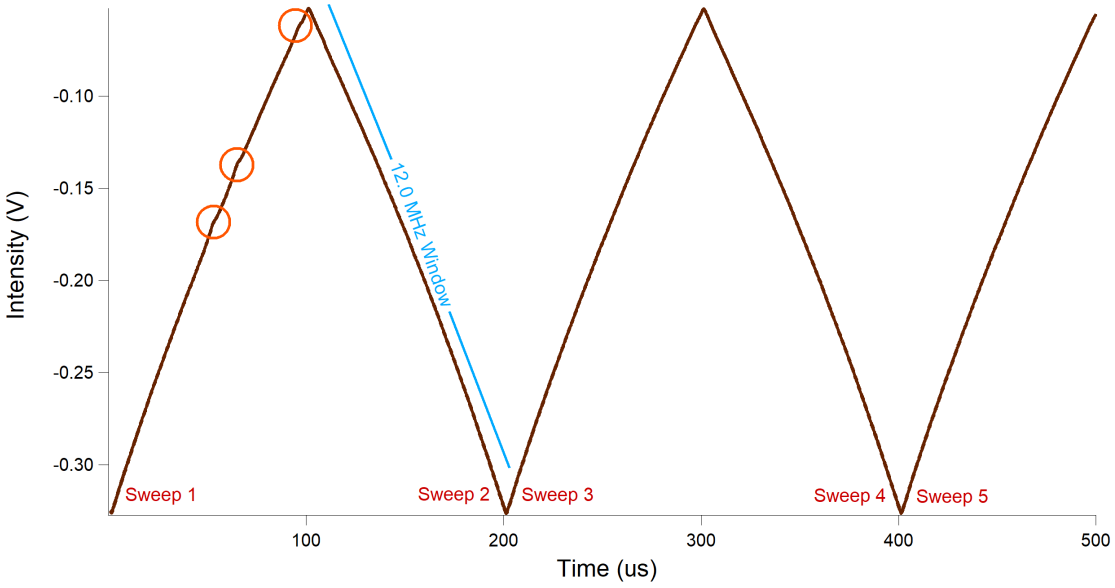

Figure 2.4: An example of a collected triangular wave. Spectral data are collected on the first sweep; spectral lines are circled. The total duration of the sweep spans a 12.0 MHz window, as marked in blue. The background sweeps are collected later, such as in sweep 5, when the spectral lines have disappeared as sample is pumped out of the vacuum chamber.

The Fast Sweep scanning method greatly enhances the spectral acquisition speed as compared to other data collection methods that utilize lock-in detection. This faster spectral acquisition allows for collection of spectral data of transient species with lifetimes on the order of microseconds, such as in photolysis or plasma initiated chemistry. Moreover, the background subtraction between the first and last data sweeps increases the spectrometer sensitivity, allowing for detection of minor chemical products. Fast Sweep also provides greater flexibility on the frequency and timescale of data collection than a traditional frequency step method, though at particularly fast and wide bandwidth operation modes, the fidelity of the frequency in the collected spectra degrade due to detector response time [25].

Chapter 3

Theoretical Methods

3.1 Introduction

As discussed in Chapters 5 and 6, a variety of computational methods were used to study chemical systems of interest. These methods include electronic structure calculations such as density functional theory (DFT) methods and coupled cluster (CC) methods, as well as computational kinetics methods including transition state theory (TST) and variational transition state theory (VTST) with one dimensional and multidimensional tunneling corrections. A brief overview of these methods, including their merits and weaknesses, as well as their utility in supporting experimental work is described in this Chapter.

3.2 Electronic Structure Calculations

The goal of any electronic structure calculation for a given chemical system is to solve the Schrödinger wave equation[26], given by Equation 3.1:

$$\hat{H}\psi = E\psi \tag{3.1}$$

where $\hat{H}$ is the Hamiltonian operator that encompasses the kinetic energy ($\hat{T} = -\frac{\hbar^2}{2m}\nabla^2$, $\hbar$ is Plank's constant and m is the mass of the particle) and potential energy ($\hat{V} = V(\mathbf{r})$) operators, Ψ is the wavefunction of the system, and E is the energy eigenvalue for the quantum state described by Ψ. Solving the Schrödinger equation allows for determination of key aspects of a chemical

system, including its energy, structure, and spectroscopic features. Such information is vital to understanding processes underlying observed chemistry, especially when complimented by laboratory data. Moreover, electronic structure data can provide important guideposts for designing and executing laboratory experiments.

The Hamiltonian becomes complicated rather quickly in molecular systems, taking the generic form[27] in Equation 3.2

$$\hat{H} = \hat{T}_n + \hat{T}_e + \hat{V}_{nn} + \hat{V}_{en} + \hat{V}_{ee} \tag{3.2}$$

where $\hat{T}_n$ and $\hat{T}_e$ represent the kinetic energy of the nuclei and electrons, respectively, and $\hat{V}$ represents the potential energy that arises from interaction between the nuclei (n), electrons (e), or both (en). This generic form, in reality, is a summation of all possible permutations of interactions between the electrons and nuclei. Solving the (simpler) time independent Schrödinger equation analytically is only possible for very simple single-electron systems such as the Hydrogen atom. For more complex many-electron systems, such as molecules, it is necessary to make approximations.

One important such approximation is the Born-Oppenheimer approximation[28]. The premise of the Born-Oppenheimer approximation is that the significant difference in the masses between nuclei and electrons allows their wave functions to be treated as separable. Moreover, because the movement of the larger nuclei is relatively quite slow in comparison to the electrons, the nuclei can be treated as fixed in space. This allows the Hamiltonian to be expressed as the sum of its electronic and nuclear components, as in Equation 3.3, and the nuclear kinetic term of the operator in Equation 3.2 to be treated as negligible.

$$\hat{H} = \hat{H}_{elec} + \hat{H}_{nuc} \tag{3.3}$$

The purely electronic energy then becomes a function of only the electronic Hamiltonian and wave function.

$$\hat{H}_{elec}\psi_{elec} = \hat{E}_{elec}\psi_{elec} \tag{3.4}$$

The purely electronic Hamiltonian is then,

$$\hat{H}_{elec} = -\frac{\hbar^2}{2m_e}\sum_i \nabla_i^2 - \sum_\alpha \sum_i \frac{Z_\alpha e'^2}{r_{i\alpha}} + \sum_j \sum_{i>j} \frac{e'^2}{r_{ij}} \tag{3.5}$$

where m_e is the mass of an electron, α is a nucleus, i and j are electrons, Z is the atomic number

of α, e$'$ is the charge of an electron, and r_{ij} is the distance between electrons i and j. Internuclear repulsion can also be included as in Equation 3.6.

$$V_{nn} = \sum_{\alpha} \sum_{\beta>\alpha} \frac{Z_\alpha Z_\beta e'^2}{r_{\alpha\beta}} \tag{3.6}$$

While the Born-Oppenheimer approximation simplifies the work of solving the Schrödinger equation, the process remains quite complex and is still only feasible for small systems.

Another vital approximation is the Hartree-Fock approximation[29–33]. Under this approximation, the many body wavefunction (ψ) used in the above equations is approximated to a Slater determinant (D), the antisymmetrized product of spin-orbitals. D is a product of spatial orbitals ϕ_i and a spin function α or β. The molecular energy (in bra-ket notation) using this wavefunction is then

$$E_{HF} = \langle D|\hat{H}_{elec} + V_{nn}|D\rangle \tag{3.7}$$

where $\hat{H}_{elec}$ and V_{nn} are defined as in Equations 3.5 and 3.6. Separating Equation 3.7 into its one and two electron operators, and separating V_{nn} as it is independent of electronic coordinates, E_{HF} becomes

$$E_{HF} = 2\sum_{i=1}^{n/2} H_{ii}^{core} + \sum_{i=1}^{n/2}\sum_{j=1}^{n/2}(2J_{ij} - K_{ij}) + V_{nn} \tag{3.8}$$

where

$$H_{ii}^{core} = \langle\phi_i| - \frac{1}{2}\nabla^2 - \sum_{\alpha}\frac{Z_\alpha}{r_{i\alpha}}|\phi_i\rangle \tag{3.9}$$

and

$$J_{ij} = \langle\phi_i\phi_j|\frac{1}{r_{ij}}|\phi_i\phi_j\rangle\,, \qquad K_{ij} = \langle\phi_i\phi_j|\frac{1}{r_{ij}}|\phi_j\phi_i\rangle \tag{3.10}$$

J_{ij} and K_{ji} are the Coulomb and Exchange integrals, respectively. As the Fock operator (the first two terms on right hand side of Equation 3.7) is dependent upon ϕ_i, the molecular orbital coefficients and energies are solved for iteratively using the Roothaan equations[34]. This process makes solving Equation 3.1 possible and efficient for more complex systems. However, while these calculations are now accessible for more complex systems, the Hartree-Fock approximation crucially neglects electron correlation effects, which leads to inaccuracies in computed structures and energies. Post-Hartree-Fock methods such as Møller-Plesset perturbation theory[35, 36], coupled cluster theory[37–40] (discussed in Section 3.2.2), configuration interaction[41, 42], and composite methods[43–46] address the issue of the electron correlation effects but come at a higher compu-

tational cost.

3.2.1 Density Functional Theory

The Post-Hartree-Fock methods described above are more accurate but the high computational cost can make their utility limited for large systems or studies involving many systems. Density Functional Theory[47–49], or DFT, provides an attractive alternative to Hartree-Fock based methods. Whereas the Hartree-Fock method relies upon the many body wavefunction, ψ, DFT methods consider the spatially dependent electron density, $\rho(\mathbf{r})$.

$$\rho_0(\mathbf{r}) = N \int ... \int |\psi(\mathbf{r}_1, \mathbf{r}_2, ...\mathbf{r}_N)|^2 d\mathbf{r}_2 ... d\mathbf{r}_N \tag{3.11}$$

where N is the number of electrons in the system.

DFT methods originate from the work of Hohenberg and Kohn[47]. The first Hohenberg-Kohn theorem states that the ground-state electron density, $\rho_0(\mathbf{r})$ as defined in Equation 3.11, uniquely determines the external potential, $V_{ext}(\mathbf{r})$, acting upon the electrons. Therefore, the ground-state properties, including the total ground-state energy and the wavefunction, can be determined by the ground-state electron density. In other words, the ground-state electronic energy (E_0) is a functional[1] of the function $\rho_0(\mathbf{r})$, yielding Equation 3.12.

$$E_0 = E_v[\rho_0] = \overline{T}[\rho_0] + \overline{V}_{ne}[\rho_0] + \overline{V}_{ee}[\rho_0] \tag{3.12}$$

$E_v[\rho_0]$ is the energy arising from the external potential, $V_{ext}(\mathbf{r})$, $\overline{T}[\rho_0]$ represents the average kinetic energy as a functional of ρ_0 and $\overline{V}[\rho_0]$ represents the average potential energy arising from nuclear-electron interaction (ne) or electron-electron interactions (ee) as a functional of ρ_0. The second Hohenberg-Kohn theorem states that for every trial density function $\rho_{tr}(\mathbf{r})$ such that $\int \rho_{tr}(\mathbf{r}) d\mathbf{r} = N$ and $\rho_{tr}(\mathbf{r}) \geq 0$ for all $\mathbf{r}$, $E_0 \leq E_v[\rho_{tr}]$. From Equation 3.12, $E_0 = E_v[\rho_0]$. Then the true ground-state electron density, ρ_0 must be the electron density that minimizes the energy functional $E_v[\rho_{tr}]$. These theorems were later proven to hold for degenerate ground states[51] as well. The Hohenberg-Kohn theorems simplify quantum chemical calculations by reducing the number of variables needed to determine electronic structure properties from 3N to just 3, and by

[1] From Levine[50], a function f(x) is a rule that associates a number with each value of the variable for which the function f is defined. A functional F[f] is then a rule that associates a number with each function f. In other words, a functional can be thought of as a function of a function that outputs a single real number.

introducing a variational principle that allows for efficient optimization of ρ_{tr}.

The Hohenberg-Kohn theorems are made practical by the Kohn-Sham method[48], which involves iteratively solving the equations described below until certain threshold criteria are reached between computations of the system's energy, density, or forces. The Kohn-Sham method begins with a model fictitious system of non-interacting electrons which have the same density as the real system, $\rho_s(\mathbf{r}) = \rho_0(\mathbf{r})$, where $\rho_s(\mathbf{r})$ is the density in the fictitious system. Since the electron probability is known, the external potential in the reference system is uniquely known. The Kohn-Sham equations can be expressed as

$$\left(-\frac{\hbar}{2m_e}\nabla^2 + V_{eff}(\mathbf{r})\right)\psi_i = \epsilon_i\psi_i \tag{3.13}$$

where

$$V_{eff} = V_{ext} + V_{Hartree}[\rho] + V_{XC}[\rho] \tag{3.14}$$

In 3.14, V_{ext} is the external potential acting upon the electrons, $V_{Hartree}[\rho]$ is the Hartree potential and $V_{XC}[\rho]$ is the exchange-correlation potential. $V_{Hartree}[\rho]$ and $V_{XC}[\rho]$ are given by

$$V_{Hartree}[\rho] = \frac{1}{2}\int\int \frac{\rho(\mathbf{r}_1)\rho(\mathbf{r}_2)}{r_{12}} d\mathbf{r}_1\mathbf{r}_2, \qquad V_{XC} = \frac{\delta E_{xc}[\rho]}{\delta\rho(\mathbf{r})} \tag{3.15}$$

where $V_{Hartree}$ describes the electrostatic interaction between electrons in the system and V_{XC} takes into account both electron exchange and correlation effects. The exchange correlation functional, $E_{XC}[\rho]$ is unknown and therefore must be approximated.

Common approximations include local density approximation (LDA)[48], local spin-density approximation (LSDA)[52, 53], generalized gradient approximations (GGA)[54–56], meta-GGAs[57], or hybrid functions[58]. Local approximations such as LDA and LSDA take V_{XC} to depend solely on local electron density and assume that this density is nearly uniform. Gradient approximations such as GGA and meta-GGA introduce a spatial dependence of the electron density which tends to yield more accurate results than local approximations. Hybrid methods include some portion of exact Hartree-Fock exchange in addition to DFT exchange correlation terms, which tends to yield more accurate results than (meta-)GGAs, but they are also computationally more expensive. The two primary functionals used for Chapters 5 and 6 are the M06-L and M06-2X, which are a meta-GGA and a global-hybrid meta-GGA, respectively. The umbrella of DFT methods can provide a

flexible cost to accuracy ratio that makes study of many systems more attainable, including larger and more complex systems. However, these methods can have a variety of weaknesses depending upon the approximations used, including poor representations of barrier heights, charge transfer, response to external fields, and weak interactions in some systems. There is not necessarily one single best functional as their performance can vary system to system and based on which property is being computed, so it is best to benchmark a given system and property against experimental data when available or highly accurate computations for the best possible performance.

3.2.2 Coupled Cluster Theory

Another method used for some calculations presented in Chapter 5, as well as the literature values used to benchmark systems for DFT calculations, is the coupled-cluster method[59–61]. In coupled-cluster theory, the wavefunction from Equation 3.1 is taken to be[62]

$$\psi = e^{\hat{T}}\Phi_0 \tag{3.16}$$

where ψ is the exact electronic wavefunction, Φ_0 is the normalized ground-state Hartree-Fock wave function, and $e^{\hat{T}}$ is the Taylor expansion:

$$e^{\hat{T}} \equiv 1 + \hat{T} + \frac{\hat{T}^2}{2!} + \frac{\hat{T}^3}{3!} + ... = \sum_{k=0}^{\infty} \frac{\hat{T}^k}{k!} \tag{3.17}$$

$\hat{T}$ is the cluster operator

$$\hat{T} \equiv \hat{T}_1 + \hat{T}_2 + ... + \hat{T}_N \tag{3.18}$$

and

$$\hat{T}_1\Phi_0 \equiv \sum_{a=N+1}^{\infty}\sum_{i=1}^{N} t_i^a \Phi_i^a, \qquad \hat{T}_2\Phi_0 \equiv \sum_{b=a+1}^{\infty}\sum_{a=N+1}^{\infty}\sum_{j=i+1}^{N}\sum_{i=1}^{N-1} t_{ij}^{ab}\Phi_{ij}^{ab} \tag{3.19}$$

In these equations, N is the number of electrons, $\hat{T}_1$ is the one-particle excitation operator, $\hat{T}_2$ is the two-particle excitation operator, Φ represents a Slater determinant, and t is a numerical coefficient. The pattern of expansion in the excitation operators holds up to $\hat{T}_N$. Coupled-cluster theory endeavors to find the t coefficient values for all a,b,c... and i, j, k... values in order to determine the wavefunction, ψ, as represented in Equation 3.16.

In coupled-cluster theory, it is necessary to assume that $\hat{T}$ is approximately equal to a truncated

expansion of the cluster operator rather than the full set in Equation 3.18. Additionally, the frozen core approximation, that is that inner-shell electron excitation can be omitted, is often invoked. Terms are also commonly approximated using perturbation theory, which are often denoted with parentheses. For example, CCSD(T) would be an implementation of coupled-cluster theory that uses full treatment of singles and doubles and approximates with perturbative triples. Even with these approximations in mind, coupled-cluster theory provides quite accurate correlation energies for closed-shell systems near equilibrium geometries. However, for complicated systems like di-radicals or those that undergo bond breaking, accessible systems such as CCSD(T) often break down. Higher order methods such as CCSDT and CCSDTQ are more accurate but prohibitively computationally expensive for all but the smallest molecules. Bearing these limitations in mind, CCSD(T) with a large basis set (aug-cc-pVTZ) was used for determination of rotational constants in Chapter 5, but was not used for characterization of reaction paths in Chapters 5 and 6 due to the high computational cost and prevalence of non-equilibrium structures along the examined minimum energy paths.

3.3 Computational Kinetics

Understanding of chemical processes begins with precise knowledge of the reactants and products of a reaction, but all of the steps in between (and sometimes outside of) these points are required for a complete picture of what is happening in a reaction. A collection of all of these points in a 3-dimensional representation of system parameters (such as bond lengths or angles) and system energy is what is referred to as a potential energy surface or PES. An example of this for an arbitrary system is shown in Figure 3.1 and a projection of this PES in the form of contours is shown in Figure 3.2. A typical chemical reaction usually has at least 3 major points of interest, often referred to as stationary points: the reactants, the products, and the transition state. The reactants and products are local minima on the PES. A transition state is defined as a saddle point, or a minimum in one direction and maximum in another. All three of these major points are labeled in Figures 3.1 and 3.2. In order for a chemical reaction to occur, the system must travel from the reactants, over the transition state saddle point, to the products, as denoted by the white line in Figure 3.1 or black dotted line in 3.2. This path of travel is taken to be the one of steepest descent on either side of the saddle point, and is often called the minimum energy pathway (MEP)

or the intrinsic reaction coordinate (IRC). Since this path is typically the most interesting feature of a PES, and it does not require three dimensions to show this path, it is often represented as a "slice" of the PES as shown in Figure 3.3.

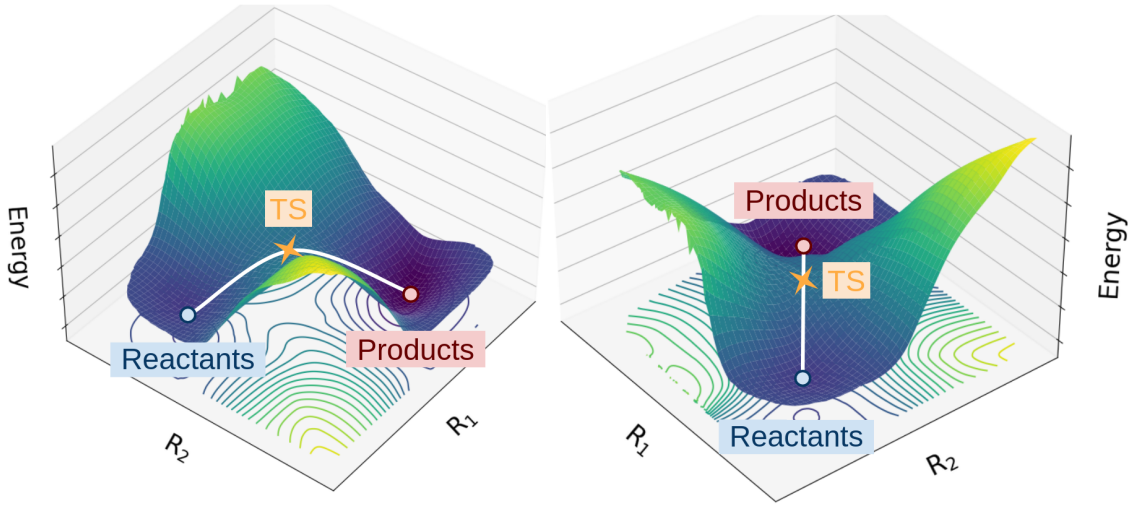

Figure 3.1: Two views of a PES for an arbitrary chemical system showing two minima and a saddle point. The reactants and products are labeled in blue and red, respectively. The transition state is denoted by a star and labeled as "TS" in orange. The reaction path is shown by a white line. R_1 and R_2 are arbitrary system parameters such as bond lengths or bond angles. Energy contours are projected on to the R_1R_2 plane.

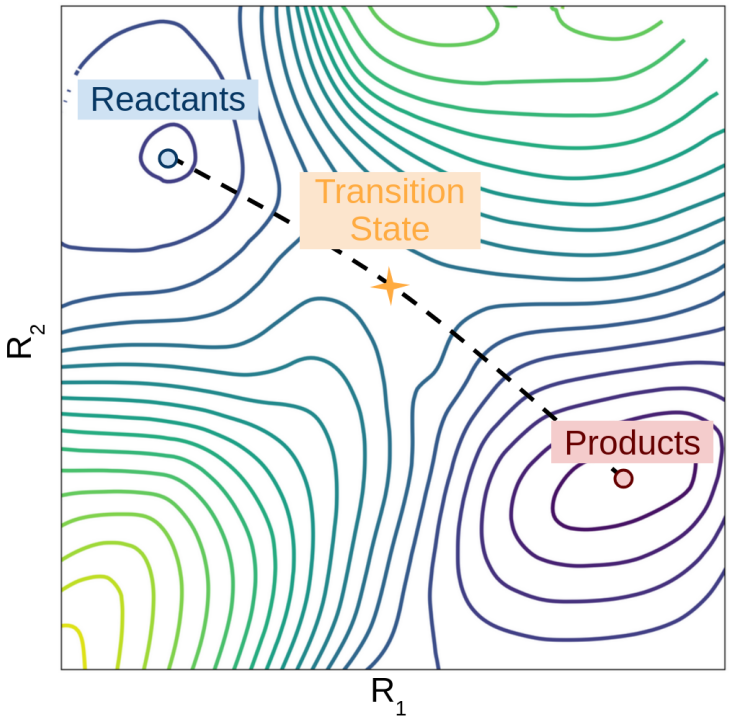

Figure 3.2: A 2-dimensional plot of the energy contours from Figure 3.1. The reactants, products, and transition state are labeled as before. The reaction path is denoted by a black dashed line.

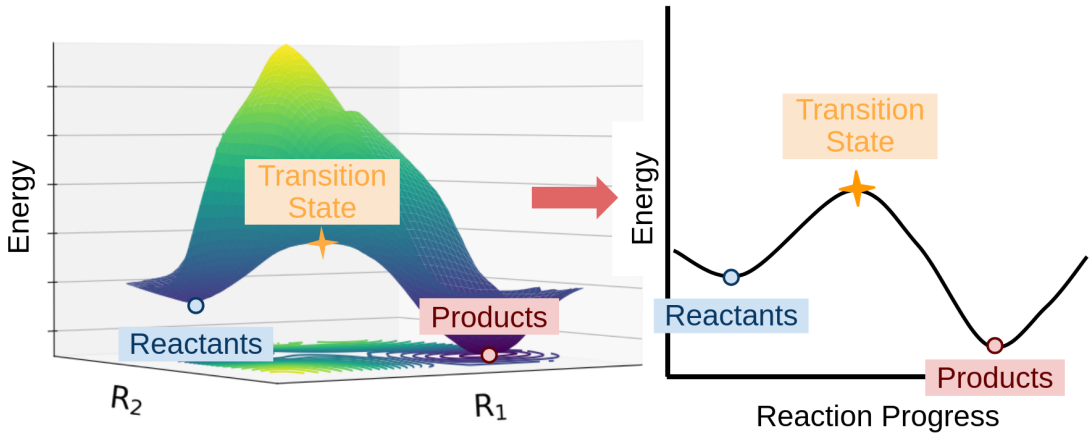

Figure 3.3: A side view of the PES (left) and the "slice" of this PES that is often used to represent a chemical reaction (right). Stationary points are labeled as before. The black line in the figure to the right denotes the reaction path.

3.3.1 Transition State Theory

An early understanding of the reaction path and its relationship to how fast a reaction occurred was developed by Arrhenius in 1889[63]. This relationship is expressed by the (modified) Arrhenius equation:

$$k = AT^n e^{\frac{-E_a}{RT}} \tag{3.20}$$

where k is the rate constant, A is a pre-exponential factor, n is a proportionality constant, E_a is the activation energy of the reaction (or the difference in energy between the reactants and the transition state in Figure 3.3), R is the universal gas constant, and T is temperature. In the unmodified version, n=0. This understanding lays an important foundation for the temperature dependence of chemical reactions. However, the capabilities of this description are limited.

Another similar representation is transition state theory, or TST[64, 65]. The basis for TST is given by the equation:

$$k = \frac{k_B T}{h} e^{-\frac{\Delta G^\ddagger}{RT}} = \frac{k_B T}{h} e^{\frac{\Delta S^\ddagger}{R}} e^{-\frac{\Delta H^\ddagger}{RT}} \tag{3.21}$$

where k is the rate constant, k_B is the Boltzmann constant, T is temperature, h is the Planck constant, $\Delta G^\ddagger$ is the Gibbs energy of activation, $\Delta S^\ddagger$ is the entropy of activation, and $\Delta H^\ddagger$ is the enthalpy of activation. This equation can also take the form of:

$$k^\ddagger(T) = \frac{k_B T}{h} \frac{Q^\ddagger(T)}{Q_r(T)} e^{\frac{-V^\ddagger}{k_B T}} \tag{3.22}$$

where $Q^\ddagger(T)$ and $Q_r(T)$ denote the temperature dependent partition functions of the transition state and reactants respectively, and $V^\ddagger$ denotes the potential energy barrier. Equations 3.21 and 3.22 provide a more complex understanding of the dependence of reactions upon temperature. However, this method is still limited by poor performance at temperature extremes and classical treatment of chemical species. Moreover, this method only considers the properties of the reactants and transition states, thus neglecting the full dimensionality of the PES shown in Figure 3.1.

3.3.2 1-Dimensional Tunneling Corrections

The limitations of Equations 3.21 and 3.22 due to classical treatment can be addressed using tunneling corrections. Tunneling corrections are applied via a multiplicative factor according to

the equation

$$k^{TST/tunn}(T) = \kappa k^{TST}(T) \tag{3.23}$$

where $k^{TST/tunn}(T)$ is the temperature dependent, tunneling corrected rate constant, κ is the transmission coefficient, and $k^{TST}(T)$ is the classical temperature dependent rate constant from Equations 3.21 and 3.22. A correction to account for tunneling was developed by Wigner[64, 66]. A modified version of this correction is typically used to eliminate divergence at certain temperatures and is given by Equation 3.24.

$$\kappa_{Wig}(T) = 1 + \frac{1}{24}\left(\frac{\hbar Im(\nu^{\ddagger})}{k_B T}\right)^2 \tag{3.24}$$

Here, $Im(\nu^{\ddagger})$ is the imaginary frequency at the saddle point which characterizes the reaction mode. However, this correction incorporates limited information, only involving one parameter related to the transition state and nothing else. It also assumes that the reaction barrier is symmetric, which is not always the case.

Another approximation was proposed by Eckart[67] which incorporates more information about the system and allows for asymmetry. The Eckart approximation is given by[68]:

$$\kappa_{Eck}(T) = \frac{exp(\frac{\Delta H_f^{0K}}{k_B T})}{k_B T}\int_0^{\infty} p(E)e^{-\frac{E}{k_B T}}dE \tag{3.25}$$

where E is the energy of the system, p(E) is the probability of transmission given by Equation 3.26, and ΔH_r^{0K} is the zero point corrected enthalpy of the reverse reaction.

$$p(E) = 1 - \left[\frac{cosh[2\pi(\alpha-\beta) + cosh[2\pi\delta]]}{cosh[2\pi(\alpha+\beta) + cosh[2\pi\delta]}\right] \tag{3.26}$$

α and β are constants given by

$$\alpha = \frac{1}{2\sqrt{C}}\sqrt{E}, \qquad \beta = \frac{1}{2\sqrt{C}}\sqrt{E-A}, \qquad \delta = \frac{1}{2\sqrt{C}}\sqrt{B-C} \tag{3.27}$$

and

$$A = \Delta H_f^{0K} - \Delta H_r^{0K}, \quad B = \left(\sqrt{\Delta H_f^{0K}} - \sqrt{\Delta H_r^{0K}}\right)^2, \quad C = (\hbar Im(\nu^{\ddagger}))^2\left[\frac{B^3}{A^2-B^2}\right]^2 \tag{3.28}$$

ΔH_f^{0K} and ΔH_r^{0K} are the zero point corrected enthalpy of the forward and reverse reactions, respectively, and $Im(\nu^{\ddagger})$ is the imaginary frequency at the saddle point which characterizes the reaction mode. While this correction allows for greater accuracy, it still only takes into account the properties of the reactants, transition state, and products. Importantly, the Wigner and Eckart corrections fail to address the multidimensional nature of a true potential energy surface as in the one shown in Figure 3.1. Corrections that take this multidimensionality into account are discussed in Section 3.3.4.

3.3.3 Variational Transition State Theory

An offshoot of transition state theory that increases the accuracy of computational kinetic predictions is variational transition state theory, or VTST. The key consideration in this framework is the location of the dynamic bottleneck of the reaction. This bottleneck is described by a hyperplane perpendicular to the reaction path that divides the reactant region of the PES from the product region. In classical TST, this hyperplane is taken to be at the saddle point[65]. In reality, a dividing hyperplane at a different location may provide a more "true" kinetic bottleneck, which occurs when the forward flux through this surface is minimized[69–73]. The location of such a hyperplane is referred to as a generalized transition state and provides more accurate computed rate constants. Equation 3.22 can be written in terms of and minimized with respect to s, the coordinate along the minimum energy pathway[74]. When minimized with respect to s, this is the canonical variation theory (CVT) rate constant[74–77].

$$k^{CVT} = \min_{s} \quad k^{GT}(T,s)) = \frac{k_B T}{h} \frac{Q^{GT}([T, s_*^{CVT}(T)])}{Q^R(T)} exp\left(\frac{-V_{MEP}(s_*(T))}{k_B T}\right) \tag{3.29}$$

Here $k^{GT}(T,s)$ is the rate constant of the form in Equation 3.22 when s $\neq$ 0 (not at the saddle point), Q is the quantum mechanical partition function of the generalized transition state (GT) or the reactants (R), and $V_{MEP}(s_*(T))$ is the potential along the MEP evaluated at s_*. Using the described variational methods lead to more accurate computed rate constants. Additionally, quantum mechanical tunneling effects can be incorporated as in Section 3.3.2. However, the same limitations regarding the true multidimensionality of the PES still apply. Corrections that address this multidimensionality are discussed in the next section.

3.3.4 Multidimensional Tunneling Corrections

More complex incorporations of tunneling effects beyond the 1-dimensional corrections discussed in Section 3.3.2 can be implemented for more accurate kinetic rate constant determinations. These multidimensional tunneling effects become quite impactful in highly curved systems. While in Figures 3.1 and 3.2 there is a relatively straight path of travel from the reactant to product regions, systems can show more complex MEPs as in Figures 3.4 and 3.5.

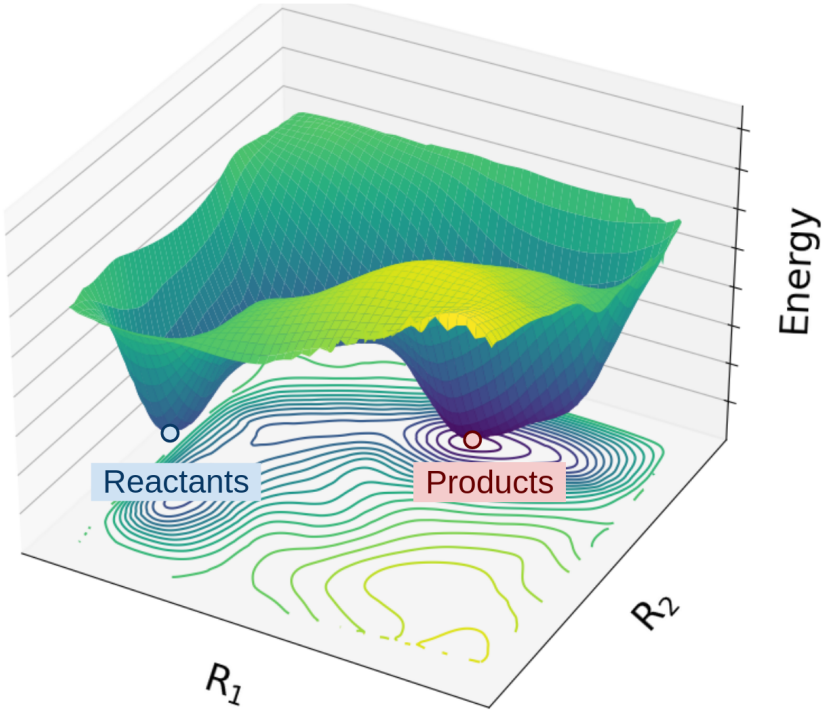

Figure 3.4: A PES of an arbitrary chemical system with a more complex MEP. Reactant and product wells are labeled and energy contours are projected onto the xy plane. This arbitrary system displays a highly curved path.

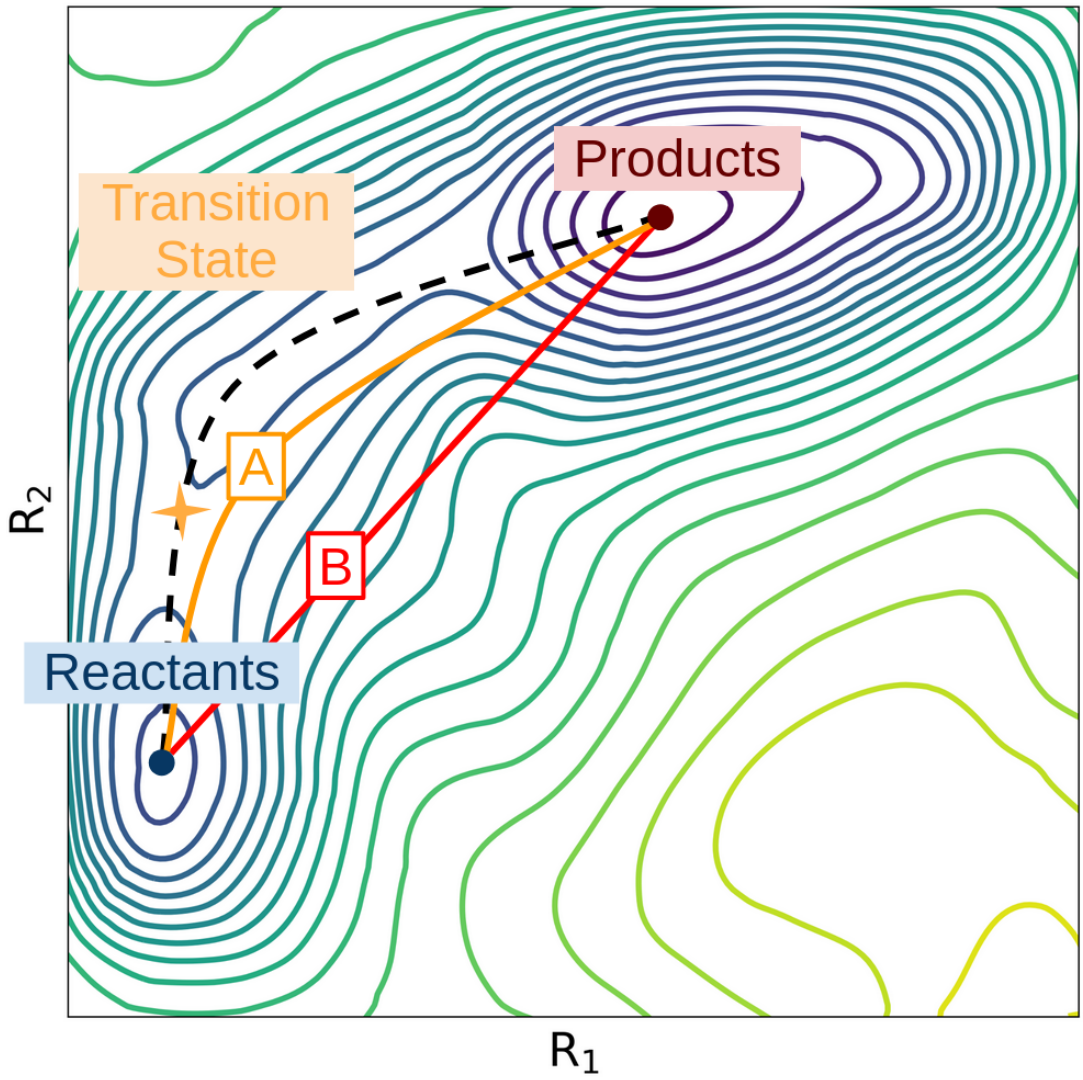

Figure 3.5: A 2-dimensional plot of the energy contours from Figure 3.4. The reactants and products are labeled as before along with the MEP as would be determined by following the path of steepest descent (black, dashed) and two alternative paths (A, orange; B, Red) that account for tunneling.

The main corrections considered in Chapter 5 are the zero curvature tunneling (ZCT)[78], small curvature tunneling (SCT)[79], large curvature tunneling (LCG4)[80], and microcanonically optimized multidimensional model (μOMT)[81]. The explanation provided here is taken with slight modification from Chapter 5, Section 5.2 and is incorporated for a complete discussion.

Key considerations in multidimensional tunneling approximations are: (1) the quantized contribution of all vibrational modes in the tunneling path (which changes the shape of the energy

barrier), and (2) the coupling between motion along the MEP and the vibrational modes perpendicular to it (which results in reaction path curvature, a major consequence of which is the so called "corner cutting" effect, shown by paths A and B in Figure 3.5). The ZCT approximation takes into account (1) but neglects the effects of (2), which leads to seriously underestimated tunneling effects. Meanwhile, SCT, LCT, and μOMT take into account both (1) and (2) to varying degrees. ZCT and SCT use the semiclassical WKB approximation, which gives transmission probability through an energy barrier as in equation: 3.30[74, 77]

$$P^T(E) = \begin{cases} 0 & E \leq E_0 \\ \{1 + e^{2\theta(E)}\} & V_a^G(s = -\infty) < E \leq V_a^G(s_*) \\ 1 - P^T(2V_a^G(s_*) - E) & V_a^G(s_*) \leq E \leq 2V_a^G(s_*) - E_0 \\ 1 & 2V_a^G(s_*) - E_0 < E \end{cases} \tag{3.30}$$

where θ is the imaginary action integral given by equation. 3.31[74, 77]

$$\theta = \frac{1}{\hbar} \int_{s<}^{s>} ds\{\mu[V^{AG}(s) - E]\}^{1/2} \tag{3.31}$$

In equation 3.31, s< and s> are turning points where $V_A^G = E$, μ is the reduced mass, and V^{AG} is the ground state adiabatic potential. A key distinction between ZCT and SCT is that μ becomes $\mu_{eff}(s)$ for SCT tunneling probability calculations. The value of $\mu_{eff}(s)$ is determined by reaction path curvature and the calculations of it are described elsewhere[77].

The LCG4 (other large curvature tunneling approximations exist and are described elsewhere [74, 77]) tunneling approximation is more complex than those of the ZCT and SCT. Key features of this approximation are that tunneling paths are straight lines that connect the reactant and product valley regions (shown by path B in Figure 3.5), it includes tunneling paths through regions of the PES that are far from the MEP, and nonadiabatic regions can be included. The primitive tunneling probability in the LCG4 method is given by equation 3.32[74]

$$P_{prim}^{LCG4}(E) = |T(E)|^2 + \left(\frac{cos\chi\{s_0(E)\hat{,}[s_0(E)]\} + cos\chi\{s_1(E)\hat{,}[s_0(E)]\}}{2} \right)^2 * exp\{-2\theta[s_0(E)]\} \tag{3.32}$$

Where T(E) is the tunneling amplitude that accounts for tunneling initiated by the vibrational modes perpendicular to the reaction coordinate and $exp\{-\theta[s_0(E)]\}cos\chi\{s_{0\,or\,1}(E)\hat{,}[s_0(E)]\}$ is the

amplitude of the tunneling contribution initiated by motion along the reaction coordinate at the classical turning point s_0 for the forward (s_0) and reverse (s_1) motion. $\hat{\eta}$ is the unit vector along the tunneling path, $\chi[s, \hat{\eta}(s_i)]$ describes the angle between the unit vector $\hat{\eta}$ and the unit vector tangent to the reactant path at s, and θ is the action integral which is defined by adiabatic reactant and product regions and a nonadiabitic region in between. This probability is constrained by equation 3.33 for $E \leq V_a^{AG}$ such that the probability tends to 0.50 at the barrier maximum.

$$P^{LCG4}(E) = \left\{ 1 + \frac{1}{2} \frac{[P_{n_{max}}^{LCG4}(V_a^{AG})]^{-1} - 1}{P_{n_{max}}^{LCG4}(V_a^{AG})} P_{n_{max}}^{LCG4}(E) \right\} \times \frac{1}{1 + [P_{n_{max}}^{LCG4}(E)]^{-1}} \tag{3.33}$$

Additional corrections are incorporated to describe tunneling into and from excited states; these are described elsewhere. [74]

The μOMT method strikes a balance between the considerations of small and large curvature tunneling approximations by simply taking the tunneling probability to be the highest of $P^{LCG4}(E)$ and $P^{SCT}(E)$. Thus, the rate constants $k^{VTST/\mu OMT}$ is the rate constant which provides the highest probability of tunneling. In other words, it can be thought of as an upper limit for the system's rate constant.

Chapter 4

Experimental Improvements

Of particular interest to the astrochemical community is the laboratory synthesis and interstellar detection of aminomethanol (NH_2CH_2OH). Previous experiments by Hays [82] and Bunn et al. [18] attempted to synthesize aminomethanol via $O(^1D)$ insertion into methylamine, which is predicted to form barrierlessly[83] with few side products being energetically accessible. However, these attempts resulted in complex chemical networks which generated a variety of detected products, including H_2CO, NH_2CHO, HCN, HNC, as well as two yet unidentified products [18]. Unfortunately, despite their theoretical plausibility, gas phase experiments have, as of yet, been unsuccessful in synthesizing aminomethanol in a detectable form. This chapter describes a variety of efforts to improve detection capabilities, whether through increased instrument sensitivity or through fine tuning of the chemistry. This chapter first describes the use of an alternate $O(^1D)$ precursor, N_2O, over O_3 used in previous experiments. Then descriptions are included for additional adaptations of the scanning routine for use with alternate equipment, addition of new features to improve the user interface, and increases in spectral sensitivity. Finally, an application of these improved sensitivity and interface measures is described and its bearing on future experiments is discussed.

4.1 Alternative Chemical Precursors

4.1.1 Chemical Reaction Networks and Modelling

As described, previous experiments by Hays[82] and Bunn et al.[18] attempted to synthesize aminomethanol but resulted in complex product networks and nondetection of aminomethanol. These experiments utilized ozone (O_3) as a photolytic precursor for on-the-fly $O(^1D)$ generation. Some of the observed extraneous products are likely produced by decomposition of excited insertion products. However, a portion of this complex network is generated by additional photolysis products of O_3, $O_2(^1\Delta)$ and $O(^3P)$, as well as reactions with O_3 itself. Generation of $O_2(^1\Delta)$ is unavoidable using O_3 as the $O(^1D)$ precursor as it is produced in equal efficiency to $O(^1D)$[84], per Reaction 4.1, where hν represents UV radiation at 248 nm.

$$O_3 + h\nu \longrightarrow O_2(^1\Delta) + O(^1D) \tag{4.1}$$

Methylamine (CH_3NH_2) is known to react with $O_2(^1\Delta)$ to form several of the observed side products directly or as part of the reaction network[85, 86], including CH_2NH, NH_2CHO, HCN, and H_2CO. Additional side products that were not observed include HCO, CO, HCNH, NH_3, O_2, H_2O, and H_2. Some species, such as H_2 and O_2, are not visible using the experimental methods outlined because they lack a permanent dipole. Change in other species, such as H_2O, is difficult to quantify since these species are always present in the experiment. Finally, some species such as CO may be visible but not have rotational transitions (or have very weak transitions) in the frequency range covered. In contrast, N_2O photodissociation does not generate $O_2(^1\Delta)$ at all and thus eliminates these side reactions.

As such, N_2O was explored as an alternative precursor for on-the-fly $O(^1D)$ generation. Upon photolysis at 193 nm, N_2O dissociates as in Reaction 4.2, where hν represents laser radiation at 193 nm[87].

$$N_2O + h\nu \longrightarrow N_2(^1\Sigma) + O(^1D) \tag{4.2}$$

The N_2 side product is expected to provide a more challenging path for further reaction with precursors and products of interest, thereby leading to an increased yield of the desired $O(^1D)$ insertion product. Additionally, as noted in Table 4.1, N_2O has a greater quantum yield of photolysis at 193 nm (nearly unity) than O_3 at 248 nm. Morever, because N_2O can be purchase in

high purity form, N_2O circumvents the pressure constraints imposed by the limited efficiency of O_3 generation from O_2.

Models of the experiment were constructed using the Framework for 0-Dimensional Atmospheric Modelling[88] (F0AM) to determine anticipated relative product yields. Models for the system utilizing O_3 as a precursor were developed by Bunn et al.[18] and chemical networks utilizing N_2O as a precursor were developed using the same methods. Briefly, many reactions were pulled from F0AM's list of reactions, which relies on the Master Chemical Mechanism (MCM)[89]. For other reactions that were not in the MCM database, namely photolysis of key species, photolysis frequencies, absorption cross sections, and quantum yields were incorporated from literature[84, 87, 90–92]. Models were run with the parameters listed in Tables 4.1, 4.2, 4.3, and 4.4.

Table 4.1: Photolysis parameters for O_3 and N_2O

Parameter	O_3	N_2O
Photolysis Wavelength (nm)	248	193
Quantum Yield of $O(^1D)$	0.90	≈ 1.00
Absorption Cross Section (cm^2)	1.08×10^{-17}	9.00×10^{-20}
Photolysis Rate Constant (s^{-1})	1.00×10^{-9}	1.40×10^{-9}

Table 4.2: Parameters used for F0AM models of the experiments using O_3 and N_2O as $O(^1D)$ precursors for the synthesis of both methanol and aminomethanol.

Parameter	Value Used
k_{dil} (s^{-1})	1.4×10^4
Pressure (Torr)	850
Temperature (K)	298
Mixing Time (s)	6.0×10^{-4}
Laser Pulse Time (s)	11×10^{-9}
Final Reaction Time (s)	2.0×10^{-3}

Table 4.4: Pressures (Torr) used for gases in the aminomethanol models with O_3 and N_2O as $O(^1D)$ precursors.

Gas Species	O_3 Aminomethanol Model Pressure (Torr)	N_2O Aminomethanol Model Pressure (Torr)
CH_3NH_2	5.00	5.00
O_3	4.756	-
O_2	470.8	-
N_2O	-	474.756
Ar	370.244	370.244

Table 4.3: Pressures (Torr) used for gases in the methanol models with O_3 and N_2O as $O(^1D)$ precursors.

Gas Species	O_3 Methanol Model Pressure (Torr)	N_2O Methanol Model Pressure (Torr)
CH_4	85	85
O_3	2.125	-
O_2	191.25	-
N_2O	-	193.375
Ar	571.625	571.625

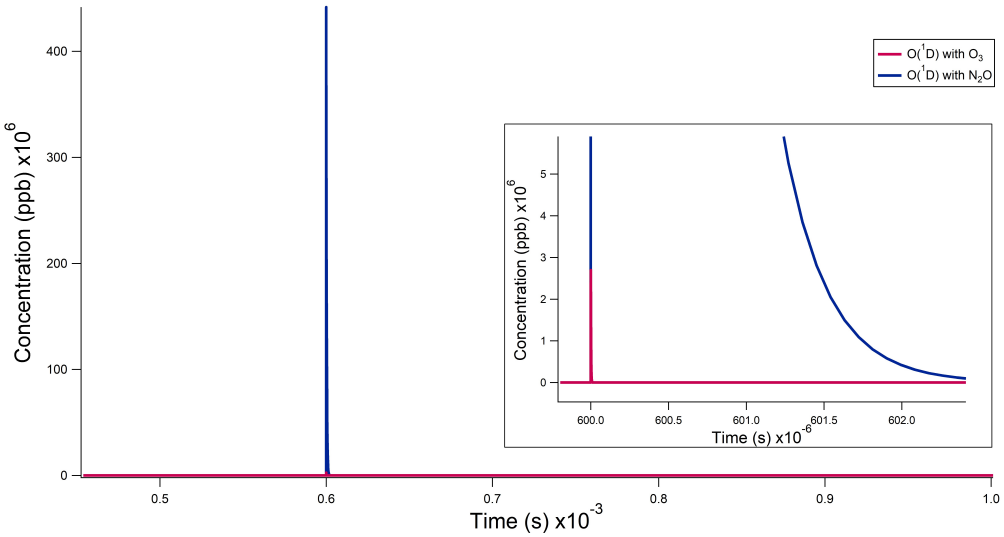

Figure 4.1: $O(^1D)$ production from O_3 and N_2O precursors. Expected $O(^1D)$ product yields are shown above in blue for N_2O and pink for O_3. An inset is shown to make the production from the O_3 precursor more clear.

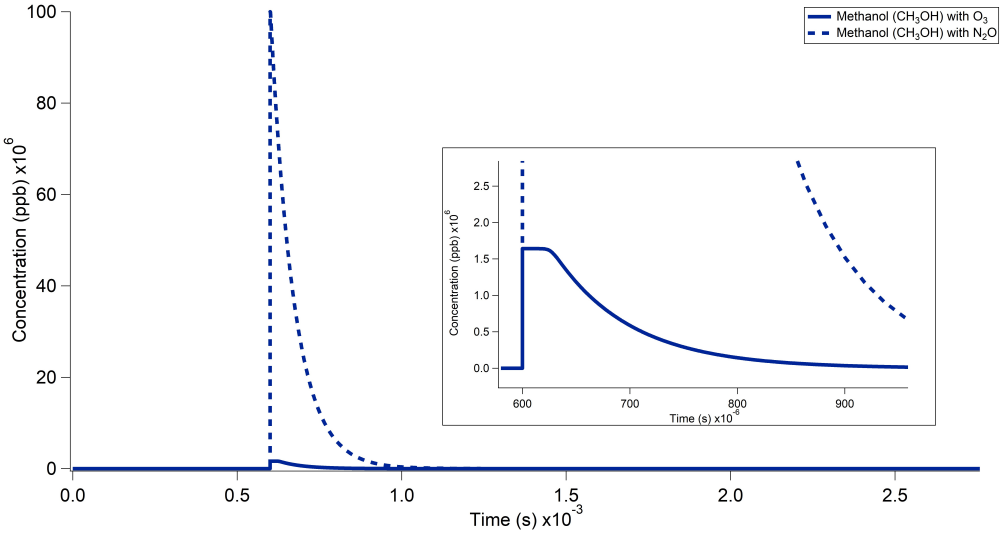

Figure 4.2: CH_3OH production from O_3 and N_2O precursors. Expected CH_3OH yields using O_3 (solid) and N_2O (dashed) as $O(^1D)$ precursors are shown. An inset is shown to make the production from the O_3 precursor more clear.

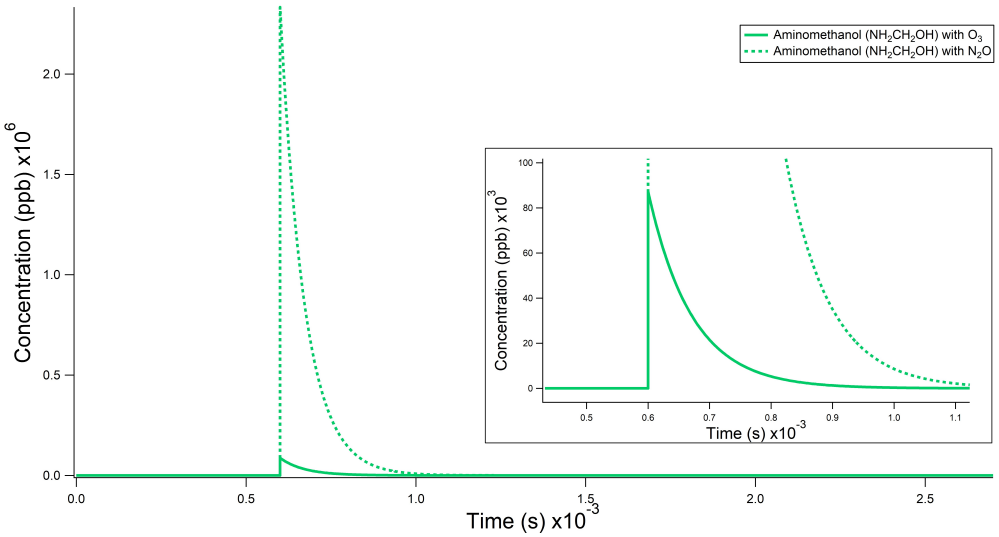

Figure 4.3: NH_2CH_2OH production from O_3 and N_2O precursors. Expected CH_3OH yields using O_3 (solid) and N_2O (dashed) as $O(^1D)$ precursors are shown. An inset is shown to make the production from the O_3 precursor more clear.

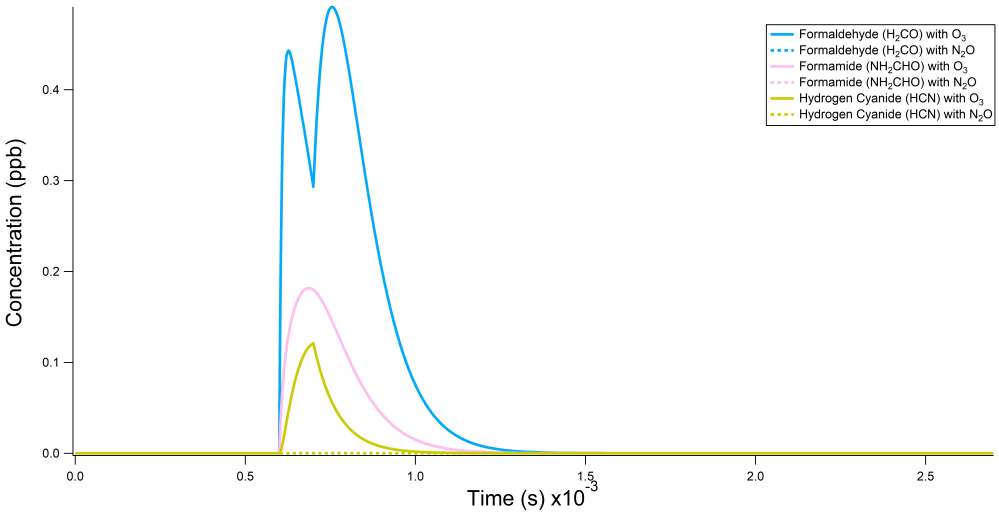

Figure 4.4: Decomposition product yields from O_3 and N_2O precursors. Expected yields of H_2CO, NH_2CHO, and HCN using O_3 (solid) and N_2O (dashed) as $O(^1D)$ precursors are shown. Yields with N_2O are expected to be zero thus no inset is shown.

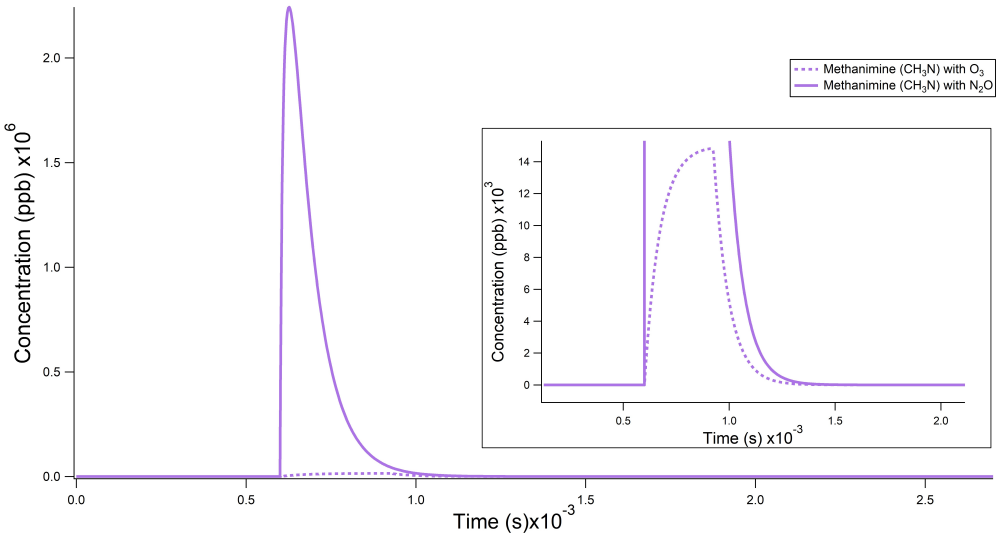

Figure 4.5: CH_2NH yield from O_3 and N_2O precursors. Expected CH_2NH yields using O_3 (solid) and N_2O (dashed) as $O(^1D)$ precursors are shown. An inset is shown to make the production from the O_3 precursor more clear.

According to these models, as shown in Figure 4.1, $O(^1D)$ production is expected to increase by nearly two orders of magnitude using N_2O over O_3 as a precursor. Effects on $O(^1D)$ production are mainly attributable to greater pressure that can be achieved from a pure N_2O cylinder. As a result, it is observed in Figures 4.2 and 4.3 that $O(^1D)$ insertion product yield increases dramatically, by a factor of nearly 80 times in the case of methanol and 30 times in the case of aminomethanol, with N_2O as the $O(^1D)$ precursor. Likewise Figure 4.4 shows that no contribution to the yield of decomposition products H_2CO, NH_2CHO, and HCN is expected with the N_2O precursor. In contrast, CH_2NH is still produced by minor channels and thus has a nonzero contribution even using N_2O as a precursor, as shown in Figure 4.5. However, this production is still reduced by a factor of over 100, which should lead to a far less convoluted spectrum. Given the promising results of the F0AM models shown above, experiments were conducted using N_2O as an $O(^1D)$ precursor on the benchmark CH_3OH system.

4.1.2 Experimental Testing

Experimental Methods

Experiments were conducted on the benchmark methanol system using both O_3 and N_2O as an $O(^1D)$ precursor. These experiments were performed using methods similar to those previously

described by our group [18, 93]. Notable differences in this experiment are that the mixing block was omitted from the experimental design and that a new excimer laser (Coherent Excistar 1000) was used. Separate lines for CH_4 (Airgas, 99.99%), Ar (Airgas, 99.996%), and a 8% O_3 in O_2 mixture or N_2O (Airgas, 99.6%) were managed by MKS 1179A flow controllers. O_3 was generated continuously using the Pacific Ozone L11 Ozone Generator, with an O_2 (Airgas, 99.994%) feed gas. The gases were mixed prior to introduction to the chamber at a backing pressure of approximately 1040 Torr , with a roughly 2:1.5:1 ratio of Ar:O_3:CH_4. The chamber achieved a base pressure of approximately 10 mTorr and an operating pressure (when gases were introduced) of approximately 30 mTorr. The gases were introduced with a pulsed valve (Parker Hannifin Series 9 general valve with 1 mm pinhole aperature) with a quartz photolysis tube attached to the faceplate, after the design of Lester and coworkers[94]. The photolysis tube was 3 cm long with an OD of 5.00 mm and an ID of 1.00 mm (wall thickness = 2.00 mm). In the case of some N_2O experiments, an additional quartz tube was explored which was 2.2 cm long with a 2.4 mm OD and 1.4 mm ID (wall thickness = 0.50 mm). The pulsed valve was run with a repetition rate of 25 Hz and driven by a pulsed driver (Parker Hannifin Iota One). The sample was photolyzed in the quartz tube using a 248 nm pulse with energy of 12.00 mJ in the case of O_3 or at 193 nm pulse with energy of 9.00 mJ in the case of N_2O.

The products exiting the photolysis tube were characterized using the multiplier chain system described previously[18, 93] and the Fast Sweep scanning method developed by Hays[23] and optimized by Zou[24]. Briefly, a microwave synthesizer (Agilent Technologies E8257D PSG) produces a 0-50 GHz signal that is then multiplied by a Virginia Diodes Inc. multiplier chain to achieve higher frequencies. In the case of these experiments, the frequency range probed was 140-225 GHz. The resultant signal was then passed through teflon lenses and focused on the supersonic expansion produced by the pulsed valve apparatus. The signal through the expansion was then focused onto the window of an InSb hot electron bolometer (QMC Ltd. QFIXBI/PTC) detector, the output from which was processed using an oscilloscope card (National Instruments PCI-5124).

Owing to the expected limited lifetime and weak signal of some products, data were collected via targeted line scans in 9 MHz windows. Lines were selected from the catalogs of species known to be present from related studies[93, 95–97] and theory [83, 98]. Scans were averaged for 50,000 averages in the case of stable species such as CH_3OH, H_2CO, and H_2O, and 80,000 averages for the radical species. Water was detected in the experiment but changes in production were difficult

to quantify, as described in Section 4.1.1.

Data Analysis

The raw data were first background subtracted using a python program previously developed by Zou[24]. The collected data were then power corrected to account for fluctuations in power from the multiplier chain system and sensitivity in the detector over the frequency range of the band. This power correction was performed by taking a 100 MHz step size scan across the 140-225 GHz range with an empty chamber, normalizing the intensity against the highest intensity data point, and dividing the intensity of the collected data by the normalized intensity of the power scan. Peak area was calculated for the power corrected scans using the peak fitting function in Igor Pro (version 6).

For observed lines, the transitions were first power corrected to account for power deviations of the multiplier chain system across the frequency range. The power corrected transitions were then fit to a Gaussian line shape using Igor Pro's (Version 6) peak fitting function, returning the peak height, full width at half maximum (FHWM), and fit error. The line data were then used to construct rotation diagrams, originally described by Goldsmith and Langer[99] for astronomical use and later adapted for laboratory use by Laas et al.[100] and again by Yocum[101], to determine temperature and relative column densities of the observed products.

Population diagrams can be constructed using equation 4.3

$$ln(\frac{8\pi k\nu^2 W}{A_{ul}hc^3 g_u}) = ln(\frac{N}{Z}) - \frac{E_u}{kT_{rot}} - lnC_\tau \tag{4.3}$$

$$C_\tau = \frac{\tau}{1 - e^{-\tau}} \tag{4.4}$$

where k is the Boltzmann constant, (ν) is the center frequency of the transition, W is the integrated line intensity, A_{ul} is the Einstein A coefficient, h is Planck's constant, c is the speed of light, g_u is the upper state degeneracy, N is the column density, Z is the partition function, E_u is the upper state energy of the transition, k is Boltzmann's constant, T_{rot} is the rotational temperature, and C_τ is the optical depth correction factor, given by equation 4.4. W can be obtained from the Gaussian fit of the line. The values of g_u, E_u, and Z at select temperatures can be obtained from the molecular catalog on Splatalogue[102] or in the included data from the Cologne Database for Molecular Spectroscopy[103–105] or the JPL Molecular Spectroscopy Database[106]. The Einstein

A coefficient must be calculated using equation 4.5 [107]

$$A_{ul} = (2.7964 \times 10^{-16}) I_{cat}(T) \nu^2 \frac{Z}{g_u} [e^{-E_l/kT_{rot}} - e^{-E_u/kT_{rot}}]^{-1} \tag{4.5}$$

Where I_{cat} is the catalog intensity of the transition, (ν) is the frequency of the transition, Z is the partition function, g_u is the upper state degeneracy, and k is the Boltzmann constant.

Equation 4.3 can then be simplified to equation 4.6 by grouping the constants and coefficients in the left hand side of equation 4.3 into a γ_u term, converting E_u from cm^{-1} to K, and incorporating the assumption that the experiment is optically thin, that is $\tau \ll 1$. This gives a C_τ of 1, resulting in the last term of equation 4.3 being zero.

$$ln(\gamma_u W) = ln(\frac{N}{Z}) - \frac{E_u}{T_{rot}} \tag{4.6}$$

The values of $ln(\gamma_u W)$ and E_u for each transition are then plotted and the data are fit to a least squares linear regression. From the equation of best fit, the slope corresponds to the $\frac{E_u}{T_{rot}}$ term and the intercept to the $ln(\frac{N}{Z})$ term. Thus, the rotational temperature and relative column density of each species can be determined from the respective parameter of the best fit line from its rotation diagram. The column densities are then normalized to a species for determination of relative abundances.

4.1.3 Results and Discussion

Power corrected transitions from CH_3OH and H_2CO are shown in Figures 4.6 and 4.7, respectively. These figures show collected transitions from all experiments, using O_3 as a precursor with the photolysis tube of 2.00 mm wall thickness (top rows), using N_2O as a precursor with the photolysis tube of 2.00 mm wall thickness (middle rows), and using N_2O as a precursor with the photolysis tube of 0.50 mm wall thickness (bottom rows). Of note, only one CH_3OH transition was observable in the system with the N_2O precursor and 2.00 mm wall thickness. Thus, it was not possible to construct a rotation diagram for this CH_3OH dataset and it is simply listed as "detected" in Table 4.5. As is evident from the scale in both Figures 4.6 and 4.7, signal intensity is much greater for H_2CO than for CH_3OH. This is partially attributable to its greater overall dipole moment (2.331 D[108] versus 1.698 D in CH_3OH[109]). The methoxy radical, $CH_3O^{\cdot}$, was observed only when the O_3 precursor was used. The observed transitions are shown in Figure 4.8, though there were

not enough transitions to construct a meaningful rotation diagram.

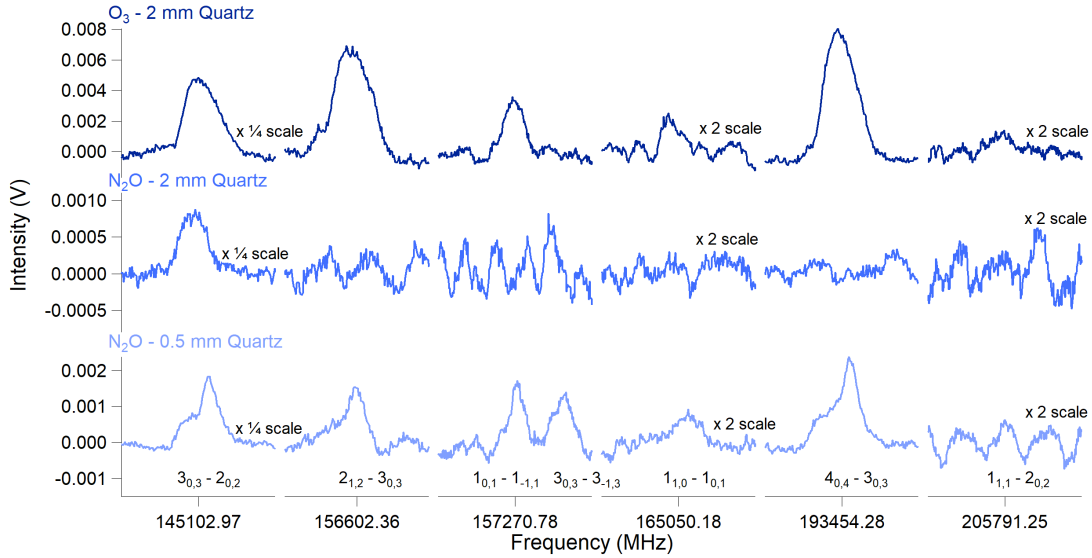

Figure 4.6: Power corrected CH_3OH transitions using the O_3 (top) and N_2O (middle, bottom) precursor to synthesize CH_3OH via $O(^1D)$ insertion. Data were collected using quartz photolysis tube with a wall thickness of 2.00 mm (top, middle) or 0.50 mm (bottom). Quantum numbers ($J_{Ka,Kc}$) of the observed transitions are noted below the lines. Additional scaling is noted where applied.

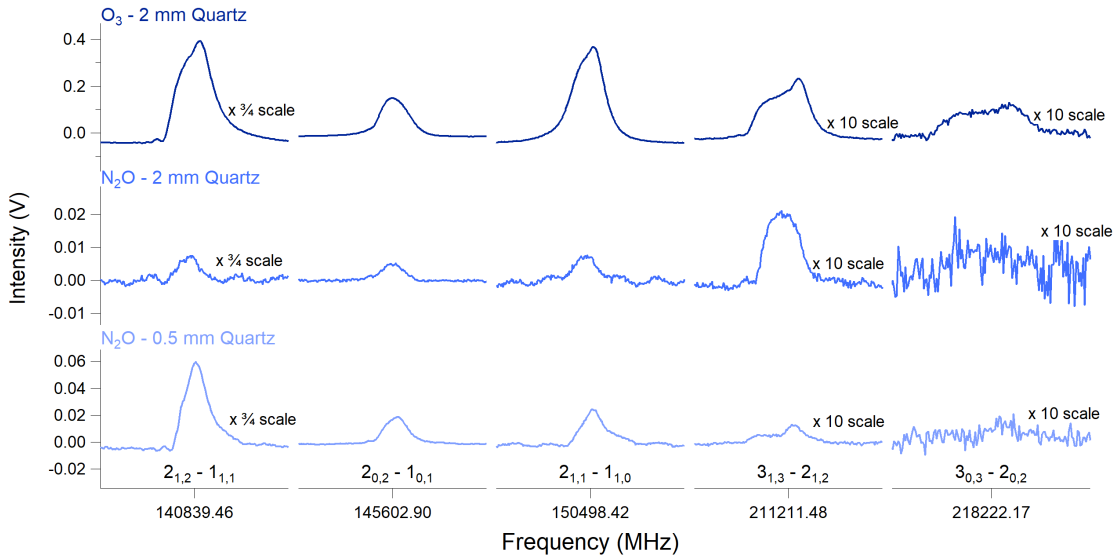

Figure 4.7: Power corrected H_2CO transitions using the O_3 (top) and N_2O (middle, bottom) precursor to synthesize CH_3OH via $O(^1D)$ insertion. Data were collected using quartz photolysis tube with a wall thickness of 2.00 mm (top, middle) or 0.50 mm (bottom). Quantum numbers ($J_{Ka,Kc}$) of the observed transitions are noted above the lines. Additional scaling is noted where applied.

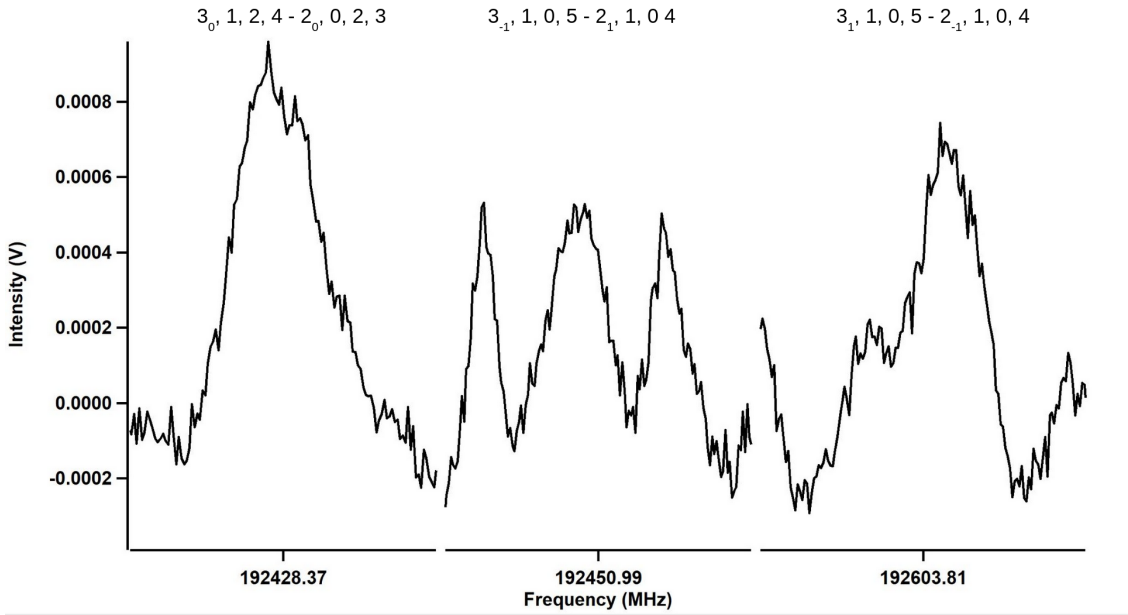

Figure 4.8: Power corrected $CH_3O^{\cdot}$ transitions using the O_3 precursor to synthesize CH_3OH via $O(^1D)$ insertion. Data were collected using quartz photolysis tube with a wall thickness of 2.00 mm. Quantum numbers (N_K, Λ, t, F) of the observed transitions are noted below the lines. No additional scaling was applied.

These transitions from Figures 4.6 and 4.7 were used to construct rotation diagrams following the procedure outlined in Section 4.1.2. Of note, the O_3 precursor data displayed quite poor fits to the data, which is reflected in the high errors associated with the T_{rot} and N_T values. It is likely that the data collected with this setup sampled the turbulent outer shell of the supersonic expansion as well as the quiescent zone of silence, resulting in multiple temperature components and fluctuating intensity. This is likely an issue of optical alignment which was fixed in subsequent experiments. Additionally, H_2CO often shows poorer fit than CH_3OH for rotation diagrams as there are multiple pathways to formation in the reaction between CH_4 and $O(^1D)$ as described by Chang and Lin [98, 110], which can result in varying degrees of collisional cooling. The experiment using N_2O as the $O(^1D)$ precursor with the thick photolysis tube displayed only one CH_3OH transition but several H_2CO transitions. This indicates a considerably reduced yield of not only the $O(^1D)$ insertion product CH_3OH, but of the decomposition and/or side products as well. The presence of some CH_3OH and H_2CO may indicate that some $O(^1D)$ production was taking place but not at the expected degree of efficiency. In contrast, in the case of a thin wall thickness (0.50 mm), the CH_3OH transitions were visible once again. The yield of both CH_3OH and H_2CO increased in this case,

though not nearly to the same degree as the O_3 precursor. The production scaling with thickness of the photolysis tube inidcated that part of the issue with decreased production was the poor transmission efficiency of quartz at a wavelength of 193 nm[111]. This was not an issue at 248 nm for the O_3 precursor as quartz has greater tranmsission efficiency at this wavelength. If N_2O is pursued as an $O(^1D)$ precursor in future experiments, it is recommended that a material transparent at 193 nm such as fused silica[111] be used for the photolysis tube over traditional quartz. This option was explored during the current study but difficulty was encountered sourcing a manufacturer that could produce photolysis tubes of the correct specifications made from fused silica. An additional factor that may have influenced these results is the lower absorption cross section of N_2O compared to O_3 (9.00×10^{-20} cm^2 vs 1.08×10^{-17} cm^2)[84, 87]. Though, the presence of both CH_3OH and H_2CO transitions with the thin walled tube show that some combination of high quantum yield and higher achievable pressure is enough to overcome this absorption cross section to generate detectable products. Scans of these products using the N_2O precursor were attempted without a photolysis tube, however product yields were too low for detectable transitions. The data from the rotation diagrams in Figures 4.9 and 4.10 are summarized in Table 4.5. Although the overall yield of reaction products did not improve using N_2O as a precursor, the ratio of CH_3OH:H_2CO between trials indicates a slight improvement in production of insertion products. The ratio of CH_3OH:H_2CO was 0.85 in the case of the O_3 precursor with a photolysis tube wall thickness of 2.00 mm and 0.94 in the case of the N_2O precursor with a photolysis tube wall thickness of 0.50 mm. The ratio of CH_3OH:H_2CO was indeterminable in the case of the N_2O precursor with a thick photolysis tube due to the number CH_3OH transitions collected.

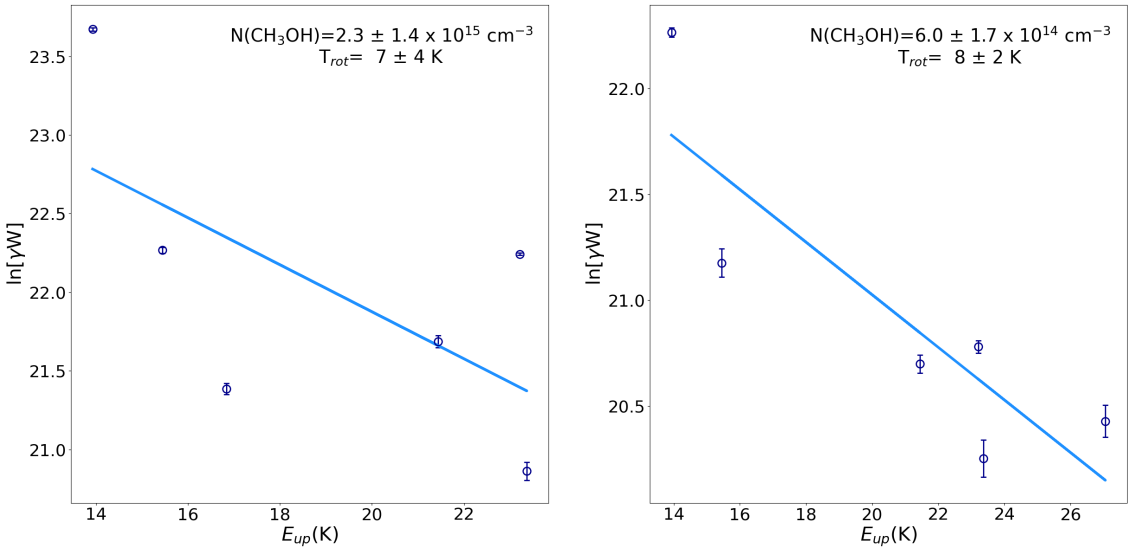

Figure 4.9: Rotation diagram constructed from collected CH_3OH transitions using the O_3 (left) or N_2O (right) precursor to synthesize CH_3OH via $O(^1D)$ insertion. Data were collected using quartz photolysis tube with a wall thickness of 2.00 mm (left) or 0.50 mm (right). Data were fit to a least squares linear regression. The rotational temperature and relative column density are derived from the slope and y intercept of the best fit line, respectively.

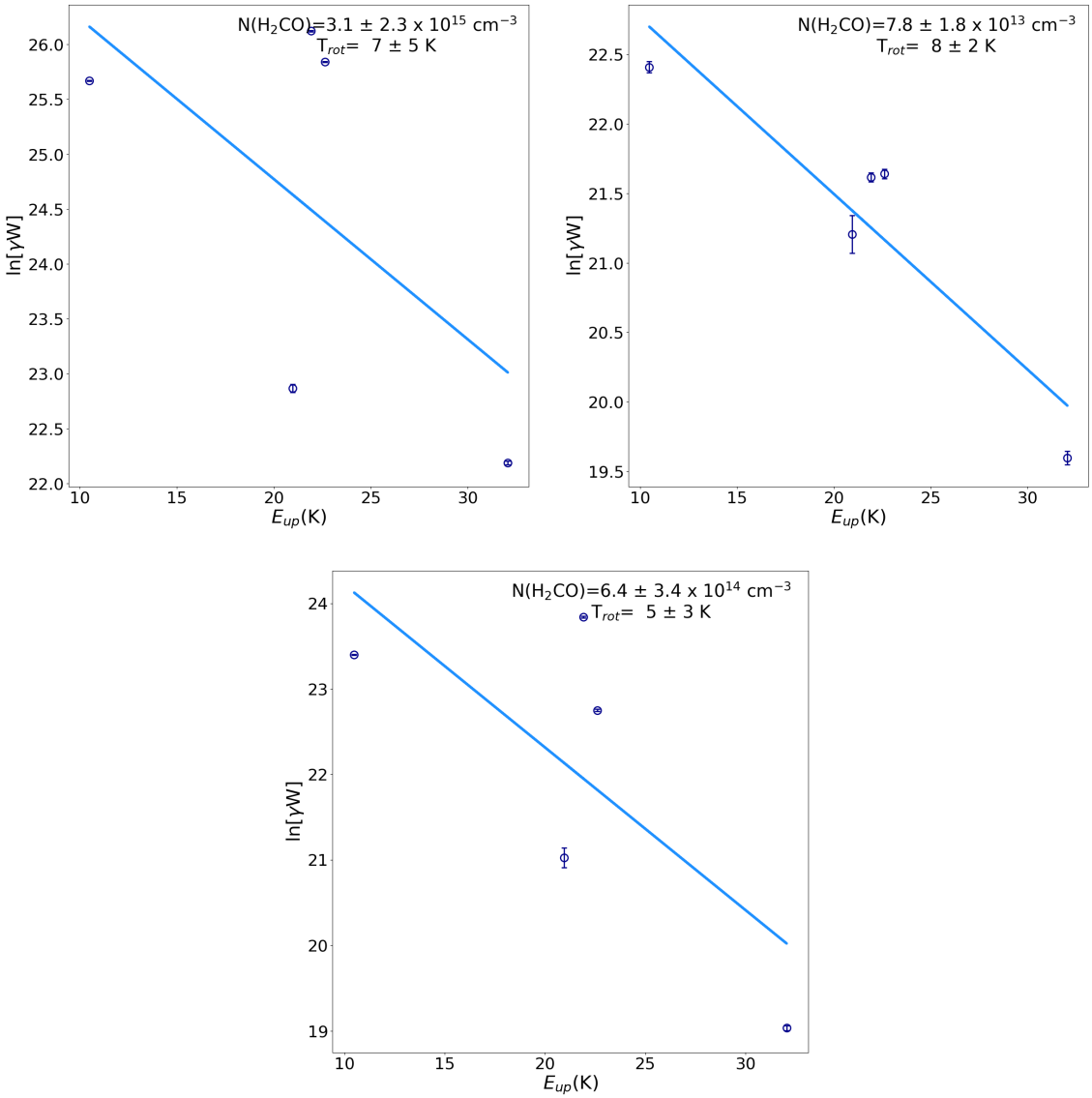

Figure 4.10: Rotation diagrams constructed from collected H_2CO transitions using the O_3 precursor (top left) or N_2O (top right, bottom) to synthesize CH_3OH via $O(^1D)$ insertion. Data were collected using quartz photolysis tube with a wall thickness of 2.00 mm. Data were fit to a least squares linear regression. The rotational temperature and relative column density are derived from the slope and y intercept of the best fit line, respectively.

Table 4.5: Rotational temperatures and relative yields of CH_3OH and H_2CO observed in synthesis of CH_3OH via $O(^1D)$ insertion.

	O_3 2.00 mm wall thickness		**N_2O** 2.00 mm wall thickness		**N_2O** 0.50 mm wall thickness	
Product	**T_{rot}(K)**	**N_T (cm^{-3})**	**T_{rot}(K)**	**N_T (cm^{-3})**	**T_{rot}(K)**	**N_T (cm^{-3})**
CH_3OH	7 ± 4	2.3 (± 1.4) x 10^{15}	Detected	Detected	8 ± 2	6.0 (± 1.7) x 10^{14}
H_2CO	7 ± 6	2.7 (± 2.3) x 10^{15}	8 ± 2	7.8 (± 1.8) x 10^{13}	8 ± 2	6.4 (± 3.4) x 10^{14}
$CH_3O^{\cdot}$	Detected	Detected	Not Detected	Not Detected	Not Detected	Not Detected

4.1.4 Conclusion

The data presented here show that N_2O is a viable aternative precursor to O_3 for $O(^1D)$ driven gas phase chemistry. However, while products are detectable when synthesized using N_2O as a precursor, they do show an overall decrease in signal intensity. Experiments run using decreased wall thickness of the quartz photolysis tube show that signal intensity scales with wall thickness, indicating the incident radiation from the laser is being cut by the low UV transmission of the quartz tube. Thus, use of a more transparent material for the photolysis tube such as fused silica may lead to increased signal intensity. Despite the lower product yields, the ratio of CH_3OH:H_2CO indicates that there is a modest increased production in the $O(^1D)$ insertion product over other products with N_2O. Based on these data, using N_2O as an $O(^1D)$ precursor may quench unwanted side reactions but still poses a challenging implementation owing to the lower absorption cross section and poor transparency of traditional glass at the wavelengths needed to initiate photolysis. Therefore, it is recommend if N_2O is pursued as a precursor in such experiments, that an appropriately transparent material such as fused silica be used in construction of the photolysis tube.

4.2 Updates to the Fast Sweep Program and Experiment Optical Configuration

4.2.1 Adapting Fast Sweep for an Alternate Oscilloscope

In addition to adjusting the chemistry of the experiment, the equipment used for data collection was updated. The efforts to adapt the fast sweep program first implemented by Hays et al. [23] and optimized by Zou[24] for use with a new oscilloscope are described here. The goals of these updates were to improve the user interface of the data collection program, and provide a more cost

effective alternative to the previously used oscilloscope card (National Instruments PCI-5124). The core principles of how the Fast Sweep program operates are described in Section 2.3.1.

The oscilloscope chosen to replace the original PCI oscilloscope card was the Rigol DS1202Z-E. This oscilloscope provides comparable resolution and better channel bandwidth and sample rate, as per Table 4.6. Most importantly, the cost of operation was significantly reduced using the Rigol oscilloscope, which is available for $369 as opposed to the recommended replacement oscilloscope card for the PCI-5124, which starts at a base price of $15,285. Replacement of the oscilloscope in the Fast Sweep code simply required updating the instrument drivers and changing the appropriate commands to use the rgds1kz instrument drivers within LabWindows. Some workarounds were needed to address quirks in the oscilloscope's data output in order to access the high quality data that was being collected by the scope. These workarounds and other attempts to maximize the oscilloscope's utility are described in Section 4.2.2.

Table 4.6: Oscilloscope operating parameters per manufacturer specification sheets[112, 113]

Parameter	NI PCI-5124	Rigol DS1202 Z-E
Max Sample Rate	200 MS/s	1 GaS/s
Resolution	12 bit	12 bit
Channel Bandwidth	150 MHz	200 MHz

4.2.2 Upgraded Program Capabilities and Quality of Life Features

Once adapted to accommodate an alternative oscilloscope, minor bugs were addressed (namely memory leaks that would cause the program to crash over a certain number of averages), several quality of life features were added, and the user interface (UI) was updated to provide a more intuitive and streamlined experience. Additional avenues to maximize the oscilloscope's potential were also explored. The user interface for the original version of Fast Sweep developed by Hays[23] and Zou[24] is shown in the top of Figure 4.11. There are a variety of UI features for controlling the synthesizer, oscilloscope, and viewing raw data within this interface. The user interface for Fast Sweep 2.0 is shown in the bottom of Figure 4.11. The many available settings in Fast Sweep v1.0 were sequestered into separate pages within the program to provide focus to the interface and clear distinction of what instrument the page controlled. Additionally, settings were separated into numbered sections to guide the user through experiment setup. Available RF settings are shown in Figure 4.12. The user is guided to set the multiplier band in use (and thus the accessible frequency

range) and the scan resolution in section 1, followed by providing scanning frequencies individually (section 2a) or in batches by uploading a linelist (section 2b), then setting modulation settings, including the deviation and rate of the local oscillator in section 3, and finally initializing the synthesizer in section 4. The graph to display collected data to the right in the UI is outside of the tab containers and thus visible no matter which tab is active. Documentation was also added such that right clicking on a section will provide a popup describing the functions within the respective section as in Figure 4.13. This was done to make information accessible as the program is being used and make the program more accessible to new users.

Figure 4.11: User interface with Fast Sweep v1.0 (top) and v2.0 (bottom). In Fast Sweep v2.0, controls for the instruments used are in appropriate tabs and data are displayed during operation in the graph region to the right. A legend populates the blank space to the right as data are added.

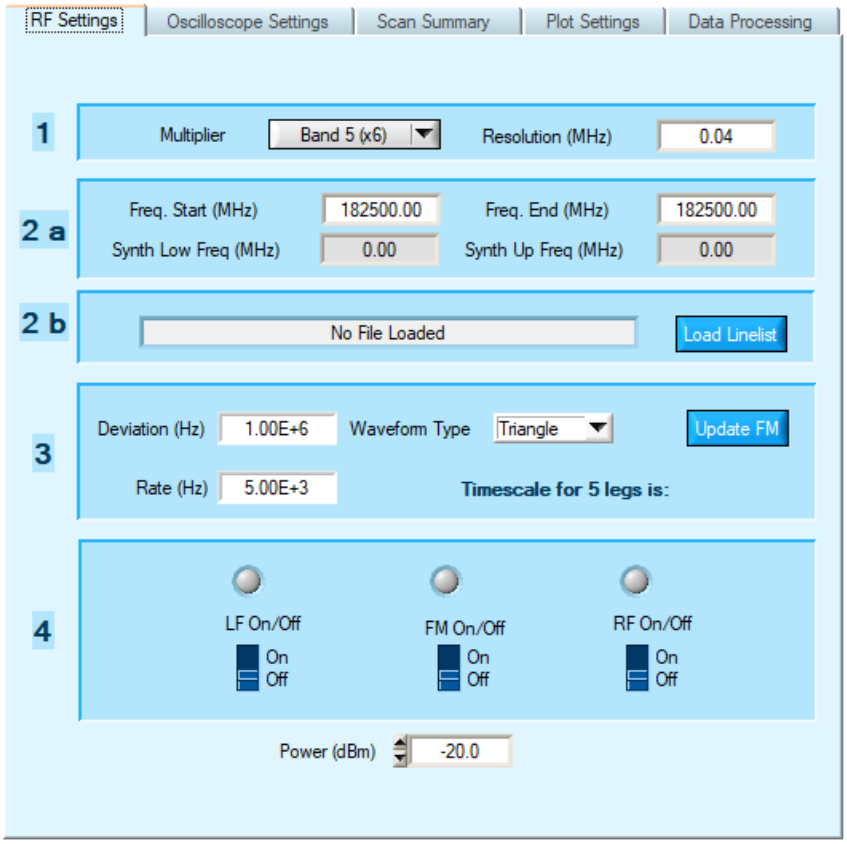

Figure 4.12: The RF settings interface to control the Agilent microwave synthesizer in Fast Sweep V2.0. Users are able to set the level of multiplication and resolution in section 1, the frequencies scanned in sections 2a or 2b, the modulation settings in section 3, and initialize the instrument in section 4.

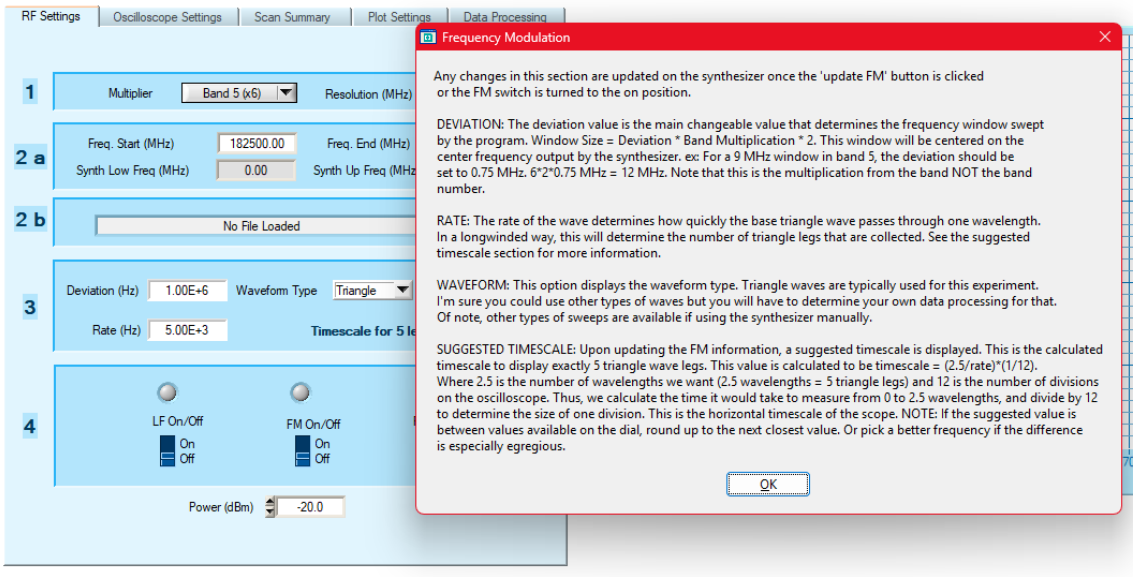

Figure 4.13: An example of a help popup provided when the user right clicks on the program with explanation of how parameters are used.

Additional features were added with the scan summary (Figure 4.14) and data processing tabs (Figure 4.15). The scan summary was implemented to provide an overview of key data collection settings as the experiment is running. The experiment title allows the user to set a naming convention for the collected data that will be incorporated into the output filename along with the center frequency of the scans and the number of averages of the scan. A progress bar was also added to give users a visual indication of how much data has been collected and how much collection remains. After data collection, the raw frequency modulated signal is plotted in the chart on the right side of the UI. Users can then process this data directly in the data processing tab and view the output data immediately within the program. This data processing allows the user to use a GUI to interface with the Sweep.py processing script written by Zou[25] rather than providing command line arguments. This feature makes the program more accessible to new students and streamlines data processing.

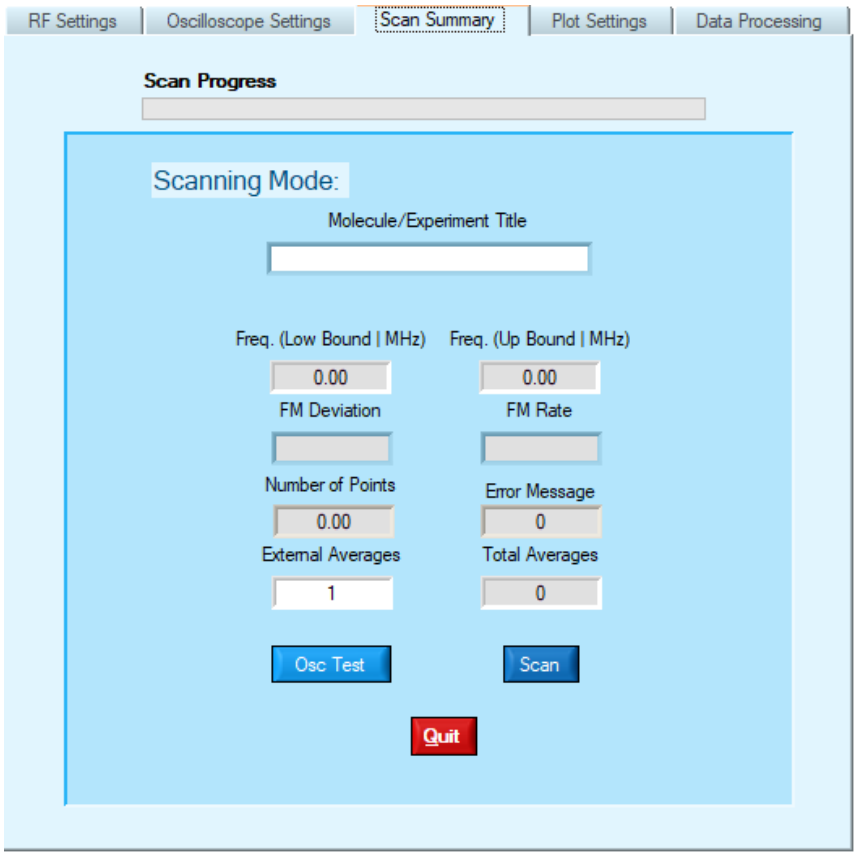

Figure 4.14: The scan summary interface to report scanning conditions in Fast Sweep v2.0. At the top, a progress bar indicates to the user how many data acquisitions are left. The mode of operation is indicated as is the naming convention. The frequencies scanned, modulation settings, and number of averages are summarized for user reference.

Figure 4.15: The data processing interface to provide a GUI for the Sweep.py processing script in Fast Sweep v2.0. The user is able to provide all arguments needed via a graphical user interface, including file names and paths, to process and view data within the Fast Sweep program.

Some challenges were encountered during implementation of the updates due to operating quirks of the oscilloscope. One such case is that the instrument driver command to read the data resulted in a maximum output of 1,000 data points, despite up to 12 million data points being collected. This issue was circumvented by utilizing USB I/O commands to pull data. The resultant output led to increased data density over the Fast Sweep v1.0 program, as shown in Figure 4.16, largely owing to the greater accessible memory in the Rigol DS1202Z-E. Another issue addressed was a large spike at the end of the data buffer caused by odd formatting at the end of the array. This was circumvented by using multiple data collection commands (as the output data buffer had a maximum character capacity), truncating the data written to the array slightly early, and concatenating the collected data arrays together into one large array.

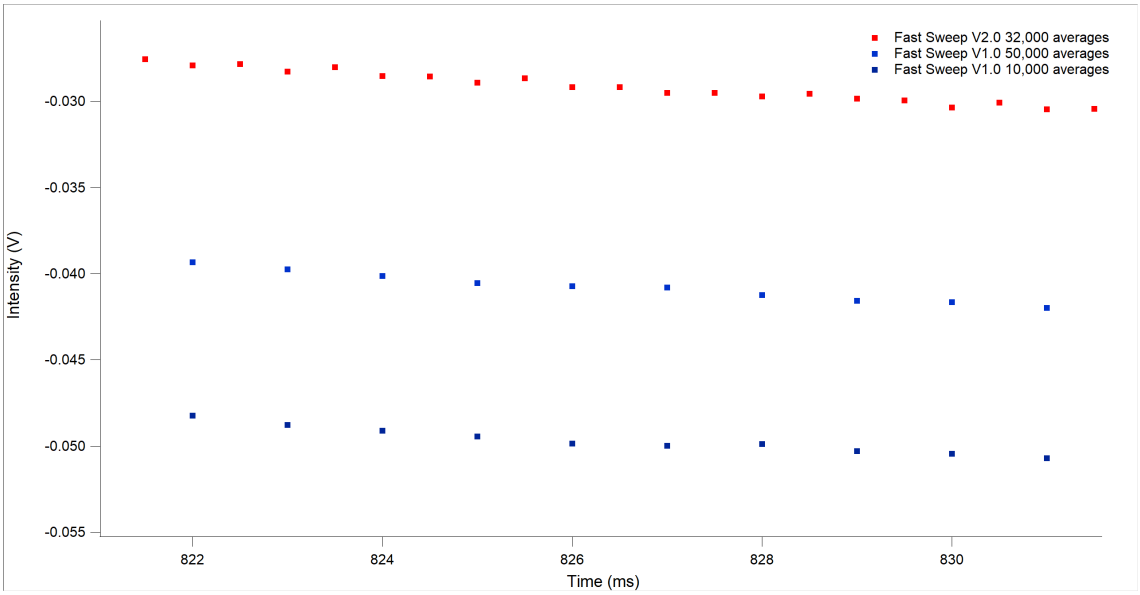

Figure 4.16: Density of the collected data points in Fast Sweep v1.0 (blue) as compared to v2.0 (red). Data output is roughly double the density with the capability of collecting with the potential for far greater density.

An additional avenue that was explored was utilizing the internal averaging function of the oscilloscope to reduce the number of processes necessary for data collection and free up resources on the computer. A combination of internal averages (those acquired on the oscilloscope) and external averages (those taken on the computer) were explored as potential solutions and the results of this are discussed in Section 4.2.4.

4.2.3 Multipass Implementation

Experimental sensitivity was enhanced after implementation of the new scanning routine through setting up a multipass optical arrangement. The motivation of this multipass optical cavity was to increase the number of "free" scans to counterbalance some of the slower aspects of data acquisition and increase signal sensitivity. Initially, a spherical cavity was explored after the design of Laas et al. [100], originally adapted from Kaur et al. [114]. Such a cavity is depicted in Figures 4.17 and 4.18. The stability of an optical cavity is measured by its g factor, as per Equation 4.7:

$$g_n = (1 - L/r_n) \tag{4.7}$$

where n is the index of the mirror, L is the length of the cavity, and r_n is the radius of curvature[115, 116]. A cavity is most stable when $0 \leq g_1 g_2 \leq 1$, which occurs when 0 < L < r or r < L < 2r. In the case of a concentric resonator, the greatest stability is achieved when $r_1 = r_2 = L/2$. Outside of these lengths, beam divergence can occur causing signal to "spill out" of the cavity and power loss to occur.

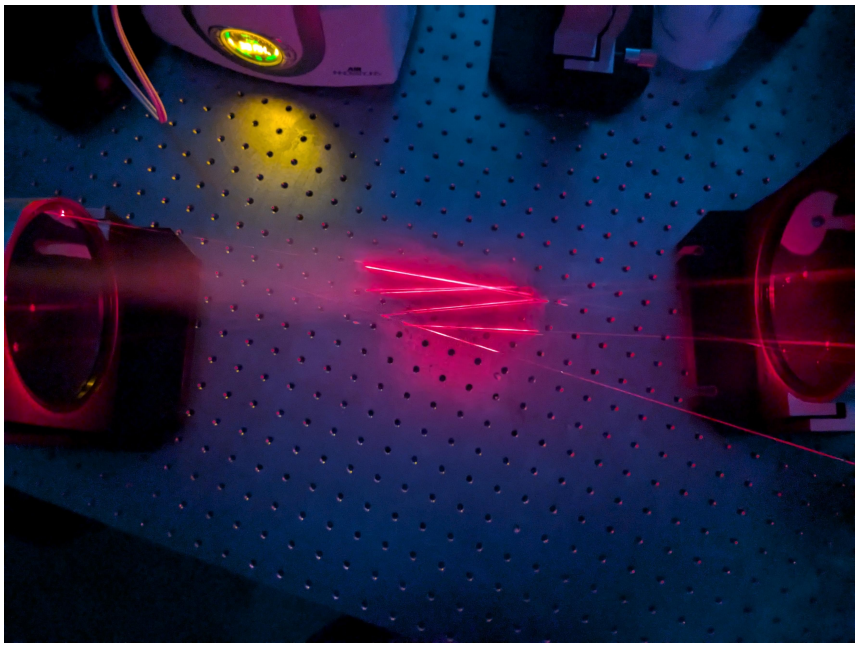

Figure 4.17: Spherical mirrors used to create a multipass optical system, aligned with a HeNe laser. Water vapor is used to better visualize the beam paths, showing tightening of the beam waist in the center of the optical path to approximately 1 inch.

This cavity used aluminum 6 inch diameter spherical mirrors with a 12 inch focal length (Edmund Optics 32-836). Figure 4.17 shows a test system on the benchtop displaying a proof of concept for the multipass. The system displays refocusing effects resulting in a tight beam waist ($\approx$ 1 inch) in the center of the cavity with an ideal cavity length of 24 inches. In the chamber, a visible helium neon (HeNe) laser (Melles Griot 25-LHR-073-249) is colinearized with the millimeter/submillimeter system consisting of the a microwave synthesizer (Agilent Technologies E8257D PSG), multiplier chain (Virginia Diodes WR5.1), PTFE lenses, and an InSb hot electron bolometer (QMC Ltd. QFIXBI/PTC). The visible system is first aligned before the non-visible system is finalized to more easily follow the optical path. When assembling this system, power measurements of the millimeter/submillimeter beam were taken at key points in the optical path using a zero bias detector (ZBD, Virginia Diodes WR5.1) processed through a lock in amplifier

(SRS 830). This detector was used as it could move freely through the beam path unlike the InSb hot electron bolometer typically used in experiments.

This configuration worked quite well on the bench top. However, once implemented into the chamber, showed significant power loss and unpredictable behavior from the millimeter beam once at the detector, as shown in Figure 4.18. This issue was primarily caused by the large size of the mirrors as well as the large mounts needed to support them. The size of the mounts made it difficult to achieve enough passes for ideal focusing to occur without blocking the beam paths of the other optics needed to focus and collimate the mm/submm beam. Smaller mirrors (Edmund Optics NT32-824) with a 7.62 cm diameter and focal length were also explored but again produced issues with spacing and configuration largely due to the size of the mounts. The mounts would scatter the beam as there were narrow clearances at the entrance and exit. While it was possible to minimize this behavior with the smaller mirrors, it was not fully avoidable given the space constraints. Power retention was significantly better in this optical system but still did not provide the sensitivity required for desired experiments.

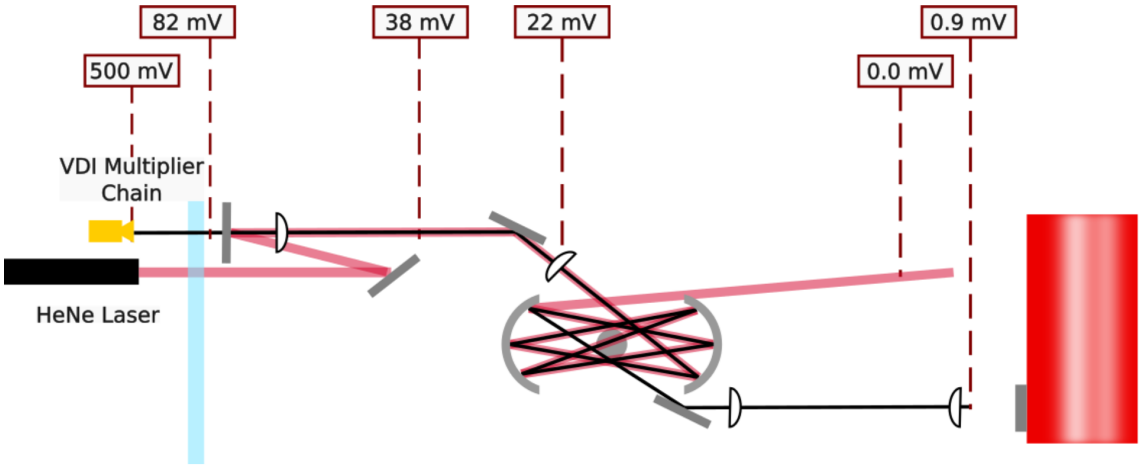

Figure 4.18: A schematic showing the optical path followed by both the HeNe laser (red) and the millimeter/submillimeter signal (black) in the spherical cavity. Power measurements taken with a ZBD are shown at key points along the optical path.

As an alternative to the previously used spherical cavity, a plane parallel cavity was explored. Flat aluminum mirrors of a 2 inch diameter (Edmund Optics 45-614) in kinematic mounts were used to create a cavity of just 8 cm centered over the sample source. A schematic of this optical configuration and the beam path behavior is shown in 4.19. This optical configuration displayed

much more predictable behavior and greater power retention along the beam path. Ultimately, this setup was able to achieve 5 passes through the sample path, as shown in Figure 4.20. The success of this system is largely attributed to its smaller usable cavity length which minimizes beam divergence effects. Whereas the stability of a cavity using spherical optics is dependent upon the length of the cavity, planar mirrors can be thought of as having infinite curvature, which will always produce a g of 1 per Equation 4.7. It also has the added benefit of greater placement flexibility and greater clearance for the beam path owing to its smaller kinematic mounts. Additionally, it is more cost effective than the larger spherical mirrors at $30 per mirror rather than $100+.

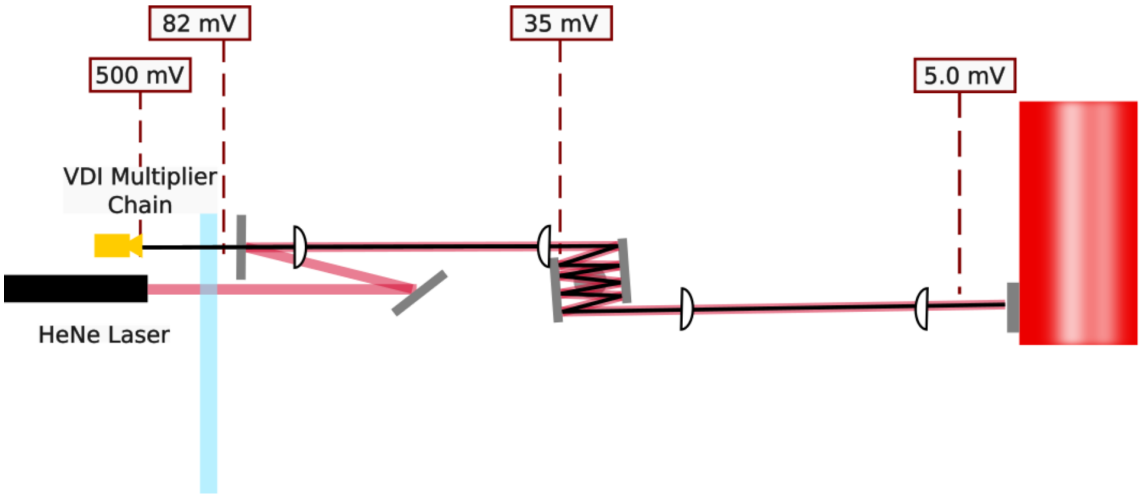

Figure 4.19: A schematic showing the optical path followed by both the HeNe laser (red) and the millimeter/submillimeter signal (black) in the planar cavity. Power measurements taken with a ZBD are shown at key points along the optical path.

Final confirmation of the behavior of the millimeter/submillimeter beam was performed by measuring the power output from the bolometer and passing a thin object through the cavity path that would block the beam. The system showed significant power loss when the beam path was blocked, occurring 5 times throughout the cavity, confirming that the millimeter/submillimeter beam was indeed making 5 passes as the HeNe did. The results of this test are shown in Figure 4.20. Power tests were performed at the center frequency of band 5 (180 GHz) with 15% modulation depth and an amplitude modulated (AM) signal, achieving a power output of 654 mV.

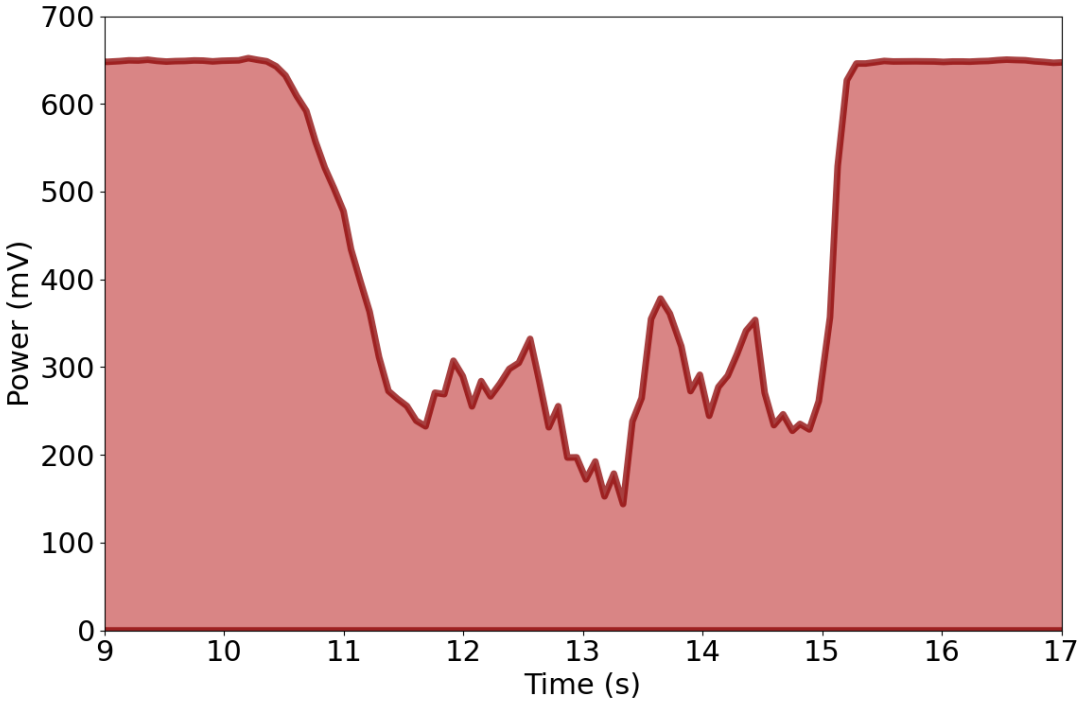

Figure 4.20: Power spectrum at the InSb bolometer when an opaque object is passed through the cavity. Five power dips occur over the optical path, indicating that the path crosses through the sample 5 distinct times.

4.2.4 Benchmarking the New Program

With both the new scanning routine and the multipass configuration implemented, benchmarking on the newly improved experiment was conducted. Benchmarking was performed again using the $O(^1D)$ insertion into CH_4 to synthesize CH_3OH as described in Section 4.1. Briefly, Ar (Airgas, 99.996%), an 8% O_3 in O_2 mixture, and CH_4 (Airgas, 99.99%) gases were balanced using MKS 1179A flow controllers in a roughly 2:1.5:1 ratio at a backing pressure of approximately 1040 Torr and introduced via a pulsed valve (Parker Hannifin Series 9 general valve with 1 mm pinhole aperature) run at a 25 Hz repition rate. O_3 was generated using the Pacific Ozone L11 Ozone Generator with O_2 (Airgass, 99.994%) feedgas. The 2.00 mm wall thickness photolysis tube was attached to the faceplate and the laser (Coherent Excistar 1000) was operated at 248 nm with a 12.00 mJ pulse energy. The data were collected using the newly optimized Fast Sweep scanning routine. Transitions of both CH_3OH and H_2CO were measured, which provided both high and low intensity product signals to benchmark against. To begin, select methanol transitions were

used to confirm that signal was indeed high enough to detect products and that the multipass did indeed increase signal intensity. As shown in 4.21, the same signal intensity is observed for these methanol transitions with the multipass configuration with 5 times fewer averages. Moreover, there is a reduction in the noise level at the baseline, leading to a greater signal to noise ratio that is beneficial for low yield or low intensity products.

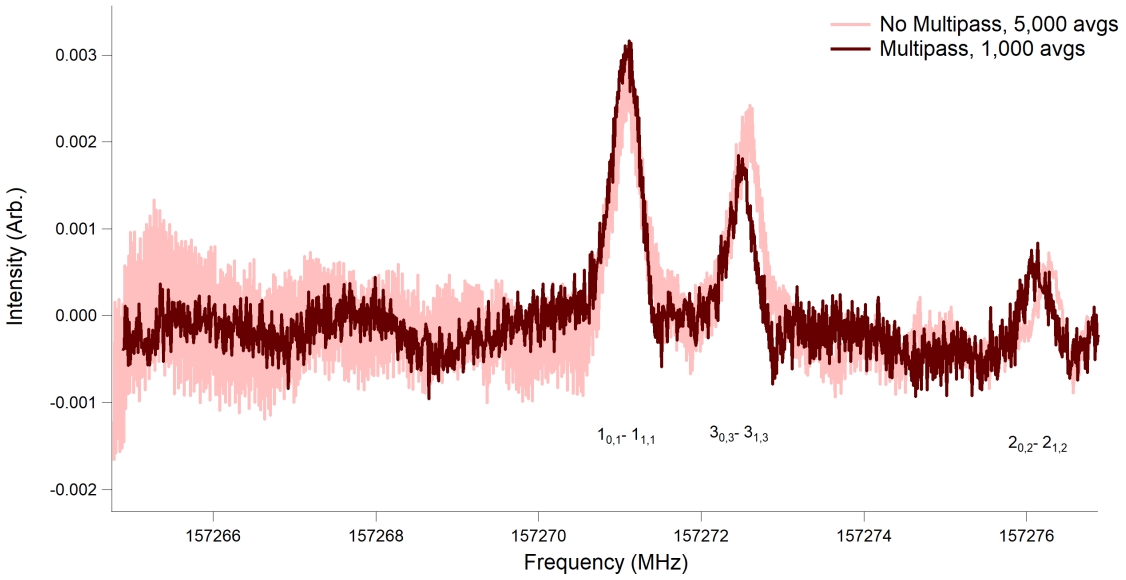

Figure 4.21: Methanol transitions with and without the multipass. The light red trace shows data collected without a multipass system (5,000 averages) and the dark red trace shows data collected with the multipass system (1,000 averages).

Next, the effects of signal averaging were explored. The purpose of this was twofold, first to confirm that signal averaging was having the intended effects; and second, to test the feasibility of exploiting the internal averaging of the oscilloscope as discussed in Section 4.2.2. The time to acquire averages through each method was measured, and as in Table 4.7 there was a significant time disparity between the oscilloscope and computer collected averages, largely due to the time to transfer data via USB and processing the data through the scanning routine. As shown in Figure 4.22, the increased averages results in a reduction in baseline noise.

Table 4.7: Time (s) to collect data using averaging on the oscilloscope and on the computer

Number of Averages	Time to Collect on Oscilloscope (s)	Time to Collect on Computer (s)
2	< 1	5.88
4	< 1	7.37
8	< 1	9.38
6	< 1	17.07
32	< 1	33.89
64	≈ 1	60.97
128	≈ 1	119.65
256	1.35	238.27
512	3.15	469.87
1024	7.60	928.38

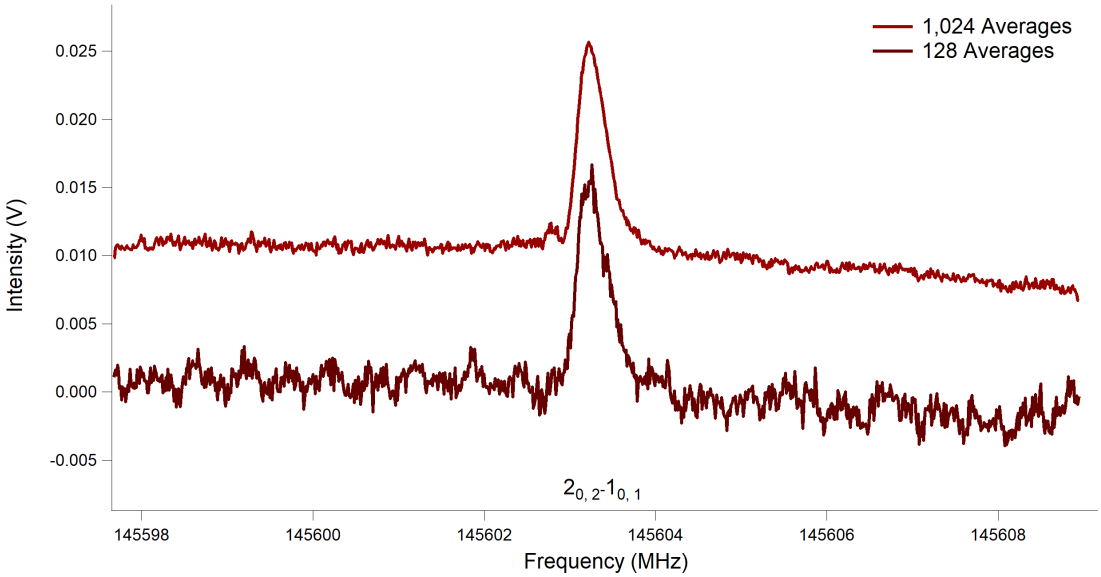

Figure 4.22: A processed acquisition of formaldehyde at 128 and 1,024 oscilloscope averages. This comparison shows the feasibility of using the oscilloscope's internal averaging feature to speed up data acquisition. Data offset for clarity.

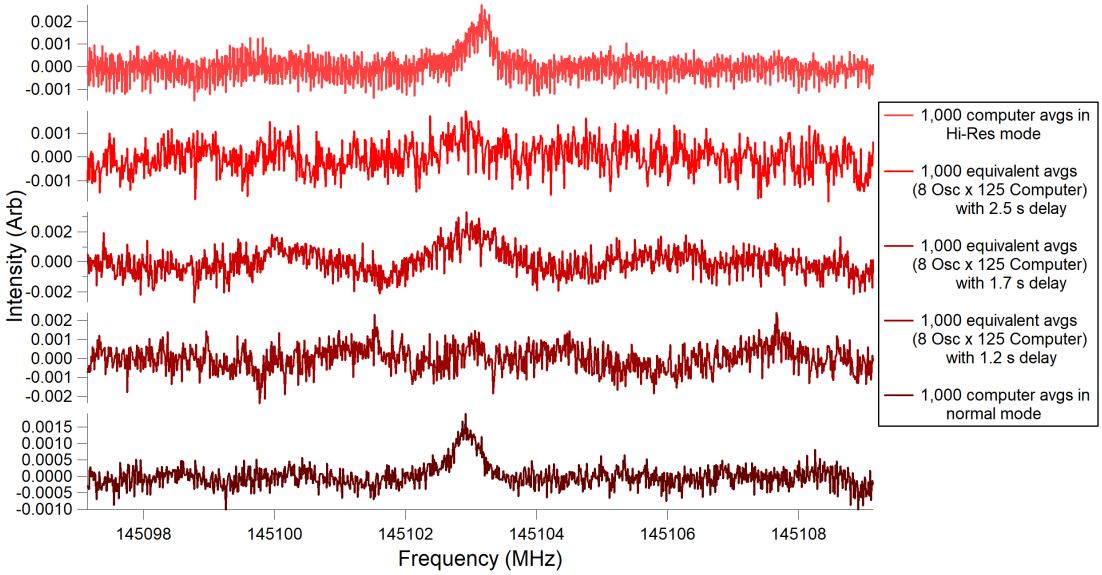

Figure 4.23: Scans taken with different available oscilloscope settings attempting to utilize the internal averaging capabilities to speed up data acquisition.

For high intensity signals such as the formaldehyde signal shown in Figure 4.22, Fast Sweep v2.0 behaved as expected, showing significant smoothing in data with greater numbers of averages, whether this was performed with the oscilloscope or computer. However, when tested on a lower intensity signal as in Figure 4.23, the signal disappeared when using averaging on the oscilloscope. This occurred regardless of the time delay set in Fast Sweep v2.0, indicating that this was not merely a matter of undersampling. However, whenever computer averaging was used, as in Figure 4.23, the signal returned, indicating this was specifically an issue with the oscilloscope's averaging function. While the documentation for the instrument and contacting the manufacturer indicated that there was no averaging or special signal processing occurring, it became apparent that the weak signal was being processed out. Indeed, attempting to use the math functions within the oscilloscope to manually average the signals resulted in an automatic smoothing factor of at least 3 times smoothing being applied during each average, which could not be removed[117, 118]. As the manufacturer was unaware of this effect and the manual averaging could not remove the smoothing effect, the only feasible option for averaging was unfortunately exporting the raw signal upon each acquisition and processing all of the averaging on the computer side. This particular issue highlights a weakness in the Fast Sweep v2.0 data pipeline and the importance of benchmarking edge cases, especially when implementing new protocols.

In theory, the speed of data acquisition can likely be greatly increased by using this internal averaging feature as data collection was much faster when it was implemented. Under the current setup, while this may work for particularly intense signals, it is likely to erroneously remove weak signals and it is unclear where the exclusion threshold may be. If this option is explored in the future, it is recommended that any replacement oscilloscope is insured to not alter or smooth data in this way. Additionally, it may increase the speed of data collection even further to have an oscilloscope that does not require updating an interface, such as a Picoscope. Such an oscilloscope would maintain the flexibility benefits provided by a usb oscilloscope over the required PCI installation as in the National Instruments oscilloscope cards but remove overhead involved in data collection.

Despite the challenges encountered due to signal averaging, ultimately the updated Fast Sweep scanning routine and multipass optics configuration successfully increased the sensitivity of the experiment for a fraction of the original cost. As shown in Figure 4.24, the same data can now be acquired with fewer averages overall and greater signal intensity. Additionally, very minor smoothing (as with a 3 pt boxcar model as implemented in Igor Pro) increases the signal to noise ratio even further. This enhanced noise reduction is believed to come from the smoothing removing signal jittering occurring as a result of the multipass optics.

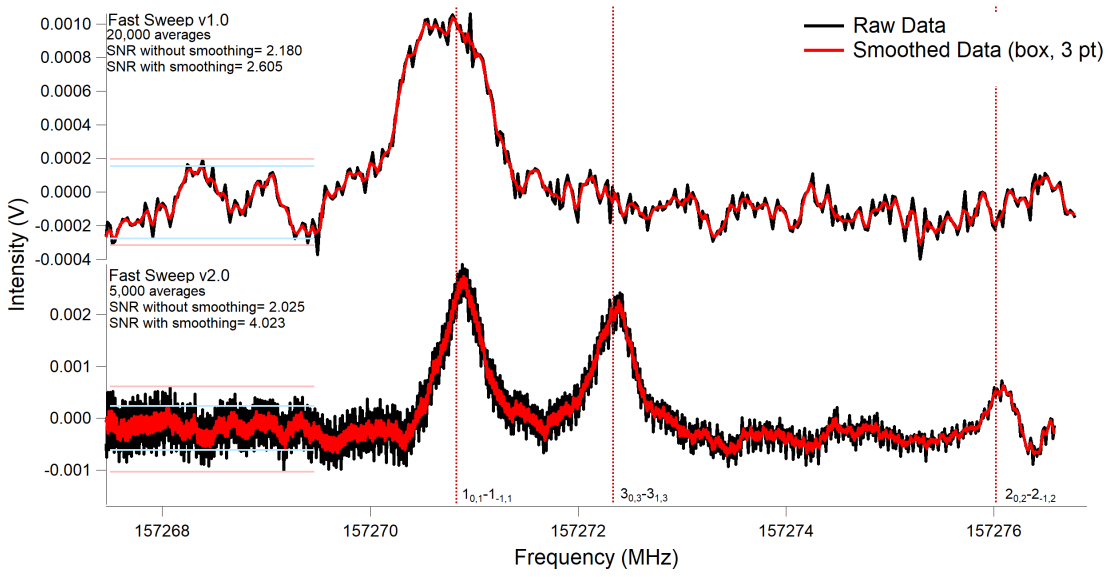

Figure 4.24: A comparison of Fast Sweep v1.0 and v2.0 covering the same frequency window. Fewer overall averages are needed to acquire better data and a better overall SNR is achieved with minimal smoothing

4.3 Benchmarking Radical Generation in a High Voltage Discharge

4.3.1 Experimental Methods

Utilizing the changes implemented in Sections 4.2, Fast Sweep Version 2.0 was used to conduct benchmarking on a high voltage discharge experiment for the purpose of determining ideal operating conditions for generation of radical species. A bubbler was used to introduce methanol (Fisher Chemical, 99.9%) seeded in an argon backing gas (Airgas, 99.996%). The resulting mixture was introduced at indicated pressures (20-100 PSI) into a stainless steel vacuum chamber with a pulsed valve (Parker Hannifin Series 9 general valve with 1 mm pinhole aperture) operating with a 25 Hz repition rate driven by a pulsed driver (Parker Hannifin Iota One). The background pressure of the vacuum chamber was 10 mTorr. The pressure differential between the gas lines and the vacuum chamber creates a supersonic expansion. A ring electrode source after the design of McCarthy and coworkers [119, 120] was used to initiate a plasma discharge for the destruction of the methanol precursor. These electrodes were made of stainless steel and had an inner diameter of 2 mm to match the pulsed valve pinhole aperture. Voltage was applied across the electrode source using a high voltage power supply (Spellman SL2PN2000) run through a ballast resistor with resistance of 2.5 kΩ.

The products in the expansion were characterized using the multiplier chain system described in previously[18, 93] and the fast sweep scanning method developed by Hays[23] and optimized by Zou[24]. Briefly, a microwave synthesizer (Agilent Technologies E8257D PSG) produces a 0-50 GHz signal that is then multiplied by a Virginia Diodes Inc. multiplier chain to achieve higher frequencies. In the case of these experiments, the frequency range probed was 140-225 GHz. The resultant signal was then passed through teflon lenses and focused on the supersonic expansion out of the pulse valve apparatus. The signal through the expansion was then focused onto the window of an InSb hot electron bolometer (QMC Ltd. QFIXBI/PTC) detector and was then processed using an oscilloscope (Rigol DS1202Z-E). Timing between instruments was controlled using a digital delay generator (Stanford Research Systems DG645) synchronized to the internal clock of the microwave synthesizer. Timings of the pulses are described in Table 4.8.

Rotational transitions of methoxy ($CH_3O^{\cdot}$) and formaldehyde (H_2CO) transitions were scanned using a 12 MHz window (1 MHz FM Deviation, 5 kHz FM Rate). $CH_3O^{\cdot}$ scans required 500 av-

Table 4.8: Delay generator settings used to synchronize instruments

Channel Label	Time Setting (ms)	Event
A	0.000	Pulse valve open
B	1.100	Pulse valve closed
C	0.850	Voltage on
D	1.350	Voltage off
E	1.200	Oscilloscope trigger on
F	2.000	Oscilloscope trigger off

erages while H_2CO scans required only 200 averages. Time traces of the product signal were taken using 256 averages. Additional species are expected to be present in the experiment, including $^{\cdot}CH_3$ and $^{\cdot}OH$, however these species are not observable using the methods described as $^{\cdot}CH_3$ lacks an appreciable dipole and the Boltzmann peak of $^{\cdot}OH$ lies much higher than the frequency range used. Data were systematically collected at a variety of operating conditions, including backing pressures ranging from 20 PSI to 100 PSI, and discharge voltages ranging from 300 V to 1000V. Scans taken at lower voltages or higher backing pressures often resulted in no observable data. This may be a result of the voltage being below the striking voltage required to generate a plasma [121] for argon under the operating conditions in the case of low voltages. In the case of high backing pressures, this may be a result of pressure broadening effects or low precursor density. Data were initially processed using the updated scanning routine described in Section 4.2, which included background subtraction between the first and fifth sweeps of the triangle wave, as well as the second and fourth sweeps. These sweeps were 100 μs in duration, thus these background subtractions provided two timing data points with a difference of approximately 100 μs for analysis. These datapoints are henceforth referred to as "early" and "late", relatively speaking.

4.3.2 Data Analysis

Data were further refined after background subtraction using several python scripts, briefly described here. These scripts are included in Appendix A.2 of this work. Background subtracted data were first smoothed using the SciPy uniform 1 dimensional filter with a filter length of 15. A spectral window of size 3 MHz around the center frequency was then created using the SpecUtils package. The purpose of this was to remove extraneous features and limit the fit to only the line of interest (especially if other lines were present in the data window, as in the case of $CH_3O^{\cdot}$). A guess of the line parameters was then generated and the line fit to equation 4.8 using SciPy's

curve fitting feature, with the dogbox fitting method employed,

$$y = v_0 + Ae^{\frac{-(x-x_0)^2}{2\sigma^2}} \tag{4.8}$$

where A dictates the height of the peak, x_0 dictates the center of the peak, and σ dictates the width. The leading term, v_0, is an arbitrary vertical offset applied to allow for better fits when deviations appeared in the baseline (i.e., an artifact of the background subtraction process). The raw, smoothed, and Gaussian fit of the data are then plotted and saved directly to the script location. The peak amplitude, area, full width at half maximum (FWHM), and fit error were then exported to a csv file.

Once the data were fit to a Gaussian equation, the fits were manually evaluated to ensure that the produced fit accurately represented the data. This was especially important in the case of $CH_3O^{\cdot}$ which had far weaker signal strength and two lines within the window of interest. Manual evaluation ensured that the correct line was being fit and that baseline artifacts did not skew the resultant fit. Occasionally, false positive fits were also generated and had to be manually removed from the dataset. Example data are shown for both H_2CO (Figures 4.25 and 4.26) and $CH_3O^{\cdot}$ (Figures 4.27 and 4.28).

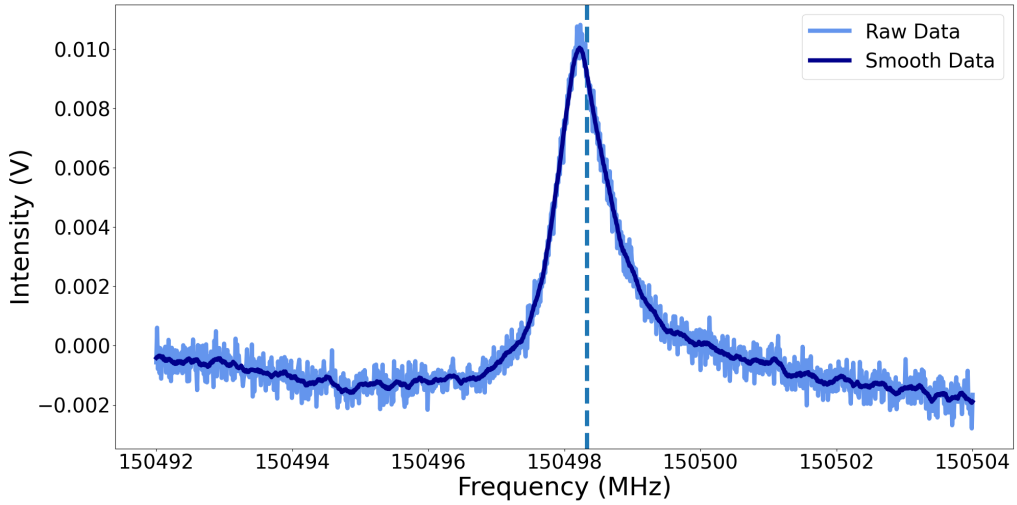

Figure 4.25: Representative background subtracted data of the H_2CO transition used for construction of heatmap data presented. Raw data are shown in light blue and smoothed data are shown in dark blue. Center frequencies used to generate spectral windows are shown with dotted lines. Data are collected at a backing pressure of 30 PSI and voltage of 650 V.

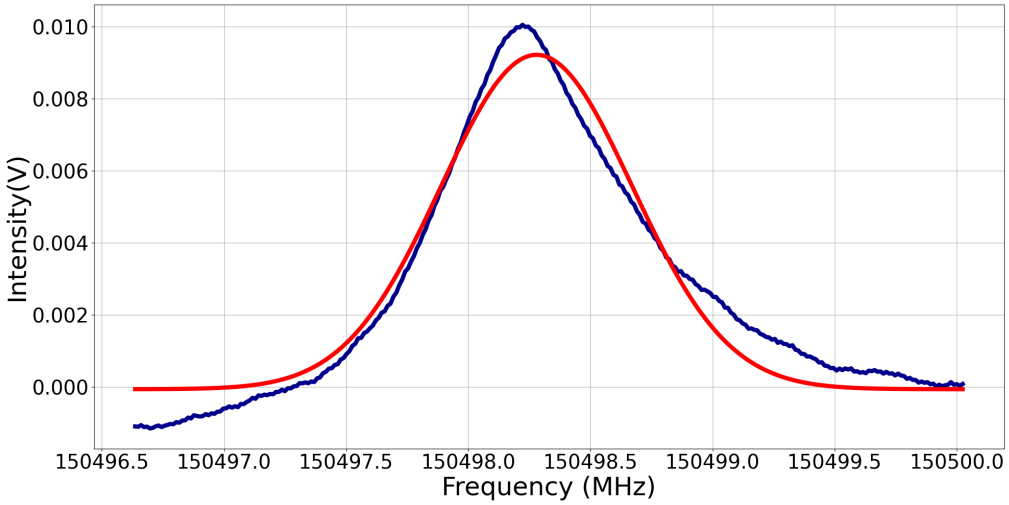

Figure 4.26: Representative Gaussian fits for H_2CO used for construction of heatmap data presented. Smoothed data are shown in dark blue and Gaussian fits are shown in red.

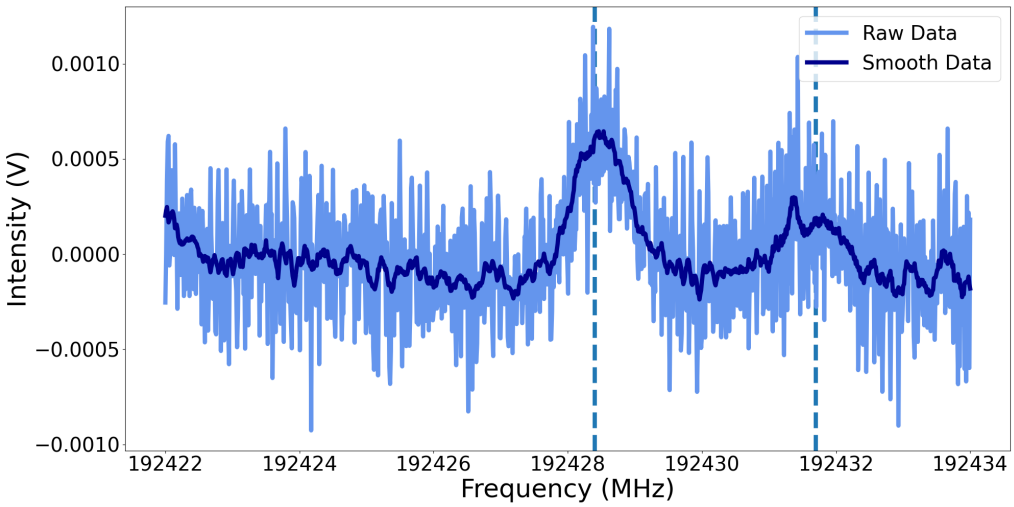

Figure 4.27: Representative background subtracted data of the $CH_3O^{\cdot}$ transitions used for construction of heatmap data presented. Raw data are shown in light blue and smoothed data are shown in dark blue. Center frequencies used to generate spectral windows are shown with dotted lines. Data are collected at a backing pressure of 30 PSI and voltage of 650 V.

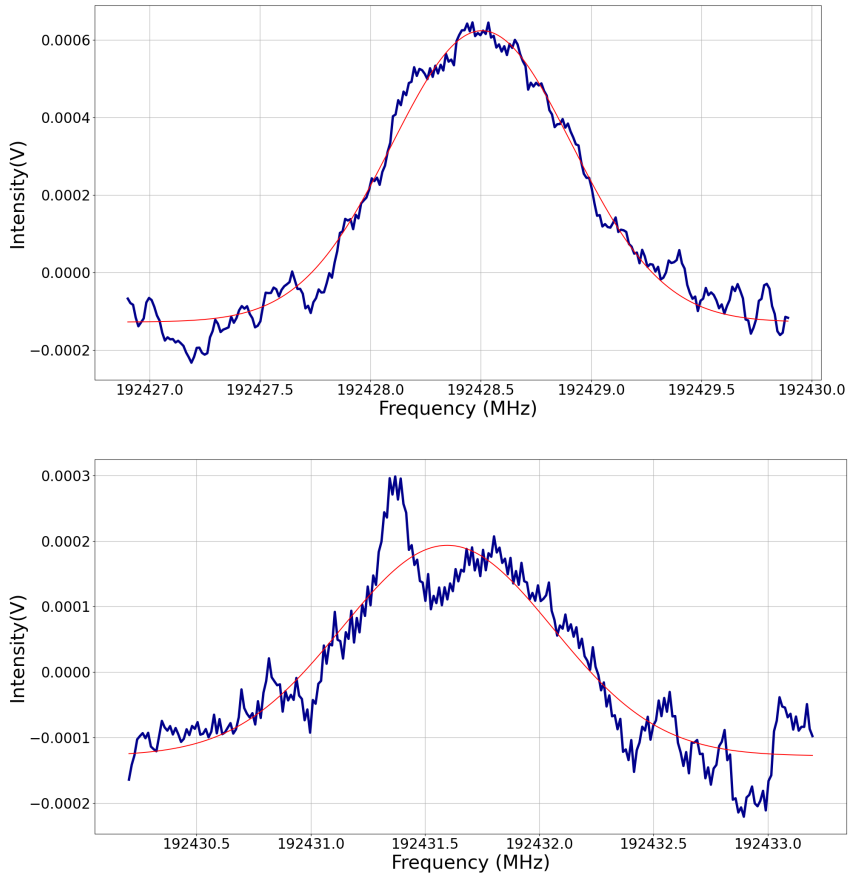

Figure 4.28: Representative Gaussian fits for $CH_3O^{\cdot}$ used for construction of heatmap data presented. Smoothed data are shown in dark blue and Gaussian fits are shown in red. A prominent noise feature is observed on the second $CH_3O^{\cdot}$ transition (right). Such noise features are adequately excluded from the gausssian fit.

The data were then appended to a master spreadsheet and a heatmap was generated using the Seaborn python package. In the case of normalized plots, data were normalized by taking the maximum value of the line parameter for a particular transition from all datasets, and dividing all data by that value. Time trace data were collected directly using the oscilloscope's "export to csv" feature in the UltraScope program that is included with the Rigol DS1202Z-E.

Altogether, a total of 1,080 spectral scans were taken for construction of the presented heat maps. From these scans, 3,240 peaks were fit using the python scripts described in this section. Each series of averaged scans took between 5-10 minutes to acquire, with scans requiring higher averages being on the higher end of that timeframe. Using alternative methods such as the Igor Pro peak fitting function to fit collected peaks would take several minutes per scan. In contrast, the gauss_off.py script is able to process a folder of 15-20 scans in approximately 30 seconds, with

no significant delay in fitting extra lines within a window. This reduces the data processing from a days long process to an accomplishable task in just a few hours even when considering manual processing and formatting of files.

4.3.3 Results and Discussion

The direct outputs from the analysis conducted as described in the 4.3.2 are included in Figures 4.29 and 4.30 for the 150498.33 MHz peak of H_2CO and 4.31, 4.32 for the 192428.4 MHz peak of $CH_3O^{\cdot}$ and 4.33 and 4.34 for the 192431.7 MHz peak of $CH_3O^{\cdot}$. While not quantitatively comparable between the datasets, general trends are qualitatively comparable between these plots. Notably, the H_2CO transition provides a much clearer signal and associated trends. As discussed in Section 4.1, this is partially attributable to the rather high dipole of H_2CO[108]. Additionally, whereas H_2CO displays a clear increase in yield with increased argon backing pressure and increased discharge voltage, $CH_3O^{\cdot}$ displays a greater yield at lower backing pressures and a more moderate voltage. Firstly, it becomes clear rather quickly that operating conditions that favor a stable discharge product are not necessarily predictive for an unstable product. Whereas one operating condition may be ideal for one product, a completely different set of conditions may be necessary for optimal production of another species. That is to say, there does not appear to be any "universal" operating condition. Secondly, these observed trends follow with the greater associated energy to generate formaldehyde directly from methanol. According to ab initio MRD-CI computations with a double zeta basis set performed by Buenker et al. [122] on electronically excited methanol dissociation, it is likely that the H_2CO formation pathway involves a non-concerted series of steps in which the O-H bond of methanol is first lengthened and a second hydrogen is attracted from the carbon side of methanol. This is in contrast to the direct loss of a hydrogen in the case of $CH_3O^{\cdot}$ without any transition state, which is consistent with many experimental observations of the O-H bond scission channel as dominant[122, 123]. Although there is some increased favorability created by greater degeneracy in the singlet states of methanol due to the lengthened O-H bonds, the presence of an energy barrier presents a greater challenge to formation. Thus, the greater required voltage for optimal H_2CO production is likely a product of the presence of this energy barrier. It may therefore be informative for future experiments to evaluate the energy landscape of expected discharge products to identify the ideal operating conditions of a high voltage discharge source.

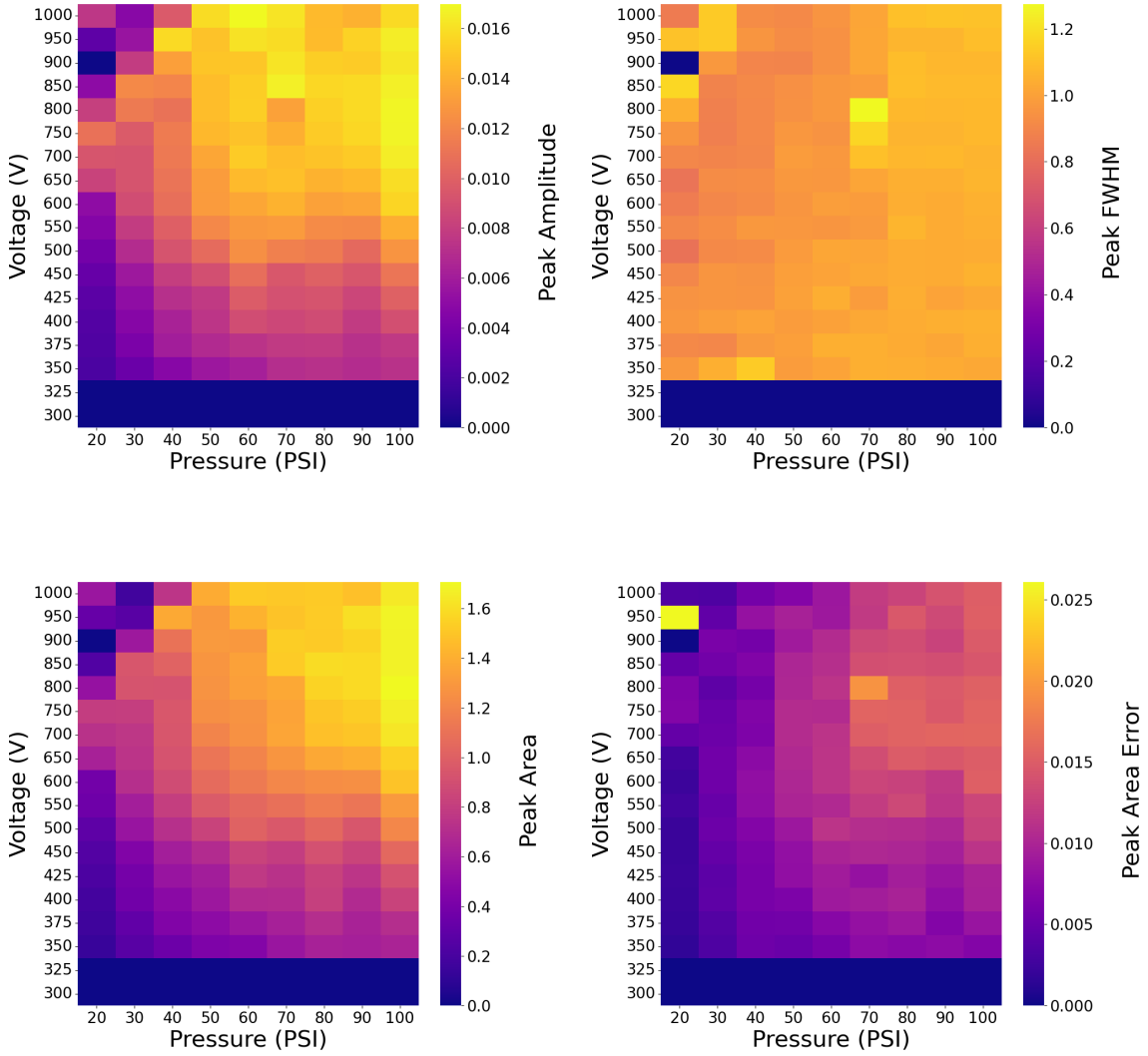

Figure 4.29: Early acquisition heatmaps of the 150498.33 MHz transition of H_2CO under a variety of backing pressure and voltage discharge conditions. Peak amplitude (top left), FWHM (top right), area (bottom left) and error in peak area (bottom right) are shown. Data are not normalized.

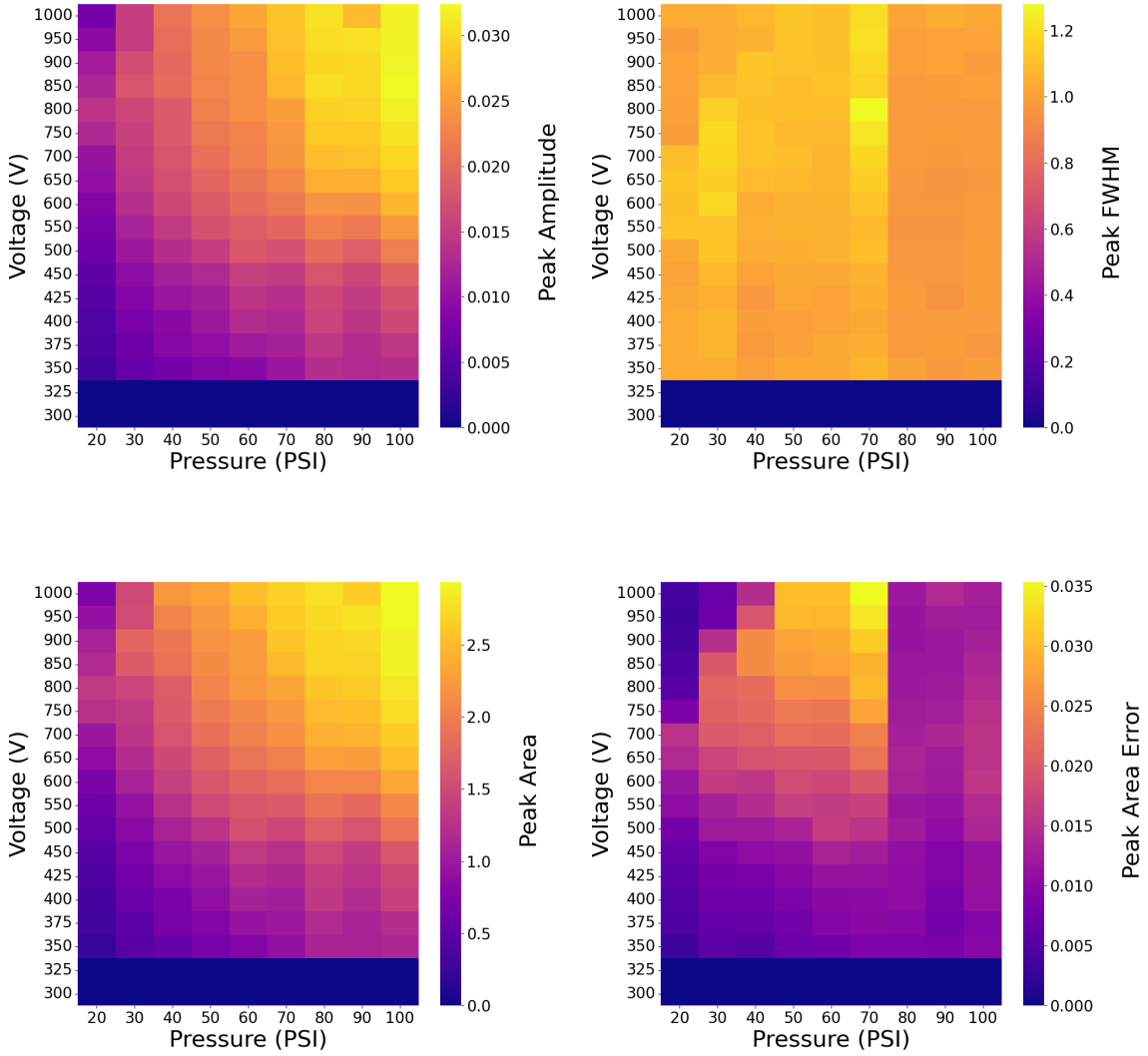

Figure 4.30: Late acquisition heatmaps of the 150498.33 MHz transition of H_2CO under a variety of backing pressure and voltage discharge conditions. Peak amplitude (top left), FWHM (top right), area (bottom left) and error in peak area (bottom right) are shown. Data are not normalized.

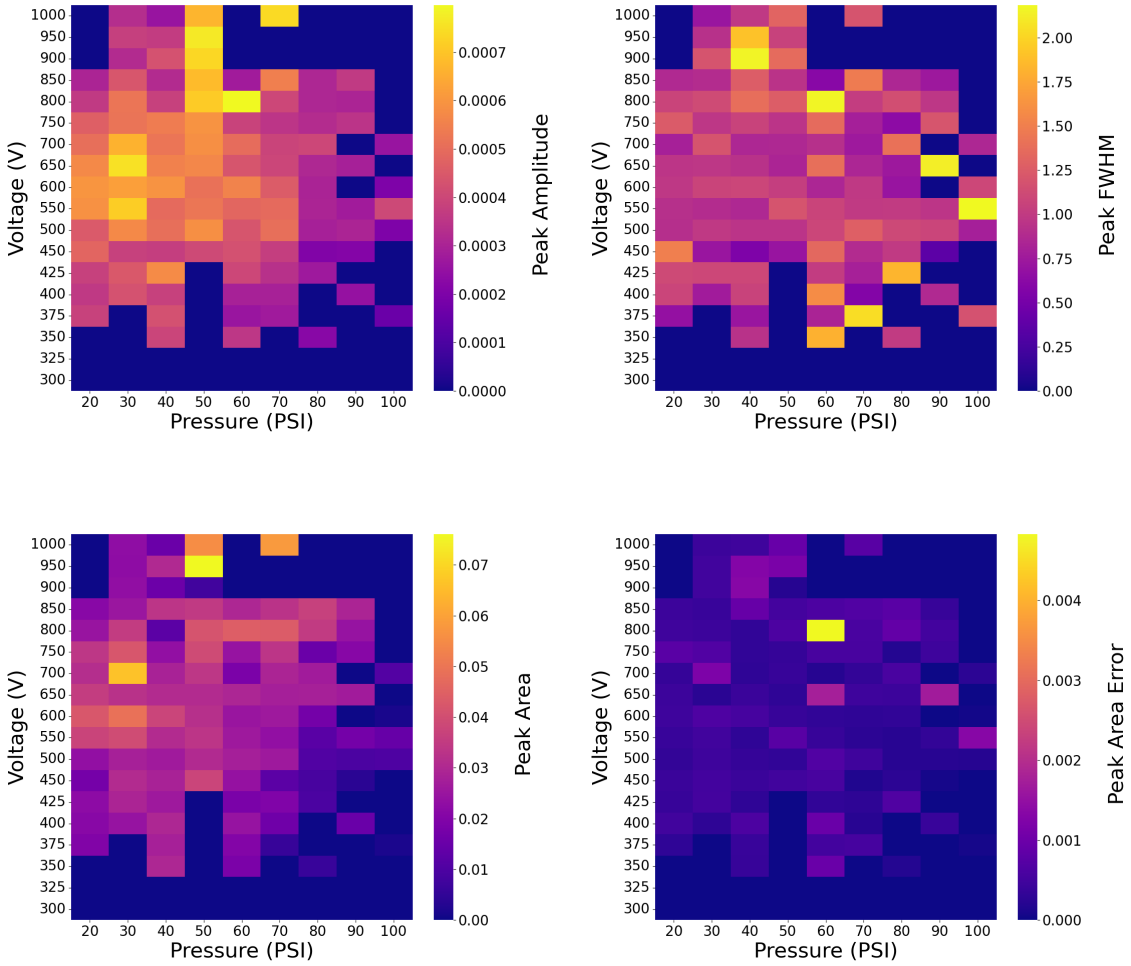

Figure 4.31: Early acquisition heatmaps of the 192428.4 MHz transition of $CH_3O^{\cdot}$ under a variety of backing pressure and voltage discharge conditions. Peak amplitude (top left), FWHM (top right), area (bottom left) and error in peak area (bottom right) are shown. Data are not normalized.

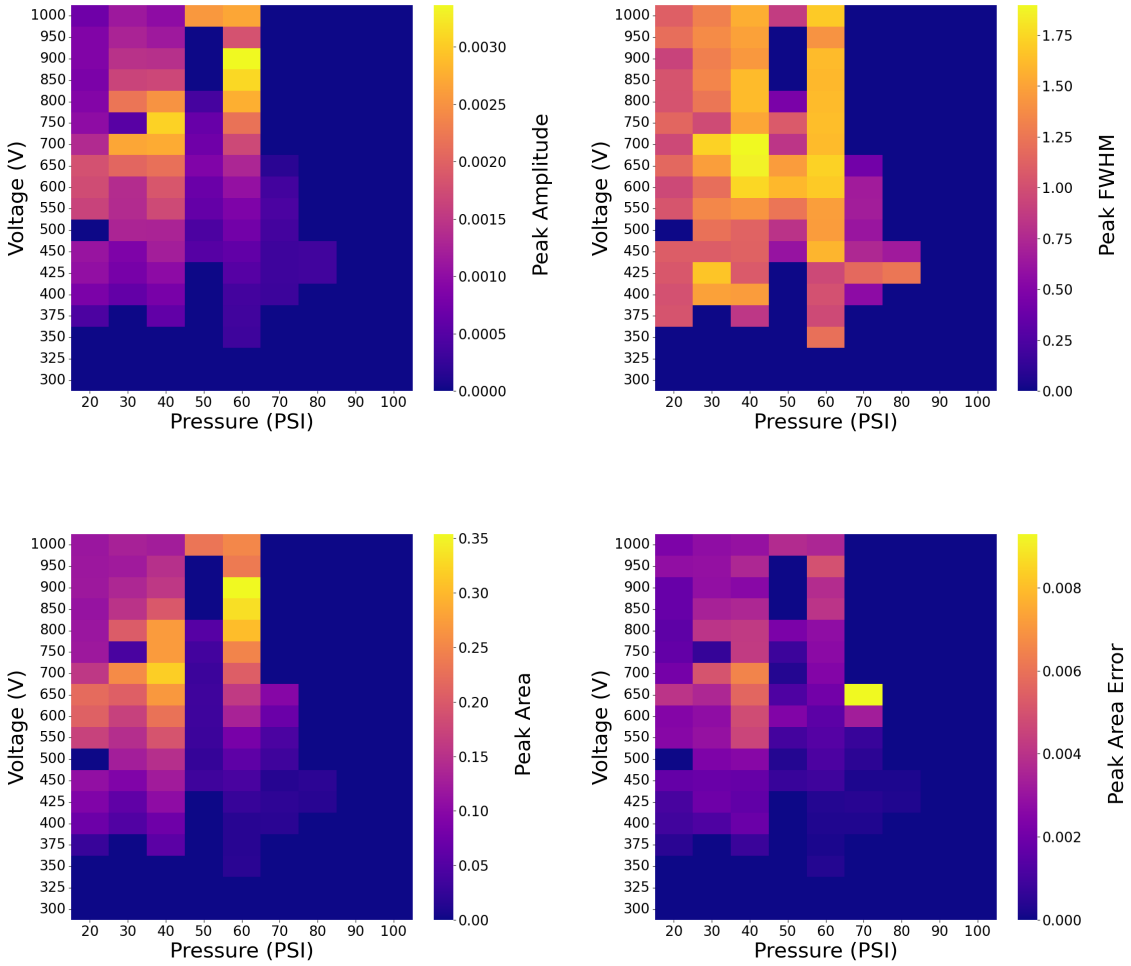

Figure 4.32: Late acquisition heatmaps of the 192428.4 MHz transition of $CH_3O^{\cdot}$ under a variety of backing pressure and voltage discharge conditions. Peak amplitude (top left), FWHM (top right), area (bottom left) and error in peak area (bottom right) are shown. Data are not normalized.

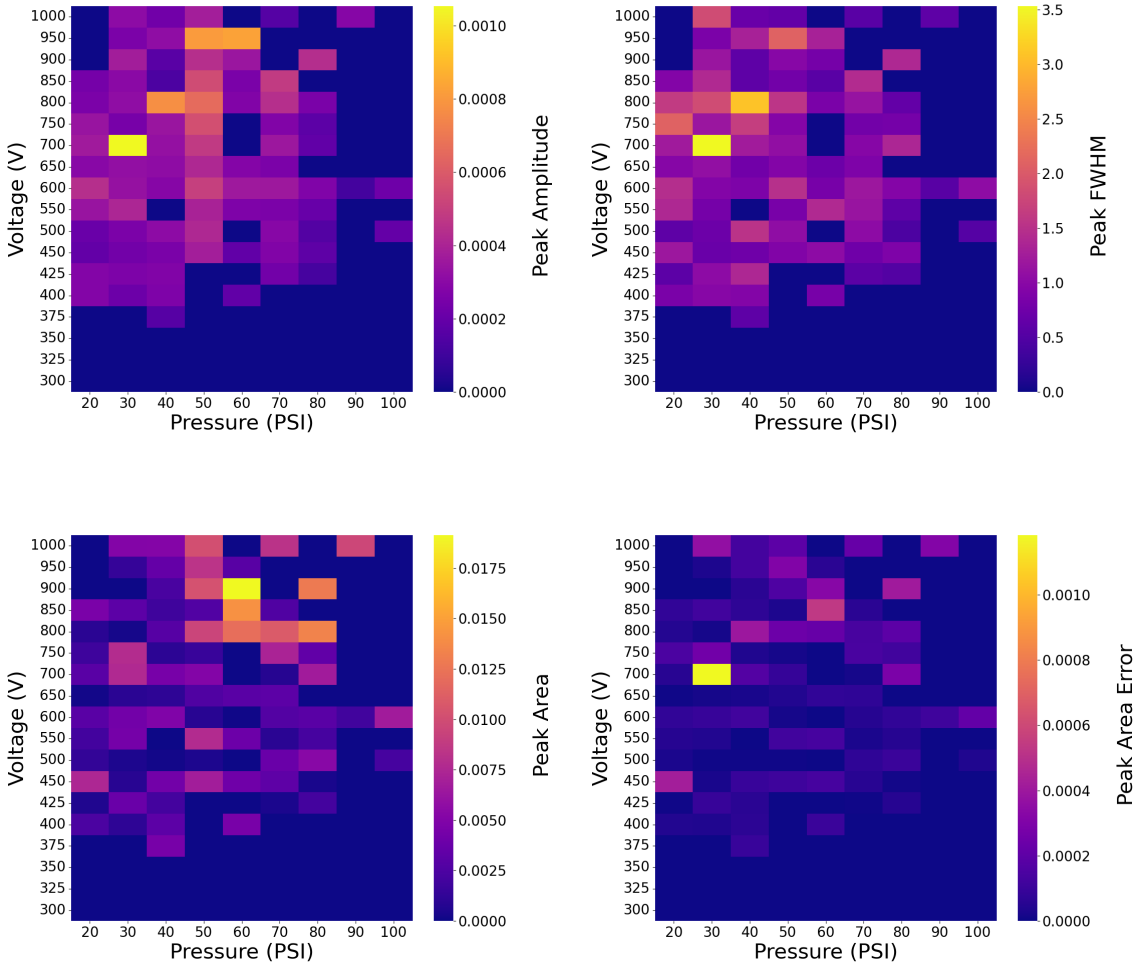

Figure 4.33: Early acquisition heatmaps of the 192431.7 MHz transition of $CH_3O^{\cdot}$ under a variety of backing pressure and voltage discharge conditions. Peak amplitude (top left), FWHM (top right), area (bottom left) and error in peak area (bottom right) are shown. Data are not normalized.

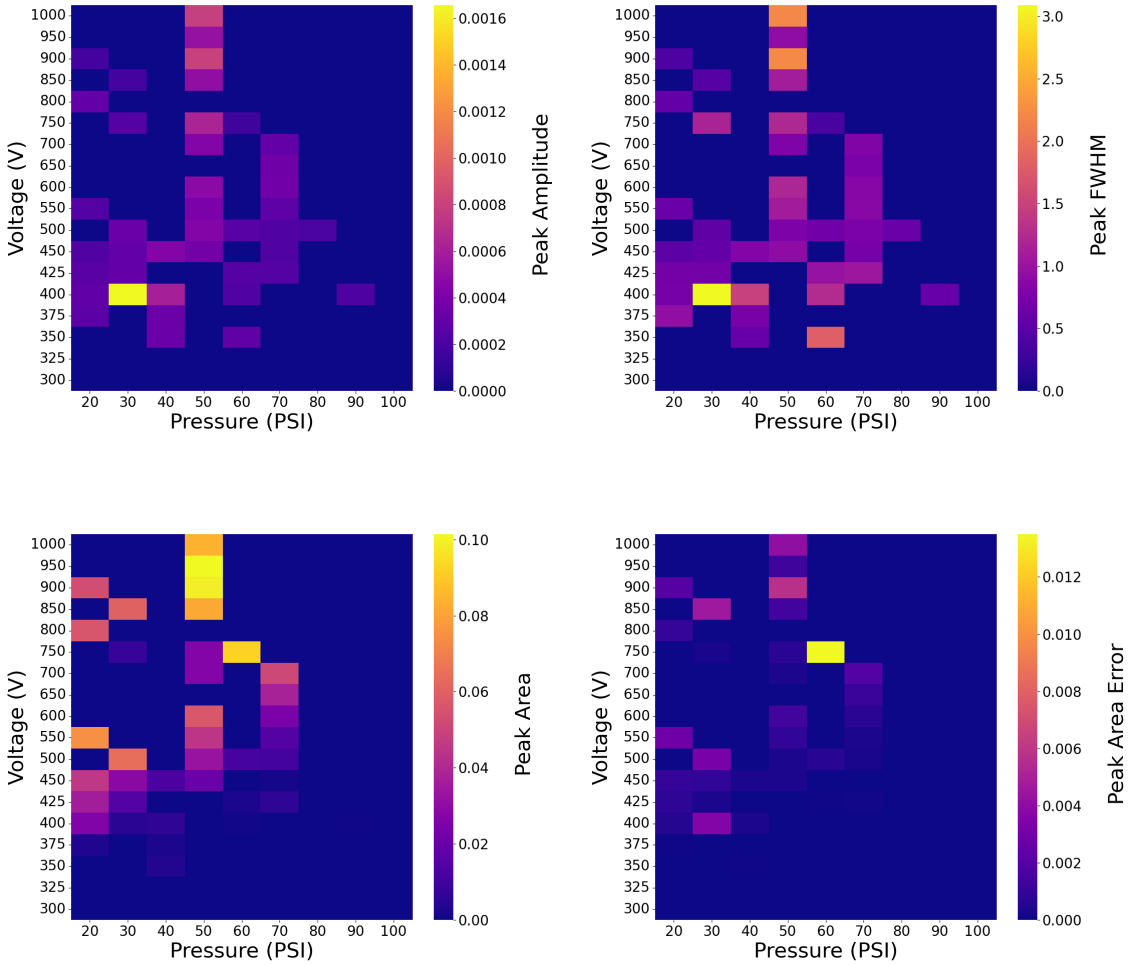

Figure 4.34: Late acquisition heatmaps of the 192431.7 MHz transition of $CH_3O^{\cdot}$ under a variety of backing pressure and voltage discharge conditions. Peak amplitude (top left), FWHM (top right), area (bottom left) and error in peak area (bottom right) are shown. Data in this figure are from a late acquisition. Data are not normalized.

Data were also normalized to facilitate comparison between species and between early and late data acquisition schemes. These normalized data are shown in Figures 4.35, 4.36, and 4.37. It is observed that the late data acquisition scheme results in increased product yield in both the case of H_2CO and $CH_3O^{\cdot}$, though to a much more significant degree for $CH_3O^{\cdot}$. The trends for the three peaks examined here remained consistent between the timing parameters tested. This is noteworthy as H_2CO may be generated as a direct decomposition product of methanol according to the mechanism described by Buenker et al. [122], or as a decomposition product of vibrationally

"hot" $CH_3O^{\cdot}$ or $^{\cdot}CH_2OH$ [98, 110] or through additional hydrogen abstractions from a primary $CH_3O^{\cdot}$ product [123]. Based on the timing of the acquisitions and the timing of the instruments noted in Table 4.8, there may be continued or even increased product formation just after the discharge voltage is removed. Such behavior may be indicative of the latter processes described above in which H_2CO is secondarily generated from a primary $CH_3O^{\cdot}$ product. This behavior is corroborated in the case of H_2CO as shown in Figures 4.38 and 4.39.

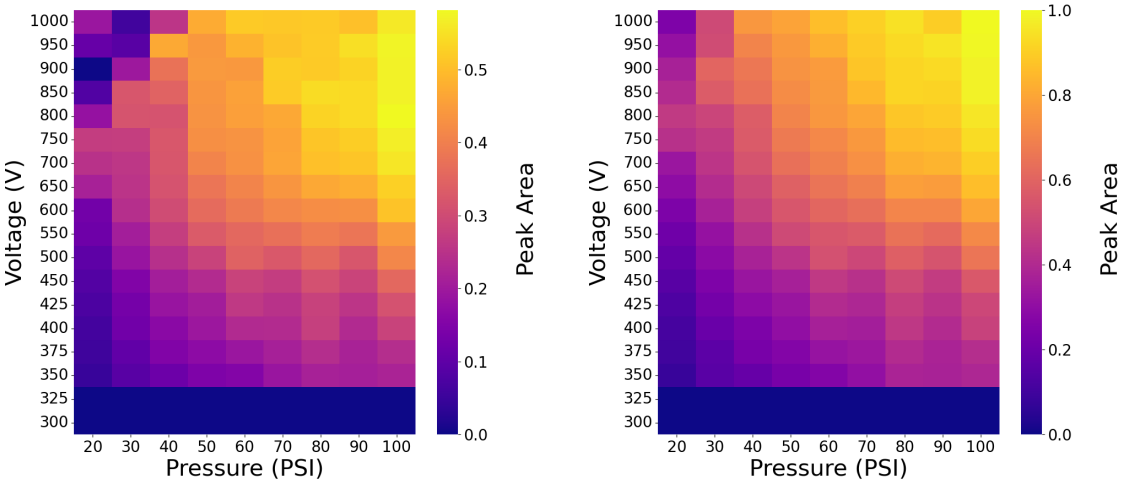

Figure 4.35: Normalized peak area heatmaps of the 150498.33 MHz transition of H_2CO under a variety of backing pressure and voltage discharge conditions. Peak areas are shown for the early (left) and late (right) acquisitions.

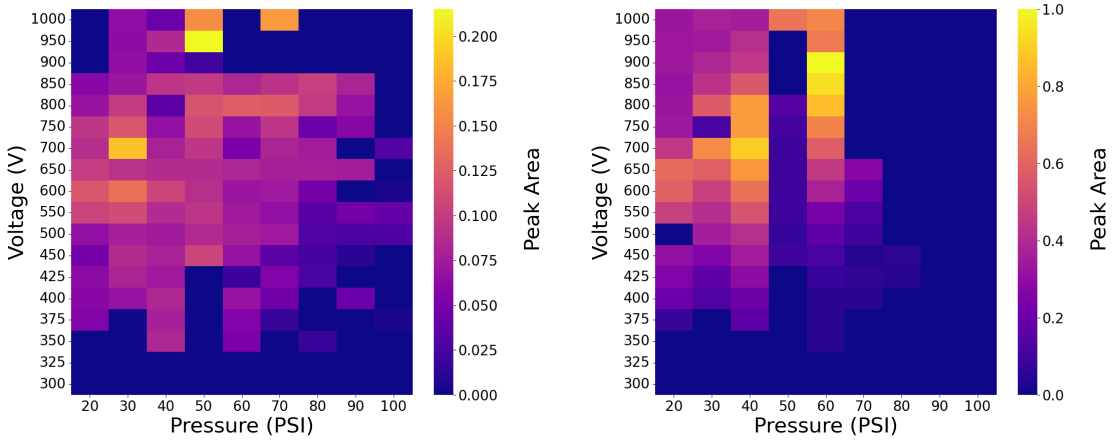

Figure 4.36: Normalized peak area heatmaps of the 192428.4 MHz transition of $CH_3O^{\cdot}$ under a variety of backing pressure and voltage discharge conditions. Peak areas are shown for the early (left) and late (right) acquisitions.

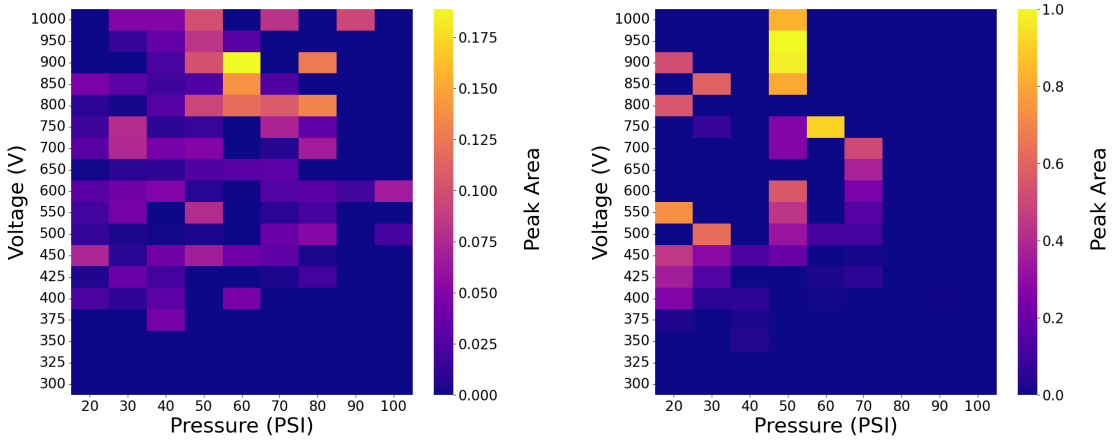

Figure 4.37: Normalized peak area heatmaps of the 150498.33 MHz transition of H_2CO under a variety of backing pressure and voltage discharge conditions. Peak areas are shown for the early (left) and late (right) acquisitions.

The heatmaps presented in Figures 4.29 through 4.37 are instructive of operating conditions but give little insight into the time dependent production behavior of the system. For this reason, time dependent product intensities were collected as in Figures 4.38 through 4.41. Respective instrument and data collection timing events are overlayed onto product traces. Data were plotted with a constant vertical offset of 0.005 V between each scan for clarity.

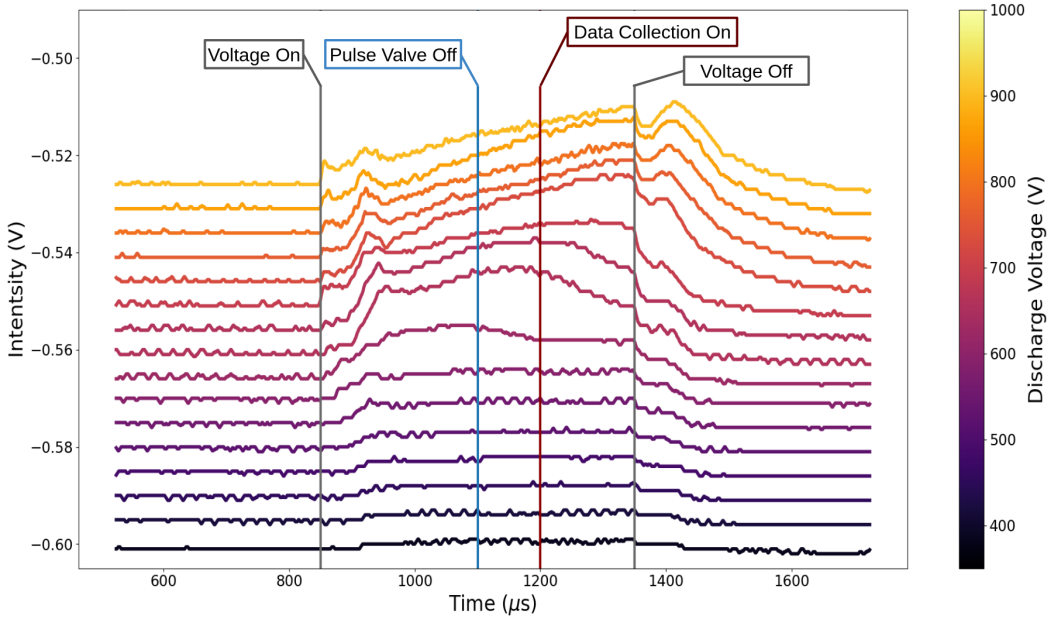

Figure 4.38: Timing of instrument events overlayed on H_2CO signal. Data are collected at the 150498.33 MHz transition of H_2CO with a backing pressure of 20 PSI. Trends were similar across pressures with increased intensities at higher pressures.

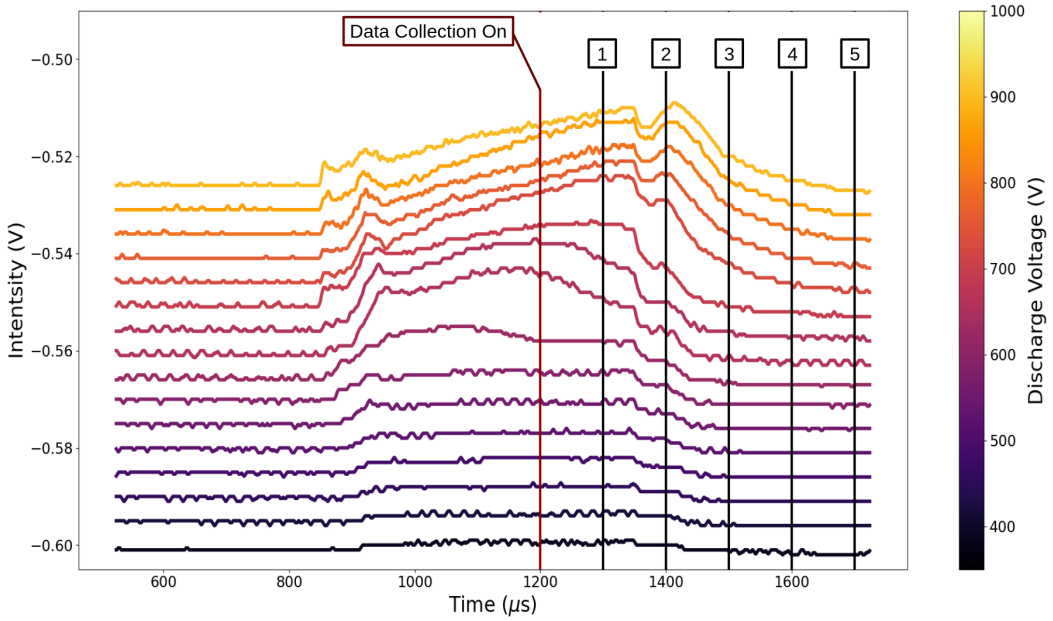

Figure 4.39: Timing of data collection events overlayed on H_2CO signal. Data are collected at the 150498.33 MHz transition of H_2CO with a backing pressure of 20 PSI. Trends were similar across pressures with increased intensities at higher pressures. The ends of data sweeps are marked 1-5.

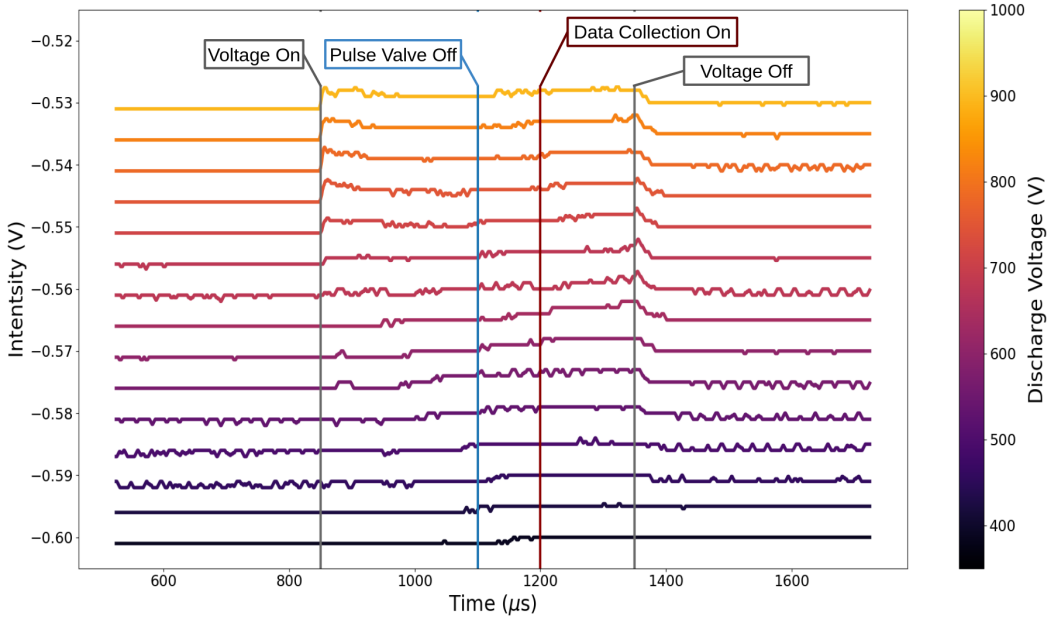

Figure 4.40: Timing of instrument events overlayed on $CH_3O^{\cdot}$ signal. Data are collected at the 192428.4 MHz transition of $CH_3O^{\cdot}$ with a backing pressure of 20 PSI. Trends were similar across pressures with increased intensities at low pressures.

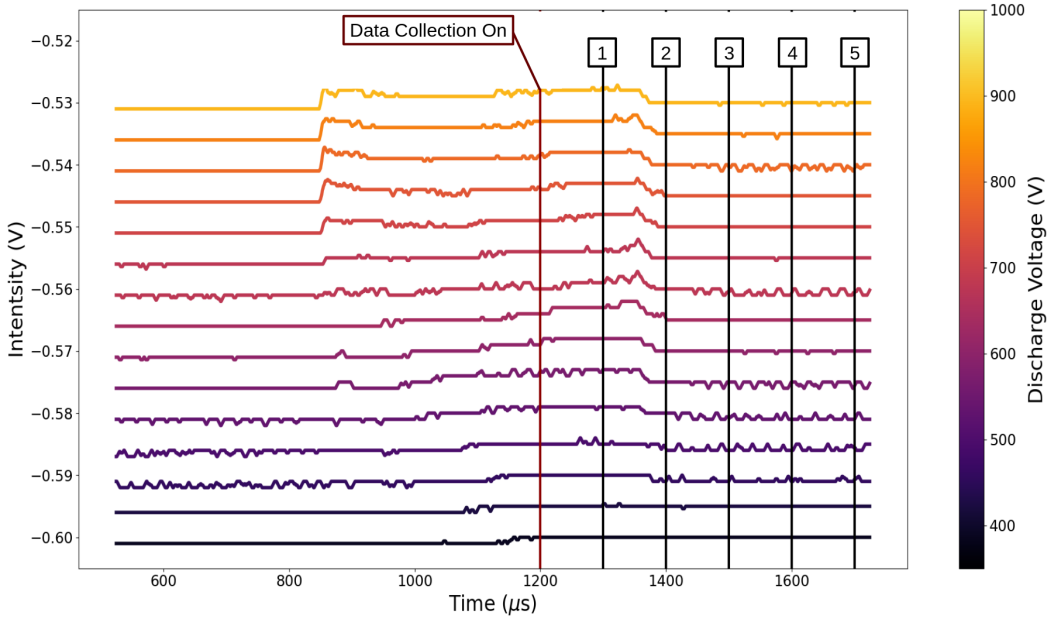

Figure 4.41: Timing of data collection events overlayed on $CH_3O^{\cdot}$ signal. Data are collected at the 150498.33 MHz transition of $CH_3O^{\cdot}$ with a backing pressure of 20 PSI. Trends were similar across pressures with increased intensities at low pressures. The ends of data sweeps are marked 1-5.

Interestingly, as is clear from Figures 4.38, there is persistent and even increased H_2CO production once the voltage is removed from the supersonic expansion. This is not the case for $CH_3O^{\cdot}$ as shown in Figure 4.40. This is indicative that H_2CO production from methanol is much slower or that H_2CO production is initiated by secondary processes. In contrast, production of $CH_3O^{\cdot}$ from methanol is most efficient from direct decomposition of methanol [122, 123]. Moreover, as shown in Figure 4.38, H_2CO production is relatively uniform at low discharge voltages. Production increases early on in the experiment timeline at mid level voltages, and shifts later in the experiment timeline at higher voltages. This behavior indicates that the mechanism of production may be changing with a switchover event near 600 V. There is some mild shifting in the case of $CH_3O^{\cdot}$, though not nearly to the extent as with H_2CO. This may be consistent with greater energy remaining in primary dissociation products after decomposition, leading to further decomposition. Finally, as shown in Figures 4.39 and 4.41, background subtraction for early and late acquisition schemes should be accurately capturing signal and baseline in processing with background subtraction. For early data acquisition schemes, data between the "4" and "5" markers are subtracted from the data between "Data Collection On" and "1" markers. For late data acquisition schemes, data between the "3" and "4" markers are subtracted from the data between "1" and "2" markers. From Figure 4.39, an additional problem to consider may be posed by residual H_2CO that persists into the background sweeps at high voltages.

4.3.4 Conclusion

The data presented here show correlation between barrier height of a reaction and operating conditions to produce the associated product. The presence of a transition state to direct production or intermediate to secondary production may require greater backing pressure and discharge voltages for optimal production. Thus, for production of a novel species via high voltage discharge in a supersonic expansion, knowledge of the potential energy landscape and routes of production will be useful for predicting ideal operating conditions. Such predictions may be made relative to stable and easily identifiable species.

Future studies are planned to examine similar production dependence on operating conditions for methylamine (CH_3NH_2). Based on the data presented here, the stable product CH_2NH will likely favor higher voltages and higher backing pressure than transient species. Thus, it may be useful to find the ideal operating conditions for CH_2NH and reduce the voltage and backing

pressure until the desired product is observed. Previous photolysis studies of methylamine indicate that scission of the N-H bond is expected to be the primary decomposition pathway, resulting in high $CH_3NH^{\cdot}$ yields[124, 125]. Thus, generation of novel radical species from methylamine will likely follow similar trends as with methanol and care should be taken to maintain lower backing pressures and discharge voltages to avoid promoting further decomposition of the desired species.

Chapter 5

Kinetic Analysis of the Decomposition of Aminomethanol and Its Protonated Analog: A Route to Strecker Synthesis in the ISM?

The text in this chapter is taken with minor modification from a revision of the submitted paper "Kinetic Analysis of the Decomposition of Aminomethanol and Its Protonated Analog: A Route to Strecker Synthesis in the ISM?" by Colton Moore and Susanna Widicus Weaver that is under consideration for publication by the Journal of Physical Chemistry A.

5.1 Introduction

Strecker synthesis[126] is the favored mechanism for the synthesis of α-amino acids on Earth. This process may therefore have been involved in the emergence of life on early Earth[127, 128] and is a promising pathway to life on other planets. Strecker synthesis proceeds first through the reaction

of an aldehyde with an amine to produce an amino alcohol, before undergoing a proton transfer followed by dehydration to form an imine. The resultant imine species then further reacts with a cyanide containing species to produce an aminonitrile. From there, the aminonitrile undergoes a series of reactions to protonate the nitrogen from the added cyanide group to form, and then lose, a NH_3 group to produce an α-amino acid. A key part of this process is the formation of and dehydration of an amino alcohol. In the Strecker synthesis of glycine, the simplest amino acid involved in life on Earth, aminomethanol (NH_2CH_2OH) is the predicted intermediate amino alcohol. [129] Though terrestrially unstable, aminomethanol is predicted to form in high abundance in the interstellar medium (ISM)[11, 12]. Aminomethanol may therefore play a key role in the formation of biomolecules throughout the universe.

Detection of aminomethanol in the ISM would confirm a key route toward the origins of life through chemistry starting from small molecules. Routes of aminomethanol formation from ammonia and formaldehyde, both with[15, 130] and without[131] catalysts, have been studied extensively with theory. The results of these studies indicate that the abundant water ice matrices on interstellar grains can easily catalyze aminomethanol formation from ammonia and formaldehyde. Woon[13] reported that the barrier of formation can be suppressed to as little as 0.6 kcal mol^{-1} when ice matrix effects are incorporated, with just two water molecules playing an active role in catalysis via the proton relay mechanism. Additional studies show that formic acid and ammonia can be effective catalysts as well[132–135]. Alternative formation pathways, including the reaction between formaldehyde and the ammonium cation in water clusters[136], and the combination of the OH radical and the $CH_2NH_2^+$ cation[137], have demonstrated low or submerged reaction barriers. The formation pathway via $O(^1D)$ insertion into methylamine[83, 138], meanwhile, is completely barrierless. Likewise, formation through a protonated intermediate in interstellar water ices and subsequent hydrogen loss was shown by Chen and Woon [14] to be barrierless, and they proposed that the protonated intermediate may actually be a precursor to the neutral form. In laboratory experiments, formation of aminomethanol via the ammonia and formaldehyde pathway [139–142] in ice analogs has been demonstrated by several groups. Infrared (IR) spectral features observed in these studies could support the protonated intermediate mechanism proposed by Chen and Woon[14], but this pathway has not yet been explicitly explored in laboratory experiments. More recently, formation via the $O(^1D)$ + methylamine pathway has been demonstrated by Singh et al.[143] in laboratory ice analogs.

The existing body of work on aminomethanol, both theory and experiment, suggests that it is plausible for aminomethanol to form on interstellar ice grains through more than one mechanism with a variety of contributing catalytic effects. Before a search for aminomethanol in the ISM can be conducted, laboratory spectroscopic characterization via rotational spectroscopy is required, as gas phase detection will be more straightforward than its IR detection in icy grain mantles. However, gas phase synthesis of aminomethanol through the same methods that prove fruitful on ices is complicated by complex networks of side reactions and decomposition pathways [18]. It is therefore important to fully characterize the reactions that may form or destroy aminomethanol to guide experiments and observations.

While aminomethanol has been extensively studied, its protonated analog has received far less attention. Redondo et al. [144, 145] have explored formation pathways of protonated aminomethanol. They found a barrier to formation from the ammonium cation and formaldehyde of 16.97 kcal mol^{-1} at the CCSD(T)/aug-cc-pVQZ//MP2/aug-cc-pVTZ level of theory, which is significantly lower than reported barriers for the analogous reaction to form neutral aminomethanol. They also studied the interconversion between the N- and O-protonated forms of aminomethanol, and the likelihood of formation of protonated glycine from protonated aminomethanol, which was deemed unlikely.

In addition to direct formation of protonated aminomethanol, protonation of neutral aminomethanol after formation is another plausible route of formation for both the N- and O- protonated forms. Proton carriers such as NH_4^+, H_3O^+, HCO^+, and H_3^+ are prevalent in the ISM and react barrierlessly with neutral molecules to form protonated species. Given the barrierless nature of protonation, it is possible to form either N- or O-protonated aminomethanol in the ISM once neutral aminomethanol desorbs from icy grains. The aforementioned theoretical studies and the plausibility of protonation from a variety of sources indicate that the protonated analog of aminomethanol may be a key reservoir for aminomethanol in the ISM.

While formation pathways for both protonated aminomethanol and neutral aminomethanol are characterized in the literature[13–15, 83, 132–135, 137, 146], decomposition via water loss is rarely mentioned in depth[131]. The focus instead remains on the larger picture of Strecker synthesis of glycine[129, 130, 136], despite the water loss decomposition step being a key barrier to the formation of glycine through Strecker synthesis. Few works provide detailed analysis of this decomposition pathway. Of those that do address decomposition in a detailed manner, most focus on the neutral

form of aminomethanol. Some works, such as those by Redondo and coworkers[145], have explored reactions of protonated aminomethanol with formic acid to produce glycine. However, the water loss channel for protonated aminomethanol decomposition is not yet well explored. This particular pathway bears consideration as its product, $CH_2NH_2^+$, is predicted to have a route via submerged reaction barriers to form $NH_2CH_2CNH^+$, which can be hydrolyzed to form glycine [147].

The reaction kinetics are often left out in many theoretical studies of molecules important to astrochemistry. Kinetic effects, especially hydrogen tunneling, are necessary for building a complete chemical picture of the ISM. From disentangling complex chemical networks observed in laboratory experiments to providing accurate models of chemistry observed in the ISM, kinetics plays a crucial role in interpreting observed phenomena. Of the aforementioned studies, only a handful took into account the kinetics of aminomethanol reactions. Of note are the work by Feldmann et al.[131], which provides Rice–Ramsperger–Kassel–Marcus (RRKM) theory rate constants for the formation and decomposition of aminomethanol, and the work of Sarkar et al.[134], which provides rate constants for the catalyzed formation of aminomethanol with water and formic acid. To the best of our knowledge, the only kinetic exploration of the water loss channel for aminomethanol is the work of Feldmann et al.[131], and none exists for the protonated form. Therefore, we present here a detailed kinetic study of the decomposition of both aminomethanol and its protonated form via the water loss channel using variational transition state theory (VTST). Additionally, we provide rotational constants for the N-protonated form of aminomethanol to assist with spectroscopic detection in laboratory experiments.

5.2 Computational Methods

5.2.1 Benchmarking and Electronic Structure

Initial computational studies focused on benchmarking the energy barriers of the decomposition pathways of aminomethanol and N-protonated aminomethanol against existing literature values. All geometry optimizations, frequency analyses, and intrinsic reaction coordinate calculations for the current work were carried out using Gaussian 16[148]. All geometry optimizations were optimized using the ”very tight” optimization keyword. The work of Singh et al.[143] focused on aminomethanol; these calculations used the CCSD(T)/CBS//MP2/aug-cc-pVTZ level of theory with zero point vibrational energy (ZPVE) corrections to obtain a reaction barrier height of 56.2

kcal/mol. The work of Redondo et al.[145] focused on the N-protonated aminomethanol system; these calculations used the CCSD(T)/aug-cc-pVQZ//MP2/aug-cc-pVTZ level of theory with ZPVE corrections to obtain a barrier height of 30.10 kcal/mol. Given that kinetics calculations using Polyrate require frequency calculations using Gaussian 16, using the CCSD(T) level of theory was not feasible in the current study. Rather, the following levels of theory were tested against the aforementioned existing work: MP2[149–153], B3LYP[154, 155], PBE0[156–158], ωB97X-D[159], M06-L[160], MN15-L[161], M06-2X[162], M08-HX[163], MN15[164], and VSXC[165]. The levels of theory tested were chosen for their availability in Gausssian 16 and potential performance in hydrogen transfer reactions.[166] Each theory level was tested with the aug-cc-pVTZ basis set[167–170] given the relatively small size of the molecules of interest. Appropriate frequency scaling factors[171, 172] for the methods used in benchmarking were applied using the "scale" keyword in Gaussian 16. Where frequency scaling factors were unavailable in databases, no scaling was applied. The energies used for benchmarking include ZPVE corrections. The Minnesota functionals were tested with a superfine grid. The mean unsigned errors (MUE) in kcal mol^{-1} of each method with respect to the the literature values are shown in Table 5.1. The level of theory that gave the lowest MUE for the neutral aminomethanol system was the M06-2X/aug-cc-pVTZ (MUE=0.61). The level of theory that gave the lowest MUE for the N-protonated system was M06-L/aug-cc-pVTZ (MUE=0.54). These theory methods provided an energy barrier for each system in agreement with those published in the literature to within experimental accuracy. The transition states for all reaction pathways with barriers were confirmed with analytical frequency calculations, which returned only one imaginary frequency per reaction. These transition states were confirmed to represent the appropriate reaction pathways with intrinsic reaction coordinates (IRCs) [173, 174].

High accuracy rotational constants were obtained for N-protonated aminomethanol using the CFOUR package[175] with a CCSD(T)[39, 176–179]/aug-cc-pVTZ basis set for both geometry optimization and frequency analysis.

5.2.2 Dynamics and Tunneling Calculations

Once an appropriate level of theory and basis set combination was determined, analysis of the reaction kinetics was carried out using variational transition state theory (VTST) as implemented in the Gaussrate17-B[180] and Polyrate17-C[181] program suites. The full computational details of these programs are described elsewhere [180, 181], so only key aspects are presented here.

Table 5.1: Difference in energies (kcal mol^{-1}) between literature values and calculated values for the reaction barrier heights ($\Delta E_{Barrier}$), overall reaction (ΔE_{rxn}), and mean unsigned error (MUE) for the decomposition of aminomethanol and N-protonated aminomethanol. All energies used in benchmarking included ZPVE corrections.

	Aminomethanol			N-Protonated Aminomethanol		
Theory Method	$\Delta E_{Barrier}$	ΔE_{rxn}	MUE	$\Delta E_{Barrier}$	ΔE_{rxn}	MUE
MP2	-2.91	-1.09	2.00	-1.00	2.19	1.59
B3LYP	-5.37	-4.71	5.04	-0.90	-1.64	1.27
PBE0	-0.17	1.71	0.95	-0.34	4.24	2.29
ωB97X-D	-0.88	-0.77	0.83	-0.10	1.61	0.85
M06-L	-5.06	-3.39	4.22	**-0.87**	**0.22**	**0.54**
MN15-L	-1.39	-2.20	1.79	0.38	1.65	1.01
M06-2X	**-0.93**	**-0.28**	**0.61**	-0.88	2.04	1.47
M08-HX	0.87	-1.49	1.18	1.59	1.14	1.37
MN15	-1.48	0.25	0.86	-2.61	1.68	2.15
VSXC	-15.49	-8.52	12.00	-1.42	-6.74	4.08

The kinetic rate constants presented in this work are computed using conventional transition state theory (denoted TST) and variational transition state theory, namely canonical variational transition state theory (denoted CVT). In conventional transition state theory, the dividing hypersurface between the reactant and product regions is presumed to be located directly on the saddle point (that is, s=0 and perpendicular to the imaginary frequency normal mode), and this theory makes the assumption that there are no recrossing effects. In contrast, variational transition state theory variationally optimizes the dividing hypersurface so that it is located at the true dynamic bottleneck of the reaction, which may or may not be directly on the saddle point. If located elsewhere ($s = s_*$), this is the generalized transition state, or GT. The optimized location of this surface is one that minimizes recrossing effects. When the TST rate constant is minimized with respect to s, one obtains the VTST CVT rate constant, given by Equation 5.1 [74–77]

$$k^{CVT}(T) = \min_{s} k^{TST}(T,s) = \frac{\sigma}{\beta h}\frac{Q^{GT}(s=s_*,T)}{Q^{R}(T)} exp[-\beta V_{MEP}(s_*(T))] \tag{5.1}$$

where k^{CVT} is the classical CVT kinetic rate constant, σ is the reaction path symmetry number, $\beta = (k_B T)^{-1}$, k_B is the Boltzmann constant, T is temperature, h is the Planck constant, Q^{GT} and Q^R are the partition functions of the generalized transition state and reactants, respectively, and $V_{MEP}(s)$ is the potential evaluated on the minimum energy pathway (MEP) at s. This is the basis for the computed CVT rate constants in this work.

Equation 5.1 does not take into account tunneling effects. Multidimensional tunneling effects

were considered using zero curvature tunneling (ZCT)[78], small curvature tunneling (SCT)[79], large curvature tunneling (LCG4)[80], and microcanonically optimized multidimensional model (μOMT)[81]. These values are denoted with CVT/MT where MT is the multidimensional tunneling method used. These effects are incorporated as in Equation 5.2[74, 182]:

$$k^{CVT/MT}(T) = \kappa^{CVT/MT}(T) k^{CVT}(T) \tag{5.2}$$

where k^{CVT} is the CVT rate constant without multidimensional tunneling and $\kappa^{CVT/MT}$ is the tunneling transmission coefficient obtained with a given multidimensional tunneling approximation. The tunneling transmission coefficient is related to the tunneling probability by equation 5.3[77]:

$$\kappa^{T}(T) = \frac{1}{k_B T} \int_{E_0}^{+\infty} P^{T}(E) e^{-(E - V^{AG})/k_B T} dE \tag{5.3}$$

where $P^T(E)$ is the quantum tunneling probability at a given energy, V^{AG} is the maximum of the adiabatic ground state potential energy (V_A^G) along the reaction coordinate, and E_0 is the lowest energy at which the reaction can occur.

Key considerations in multidimensional tunneling approximations are: (1) the quantized contribution of all vibrational modes in the tunneling path (which changes the shape of the energy barrier), and (2) the coupling between motion along the MEP and the vibrational modes perpendicular to it (which results in reaction path curvature, a major consequence of which is the so called "corner cutting" effect). The ZCT approximation takes into account (1) but neglects the effects of (2), which leads to seriously underestimated tunneling effects. Meanwhile, SCT, LCT, and μOMT take into account both (1) and (2). ZCT and SCT use the semiclassical WKB approximation, which gives transmission probability through an energy barrier as in equation: 5.4[74, 77]

$$P^{T}(E) = \begin{cases} 0 & E \leq E_0 \\ \{1 + e^{2\theta(E)}\} & V_a^G(s = -\infty) < E \leq V_a^G(s_*) \\ 1 - P^T(2V_a^G(s_*) - E) & V_a^G(s_*) \leq E \leq 2V_a^G(s_*) - E_0 \\ 1 & 2V_a^G(s_*) - E_0 < E \end{cases} \tag{5.4}$$

where θ is the imaginary action integral given by equation. 5.5[74, 77]

$$\theta = \frac{1}{\hbar}\int_{s<}^{s>} ds\{\mu[V^{AG}(s) - E]\}^{1/2} \tag{5.5}$$

In equation 5.5, s< and s> are turning points where $V_A^G = E$, μ is the reduced mass, and V^{AG} is the ground state adiabatic potential. A key distinction between ZCT and SCT is that μ becomes $\mu_{eff}(s)$ for SCT tunneling probability calculations. The value of $\mu_{eff}(s)$ is determined by reaction path curvature and the calculations of it are described elsewhere[77].

The LCG4 tunneling approximation is more complex than those of the ZCT and SCT. Key features of this approximation are that tunneling paths are straight lines that connect the reactant and product valley regions, it includes tunneling paths through regions of the PES that are far from the MEP, and nonadiabatic regions can be included. The primitive tunneling probability in the LCG4 method is given by equation 5.6[74]

$$P_{prim}^{LCG4}(E) = |T(E)|^2 + \left(\frac{cos\chi\{s_0(E)\hat{,}[s_0(E)]\} + cos\chi\{s_1(E)\hat{,}[s_0(E)]\}}{2}\right)^2 * exp\{-2\theta[s_0(E)]\} \tag{5.6}$$

Where T(E) is the tunneling amplitude that accounts for tunneling initiated by the vibrational modes perpendicular to the reaction coordinate and $exp\{-\theta[s_0(E)]\}cos\chi\{s_{0\,or\,1}(E)\hat{,}[s_0(E)]\}$ is the amplitude of the tunneling contribution initiated by motion along the reaction coordinate at the classical turning point s_0 for the forward (s_0) and reverse (s_1) motion. $\hat{\eta}$ is the unit vector along the tunneling path, $\chi[s, \hat{\eta}(s_i)]$ describes the angle between the unit vector $\hat{\eta}$ and the unit vector tangent to the reactant path at s, and θ is the action integral which is defined by adiabatic reactant and product regions and a nonadiabitic region in between. This probability is constrained by equation 5.7 for $E \leq V_a^{AG}$ such that the probability tends to 0.50 at the barrier maximum.

$$P^{LCG4}(E) = \left\{1 + \frac{1}{2}\frac{[P_{n_{max}}^{LCG4}(V_a^{AG})]^{-1} - 1}{P_{n_{max}}^{LCG4}(V_a^{AG})} P_{n_{max}}^{LCG4}(E)\right\} \times \frac{1}{1 + [P_{n_{max}}^{LCG4}(E)]^{-1}} \tag{5.7}$$

Additional corrections are incorporated to describe tunneling into and from excited states; these are described elsewhere. [74]

The μOMT method strikes a balance between the considerations of small and large curvature tunneling approximations by simply taking the tunneling probability to be the highest of $P^{LCT}(E)$ and $P^{SCT}(E)$.

The minimum energy path was optimized from -2.9 Å < s < 4.0 Å along the path of steepest descent on either side of the saddle point using the Page-McIver integrator. A step size of 0.001 Å was used. Non-redundant internal coordinates were used to describe the systems and the RODS keyword was used to reorient the general transition state dividing surface. A reaction path symmetry number (σ) of 1 was used for both reactions as both transition states had C_1 symmetry and both reactants had C_s symmetry, resulting in a symmetry number of 1 [75]. Appropriate frequency scaling factors for each system were incorporated based on the functional and basis set used[171, 183, 184].

5.3 Reaction Energetics

The energies of the stationary points of the aminomethanol decomposition pathway and the N-protonated aminomethanol decomposition pathway were benchmarked against the work of Singh et al.[143] and Redondo et al.[145], respectively. The energies of these points at both levels of theory used for the kinetics calculations are shown in Figures 5.1 and 5.2. The barrier height energies are in good agreement with the previous work, with an energy difference of 0.61 kcal mol^{-1} for aminomethanol and 0.54 kcal mol^{-1} for N-protonated aminomethanol. At the chosen levels of theory, both the barrier height and overall reaction energies were within 1 kcal mol^{-1} of literature values.

The molecular ions NH_4^+, H_3O^+, HCO^+, and H_3^+ are all common proton carriers in the ISM and may be present in relevant laboratory experiments. As such, their reactions with aminomethanol were examined using the DFT methods applied to the kinetics to show the feasibility of protonation. The results of these calculations are shown in Figure 5.2. The feasibility of protonation from these species at both the N and O sites of aminomethanol were examined. It was found that each carrier protonates aminomethanol easily at either the N or O site, with no barrier. That is to say, the transition state search spontaneously converged to the products. A relaxed scan of the protonation reaction was performed in Gaussian 16 for the NH_4^+ protonation reaction which displayed a smooth downward trend in energy as the reaction progressed, indicating that the reaction had no barrier. These findings are consistent with the work of Redondo et al. [145] as well as the known barrierless nature of ion-molecule reactions.

The facile nature of protonation of aminomethanol and high reactant energies shown in Fig-

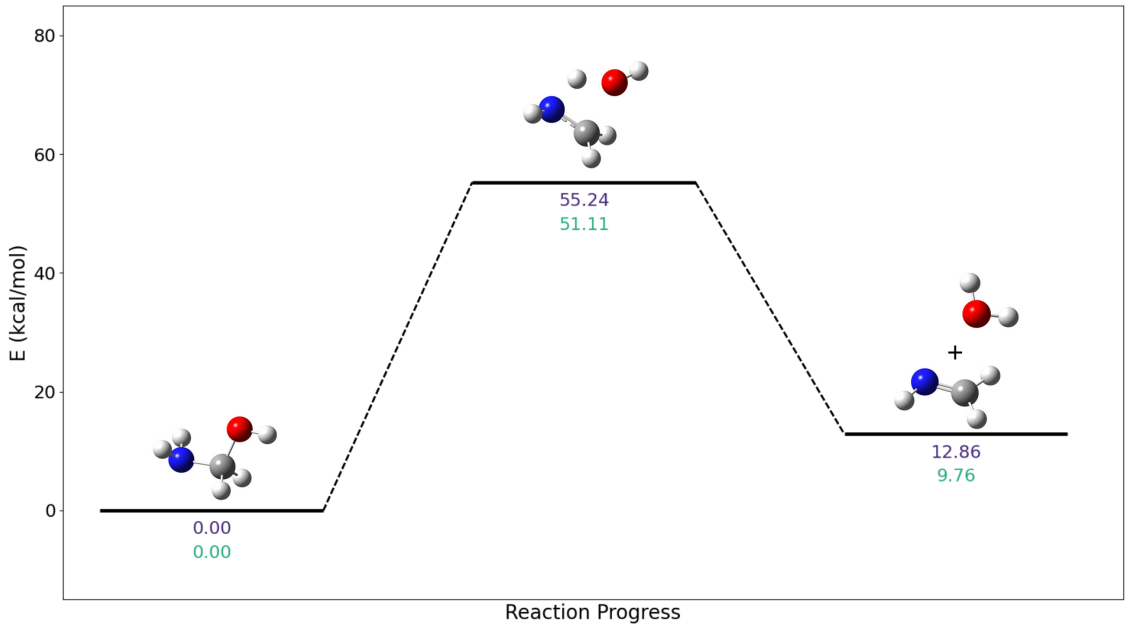

Figure 5.1: Reaction coordinate diagram for the aminomethanol decomposition into methanimine (CH_2NH) and water. Energies with ZPVE corrections in kcal mol^{-1} are shown at the M06-2X/aug-cc-pVTZ level of theory in purple (top number) and the M06-L/aug-cc-pVTZ level of theory in green (bottom number).

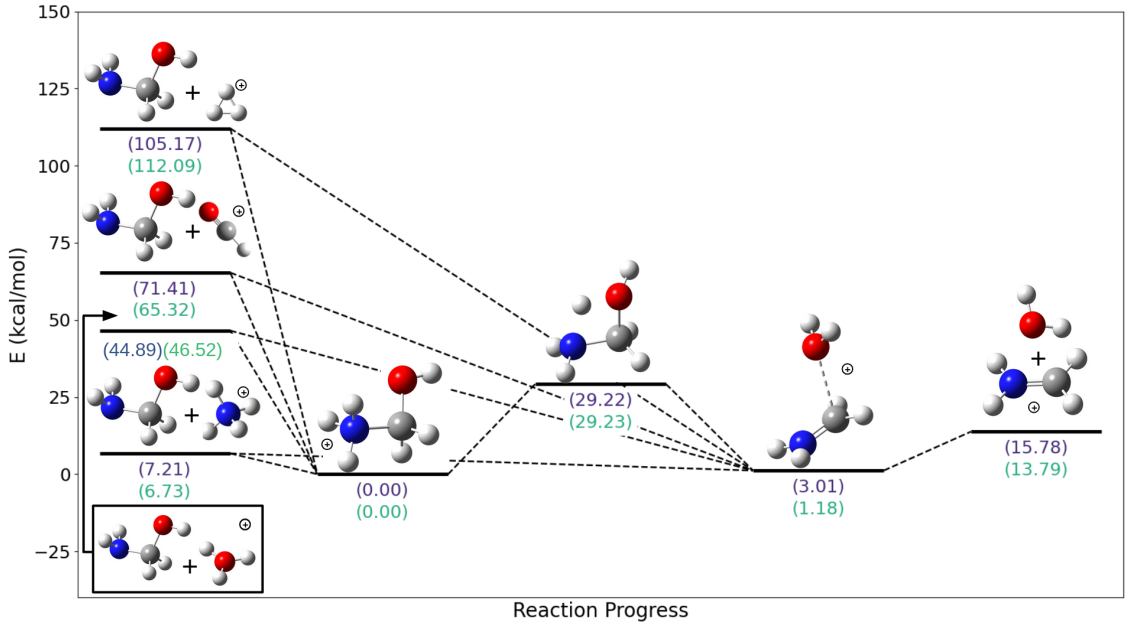

Figure 5.2: Reaction coordinate diagram showing the formation of protonated aminomethanol from aminomethanol and common proton carriers in the ISM (H_3^+, HCO^+, H_3O^+, NH_4^+). Energies with ZPVE corrections in kcal mol^{-1} are shown at the M06-2X/aug-cc-pVTZ level of theory in purple (top number) and the M06-L/aug-cc-pVTZ level of theory in green (bottom number).

ure 5.2 indicate that protonation is possible in the interstellar medium. If protonation were to occur, it is likely that the energy imparted into the molecule by the protonation process will cause decomposition into $CH_2NH_2^+$ and H_2O for all cases except that of NH_4^+. These results indicate that gas phase formation of either N-protonated or O-protonated aminomethanol from neutral aminomethanol readily leads to decomposition in all but one case. Conversely, in gas phase laboratory experiments, stabilization could occur through collisional de-excitation, such as in a supersonic expansion.

In addition to reaction coordinates, more detailed reaction energetics are obtained through the kinetics calculations performed using the Polyrate program suite. Potential energy curves for the reaction path are shown in Figure 5.3. The vibrationally adiabatic potential energy, V_a^G, is represented by Equation 5.8,

$$V_a^G = V_{MEP} + \epsilon_{int}^G \tag{5.8}$$

where V_{MEP} is the potential energy of the minimum energy pathway of the reaction and ϵ_{int}^G is the zero point energy from the normal mode vibrations orthogonal to the reaction coordinate. It is evident from both the reaction coordinates and the potential energy curves that the barrier for the decomposition of N-protonated aminomethanol is significantly lower than that of the neutral system. Thus, based only upon barrier height, one may expect the decomposition of the protonated form of aminomethanol to occur faster than the neutral form. However, less obviously, there is a slight shift in the potential energy curves of N-protonated aminomethanol toward the reactants and an overall flattened energy barrier.

5.4 Reaction Kinetics

5.4.1 Reaction Path Curvature and Coupling of Vibrational Modes

Further analysis of these systems was performed by examining the reaction path curvature along the MEP. Scalar reaction path curvature for both systems at their respective level of theory is shown in Figure 5.4. Peaks in the reaction path curvature are indicative of electronic structure changes, such as bond breakage, bond formation, or redistribution of charge in a molecule as it traverses the minimum energy pathway of a reaction. This information can be used to gain mechanistic insight into the processes underlying a reaction. As is seen in Figure 5.4, there is a slight shift in the minimum curvature at the center toward the reactants ($s < 0.0$ Bohr) in the

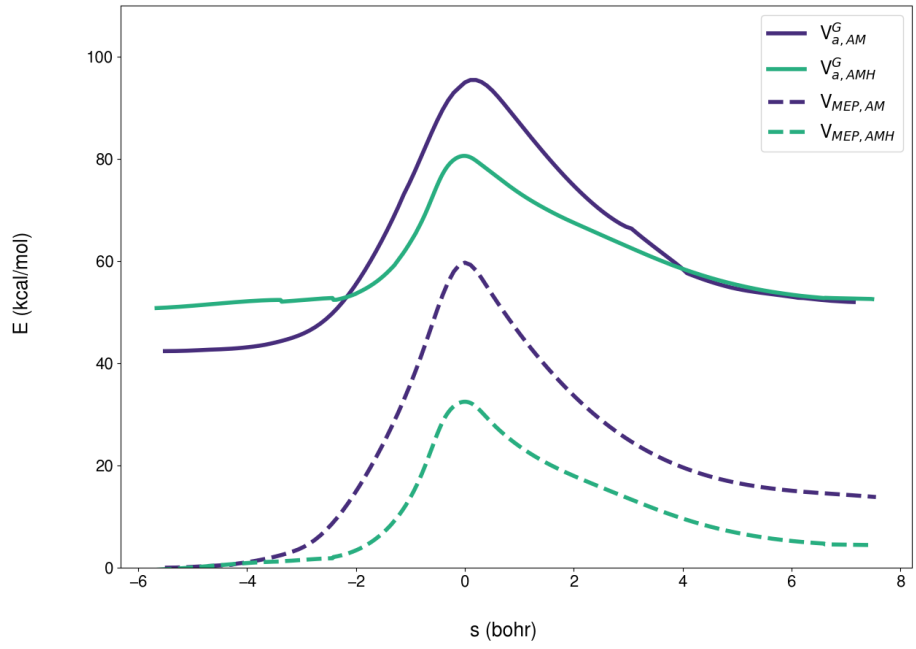

,

Figure 5.3: Potential energy curves showing the energy along the minimum energy pathway (V_{MEP}) with solid lines and the vibrationally adiabatic potential energy (V_a^G) with dashed lines. The curves in purple show these data for the neutral aminomethanol system and the curves in green for the protonated aminomethanol system.

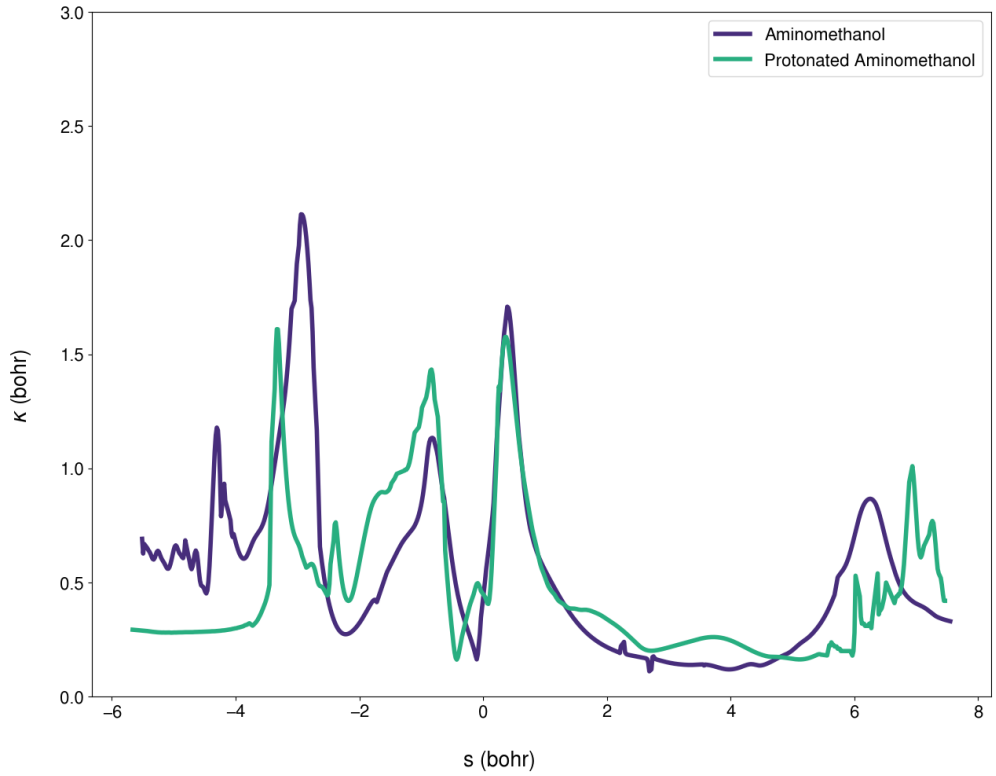

Figure 5.4: Scalar reaction path curvature for the water loss decomposition pathway of aminomethanol (purple) and N-protonated aminomethanol (green).

case of N-protonated aminomethanol as compared with the neutral system. This suggests that the true dynamic bottleneck and the transition state structure in the protonated system both lie closer to the reactants than in the neutral system. Additionally, the curvature of the reaction path for the N-protonated form of aminomethanol displays a broadened curvature peak near the reactants, indicating this event may be more prolonged than in the neutral form.

The scalar curvature of the path can be decomposed into the coupling coefficients of each normal modes (m) with the motion along the reaction path (F) to identify the contribution each mode makes to the reaction[185–189]. The relationship between scalar curvature (κ) and the reaction path is given by Equation 5.9

$$\kappa = \left(\sum B_{m,F}(s)^2\right)^{1/2} \tag{5.9}$$

Thus, both positive and negative curvature coupling coefficients influence the motion of the molecule along the path, with vibrational modes having a positive coupling coefficient assisting the progression of the reaction, and modes having negative coupling coefficients resisting the

progression of the reaction. Through decomposition of the reaction path curvature into the coupling coefficients of these vibrational modes, it becomes clearer where mechanistic differences arise between the protonated and neutral system. The scalar path curvature, as well as the coupling coefficients of selected vibrational modes that show strong assistance or resistance of the reaction progression are shown in Figures 5.5 and 5.6. Each vibrational mode of the molecule is labeled with a descriptor of the motion and changes in the molecular structure from the corresponding IRC calculation are overlaid.

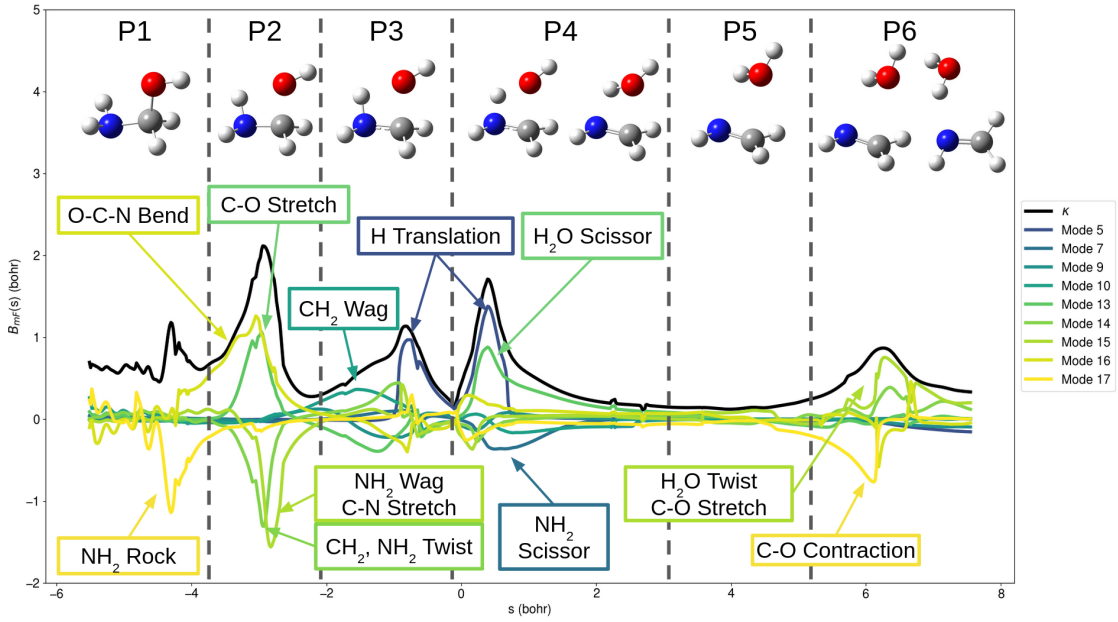

Figure 5.5: Scalar reaction path curvature (κ) and decomposition of the reaction path curvature into the mode coupling constants B_{mF}(s) for aminomethanol.

As is evident from Figures 5.5 and 5.6, there are slight differences in the phases of the reaction progression despite the reactants, transition state, and products appearing to have somewhat similar structures. Water loss from the aminomethanol molecule shown in Figure 5.5 begins with twisting of the NH_2 group to bring the hydrogen to be transferred into the O-C-N plane in Phase 1 (P1). In Phase 2, the C-O bond lengthens and breaks, the CH_2NH fragment also becomes more flattened. In Phase 3, the hydrogen atom migrates towards the OH fragment and a C-N double bond begins to form. In Phase 4, the transition state structure determined by the classic transition state search in Gaussian 16 is observed. A bond forms between the migrating hydrogen and the OH fragment to form the leaving water molecule. The C-N double bond is now fully formed. In Phase 5, the products move away from one another. In Phase 6, the leaving water molecule reorients to

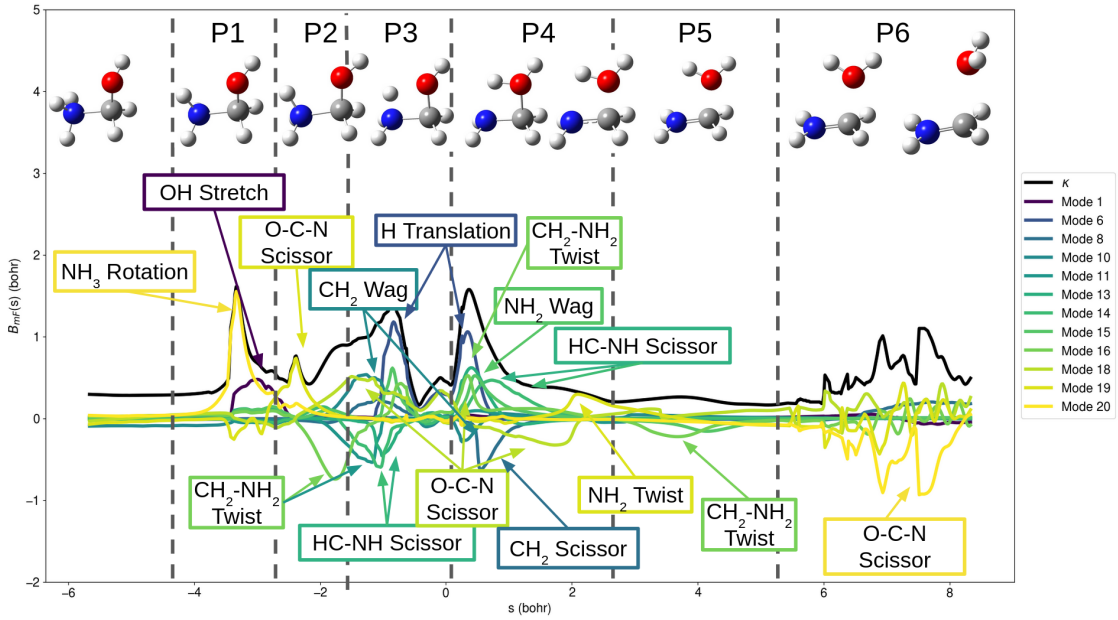

Figure 5.6: Scalar reaction path curvature (κ) and decomposition of the reaction path curvature into the mode coupling constants B_{mF}(s) for for protonated aminomethanol.

act as a hydrogen bond donor to the nitrogen on the methanimine product, stabilizing the product cluster.

In the protonated system, Phase 1 is marked by rotation of the NH_3 group to again bring the hydrogen into the O-C-N plane. In Phase 2, the NH_3 group twists into an eclipsed geometry and the N-H bond begins lengthening. In Phase 3, the N-H bond continues lengthening and a reduction in the O-C-N bond angle is observed. The N-H bond of the migrating hydrogen then breaks. Note that in the N-protonated system, the curvature minimum is shifted towards the reactants, as is observed with the energy curves in Figures 5.3 and 5.4. As in neutral aminomethanol, in Phase 4 an H-O bond forms and a C-N double bond begins to form. In contrast to the neutral system, the C-O bond breaks in Phase 4 nearly simultaneously with the H-O bond formation. In Phase 5, the H_2O molecule separates from the $CH_2NH_2^+$ product and the C=N bond forms. There is slight rearrangement of the $CH_2NH_2^+$ cation as the double bond forms and the molecule adopts a planar structure. In Phase 6, the products continue to separate. Whereas the neutral form displays movement of the water product to the N site and stabilization via hydrogen bonding, in the protonated form, the lost water merely rotates to form an ion-neutral complex, maintaining association between the water and carbon atom. This results in a prolonged curvature feature in the pathway of the protonated form. These decomposition paths were examined with the IRC

calculations performed in Gaussian 16 at the M06-L, M062X, and MP2 level of theory with the aug-cc-pVTZ basis set. Likewise, the structures reported by Riffet et al.[136] at the B3LYP/6-31G(d) level of theory show similar transition states to those shown here. The observed phases of the decomposition pathways remained the same regardless of the level of theory used. Thus, we conclude that intramolecular hydrogen atom transfer and subsequent water loss occurs through similar but slightly different mechanistic phases for aminomethanol and N-protonated aminomethnaol. The most notable differences in these mechanistic phases are the timing of the C-O bond breakage and delocalization of electrons about the C-N bond, and the greater degree of heavy atom movement (i.e., the O-C-N bond angle reduction) in the protonated system.

Table 5.2: Assistive and resistive vibrational modes in the decomposition of neutral aminomethanol.

Phase	Phase Description	Assistive Motion	Resistive Motion
1	NH_2 rotation H-N-C-O in plane	-	NH_2 rocking
2	C-O bond breaks C-N double bond forming	O—C—N outward bend C-O stretch	NH_2wag C-N stretch CH_2, NH_2 twist
3	H migration	H atom translation CH_2 wag NH_2 wag	H_2O scissor H_2O rocking
4	N-H bond breaks H-O bond forms C=N bond forms	H atom translation H_2O scissor	NH_2 scissor NH_2 wag
5	Product separation	-	-
6	Product separation O-H—N hydrogen bond	H_2O twist C-O stretch	C-O bond contracts

The vibrational modes that assist or resist in the progression of these reactions are, for the most part, intuitive. These motions are labeled in Figures 5.5 and 5.6 and summarized in Tables 5.2 and 5.3. Normal mode motions were characterized according to their scaled vibrational motions in Gaussian 16 and cross referenced to the vibrational energy level corresponding to the s value associated with the curvature feature. The stationary point that was most similar to the structure at the curvature feature was used to assign the motion associated with a particular vibrational mode. The stationary points used were the reactant for Phases 1 in the neutral system and 1 and 2 in the protonated system, the transition state structures for Phases 2, 3, and 4 in the neutral system and 3 and 4 in the protonated system, and the product complex for Phases 5 and 6 in both systems. Again, the systems show similar reaction phases with notably different timings

Table 5.3: Assistive and resistive vibrational modes in the decomposition of N-protonated aminomethanol.

Phase	Phase Description	Assistive Motion	Resistive Motion
1	NH_3 rotation H-N-C-O in plane	NH_3 rotation OH stretch	-
2	H migration	O−C−N scissor	-
3	C-O bond lengthens N-H bond breaks H migration	H atom translation CH_2 wag O−C−N scissor	CH_2−NH_2 twist HC-NH scissor
4	H-O bond forms C-O bond breaks	H atom translation CH_2−NH_2 twist NH_2 wag HC-NH scissor O−C−N scissor	CH_2 scissor CH_2 wag
5	C=N bond forms Product separation	NH_2 twist	-
6	Product separation H_2O twisting	-	O−C−N scissor

for N-H and O-H bond breakage and formation, respectively. Phase 2 appears to be the most significant event in the neutral system showing significant resistance to breaking the C-O bond. In contrast, the protonated system has similar sized curvature peaks across the MEP. Both systems are greatly assisted on either side of the transition state by translation of the hydrogen atom from the N to O site of the molecule. In the neutral system, there are few modes but those present make substantial contribution to motion along the MEP. In the protonated system, many modes contribute to motion along the MEP, each making small contributions. Moreover, while the neutral system has a large peak characterized by significant resistance, phases in the protonated system are characterized to a greater degree by assistive motions. Additionally, the O-C-N scissoring motion shows numerous assists to the reaction progression in the protonated system prior to s=0 and resistive character in the product region.

From the analysis of the normal vibrational modes presented above, two differences between water loss decomposition in the protonated and neutral aminomethanol systems become clear. First, while a similar normal mode motion is the main contributor to motion along the MEP, there are overall more normal modes that contribute to the reaction progress in the protonated system. The normal modes that have positive coupling to the reaction path in the protonated system appear to drive a reduction in the O-C-N angle, making much of the reaction possible without first undergoing a C-O bond breakage. Second, the curvature peak in Phase 3 of the protonated system is elongated over a greater range of s values, indicating more gradual electronic structure

changes associated with hydrogen atom movement and N-H and C-O bond breakage. This gradual electronic structure change may cause a broadening of the reaction barrier.

5.4.2 Reaction Rate Constants

Given the differences in reaction barrier width and reaction phases, it is pertinent to examine the reaction rate constants with inclusion of tunneling effects. Such effects are of particular interest to reactions occurring in the interstellar medium given the low temperature and low number density of molecules. Selected rate constants are presented in Tables 5.4 and 5.5. At low temperatures (< 300 K), there are significant contributions to the rate constant due to tunneling effects, with a profound rate enhancement for both systems at low temperatures. This effect is greater for the neutral system than for the protonated system, consistent with a narrower reaction barrier. Predictions of rate constants at such low temperatures are difficult, so these values should be taken with caution. Experimentally measured rate constants at low temperatures are needed to confirm the calculated kinetics at low temperatures. Despite the intense effects of hydrogen tunneling at low temperatures, the rate constants of decomposition of both aminomethanol and its N-protonated analog remain small. This indicates that while hydrogen tunneling will result in a significant rate enhancement, forward progression of the reactions to form imines for the next step of Strecker synthesis in the interstellar medium will likely rely on the catalytic effects of ice surfaces, energy imparted from other sources such as radiation (ultraviolet or X-ray), energy imparted from collisions or chemical reactions (such as the protonation of aminomethanol), or from warming of the icy bodies where these molecules are formed (as in atmospheric entry of comets or warming of ice mantles in protoplanetary disks). However, at temperatures of 300 K and above, N-protonated aminomethanol does display rate constants that indicate forward progression of Strecker synthesis is possible. This also indicates that for laboratory experiments, the neutral system is a better candidate for gas phase detection due to greater stability and that proton rich environments may promote decomposition of neutral aminomethanol via protonation and subsequent water loss.

Table 5.4: Rate Constants (s^{-1}) for aminomethanol decomposition. Values with an * indicate the tunneling correction that produces the largest rate constant, which is used as the $k_{\mu OMT}$ value.

T(K)	TST	CVT	CVT/ZCT	CVT/SCT	CVT/LCG4	CVT/μOMT
100	4.3(-109)	4.2(-109)	7.7(-72)	4.0(-63)*	8.0(-68)	4.0(-63)
200	1.7(-48)	1.7(-48)	3.2(-42)	6.5(-39)*	1.0(-39)	6.5(-39)
300	2.9(-28)	2.9(-28)	1.8(-26)	3.8(-25)*	9.4(-26)	3.8(-25)
400	4.0(-18)	4.0(-18)	2.6(-17)	9.9(-17)*	2.8(-17)	9.9(-17)
500	5.2(-12)	5.1(-12)	1.5(-11)	3.1(-11)*	1.4(-11)	3.1(-11)
600	6.3(-08)	6.2(-08)	1.3(-07)	2.0(-07)*	1.2(-07)	2.0(-07)
700	5.3(-05)	5.3(-05)	8.9(-05)	1.2(-04)*	8.5(-05)	1.2(-04)
800	8.5(-03)	8.4(-03)	1.2(-02)	1.6(-02)*	1.2(-02)	1.6(-02)
900	4.4(-01)	4.4(-01)	5.9(-01)	7.1(-01)*	5.8(-01)	7.1(-01)
1000	1.1(+01)	1.1(+01)	1.3(+01)	1.5(+01)*	1.3(+01)	1.5(+01)

Table 5.5: Rate Constants (s^{-1}) for N-Protonated Aminomethanol decomposition. Values with an * indicate the tunneling correction that produces the largest rate constant, which is used as the $k_{\mu OMT}$ value.

T(K)	TST	CVT	CVT/ZCT	CVT/SCT	CVT/LCG4	CVT/μOMT
100	2.1(-52)	2.1(-52)	1.8(-36)	2.3(-33)	1.1(-32)*	1.1(-32)
200	2.3(-20)	2.3(-20)	1.1(-17)	3.4(-16)	3.8(-16)	4.7(-16)
300	1.1(-09)	1.1(-09)	7.8(-09)	2.6(-08)*	1.0(-08)	2.6(-08)
400	2.3(-04)	2.3(-04)	6.4(-04)	1.1(-03)*	6.1(-04)	1.1(-03)
500	3.9(-01)	3.8(-01)	7.1(-01)	9.4(-01)*	6.8(-01)	9.4(-01)
600	5.5(+01)	5.5(+01)	8.3(+01)	9.9(+01)*	8.0(+01)	9.9(+01)
700	1.9(+03)	1.9(+03)	2.6(+03)	2.9(+03)*	2.5(+03)	2.9(+03)
800	2.8(+04)	2.8(+04)	3.5(+04)	3.9(+04)*	3.5(+04)	3.9(+04)
900	2.3(+05)	2.3(+05)	2.7(+05)	2.9(+05)*	2.7(+05)	2.9(+05)
1000	1.2(+06)	1.2(+06)	1.4(+06)	1.5(+06)*	1.4(+06)	1.5(+06)

The first two columns of Tables 5.4 and 5.5 show the TST and CVT rate constants, respectively. The next three entries show the CVT rate constants with the multidimensional tunneling corrections ZCT, SCT, LCG4, and μOMT. There is a maximal variational effect (k_{TST}/k_{CVT}) for both systems of approximately 1.03 at 60 K. Thus, there is minimal variational effects for both systems

The aminomethanol system displays dominance of the SCT approximation across the range of temperatures at which rate constants were computed, while the protonated system shows a switchover from the SCT approximation to the LCG4 approximation near 200 K. An Arrhenius plot comparing the rate constants of the two systems is shown in Figure 5.7. As may be expected, the rate constants of the protonated system are larger than those for the neutral system, with a widening of this gap at lower temperatures. In Figure 5.8, an Arrhenius plot for each system

without tunneling (CVT) and with tunneling corrections (ZCT, SCT, and LCG4) is shown. This figure demonstrates the profound effect that hydrogen tunneling has on these systems, inducing non-Arrhenius behavior at low temperatures.

The μOMT rate constants for both systems are plotted together in Figure 5.9. There is a clear difference in the degree of concavity, and thus tunneling, of the Arrhenius plot for aminomethanol and N-protonated aminomethanol. Neutral aminomethanol shows a high degree of concavity, which indicates a large effect of hydrogen tunneling on the rate constant. In contrast, N-protonated aminomethanol shows a much more subtle concavity, indicating that hydrogen tunneling has a less profound effect on the rate constant as compared with neutral aminomethanol. These observed differences are likely due to the width of the energy barrier and the role of heavy atom movement for the reaction discussed in the vibrational mode analysis. This difference in reaction phases is likely the cause of the hindered hydrogen tunneling effects despite both systems undergoing very similar reaction phases. These differences are not immediately apparent by simply looking at the energy of the transition states of the decompositions. It is through careful analysis of the intrinsic reaction coordinate and especially the reaction kinetics that the presence and impact of these minute differences can be observed. The separation of the μOMT rate constants at low temperatures indicates that the protonated form of aminomethanol is a more promising candidate for forward progression of the Strecker synthesis pathway. Altogether, this highlights the combined role of reaction barrier height and width in reaction rate constants and the role protonation may play in furthering chemistry in the ISM.

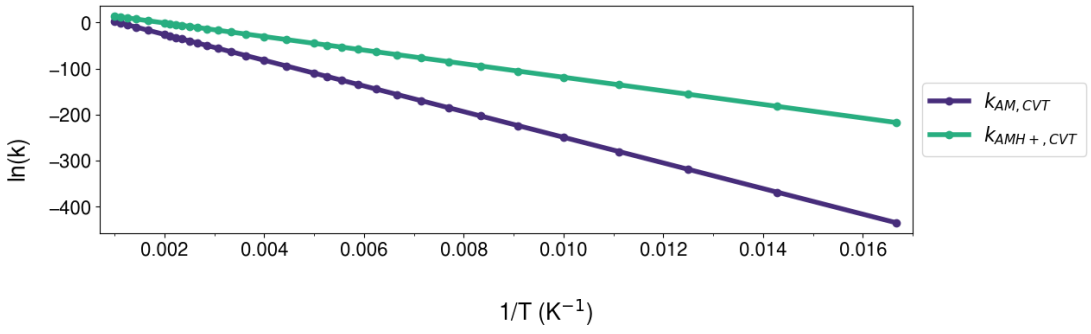

Figure 5.7: Arrhenius plot showing the CVT rate constants for both aminomethanol and N-protonated aminomethanol.

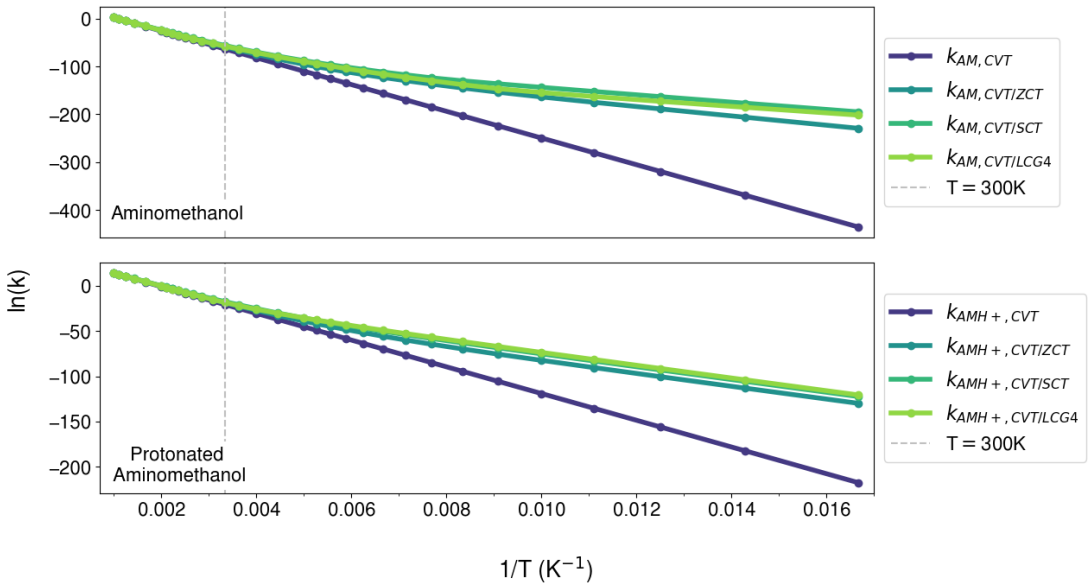

Figure 5.8: Arrhenius plot showing temperature dependence of the rate constants for both systems.

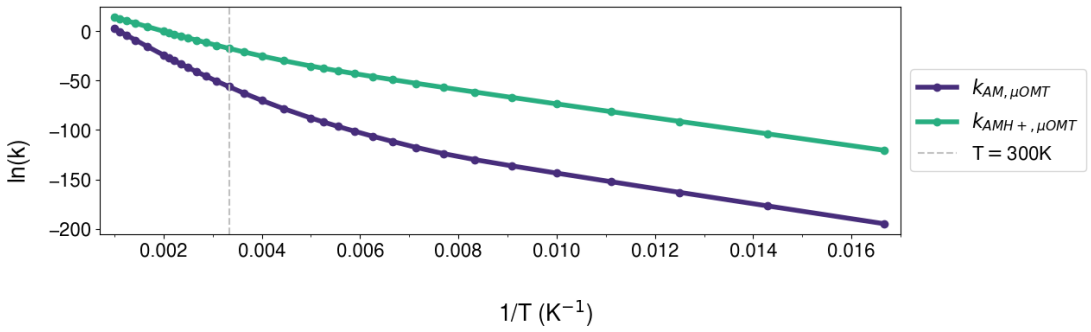

Figure 5.9: An Arrhenius plot showing the μOMT rate constant for each system, which is the greatest rate constant at each temperature point.

5.5 Rotational Prediction of N-Protonated Aminomethanol

N-protonated aminomethanol shows facile formation pathways from the reaction between aminomethanol, which has been synthesized in interstellar ice analog experiments, and common proton carriers in the ISM. Additionally, the work of Chen et al. [14] suggests that protonated aminomethanol may be an intermediate for the synthesis of aminomethanol in the ISM. Given the challenge to decomposition via water loss under typical conditions of the ISM (if energy from the formation is quenched) and the ease of formation for this protonated analog, it is possible that N-protonated

aminomethanol may be observed in laboratory experiments or in the interstellar medium. As such, calculations were performed to determine rotational and centrifugal distortion constants for the N-protonated analog of aminomethanol, the results of which are presented in Table 5.6. Stick spectra of the predicted pure rotational transitions are shown in Figure 5.10 at both T=30 K (blue) and T=300 K (red). N-protonated aminomethanol displays a Boltzmann peak centered around 200 GHz at T=30 K and centered slightly below 600 GHz at T=300 K. Calculations were carried out at the CCSD(T)/aug-cc-PVTZ level of theory using CFOUR. Catalog predictions were made from the rotational constants and centrifugal distortion constants using Pickett's CALPGM suite of programs[190] with Watson's S reduced Hamiltonian in the Ir representation. The input files for the catalog file are included in Appendix A.3.

Table 5.6: Rotational and Centrifugal Distortion Constants for N-Protonated Aminomethanol Determined at the CCSD(T)/aug-cc-PVTZ Level of Theory.

Parameter	Value	Unit
A	34351.8	MHz
B	9878.8	MHz
C	8440.5	MHz
D_J	8.802	kHz
D_{JK}	-21.944	kHz
D_K	196.974	kHz
d_1	-1.838	kHz
d_2	1.217	Hz
μ_a	-3.610	D
μ_b	0.938	D
μ_c	0.000	D

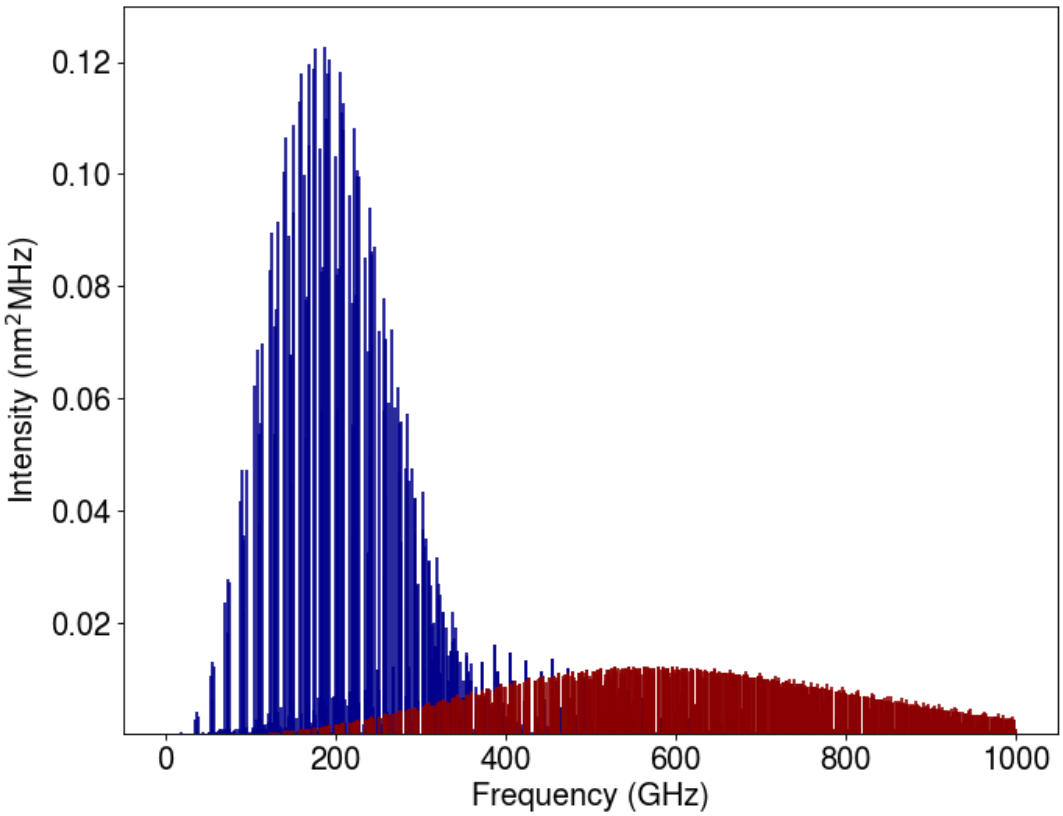

Figure 5.10: A stick spectrum prediction of N-protonated aminomethanol at T=30 K (blue) and T=300 K (red).

5.6 Conclusion

We report here reaction coordinates for the protonation of aminomethanol by common proton carriers in the ISM at both the M06-2X/aug-cc-pVTZ and M06-L/aug-cc-pVTZ level of theory. For all species except NH_4^+, the energy imparted by protonation is higher than the barrier to rearrangement and subsequent water loss, indicating that protonation of aminomethanol may be a potential pathway to protonated methanimine $CH_2NH_2^+$, which can undergo further reactions detailed by Walch et al.[147] to form glycine. We also report a detailed kinetic analysis of the decomposition via a 1,3 hydrogen transfer and subsequent water loss of both aminomethanol and its N-protonated analog at the M06-2X/aug-cc-pVTZ and M06-L/aug-cc-pVTZ levels of theory, respectively. These methods were chosen by benchmarking the reaction barrier against the existing literature for the lowest mean unsigned error. Results of kinetic analysis of both systems indicate

that the reaction barrier is lower for the protonated system, as is consistent with the literature, leading to a greater rate constant. However, close examination of the potential energy of the two systems along their MEPs shows a flattened energy barrier and a shift of the peak toward the reactants in the case of the protonated system. Further analysis of the reaction path curvature and the coupling constant, $B_{m,F}$, for the normal modes show that although the class of decomposition is the same, there are slight differences in the reaction phases that impact the kinetic rate constants, particularly in the case of hydrogen tunneling. Whereas aminomethanol decomposes by elongation of the C-O bond and loss of the OH group, before a hydrogen transfer from the nitrogen to oxygen atom and subsequent dissociation of the product complex, N-protonated aminomethanol decomposes by loss of the migrating hydrogen first before the leaving H_2O group is formed and the C-O bond breaks. Additionally, multiple phases of the N-protonated aminomethanol decomposition are assisted by an O-C-N scissoring normal mode, emphasizing the importance of heavy atom movement in its decomposition. These small differences in how decomposition occurs result changes in reaction path curvature, indicating that the electronic structure changes necessary for reaction progression in the neutral system are more discrete and result in a narrower reaction barrier than those of the N-protonated system. As a result of these differences, hydrogen tunneling in the protonated system has a reduced rate enhancement effect compared to the neutral system, observed as a reduced degree of concavity in the Arrhenius plot. These results highlight the gap that analysis of only the energies of the stationary points of a reaction surface leaves in our understanding of chemical systems. In contrast, detailed kinetic analysis of such chemical systems unveils surprising features that may contribute to our understanding of the chemistry observed in the laboratory or in the ISM.

The small kinetic rate constants at low temperatures, even with hydrogen tunneling effects included, indicate that spontaneous decomposition into either methanimine or protonated methanimine for aminomethanol or N-protonated aminomethanol, respectively, is quite unlikely without catalysis or energy in the form of radiation in the ISM. Thus, both aminomethanol and N-protonated aminomethanol may exist long enough in the ISM to be observed. Predicted rotational constants for aminomethanol have already been reported in the literature. We report rotational constants for the N-protonated system at the CCSD(T)/aug-cc-PVTZ level, as well as stick spectra at T=30 K and T=300 K, showing Boltzmann peaks near 200 GHz and 600 GHz, respectively. The kinetic rate constants for both aminomethanol and its N-protonated analog are sufficiently small

that these products may be observed in laboratory experiments and in the ISM. While Strecker synthesis of glycine may be possible with these species, progression through this synthesis pathway will rely on external sources of energy or catalysis rather than spontaneous decomposition.

Chapter 6

Catalytic Effects of Astrochemically Relevant Species on the Decomposition of Aminomethanol

6.1 Introduction

Aminomethanol (NH_2CH_2OH) is an aminoalcohol that is a key predicted intermediate in the stepwise Strecker synthesis of the simplest α-amino acid, glycine, in interstellar chemistry[129]. It is predicted to form in high abundance in the interstellar medium (ISM)[11, 12] from NH_3 and H_2CO, with advantageous barrier lowering effects in interstellar ice mantles[13, 15, 130–135]. Alternatively it may form from reactions of NH_2 and CH_2OH on icy dust grain surfaces[191]. Indeed, experiments have shown the feasibility of its formation in laboratory ice analogs[139–143]. However, gas phase synthesis and characterization of aminomethanol to support its interstellar detection via radio astronomy has thus far remained elusive due to complex chemical product networks[18].

While many theoretical studies exist on the formation of aminomethanol, few examine the expected decomposition pathway, an intramolecular hydrogen transfer followed by water loss. Of

those that do, they often take into account effects of catalysis from a limited number of species[15] or the kinetics of the reaction[131], but to the best of our knowledge, never both at the same time. The catalytic effects of species in these ice mantles bears consideration as even one or two catalytic molecules can have a profound effect on the barrier height of reactions as shown by Woon[13]. While the composition of these ice mantles is understood to have contributions from H_2O, CO_2, CO, CH_3OH, NH_3, and CH_4[192], works discussing catalytic effects of anything other than H_2O are lacking. This leaves a gap in the literature for species that may play a similar catalytic role such as CH_3OH and NH_3, especially in water poor ice mantles. Moreover, for laboratory synthesis of such an elusive species, understanding of how expected precursors such as H_2CO, NH_3, CH_3NH_2, and even other aminomethanol molecules interact with aminomethanol is critical to controlling the chemistry for laboratory detection and characterization. The kinetics of the reaction are also critical given the nature of the reaction: a high barrier proton transfer reaction occurring in an ultracold environment. Such a reaction is a prime candidate for hydrogen tunneling and kinetic isotope effects that may have a profound effect on the timescale and expected yields of the reaction. For these reasons, the work in this chapter examines in detail the effect that common ice mantle species (H_2O, CH_3OH, NH_3), expected precursors and products in laboratory synthesis (H_2CO, NH_3, CH_3NH_2, NH_2CH_2OH), and other rarer but potentially more impactful catalysts (HCOOH, H_2S) have on the intramolecular hydrogen transfer and water loss decomposition pathway for aminomethanol.

6.2 Computational Methods

6.2.1 Benchmarking

Initial computational work began with benchmarking the energy barrier to decomposition of aminomethanol in the uncatalyzed system against the work of Singh et al.[143], which used computations at the CCSD(T)/CBS//MP2/aug-cc-pVTZ level with zero point vibrational energy (ZPVE) corrections to obtain a reaction barrier height of 56.2 kcal/mol. Several levels of theory were benchmarked against the aforementioned work, including: MP2[149–153], B3LYP[154, 155], PBE0[156–158], ωB97X-D[159], M06-L[160], MN15-L[161], M06-2x[162], M08-HX[163], MN15[164], and VSXC[165]. Computations using the Minnesota functionals (M06L, M06-2X, M08-HX, MN15, and MN15-L) were performed using a superfine grid. Methods benchmarked were chosen for their availability in

Gaussian 16 as well as potential performance in accurately predicting hydrogen transfer reaction barrier heights[166]. The aug-cc-pVTZ basis set[167–170] was used for each of the benchmarking calculations given the small size of the system of interest. Geometry, frequency, and intrinsic reaction coordinate calculations were performed using Gaussian 16[148]. Geometry optimizations were performed using the "very tight" convergence critera. Analytical frequency calculations were used to confirm the nature of the transition states, which returned only one imaginary frequency per reaction. Frequencies of each benchmarked system were scaled using appropriate scaling factors[171, 172] using the "scale" keyword when available. When frequency scaling factors were not available, no scaling was applied. Intrinsic reaction coordinates (IRCs) were used to confirm that the transition states indeed represented the reaction of interest[173, 174]. The results of the benchmarking are shown in Table 6.1. The M06-2X level of theory showed the lowest mean unsigned error (MUE) at 0.61 kcal mol^{-1}, which is within chemical accuracy.

Table 6.1: Difference in energies (kcal mol^{-1}) between literature values and calculated values for the reaction barrier heights ($\Delta E_{Barrier}$), overall reaction (ΔE_{rxn}), and mean unsigned error (MUE) for the unvatalyzed decomposition of aminomethanol. All energies used in benchmarking included ZPVE corrections.

Theory Method	$\Delta E_{Barrier}$ (kcal/mol)	ΔE_{rxn} (kcal/mol)	MUE (kcal/mol)
MP2	-2.91	-1.09	2.00
B3LYP	-5.37	-4.71	5.04
PBE0	-0.17	1.71	0.95
ωB97X-D	-0.88	-0.77	0.83
M06-L	-5.06	-3.39	4.22
MN15-L	-1.39	-2.20	1.79
M06-2X	**-0.93**	**-0.28**	**0.61**
M08-HX	0.87	-1.49	1.18
MN15	-1.48	0.25	0.86
VSXC	-15.49	-8.52	12.00

6.2.2 Identification and Characterization of Catalytic Microclusters

Once the M06-2X/aug-cc-PVTZ theory level and basis set combination was determined to be the best option for aminomethanol, this combination was used to test the catalytic roles of various astrochemically relevant species. Catalysts were tested by performing transition state optimizations with at least "tight" convergence criteria. The loosely associated cluster complexes when $N_{catalyst}$ = 2 proved difficult for achieving "very tight" convergence. A frequency scaling factor of 0.971 was used in all transition state and frequency calculations using the "scale" keyword[171]. No dispersion corrections were added to these systems as the effects of these corrections are highly

system specific when using the Minnesota functionals, leading to more accurate results in some cases and over-binding in other cases[193].

Each catalyst was examined as a hydrogen bond donor, acceptor, proton relay facilitator, and in combined effects for small clusters ($N_{catalyst} = 2$). Catalysts showed a tendency to converge to hydrogen bond acceptors at the O site of aminomethanol (OH—Cat), hydrogen bond acceptors at the N site of aminomethanol (NH—Cat), and to act as both a hydrogen bond acceptor at the O site and hydrogen bond donor at the N site (Dual H Bond). The dual hydrogen bond donor and acceptor orientation notably is distinct from the orientations that allowed for the proton relay mechanism to take place and is another form of passive catalysis. The data labeled as "clusters" took the form of one active catalyst and one passive catalyst acting as a hydrogen bond acceptor at the O site of aminomethanol. An example of each of these geometries is shown in Figure 6.2. Some of these geometries failed to converge or converged to the geometry of a different system. In particular, more acidic species such as H_2O and H_2S showed a tendency to converge towards dual hydrogen bonding or the relay mechanism rather than a hydrogen bond acceptor.

These microclusters were examined using pre- and post-reaction complexes rather than infinitely separated products, as this result is most pertinent to ices where reactions would be expected to occur. Cartesian coordinates of the stationary points, including the pre- and post-reaction complexes, as well as the transition states are provided in Appendix A.4. In addition to barrier lowering effects, the effect of catalysts on barrier shape was examined using intrinsic reaction coordinate calculations. These computations were performed using a step size of 0.05 Bohr (StepSize=5), a path of 100 points, and "tight" convergence criteria.

6.2.3 Computation of Rate Constants

Rate constants of all reactions were computed using the Kisthelp Program[68]. Thermal reaction rate constants were computed using traditional transition state theory (TST) and TST with Wigner and Eckart one dimensional tunneling corrections (TST/W and TST/Eck, respectively). TST, TST/W, and TST/Eck rate constants were calculated for the uncatalyzed system and all catalyzed systems as unimolecular reactions. The optimized pre- and post-reaction clusters were used as a singular reactant or product, respectively. The temperature dependent TST rate constant is

calculated using the Equation 6.1.

$$k^{TST}(T) = \sigma \frac{k_b T}{h} \left(\frac{RT}{P^0} \right)^{\Delta n} e^{-\Delta G^{0,\ddagger}(T)/(k_b T)} \tag{6.1}$$

Where σ is the reaction path degeneracy, k_b is the Boltzmann constant, h is Planck's constant, $\frac{RT}{P^0}$ has units of inverse concentration, $\Delta n = 1$ or 0 for bimolecular or unimolecular reactions, respectively, and $G^{0,\ddagger}(T)$ is the standard Gibbs free energy of activation for the reaction.

One dimesional tunneling corrections were incorporated using the settings in KistHelp, which computes tunneling corrected rate constants using Equation 6.2.

$$k^{TST/Tunn} = \chi(T) k^{TST} \tag{6.2}$$

Where $\chi(T)$ is a multiplicative transmission coefficient and k^{TST} is the TST rate constant from Equation 6.1. In the case of the Wigner correction, $\chi(T)$ is given by Equation 6.3.

$$\chi(T) = 1 + \frac{1}{24} \left(\frac{h Im(\nu^{\ddagger})}{k_b T} \right)^2 \tag{6.3}$$

Where $Im(\nu^{\ddagger})$ is the imaginary frequency of the transition state. In the case of Eckart corrections, $\chi(T)$ is given by Equation 6.4.

$$\chi(T) = \frac{e^{\Delta H_r^{\ddagger,0K}/(k_b T)}}{k_b T} \int_0^{\infty} p(E + A) e^{E/(k_b T)} dE \tag{6.4}$$

Where $\Delta H_r^{\ddagger,0K}$ is the ZPE corrected energy barrier in the reverse direction, p(E+A) is the probability of transmission through the energy barrier above the energy A (the difference between the ZPE corrected forward and reverse reaction barriers). The transmission probability is dependent on the shape of the energy barrier, as determined from forward and reverse barrier heights as well as the imaginary frequency of the transition state.

Reaction path symmetry numbers were considered using the methods outlined by Fernandez-Ramos et al.[75]. The reaction path symmetry number is taken to be

$$\sigma_F = \frac{\sigma_{rot,R}}{\sigma_{rot,TS}} \tag{6.5}$$

Where σ is the rotational symmetry number of the forward reaction (F), reactants (R), or the

transition state (TS). The symmetry number of a species is determined by its point group[75]. The symmetry numbers of the optimized complexes were used for for $\sigma_{rot,R}$. As frequency scaling was applied in the Gaussian 16 frequency calculations, no additional frequency scaling was applied in the KistHelp program. TST rate constants were calculated for a temperature range from 60K to 1,000K. All computed rate constants are available in Appendix A.4.

6.3 Barrier Height Effects

In the present study, a variety of catalysts with relevance to laboratory astrochemical experiments and in situ interstellar ices were explored. These catalysts were chosen for their prevalence in interstellar ices (H_2O, CH_3OH[192]), their role in laboratory attempts to synthesize aminomethanol (CH_3NH_2[18, 143], H_2CO and NH_3[139–142], NH_2CH_2OH), or their recent detection in interstellar ices with the James Webb Space Telescope (HCOOH[194]). H_2S has not yet been observed in interstellar ices[195] however it has been observed as the most prevalent sulfur bearing ice species in comets[196] and is known to form efficiently on ice grains via successive hydrogenation of atomic sulfur[197]. A reaction coordinate of the uncatalyzed decomposition of aminomethanol via water loss, including optimized structures of the reactants, transition state, and products, is shown in Figure 6.1. An example of the optimized transition state geometry for each examined catalytic mechanism is shown in Figure 6.2. An overview of the catalytic effects of the examined species on this reaction are shown in Figures 6.3 and 6.4.

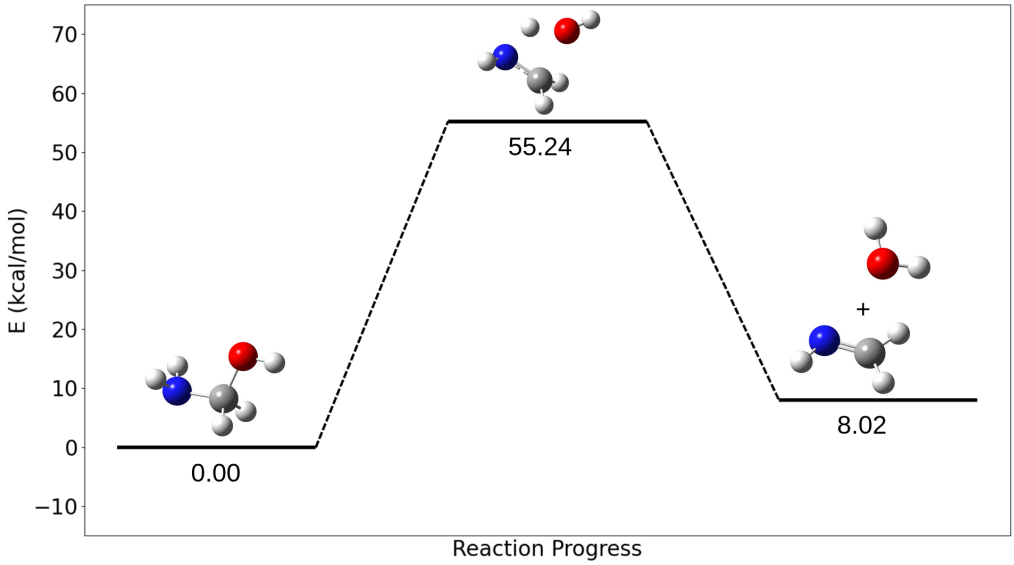

Figure 6.1: Reaction coordinate diagram of aminomethanol decomposition via 1,3-hydrogen transfer and water loss showing optimized structures at the M06-2X/aug-cc-pVTZ level of theory with ZPVE corrections.

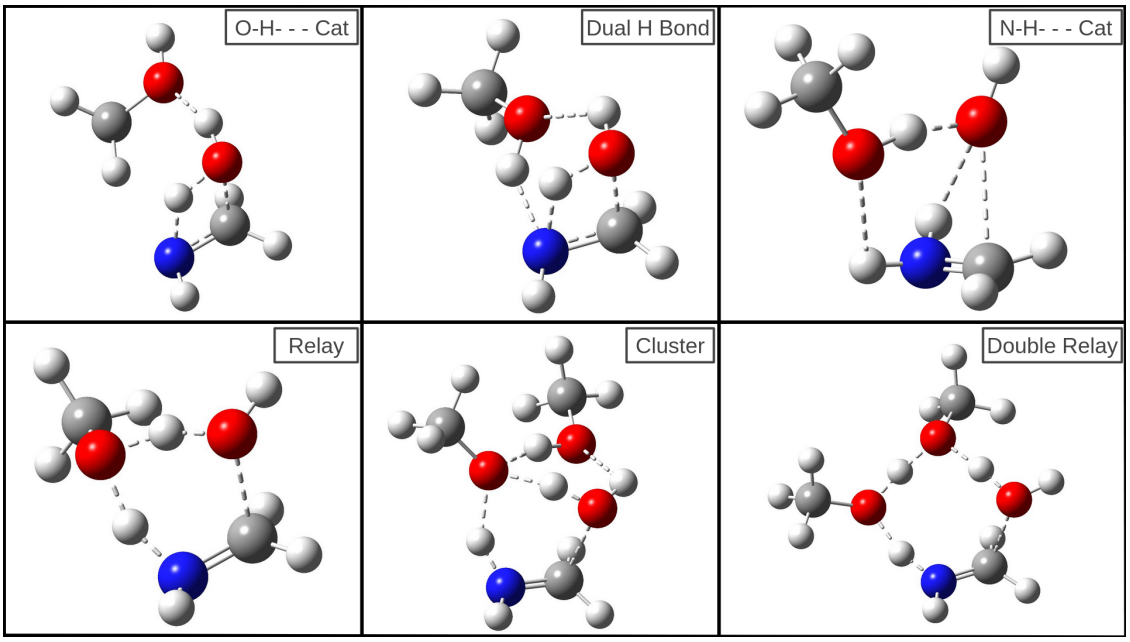

Figure 6.2: Optimized transition state geometries at the M062X/aug-cc-pVTZ level of theory of each catalytic mechanism examined for methanol.

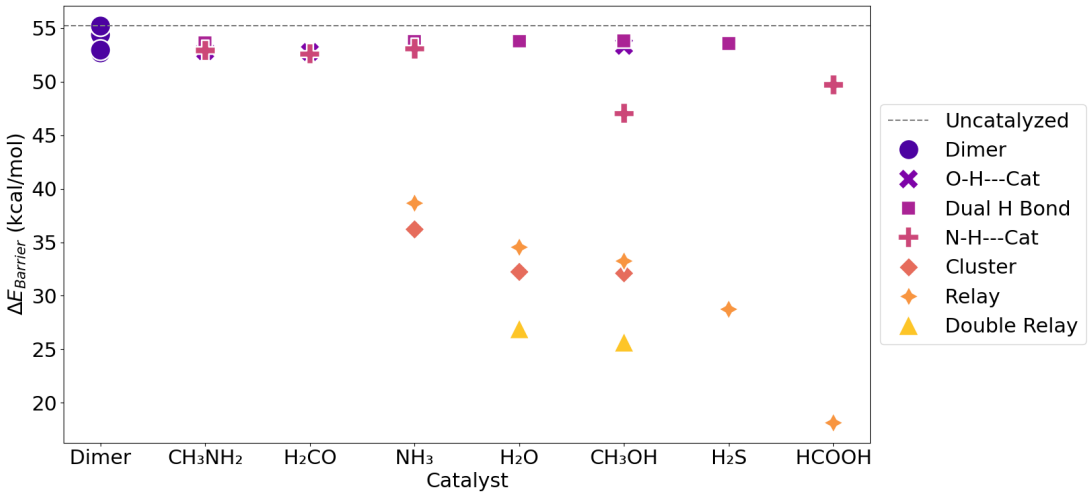

Figure 6.3: Reaction barrier heights between optimized pre-reaction clusters and optimized transition states at the M06-2X/aug-cc-pVTZ level of theory with ZPVE corrections. Datapoints are colored by the catalytic mechanism examined as shown in the legend.

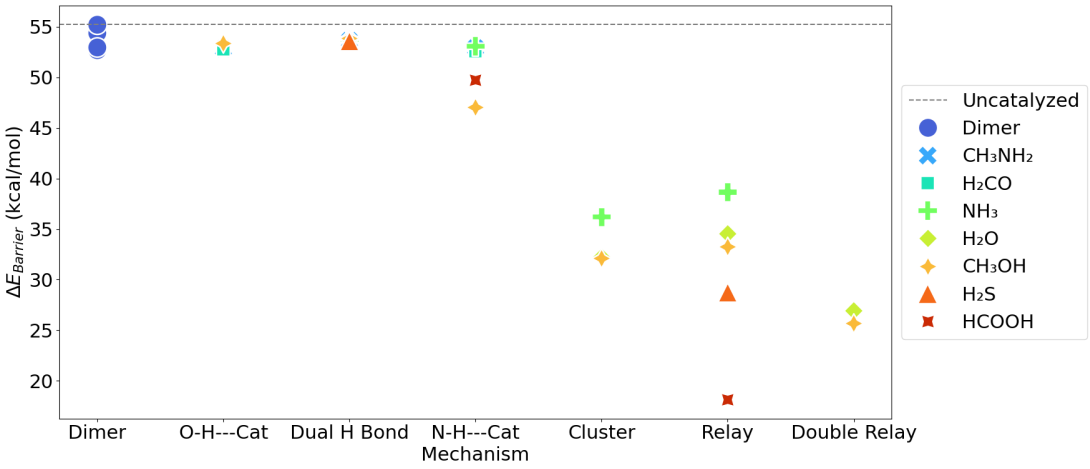

Figure 6.4: Reaction barrier heights between optimized pre-reaction clusters and optimized transition states at the M06-2X/aug-cc-pVTZ level of theory with ZPVE corrections. Datapoints are colored by the catalyst identity as shown in the legend.

Globally, the effectiveness of a catalyst in lowering barrier height appears to depend most on its ability to act as a proton relay facilitator. As found by Woon[13] previously, additional active catalysts lower barrier height further. Interestingly, incorporation of an additional passive catalyst as in the Figure 6.4 category labeled "Cluster", showed further reduction in barrier heights over just the active catalyst in the proton relay. While of potential interest in gas phase astrochemical

experiments, such as those that use pulsed valves that can produce microclusters like those studied here, this effect is not pronounced enough to overcome the energy barrier for decomposition of aminomethanol in the ISM. Initially, a third active catalyst in the proton relay was considered as well. However, no additional barrier lowering effects were observed relative to two active catalysts and these systems were not pursued further. This is contrary to the effect predicted by Woon[13] in the synthesis of aminomethanol and is most likely the result of the small path of travel in a 1,3-intramolecular hydrogen transfer compared to an intermolecular system. Simply from steric constraints, additional proton relay facilitators are likely prohibitive to further barrier lowering effects as they force movement of the heavy atoms of aminomethanol.

While the mechanism of catalysis clearly suppresses reaction barrier height, the identity of the examined catalysts is of importance as well. Water is often the primary catalyst of interest in a proton transfer reaction such as that presented here[13, 15]. Other species such as ammonia or methanol are sometimes examined in other contexts [198–201], but to the best of our knowledge have not been examined in astrochemical contexts. However, as shown in Figure 6.3, many species are capable of suppressing barrier height via the proton relay mechanism. Relatively abundant species such as methanol and ammonia should not be discounted when considering such effects, especially in water poor environments. Additionally, while lower in abundance in the ISM, species such as formic acid may have an even more profound catalytic effect on observed chemistry. Perhaps unsurprisingly, trends in catalytic effectiveness for the presented reaction generally followed with acidity of the catalyst, with more acidic catalysts showing greater barrier suppression via the proton relay mechanism. This correlation was relatively well clustered for NH_3, H_2O, and CH_3OH. However, there was greater deviation from the trendline for H_2S and HCOOH as shown by Figure 6.5. This may indicate that while acidity is certainly correlated, there may be other factors at play such as sterics or electron delocalization that make this property only modestly predictive.

Table 6.2: Computed barrier heights between the optimized pre-reaction complex and transition state for the relay mechanism (kcal/mol) and literature gas phase acidity (kcal/mol)[202–204]

Species	$\Delta E_{Barrier,relay}$ **(kcal/mol)**	ΔH^o_{acid}**(kcal/mol)**
NH_3	38.65	399.6
H_2O	34.53	390.8
CH_3OH	33.24	380.6
H_2S	28.74	351.2
HCOOH	18.12	345.2

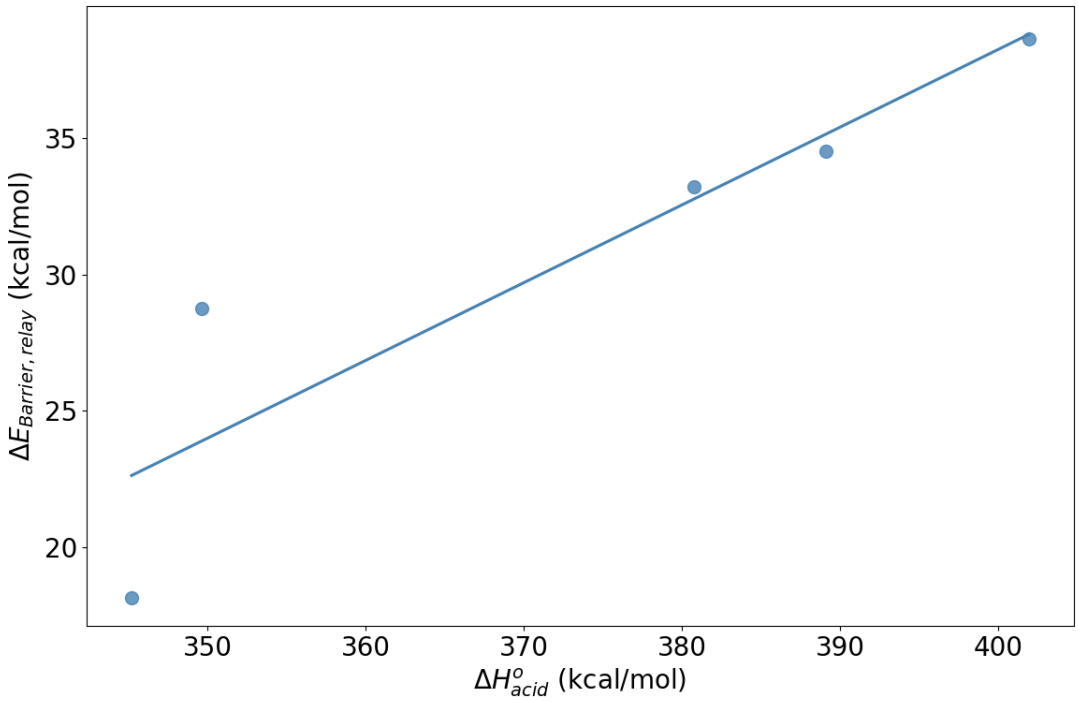

Figure 6.5: Computed barrier heights between the optimized pre-reaction complex and transition state for the relay mechanism (kcal/mol) and literature gas phase acidity (kcal/mol).

In addition to species of interest in the ISM, species that may be present in laboratory experiments synthesizing or isolating aminomethanol were also examined. Methylamine has been used as a precursor for aminomethanol synthesis via barrierless insertion of O(^{1}D). This has proven successful in the solid phase [143] but aminomethanol detection in the gas phase remains elusive with this method[18]. Alternatively, synthesis from ammonia and formaldehyde has proven fruitful in laboratory ices [141, 142, 205], though the high aminomethanol formation barrier provides a clear challenge to gas phase experiments. Thus, the catalytic effects of these precursors as well as other aminomethanol molecules are presented here to inform attempts at laboratory synthesis. Methylamine, formaldehyde, and other aminomethanol molecules (dimers) appear to be quite poor catalysts for decomposition as shown in Figure 6.3. Ammonia and water show significant barrier suppression of up to almost 20 kcal/mol and 30 kcal/mol below the uncatalyzed reaction, respectively. However, the high barrier to the uncatalyzed reaction and endothermicity of the reaction overall suggests that if aminomethanol is synthesized and entered into the gas phase with sufficiently low density and energy, it should remain stable long enough for laboratory detection even

if catalyzed by ammonia, methylamine, formaldehyde, water, or other aminomethanol molecules.

6.4 Barrier Shape Effects

Reaction barrier height is often considered the most important factor in reaction feasibility. However, in the harsh environment of the ISM, hydrogen tunneling is expected to play a significant role in reactions[206–208]. This is of particular interest in a reaction such as the decomposition of aminomethanol given it is primarily a hydrogen transfer reaction. Presented here are the results of IRC computations from optimized transition state complexes. Of note, these IRC computations do not include ZPVE corrections due to the limitations of Gaussian 16. These computations are presented primarily for qualitative analysis of these systems as ZPVE corrections along the IRC path would be expected to change the overall barrier shape in highly accurate multidimensional tunneling models[74].

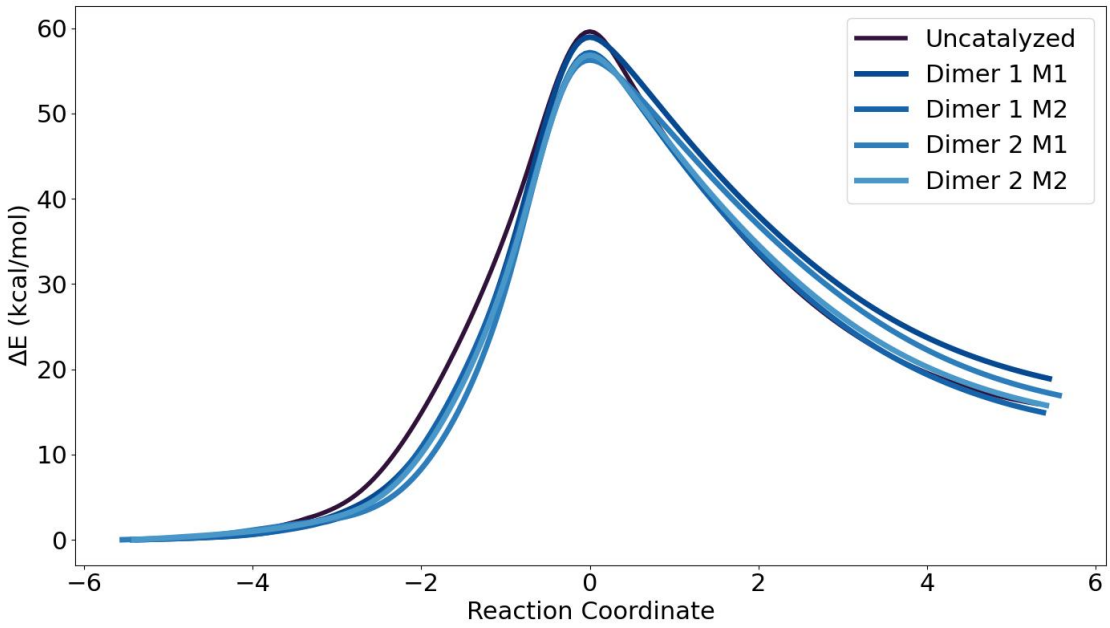

Figure 6.6: Computed intrinsic reaction coordinates for dimer systems of aminomethanol. Calculations were carried out at the M06-2X/aug-cc-pVTZ level of theory without ZPVE corrections.

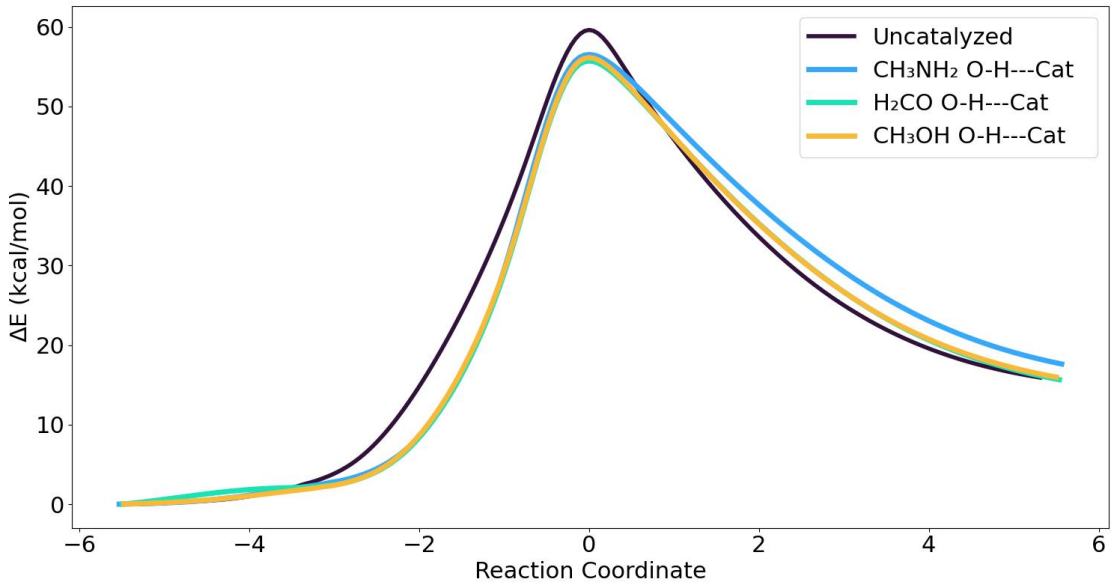

Figure 6.7: Computed intrinsic reaction coordinates for systems displaying passive catalysis via hydrogen bonding at the O site of aminomethanol. Calculations were carried out at the M06-2X/aug-cc-pVTZ level of theory without ZPVE corrections.

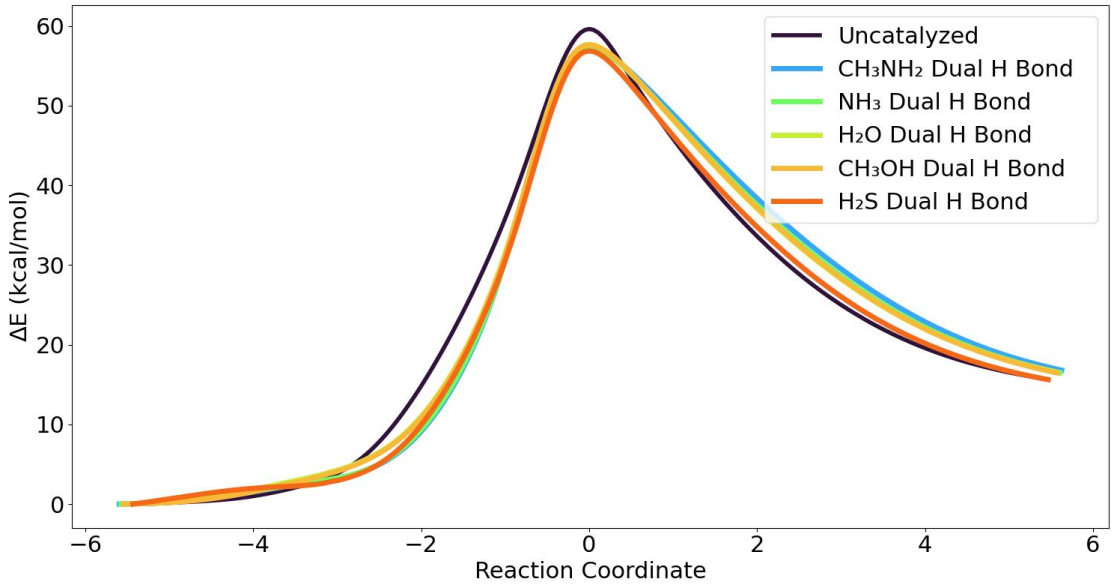

Figure 6.8: Computed intrinsic reaction coordinates for systems displaying passive catalysis via accepting hydrogen bonding at the O site of aminomethanol and donating at the N site. Calculations were carried out at the M06-2X/aug-cc-pVTZ level of theory without ZPVE corrections.

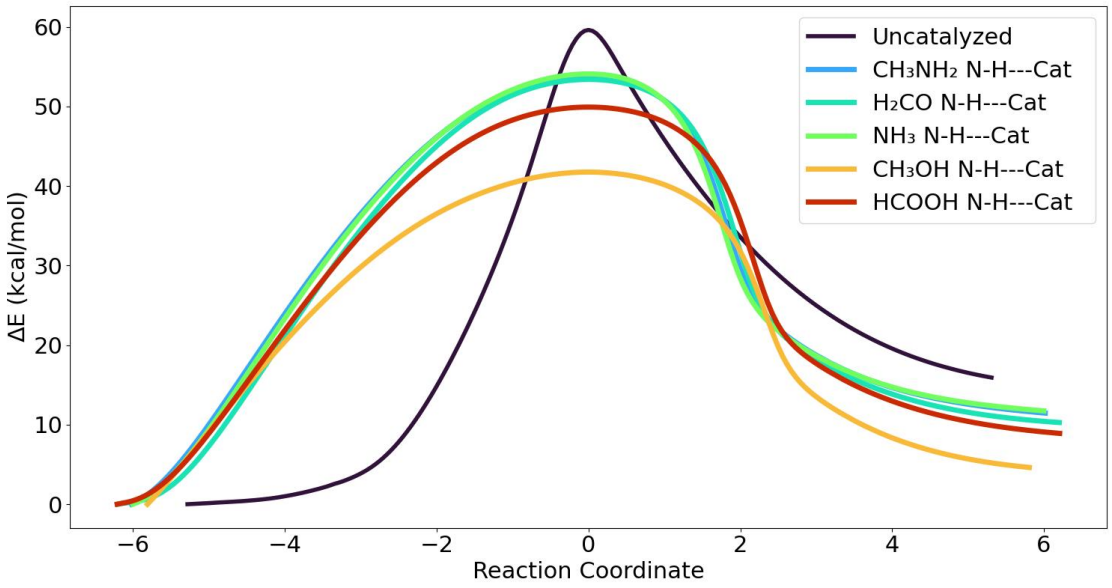

Figure 6.9: Computed intrinsic reaction coordinates for systems displaying passive catalysis via hydrogen bonding at the N site of aminomethanol. Calculations were carried out at the M06-2X/aug-cc-pVTZ level of theory without ZPVE corrections.

Many systems showed little, if any difference in barrier shape due to passive catalysis, with the exception of the N-H—Cat mechanism. The effects of passive catalysis in the form of dimers, the O-H—Cat mechanism, and the dual hydrogen bond mechanism are shown in Figures 6.6, 6.7, and 6.8, respectively. However, when the catalyst acted as a hydrogen bond acceptor at the N site of aminomethanol, rather drastic changes in the shape of the reaction barrier were observed, as in Figure 6.9. This form of interaction increased separation of the reaction phases and promoted asynchronicity, leading to distinct events of loss of an OH group, followed by hydrogen abstraction at the N site with little movement of the leaving hydrogen, and finally water loss. In other systems, the intrinsic reaction coordinate showed simultaneous lengthening of the C-O bond and migration of the leaving hydrogen from the N site toward the O site. This contrast of light atom movement (hydrogen) versus heavy atom movement of the OH group could explain why the reaction barrier broadened so significantly. These IRC data suggest that basic species such as NH_3 and CH_3NH_2, and other hydrogen bond acceptors such as the carbonyl groups in H_2CO and HCOOH may demonstrate protective effects against aminomethanol decomposition due to barrier broadening.

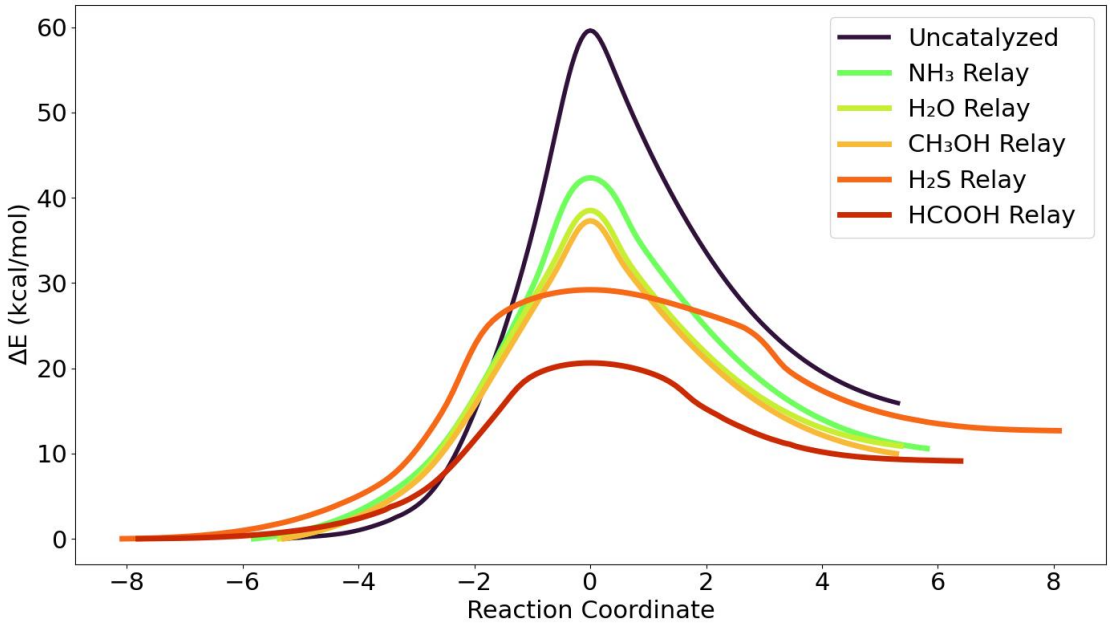

Figure 6.10: Computed intrinsic reaction coordinates for systems displaying the proton relay mechanism with $N_{Catalysts} = 1$. Calculations were carried out at the M06-2X/aug-cc-pVTZ level of theory without ZPVE corrections.

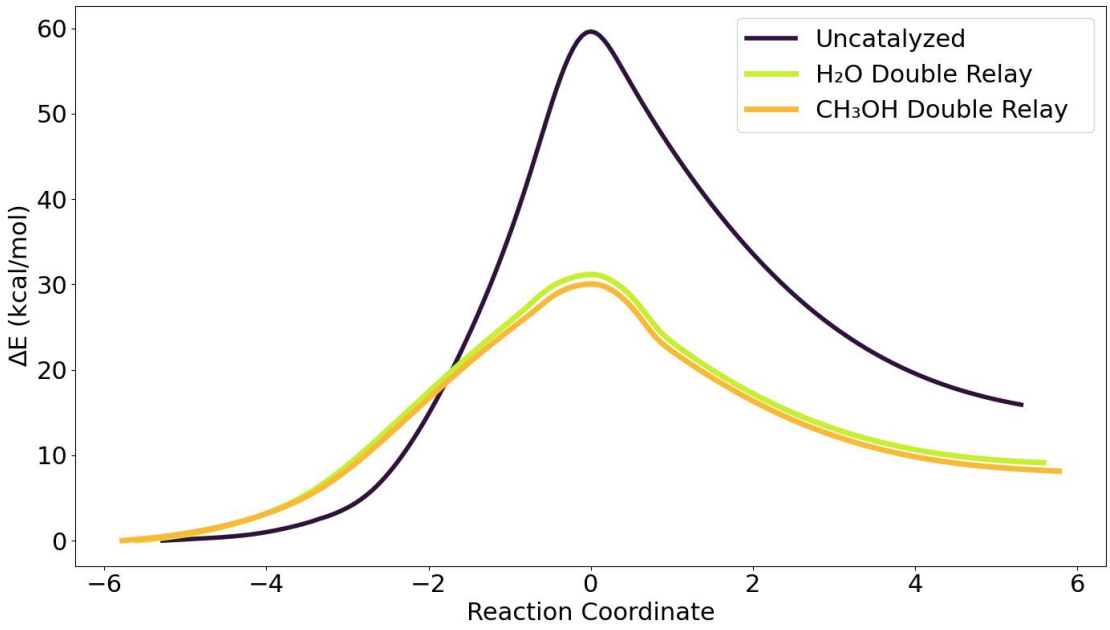

Figure 6.11: Computed intrinsic reaction coordinates for systems displaying the proton relay mechanism with $N_{Catalysts} = 2$. Calculations were carried out at the M06-2X/aug-cc-pVTZ level of theory without ZPVE corrections.

Inclusion of a catalyst as a proton relay facilitator also caused a broadening effect, albeit more modest than in the case of hydrogen bond acceptors at the N site of aminomethanol. The greatest barrier broadening effects due to a single catalyst were observed in the H_2S and HCOOH relay systems as shown in Figure 6.10. This broadening effect is in addition to significant barrier lowering effects. The water, methanol, and ammonia systems remained relatively impervious to this effect in the case of one and two active catalysts. However, the inclusion of one active catalyst and one passive catalyst induced visible broadening in all three systems.

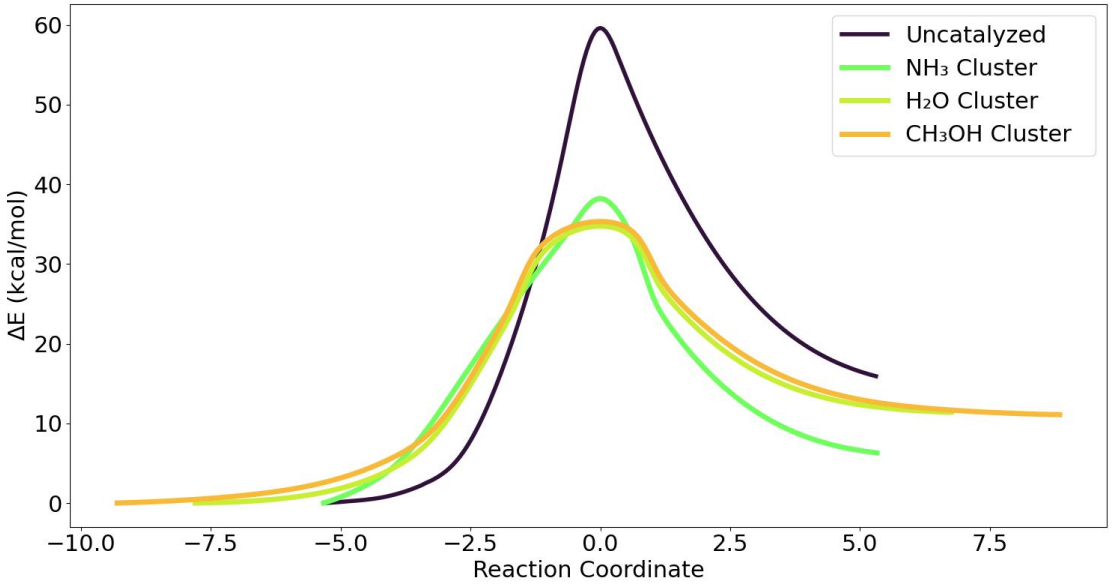

Figure 6.12: Computed intrinsic reaction coordinates for systems displaying simultaneous effects from the proton relay mechanism and hydrogen bonding. Calculations were carried out at the M06-2X/aug-cc-pVTZ level of theory without ZPVE corrections.

It seems that inclusion of active catalysts via the proton relay mechanism indeed leads to barrier lowering effects making hydrogen transfer reactions more energetically accessible. However, there may be a secondary effect to this catalysis that leads to barrier broadening ranging from mild in most cases to quite significant in a select few cases, as with H_2S and HCOOH. These broadened barriers may lead to decreased tunneling effects if the reaction remains concerted or it may make the reaction path more energetically accessible if the effect is so great that the reaction becomes separated into step-wise mechanisms, as observed by Bovolenta et al. in water catalyzed synthesis of aminomethanol[15]. Since both scenarios are plausible, there may be unpredictable effects in catalyzed hydrogen transfer reactions such as those presented here. Such systems are

excellent candidates for further study with sophisticated computational methods, especially those that consider the full dimensionality of the reaction potential energy surface.

6.5 Reaction Kinetics

In addition to reaction barrier height and shape, reaction rate constants were calculated using the Kisthelp program as described previously. All computed rate constants are included in the supplementary information of this work. An overview of the reaction rate constants without (TST) and with (Wigner and Eckart) tunneling corrections are shown in Figures 6.13 and 6.14. The trends within these plots are consistent with the discussion in the previous two sections and are relatively straightforward, especially in the case of the computed TST and TST/Wigner rate constants. Which is to say that relatively little effect on the rate constant is observed for systems with passive catalysis as in the case of dimers, the O-H—Cat mechanism, or the dual hydrogen bonding mechanism (Arrhenius plots are provided in the supplemental information). In the case of the N-H—Cat mechanism, the barrier broadening effects lead to reduced reaction rates when tunneling is considered. When using the asymmetric Eckart approximation, the impact of increased barrier width on tunneling is more readily observed, as in Figure 6.9. Nearly no curvature is observed in the Arrhenius plot for broadened systems, while the curvature remains quite clear in the uncatalyzed system. This indicates that little if any tunneling is occurring in these systems[209, 210]. The ability to act as a proton relay facilitator has the greatest impact on the reaction rate enhancement overall, and more acidic species show greater propensity for rate enhancement. The latter two effects are visible in Figures 6.15 and 6.16.

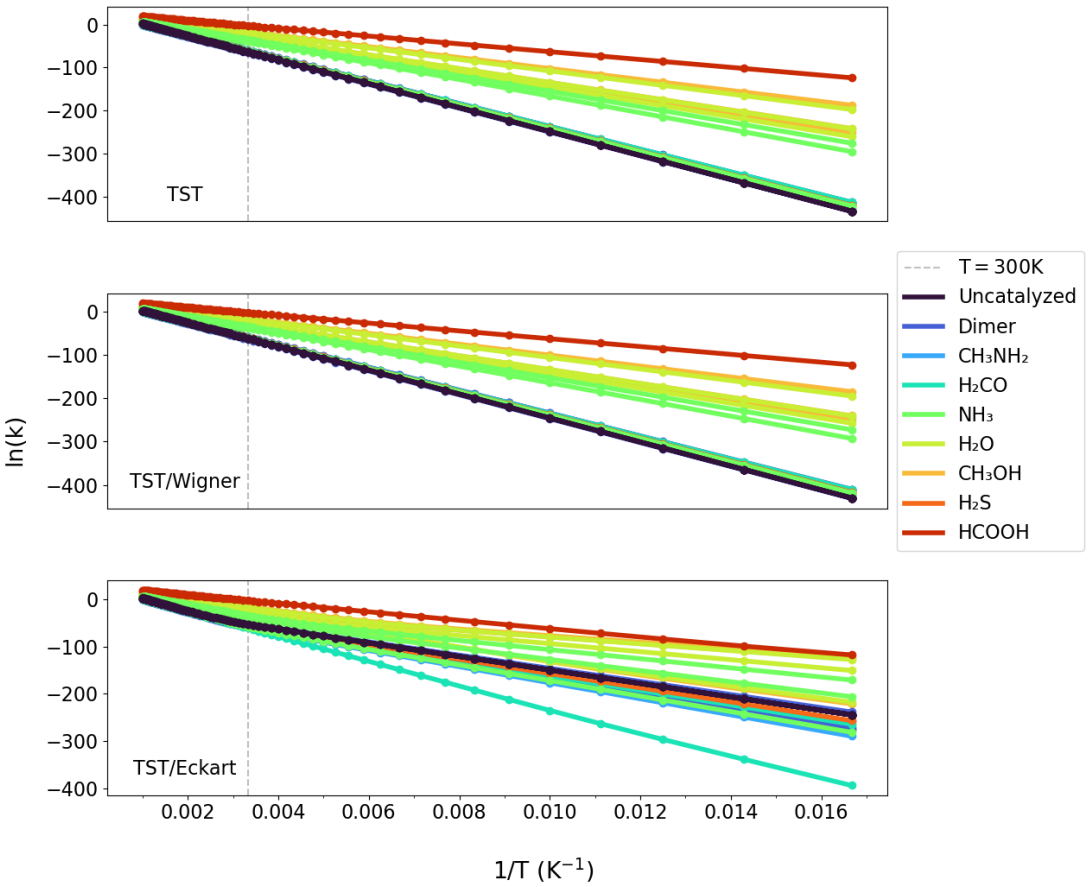

Figure 6.13: Arrhenius plots showing the reaction rate constants for all examined systems colored by catalyst identity. Plots are annotated with tunneling corrections employed.

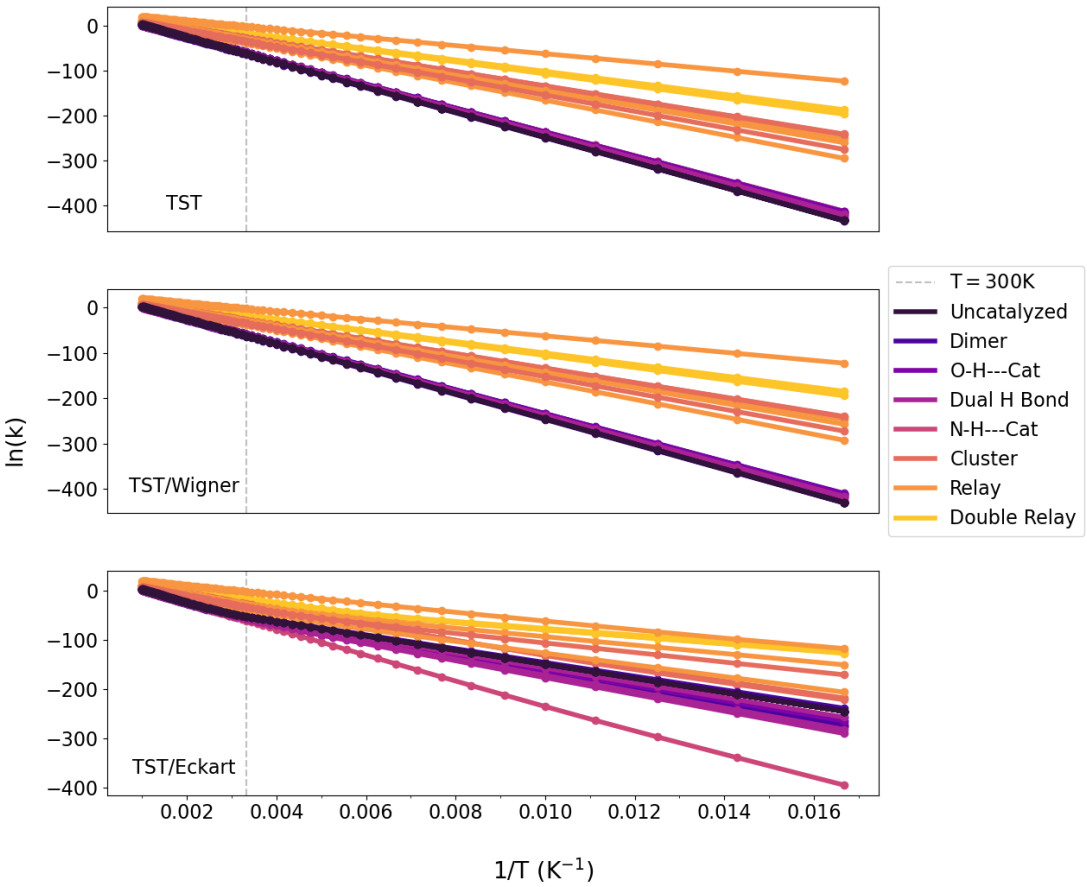

Figure 6.14: Arrhenius plots showing the reaction rate constants for all examined systems colored by mechanism. Plots are annotated with tunneling corrections employed.

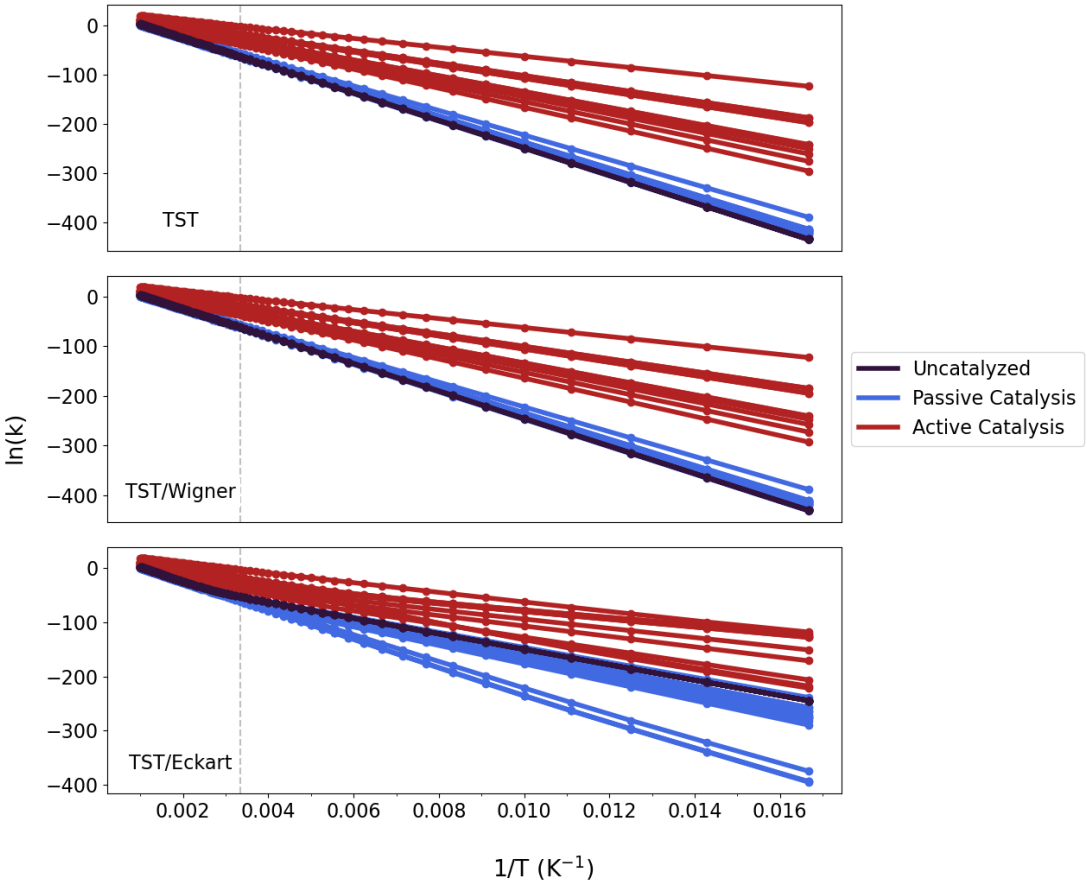

Figure 6.15: Arrhenius plots showing the reaction rate constants for all examined systems colored by whether the mechanism of catalysis is active (red) or passive (blue). Plots are annotated with tunneling corrections employed.

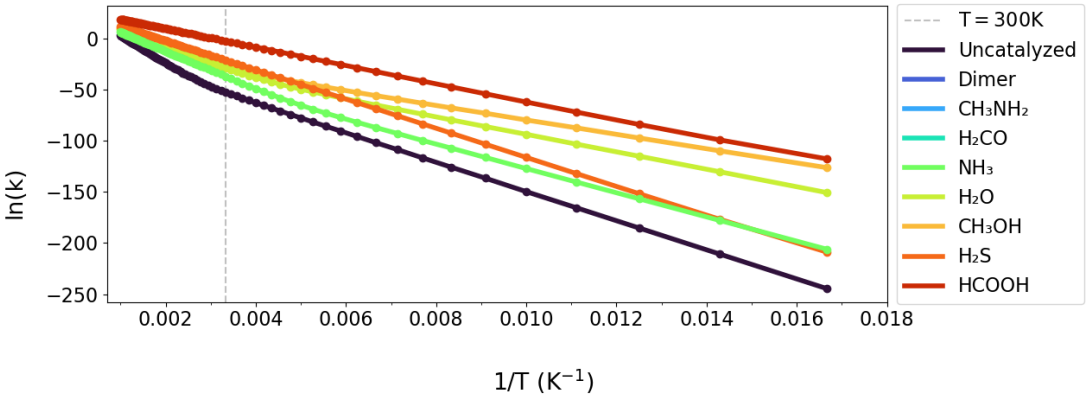

Figure 6.16: Arrhenius plots showing the reaction rate constants for all systems with the relay mechanism colored by catalyst identity.

Selected rate constants for the most extreme rate reductions and enhancements are shown in Tables 6.3, 6.4, and 6.5. At low temperatures, the impact of barrier shape on the reaction rate coefficient is observable in the form of small rate constants at low temperatures, as in Tables 6.3 and 6.4. However, at high temperatures where energy levels above the reaction barrier height are accessible, rate enhancement is observed. This is especially noticeable in the case of H_2S in Table 6.4. HCOOH does not display this low temperature rate impediment and high temperature enhancement, which may be attributed to the significant reduction in barrier height and the overall lesser degree of barrier broadening in HCOOH as compared with H_2S.

Table 6.3: Thermal rate constants (s^{-1}) with Eckart tunneling corrections for systems with significant rate reduction effects due to the N-H—Cat mechanism

T (K)	Uncatalyzed	CH_3NH_2	H_2CO	NH_3	CH_3OH	HCOOH
60	5.89E-107	2.89E-172	8.34E-172	5.75E-172	8.93E-155	1.68E-163
100	8.48E-66	4.95E-103	7.29E-103	3.52E-103	8.43E-91	7.79E-97
200	1.64E-34	4.65E-46	2.13E-46	2.68E-46	8.07E-40	3.44E-43
300	1.63E-23	8.53E-27	2.36E-27	4.78E-27	1.12E-22	3.88E-25
400	1.51E-16	4.16E-17	8.88E-18	2.27E-17	4.61E-14	4.65E-16
500	3.15E-11	2.88E-11	5.27E-12	1.54E-11	7.09E-09	1.38E-10
600	2.00E-07	2.33E-07	3.84E-08	1.23E-07	2.08E-05	6.36E-07
700	1.21E-04	1.47E-04	2.26E-05	7.68E-05	6.34E-03	2.68E-04
800	1.59E-02	1.86E-02	2.72E-03	9.69E-03	4.63E-01	2.51E-02
900	7.28E-01	8.12E-01	1.14E-01	4.20E-01	1.32E+01	8.71E-01
1000	1.59E+01	1.68E+01	2.27E+00	8.65E+00	1.93E+02	1.48E+01

Table 6.4: Selected thermal rate constants (s^{-1}) with Eckart tunneling corrections for systems with significant rate enhancement effects due to the relay mechanism ($N_{Catalyst}$=1)

T (K)	Uncatalyzed	NH_3	H_2O	CH_3OH	H_2S	HCOOH
60	5.89E-107	3.01E-90	3.33E-66	1.29E-55	1.89E-91	6.82E-52
100	8.48E-66	5.22E-56	1.80E-41	2.13E-35	2.82E-51	8.92E-28
200	1.64E-34	3.94E-29	2.48E-22	1.53E-19	2.49E-20	2.25E-08
300	1.63E-23	6.60E-17	3.20E-13	4.60E-12	5.18E-10	7.57E-02
400	1.51E-16	2.77E-10	1.50E-07	7.40E-07	7.49E-05	1.43E+02
500	3.15E-11	2.95E-06	5.04E-04	1.67E-03	9.40E-02	1.34E+04
600	2.00E-07	1.49E-03	1.22E-01	3.26E-01	1.10E+01	2.79E+05
700	1.21E-04	1.31E-01	6.43E+00	1.49E+01	3.31E+02	2.46E+06
800	1.59E-02	3.82E+00	1.29E+02	2.7E+02	4.29E+03	1.26E+07
900	7.28E-01	5.35E+01	1.35E+03	2.63E+03	3.16E+04	4.50E+07
1000	1.59E+01	4.48E+02	8.95E+03	1.66E+04	1.55E+05	1.26E+08

Table 6.5: Selected Thermal rate constants (s^{-1}) with Eckart tunneling corrections for systems with significant rate reduction effects due to the double relay mechanism ($N_{Catalyst}$=2)

T (K)	Uncatalyzed	H_2O	CH_3OH
60	5.89E-107	3.91E-56	8.40E-54
100	8.48E-66	1.87E-35	3.43E-34
200	1.64E-34	1.86E-17	1.50E-16
300	1.63E-23	8.74E-09	4.39E-08
400	1.51E-16	2.92E-04	1.10E-03
500	3.15E-11	1.59E-01	5.13E-01
600	2.00E-07	1.08E+01	3.17E+01
700	1.21E-04	2.24E+02	6.17E+02
800	1.59E-02	2.21E+03	5.82E+03
900	7.28E-01	1.33E+04	3.39E+04
1000	1.59E+01	5.66E+04	1.41E+05

6.6 Conclusion

In this work, several astrochemically relevant catalysts were examined in various passive and active catalytic roles on the 1,3-hydrogen transfer and water loss decomposition of aminomethanol. Catalysts included aminomethanol dimers, relevant precursors for laboratory synthesis (CH_3NH_2, H_2CO, NH_3), the most common components of interstellar ice matrices (NH_3, H_2O, CH_3OH), and rarer species likely to have greater catalytic effects (H_2S, HCOOH). All catalysts induced some level of reduction in barrier height with active catalysts facilitating the proton relay mechanism showing the greatest impact on barrier height. Additional barrier lowering effects occurred when another catalyst was included, whether that was a passive or active catalyst, with the active catalyst having a greater impact. Relatively basic species showed very little reduction in barrier height. Species with higher gas phase acidity, notably H_2S and HCOOH, acting as proton relay facilitators generally showed significant reductions in reaction barrier height, with reductions as large as 37 kcal/mol.

Reaction barrier shape was also examined using IRC calculations. Most passive catalytic mechanisms showed little change in barrier shape, with the exception of the catalyst acting as a hydrogen bond acceptor at the N site of aminomethanol. In these cases, which occurred with CH_3NH_2, H_2CO, NH_3, CH_3OH, and at the carbonyl of HCOOH, significant barrier broadening was observed, which may have protective effects against decomposition of aminomethanol. Additionally, barrier broadening was observed in some cases when the system underwent catalysis via the proton relay

mechanism, with the greatest effects being from H_2S, HCOOH, and when the combined effects of active and passive catalysis were included.

These barrier height and shape effects led to both reaction rate impediment and enhancement. Molecules acting as a hydrogen bond acceptor at the N site significantly reduced reaction rate constants when Eckart tunneling corrections were included. Conversely, catalysts acting as relay facilitator led to reaction rate enhancement and variable reaction barrier broadening. This two fold effect can cause complicated reaction rate behavior, leading to impediment in some temperature regimes and enhancement in others.

From the results presented here, it is clear that while reaction barrier height can be suppressed dramatically, progression of the Strecker synthesis of glycine remains an uphill endeavor. Additional energy in the form of radiation, thermal warming, or excess energy from other chemical processes would be needed to facilitate decomposition into methanimine and water in the ISM. Thus, decomposition of aminomethanol via 1,3-hydrogen transfer and subsequent water loss is unlikely to be a significant source of methanimine in the ISM. While these results do not indicate that the barrier of this reaction can be lowered enough to become significant in the ISM, the general trends of these catalysts are likely applicable to other hydrogen transfer reactions. Moreover, we have shown that other species such as NH_3, CH_3OH, H_2S, and HCOOH are able to act in similar catalytic roles as water and their potential effects on reaction barriers should not be overlooked, especially in water poor regions of the ISM. In contrast to the progression of the Strecker synthesis, the high barrier to decomposition bodes well for laboratory and observational investigation. Coincident species in laboratory experiments are unlikely to facilitate decomposition into methanimine (CH_2NH) and water on timescales that impede detection and characterization. Thus, laboratory characterization of aminomethanol and its observation in the ISM remain viable endeavors.

Chapter 7

Summary and Future Prospects

7.1 Summary

This dissertation presents several laboratory and theoretical efforts to facilitate production and characterization of aminomethanol in laboratory experiments to support radioastronomical searches. The first section of this dissertation has described a variety of efforts to improve the chemistry, sensitivity, and user-friendliness of a rotational spectrometer. N_2O was explored as an alternate chemical source of $O(^1D)$ for use in gas phase synthesis of terrestrially unstable molecules. It was found to be possible though future experiments may fare best if an alternate material, namely fused silica, can be sourced for construction of a photolysis tube. The scanning routine used to collect data on this spectrometer was improved to be more user friendly. Additionally, a multipass optical system was installed, which increased sensitivity of the spectrometer five-fold. Finally, systematic benchmarking was performed on a similar spectrometer with a high voltage discharge source testing a variety of backing pressures and operating voltages to determine the best operating conditions for radical generation.

In the second section of this dissertation, a detailed kinetic analysis of the decomposition of aminomethanol and its protonated analog was conducted. The feasibility of protonation of aminomethanol by a variety of proton carriers in the ISM was shown using density functional theory. The decomposition pathways were then explored using variational transition state theory with multidimensional tunneling corrections and normal mode analysis. From these methods, we have shown that while decomposition of the protonated analog is more energetically accessible,

the protonated system displays reduced tunneling effects compared to the neutral system. Normal mode analysis of these systems shows that heavy atom movement is likely the cause of the reduced tunneling effects. Additionally, highly accurate rotational constants are predicted for N-protonated aminomethanol to aid identification in the lab as well as the ISM.

In the final section, a variety of catalytic microclusters relevant to interstellar and laboratory based synthesis of aminomethanol were investigated. Species were explored as both passive and active catalysts in the decomposition of aminomethanol. In this study, we have shown profound catalytic and protective effects in these microclusters on the aminomethanol molecule. Although none of these orientations lower the reaction barrier to a level that may promote further steps of the Strecker synthesis of glycine in the interstellar medium, the role of abundant and rare ice species in proton transfer reactions remains significant to the field of astrochemistry. This work shows that these more minor species should not be discounted. Moreover, we show that many common species used in the laboratory synthesis of aminomethanol can have protective effects against decomposition and hydrogen tunneling due to barrier widening effects.

7.2 Future Prospects

The work outlined in Section 4.1 demonstrates a potential alternate path for operation of the spectrometer if side reactions need to be quenched. Section 4.2 demonstrates the construction of a more user friendly and sensitive spectrometer setup that can, and has been, used by even the newest members of our lab. Section 4.3 lays the ground work for future synthesis of radical species using a high voltage ring electrode source. A similar investigation of methylamine is currently underway with the intent of extrapolating from analogous species (H_2CO to CH_2NH and $CH_3O^{\cdot}$ to CH_3NH) for generation of novel radicals relevant to Titan's atmosphere.

In Chapters 5 and 6, aminomethanol decomposition pathways were explored to determine whether previous efforts to synthesize this molecule in the gas phase were unsuccessful due to catalysis by precursors or other species present in the synthesis environment. While some catalytic effects were observed, these results indicate that catalysis or even protonation is unlikely to be the cause of the non-detection in previous experiments. It's likely that previous investigations were unsuccessful due to the highly exothermic nature of the synthesis pathways explored in the gas phase or other more favorable reaction pathways. However, this bodes well for laboratory synthesis

of aminomethanol and suggests that proven methods of synthesis such as on ice analogues followed by desorption into the gas phase may be a fruitful direction for characterization with rotational spectroscopy. This synthesis and characterization of aminomethanol appears to be a chemical problem uniquely well-suited to the SubLIME technique[101, 211]. Experiments are currently being planned for synthesis and characterization of aminomethanol using SubLIME.

Appendix A

Appendix

A.1 Appendix for Chapter 4.1

Below are relevant reactions included in the F0AM models used in Chapter 4. Much of the below networks were originally constructed by Hayley Bunn[18]. Additional reactions are known or believed to occur in the experiments models represent but may not have been included due to lack of literature rate constants.

A.1.1 Methanol Networks

Table A.1: Photolysis parameters incorporated for select species at 193 nm to determine photolysis rate constants. Photolysis rate constants were computed using F0AM's "J Bottom Up" procedure.

Reaction	Cross Section	Quantum Yield	Reference
$N_2O \xrightarrow{193nm} O(^1D) + N_2$	8.95E-20	1.00	[87, 91, 212]
$CH_3NH_2 \xrightarrow{193nm} CH_3NH + H$	1.80E-18	0.09	[213]
$CH_3OH \xrightarrow{193nm} CH_3O + H$	3.4611E-19	0.86	[90, 212, 214]

Table A.2: The reaction network used to model . Lines marked in lime (as in line 1) are reactions exclusive to systems with O_3 as a precursor. Lines marked in cyan (as in line 2) are reactions exclusive to systems with N_2O as a precursor. All other reactions are the same in both models.

Reaction	Rate Constant (cm mol^{-1} s^{-1})	Branching Ratio (if applicable)	Reference
$O_3 \xrightarrow{248nm} O(^1D) + O_2$	6.073E-05	0.90	[89]
$N_2O \xrightarrow{193nm} O(^1D) + N_2$	See A.1	0.90	[87, 91]
$O(^1D) + Ar \longrightarrow O(^3P) + Ar$	3.00E-13	-	[84]
$O(^1D) + O_2 \longrightarrow O(^3P) + O_2(^1\Delta)$	3.95E-11	0.80	[84]
$O(^1D) + O_2 \longrightarrow O(^3P) + O_2(^1\Sigma)$	3.95E-11	0.20	[84]
$O(^1D) + O_3 \longrightarrow O_2 + O_2$	2.42E-10	0.50	[84]
$O(^1D) + O_3 \longrightarrow O(^3P) + O(^3P)$	2.42E-10	0.50	[84]
$O(^1D) + N_2O \longrightarrow 2\,NO(X^2\Pi)$	7.20E-11	0.56	[215, 216]
$O(^1D) + N_2O \longrightarrow N_2(X^1\Sigma_g^+) + O_2$	4.40E-11	0.40	[216]
$O(^1D) + N_2O \longrightarrow O(^3P) + N_2O$	4.00E-12	0.04	[216]
$O(^1D) + N_2 \longrightarrow O(^3P) + N_2$	2.6E-11	-	[84]
$N + O_2 \longrightarrow NO + O$	1.50E-11	-	[84]
$N + NO \longrightarrow O + N_2$	2.10E-11	-	[84]
$O(^1D) + CH_4 \longrightarrow CH_3OH^*$	1.75E-10	-	[84]
$CH_3OH^* \longrightarrow CH_3OH$	3.00E-13	-	Estimate based on other relaxation processes in NASA JPL Photochemical Database[84]
$CH_3OH^* \longrightarrow H_2CO + H_2$	1.07E-10	-	[98, 110]
$CH_3OH^* \longrightarrow CH_3O^{\cdot} + H$	8.37E-09	-	[98, 110]
$CH_3OH^* \longrightarrow CH_2OH + H$	5.97E-11	-	[98, 110]
$CH_3OH^* \longrightarrow HCOH + H_2$	6.93E-10	-	[98, 110]
$CH_3OH^* \longrightarrow CH_3 + OH$	1.23E-13	-	[98, 110]
$CH_3OH^* \longrightarrow CH_2 + H_2O$	2.56E-09	-	[98, 110]
$CH_3O^{\cdot} + H \longrightarrow CH_2OH + H$	1.78E-10	-	[98, 110]
$CH_2OH + H \longrightarrow CH_3O^{\cdot} + H$	1.74E-12	-	[98, 110]
$CH_3O^{\cdot} + H \longrightarrow H_2CO + 2\,H$	3.87E-09	-	[98, 110]

$CH_2OH + H \longrightarrow H_2CO + 2\,H$	6.32E-08	-	[98, 110]
$HCOH \longrightarrow H_2CO$	1.39E-10	-	[217]
$H_2CO \longrightarrow HCOH$	1.52E-10	-	[217]
$H_2CO \longrightarrow CO + H_2$	2.05E-10	-	[217]

A.1.2 Aminomethanol Networks

Table A.4: Reaction Network. Lines marked in lime (as in line 1) are reactions exclusive to systems with O_3 as a precursor. Lines marked in cyan (as in line 2) are reactions exclusive to systems with N_2O as a precursor. All other reactions are the same in both models.

Reaction	Rate Constant (cm mol^{-1} s^{-1})	Branching Ratio (if applicable)	Reference
$O_3 \xrightarrow{248nm} O(^1D) + O_2(^1D)$	6.073E-05	0.90	[89]
$N_2O \xrightarrow{193nm} O(^1D) + N_2$	See A.1	0.90	[87, 91]
$O(^1D) + Ar \longrightarrow O(^3P) + Ar$	3.00E-13	-	[84]
$O(^1D) + O_2 \longrightarrow O(^3P) + O_2(^1\Delta)$	3.95E-11	0.80	[84]
$O(^1D) + O_2 \longrightarrow O(^3P) + O_2(^1\Sigma)$	3.95E-11	0.20	[84]
$O(^1D) + O_3 \longrightarrow O_2 + O_2$	2.42E-10	0.50	[84]
$O(^1D) + O_3 \longrightarrow O(^3P) + O(^3P)$	2.42E-10	0.50	[84]
$O_3 + CH_3NH_2 \longrightarrow$ Unknown	7.40E-21	-	[218]
$O_2(^1\Delta) + CH_3NH_2 \longrightarrow H_2CO + NH_2OH$	5.96E-19	0.10	[86]
$O_2(^1\Delta) + CH_3NH_2 \longrightarrow CH_2NH + H_2O_2$	5.96E-19	0.10	[86]
$O_2(^1\Delta) + CH_3NH_2 \longrightarrow CH_2NH + H_2OO$	5.96E-19	0.10	[86]
$O_2(^1\Delta) + CH_3NH_2 \longrightarrow NH_2CHO + H_2O$	5.96E-19	0.175	[86]
$O(^1D) + N_2O \longrightarrow 2\,NO(X^2\Pi)$	7.20E-11	0.56	[215, 216]

$O(^1D) + N_2O \longrightarrow N_2(X^1\Sigma_g^+) + O_2$	4.40E-11	0.40	[216]
$O(^1D) + N_2O \longrightarrow O(^3P) + N_2O$	4.00E-12	0.04	[216]
$O(^1D) + N_2 \longrightarrow O(^3P) + N_2$	2.6E-11	-	[84]
$N + O_2 \longrightarrow NO + O$	1.50E-11	-	[84]
$N + NO \longrightarrow O + N_2$	2.10E-11	-	[84]
$O(^1D) + CH_3NH_2 \longrightarrow NH_2CH_2OH$	1.75E-10	0.50	Estimate based on other $O(^1D)$ insertions in NASA JPL Photochemical Database[84]
$O(^1D) + CH_3NH_2 \longrightarrow CH_3NHOH$	1.75E-10	0.50	Estimate based on other $O(^1D)$ insertions in NASA JPL Photochemical Database[84]
$NH_2CH_2OH \longrightarrow H_2CO + NH_3$	1.6E-16	-	[131]
$NH_2CH_2OH \longrightarrow CH_2NH + H_2O$	2.4E-25	-	[131]
$O(^3P) + CH_3NH_2 \longrightarrow CH_3N + H_2O$	5.65E-13	-	[219]
$NH_2CHO \longrightarrow CO + NH_3$	3.62E-10	-	[220]

Product photolysis for H_2CO and CH_2NH rate constants were also incorporated into these models using the data available in F0AM[88], which is based on the Master Chemical Mechanism[89].

A.2 Appendix for Chapter 4.3

This appendix contains the data processing script used to process the data from Chapter 4.3. The python script is provided as used below.

A.2.1 Gaussian Peak Fitter

```
import glob
import os
import numpy as np
import pandas as pd
import matplotlib.pyplot as plt
import astropy.units as u
from astropy.modeling import models, fitting, custom_model
from astropy.convolution import convolve, Box1DKernel
from numpy import trapz
from pathlib import Path
from scipy import integrate
from scipy.optimize import curve_fit
from scipy.ndimage import uniform_filter1d
from specutils import Spectrum, SpectralRegion
from specutils.analysis import centroid, fwhm
from specutils.fitting import fit_lines, find_lines_threshold, find_lines_derivative,
 ↪  estimate_line_parameters, fit_generic_continuum
from specutils.manipulation import noise_region_uncertainty, extract_region

#%%Settings
smooth_factor = 15
auto_ID= False
center_freq = [150498.334] #center frequency in MHz
guess = []


#%% Define my functions!
def gauss_off(x, v0, a, x0, sigma):
    return  v0 + (a * np.exp(-(x - x0)**2 / (2 * sigma**2))) #Gaussian curve with a vertical
     ↪  offset

def gauss_fwhm(x, v0, a, x0, sigma):
        return 2*(np.sqrt(2*np.log(2))*sigma)

def gauss_amp(x, v0, a, x0, sigma):
        return a

#%% Location information
pathname = Path.cwd()
folder = os.path.basename(pathname)

#%% Make a list of all the .dat files in the folder
file_list = sorted(glob.glob("*.dat"))

#%%make a new file to store the data in
new_file = open("%s_data.csv" %folder, "w")
df=pd.DataFrame(columns=['filename', 'center frequency', 'peak area', 'peak area error','fwhm',
 ↪  'peak amplitude'])

for (h) in file_list:
#reads in data iteratively from the files in the folder and saves to an array for freq and inten
        data = np.genfromtxt(h, delimiter=",", skip_header=1, names=["x", "y"])
        #frequency = 192428.3 #h[-19:-10] uncomment to pull from header
        freq = data['x']
```

```
52          inten = data['y']
53          inten_smooth = uniform_filter1d(inten, smooth_factor) #smooth data so peaks are easier to
            ↪ fit
54
55          #%% Estimate noise in spectrum and find peak centers in spectrum
56          spectrum1=Spectrum(flux=inten_smooth*u.V, spectral_axis=freq*u.MHz) #sets the spectrum as
            ↪ intensity (V) vs frequency (MHz)
57          noise_region = SpectralRegion(freq[1]*u.MHz, freq[100]*u.MHz) #defines a region to gather
            ↪ noise info from (first 100 points)
58          spectrum = noise_region_uncertainty(spectrum1, noise_region) #generates new spectrum with
            ↪ noise uncertainty information
59
60          if auto_ID == True:
61                  lines = find_lines_threshold(spectrum, noise_factor=5) #detects lines that have
                    ↪ an intensity of at least 3x the noise level !! play with this !!
62                  lines2 = lines[lines['line_type'] == 'emission'] #makes a qTable of only emission
                    ↪ type lines (can change if want "absorption")
63                  centers = lines2['line_center'] #pulls only the line centers of emission lines
64                  centers_val = centers.value
65                  print(centers_val)
66                  #print(lines2) #uncomment to see lines fit
67          else:
68                  centers_val=center_freq
69
70          fig, ax = plt.subplots(figsize=(20,10))
71          fig.subplots_adjust(bottom=0.2)
72          fig.set_tight_layout(True)
73          for j in centers_val:
74                  plt.axvline(j, 0, 1,linestyle='--') #plot identified peak centers from auto find
75          plt.plot(freq, inten, color='cornflowerblue', linewidth=4, label='raw data')
76          plt.plot(freq, inten_smooth, color='darkblue', linewidth=4, label='smooth data')
77          plt.xlabel('Frequency (MHz)', fontsize = 22)
78          plt.ylabel('Intensity (V)', fontsize = 22)
79          plt.xticks(fontsize=14)
80          plt.yticks(fontsize=14)
81          plt.ticklabel_format(useOffset=False)
82          plt.legend()
83          plt.savefig("%s_data.png"%h[:-4])
84          plt.close()
85
86          #%% For each line center, cuts a window out of the spectrum and fits the line to a 3
            ↪ component gaussian, returns graph, info
87          for j in centers_val:
88                  lineregion = SpectralRegion((j-1.7)*u.MHz, (j+1.7)*u.MHz) #Create a sub spectrum
                    ↪ centered on the line, with a 3 MHz Window !! play around if needed!!
89                  subspec = extract_region(spectrum, lineregion) #store subspectrum
90
91          #%%Do a quick estimate of line shape to provide a guess for the amplitude, line center,
            ↪ stddev, etc
92                  ricker = models.RickerWavelet1D()
93                  ricker.amplitude.estimator = lambda s: max(s.flux)
94                  ricker.x_0.estimator = lambda *args: centroid(args[0], region=None)
95                  ricker.sigma.estimator = lambda *args: fwhm(args[0])
96                  info = estimate_line_parameters(subspec, ricker)
97                  fwhm_val = fwhm(subspec).value
```

```
                Amp_guess = info.amplitude.value
                x_0_guess = info.x_0.value
                s_guess = info.sigma.value

                guess=[0.0,Amp_guess,j,s_guess] #update the guess with estimate values

                #let program keep going even when error but tell user which fits failed
                try:
                        popt, pcov = curve_fit(gauss_off, subspec.spectral_axis, subspec.flux,
                         ↪  p0=guess,method='dogbox')
                        fit_fwhm = gauss_fwhm(subspec.spectral_axis.value, *popt) #get fwhm from
                         ↪  the fit
                        fit_amp = gauss_amp(subspec.spectral_axis.value, *popt)
                        area = np.trapz(gauss_off(subspec.spectral_axis.value, *popt)) #find area
                         ↪  under curve
                        e_area = np.sqrt(sum(np.diag(pcov)))*area
                        #print("The area is %.2e with an error of %.2e"%(area, e_area))
                        df.loc[len(df)]=[h[:-4],j, area, e_area,fit_fwhm, fit_amp]

                        fig, ax = plt.subplots(figsize=(20,10))
                        fig.subplots_adjust(bottom=0.2)
                        fig.set_tight_layout(True)
                        plt.plot(subspec.spectral_axis, subspec.flux,
                         ↪  color='darkblue',linewidth=4)
                        plt.plot(subspec.spectral_axis.value,
                         ↪  gauss_off(subspec.spectral_axis.value, *popt), 'r-', label='fit')
                        ax = plt.gca()
                        e_area = np.sqrt(sum(np.diag(pcov)))*area

                        ax.get_xaxis().get_major_formatter().set_useOffset(False)
                        plt.xticks(fontsize=14)
                        plt.yticks(fontsize=14)
                        plt.xlabel('Frequency ({})'.format(subspec.spectral_axis.unit), fontsize
                         ↪  = 22)
                        plt.ylabel('Intensity({})'.format(subspec.flux.unit), fontsize = 22)
                        plt.grid(True)
                        plt.savefig("%s_%s_gaussfit.png"%(h[:-4],j))
                        plt.close()
                except RuntimeError:
                        print("Error - curve_fit failed for line center %f in file %s"%(j, h))
                        df.loc[len(df)]=[h[:-4],j, 'error', 'error','error', 'error']



        #plt.show()
df.to_csv("%s_data.csv" %folder, index=False)
```

A.3 Appendix for Chapter 5

The information in this appendix is the supplementary information for work in consideration, "Kinetic Analysis of the Decomposition of Aminomethanol and Its Protonated Analog: A Route

to Strecker Synthesis in the ISM?" by Colton Moore and Susanna Widicus Weaver.

A.3.1 Cartesian Coordinates Used for Polyrate Calculations

Table A.6: Cartesian coordinates of stationary points along the minimum energy pathway used in the Polyrate input files for the aminomethanol water loss decomposition reaction. Geometries were optimized at the M06-2X/aug-cc-PVTZ level of theory using "very tight" convergence criteria. Transition states had only one imaginary frequency and were confirmed using intrinsic reaction coordinate (IRC) calculations.

Species	Atom	X	Y	Z
Reactant	C	0.00000000	0.53665900	0.00000000
	N	1.21458500	-0.21072700	0.00000000
	O	-1.13176300	-0.33340200	0.00000000
	H	1.26514700	-0.80534800	0.81732900
	H	1.26514700	-0.80534800	-0.81732900
	H	-0.02022000	1.17172000	0.88849400
	H	-0.02022000	1.17172000	-0.88849400
	H	-1.93784000	0.18960800	0.00000000
Transition State	C	0.34674300	0.67867300	0.00791800
	N	1.07101400	-0.44409800	-0.15724800
	O	-1.18310600	-0.22436100	0.12858900
	H	1.45935600	-0.74710000	0.72996300
	H	-0.21258200	-0.87713500	-0.18651400
	H	0.35936900	1.25523900	0.92975900
	H	0.11280200	1.25775300	-0.88099100
	H	-1.83165100	-0.05722000	-0.56770000
Product 1	C	0.05628000	0.58161300	0.00000000
	N	0.05628000	-0.67892000	0.00000000
	H	-0.84470400	1.19897900	0.00000000
	H	1.00887600	1.10807900	0.00000000
	H	-0.89581200	-1.04429500	0.00000000
Product 2	O	0.00000000	0.00000000	0.11638400
	H	0.00000000	0.76260600	-0.46553600
	H	0.00000000	-0.76260600	-0.46553600

Table A.7: Cartesian coordinates of stationary points along the minimum energy pathway used in the Polyrate input files for the N-Protonated aminomethanol water loss decomposition reaction. Geometries were optimized at the M06-L/aug-cc-PVTZ level of theory using "very tight" convergence criteria. Transition states had only one imaginary frequency and were confirmed using intrinsic reaction coordinate (IRC) calculations.

Species	Atom	X	Y	Z
Reactant	C	0.00000000	0.60563300	0.00000000
	N	1.03207900	-0.49336500	0.00000000
	O	-1.17892700	-0.09801800	0.00000000
	H	1.98455600	-0.13564700	0.00000000
	H	0.90222800	-1.08493700	0.82054100
	H	0.17763900	1.20764500	0.89541200
	H	0.17763900	1.20764500	-0.89541200
	H	-1.93742800	0.49413100	0.00000000
	H	0.90222800	-1.08493700	-0.82054100
Transition State	C	-0.00273000	0.68566200	-0.00465100
	N	-1.06035800	-0.30742500	0.02211300
	O	1.08769600	-0.32298300	-0.10091000
	H	-1.63867300	-0.34141700	-0.80742700
	H	0.15196000	-1.02674000	0.03140900
	H	0.02642700	1.29919400	-0.89697600
	H	0.08528800	1.26890500	0.90506400
	H	1.75666700	-0.28131100	0.60050500
	H	-1.64435600	-0.29676600	0.84782000
Product 1	C	0.00000000	0.00000000	0.00000000
	N	0.00000000	0.00000000	1.27256400
	H	0.86689700	0.00000000	1.80926700
	H	0.94089000	0.00000000	-0.53591000
	H	-0.94089000	0.00000000	-0.53591000
	H	-0.86689700	0.00000000	1.80926700
Product 2	O	0.00000000	0.00000000	0.11800900
	H	0.00000000	0.75603900	-0.47203500
	H	0.00000000	-0.75603900	-0.47203500

A.3.2 Verification of Structural Consistency Between Methods Used

Table A.8: Absolute energies (Hartrees) and energy differences between key stationary points calculated at the CCSD(T)/aug-cc-pVTZ//M06-2X/aug-cc-pVTZ and CCSD(T)/aug-cc-pVTZ//M06-L/aug-cc-pVTZ level of theory, respectively.

Species	E(Hartree) CCSD(T)// M06-2X	E(Hartree) CCSD(T)// M06-L	Δ E(Hartree)	Δ E(kcal/mol)
Aminomethanol	-170.85	-170.85	0.00	0.02
Aminomethanol TS	-170.75	-170.75	0.00	0.09
Water	-76.34	-76.34	0.00	0.01
Methanimine	-94.48	-94.48	0.00	0.02
N-Protonated Aminomethanol	-171.19	-171.19	0.00	0.09
Protonated Aminomethanol TS	-171.14	-171.14	0.00	0.08
O-Protonated Aminomethanol	-171.19	-171.19	0.00	0.42
Water	-76.34	-76.34	0.00	0.01
Protonated Methanimine	-94.82	-94.82	0.00	0.01

The single point energy of each relevant stationary point was calculated after first optimizing with each of the chosen DFT functionals and an aug-cc-pVTZ basis set. Deviations in the energy calculated at the CCSD(T)/aug-cc-pVTZ level were well within 1.0 kcal/mol. Thus, it was concluded that the structural parameters of the species examined showed little variation between the two methods used for kinetics calculations.

A.3.3 Additional Vibrational Modes

All vibrational modes over the course of the presented reactions are shown in Figure A.1 for neutral aminomethanol and Figure A.2 for N-Protonated aminomethanol. In the neutral system, most vibrational modes were spectator modes. In the protonated system, there were small contributions from a number of normal modes, especially near the saddle point, which is consistent with the coupling constant contributions observed in 5.6. Each system displayed one vibrational mode with a significant change over the course of the reaction. The additional spectator modes shown here

that were not included in the curvature plots in the main text displayed little if any contribution to the reaction path curvature.

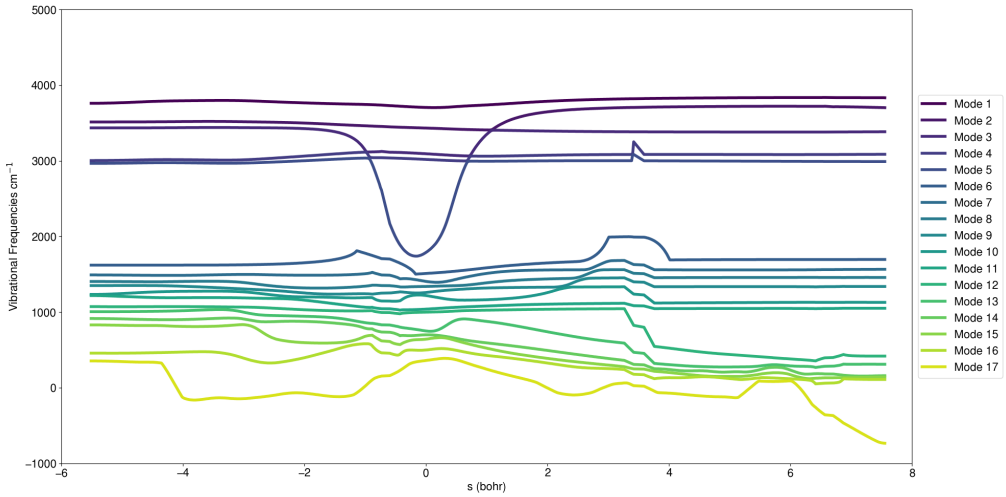

Figure A.1: All normal vibrational modes over the MEP for aminomethanol decomposition via water loss.

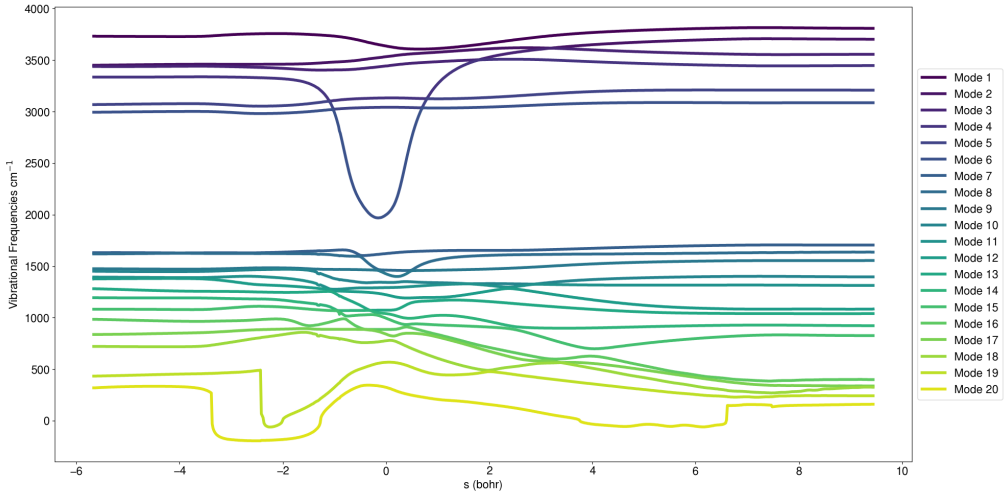

Figure A.2: All normal vibrational modes over the MEP for N-protonated aminomethanol decomposition via water loss.

A.3.4 Additional Files

The .var and .int files used to construct catalog files are included below.

N-Protonated Aminomethanol 30 K .var File

```
N_ProtAM                                  ThuThu NThu Dec 09 10:06:28 2021
  15   72    5    0    0.0000E+000    1.0000E+005    1.0000E+000 1.0000000000
s 1    1     0  ,    ,  , ,    ,    ,   ,     ,    ,,,,
        10000  3.435179974120910E+004 1.00000000E-037 /A_gs
        20000  9.878819000654900E+003 1.00000000E-037 /B_gs
        30000  8.440470208206800E+003 1.00000000E-037 /C_gs
          200 -8.802290000000000E-003 1.00000000E-037 /-DJ_gs
         1100  2.194410000000000E-002 1.00000000E-037 /-DJK_gs
         2000 -1.969740000000000E-001 1.00000000E-037 /-DK_gs
        40100 -1.838440000000000E-003 1.00000000E-037 /d1_gs
        41000  1.216870000000000E-005 1.00000000E-037 /d2_gs

```

N-Protonated Aminomethanol 30 K .int File

```
N_ProtAM
   1      00005   519.9997   0 250     -9.   -9.     1000.0   30.
 001  -3.61020131  /mu_a
 002  0.93793197  /mu_b
 003  0.0000000  /mu_c
```

N-Protonated Aminomethanol 300 K .var File

```
N_ProtAM                                ThuThu NThu Dec 09 10:06:28 2021
  15   72    5    0    0.0000E+000    1.0000E+005    1.0000E+000 1.0000000000
s 1    1     0  ,    ,  , ,    ,    ,   ,     ,    ,,,,
        10000  3.435179974120910E+004 1.00000000E-037 /A_gs
        20000  9.878819000654900E+003 1.00000000E-037 /B_gs
        30000  8.440470208206800E+003 1.00000000E-037 /C_gs
          200 -8.802290000000000E-003 1.00000000E-037 /-DJ_gs
         1100  2.194410000000000E-002 1.00000000E-037 /-DJK_gs
         2000 -1.969740000000000E-001 1.00000000E-037 /-DK_gs
        40100 -1.838440000000000E-003 1.00000000E-037 /d1_gs
        41000  1.216870000000000E-005 1.00000000E-037 /d2_gs

```

N-Protonated Aminomethanol 300 K .int File

```
N_ProtAM
   1      00005   16406.9882   0 250     -9.   -9.     1000.0   300.
 001  -3.61020131  /mu_a
 002  0.93793197  /mu_b
 003  0.0000000  /mu_c
```

A.4 Appendix for Chapter 6

The information in this appendix is the supplemental information for the work to be submitted: "Catalytic Effects of Astrochemically Relevant Species on the Decomposition of Aminomethanol" by Colton Moore, Ruby Neisser, and Susanna Widicus Weaver.

A.4.1 Reaction Energies for Complexes

Table A.9. Zero point corrected energies for stationary points along the reaction path for optimized clusters

Catalyst	**Mechanism**	**Reactants (EE+ZPVE) (Hartrees)**	**TS (EE+ZPVE) (Hartrees)**	**Products (EE+ZPVE) (Hartrees)**
Uncatalyzed	-	-171.011757	-170.923729	-170.998971
CH3NH2	O-H—Cat	-266.805150	-266.720921	-266.792294
CH3NH2	Dual H Bond	-266.805209	-266.719703	-266.792293
CH3NH2	N-H—Cat	-266.801800	-266.717458	-266.791625
CH3OH	2Relay	-402.368664	-402.327756	-402.359477
CH3OH	Cluster	-402.370146	-402.318992	-402.355885
CH3OH	O-H—Cat	-286.687512	-286.602489	-286.672019
CH3OH	Dual H Bond	-286.691523	-286.605713	-286.679449
CH3OH	N-H—Cat	-286.689002	-286.614060	-286.678619
CH3OH	Relay	-286.688813	-286.635840	-286.679449
Dimer	Dimer 2 M1	-342.032562	-341.948592	-342.020433
Dimer	Dimer 2 M2	-342.032519	-341.945857	-342.024386
Dimer	Dimer 1 M1	-342.030227	-341.942256	-342.013019
Dimer	Dimer 1 M2	-342.031063	-341.946672	-342.024481
H2CO	O-H—Cat	-285.491267	-285.407161	-285.475870
H2CO	N-H—Cat	-285.490305	-285.406486	-285.479513
H2O	2Relay	-323.849911	-323.807011	-323.839147
H2O	Cluster	-323.851082	-323.799722	-323.837988
H2O	Dual H Bond	-247.431960	-247.346241	-247.419267
H2O	Relay	-247.429706	-247.374674	-247.419267
H2S	Dual H Bond	-570.388242	-570.302854	-570.373883
H2S	Relay	-570.387947	-570.342153	-570.374360
HCOOH	Weird	-360.765956	-360.721666	-360.770532
HCOOH	Relay	-360.764696	-360.735815	-360.754863
HCOOH	N-H—Cat	-360.748979	-360.669748	-360.739676
NH3	Cluster	-284.061851	-284.004160	-284.054782
NH3	Dual H Bond	-227.540013	-227.454359	-227.527066
NH3	N-H—Cat	-227.537182	-227.452598	-227.526661
NH3	Relay	-227.537181	-227.475590	-227.527035

Table A.10. Zero point corrected barrier heights and reaction energies for optimized clusters

Catalyst	**Mechanism**	$\mathbf{E}_{Barrier,F}$ **(kcal/mol)**	$\mathbf{E}_{rxn,F}$ **(kcal/mol)**	$\mathbf{E}_{Barrier,R}$ **(kcal/mol)**	$\mathbf{E}_{rxn,R}$ **(kcal/mol)**
Uncatalyzed	-	55.237570	8.023215	47.214355	-8.023215
CH3NH2	O-H—Cat	52.853698	8.067140	44.786558	-8.067140
CH3NH2	Dual H Bond	53.655015	8.104790	45.550225	-8.104790
CH3NH2	N-H—Cat	52.924605	6.384813	46.539792	-6.384813
CH3OH	2Relay	25.669770	5.764842	19.904928	-5.764842
CH3OH	Cluster	32.099135	8.948777	23.150358	-8.948777
CH3OH	O-H—Cat	53.351933	9.721858	43.630075	-9.721858
CH3OH	Dual H Bond	53.845775	7.576435	46.269340	-7.576435
CH3OH	N-H—Cat	47.026105	6.515332	40.510773	-6.515332
CH3OH	Relay	33.240558	5.875910	27.364648	-5.875910
Dimer	Dimer 2 M1	52.691175	7.610947	45.080228	-7.610947
Dimer	Dimer 2 M2	54.380405	5.103457	49.276948	-5.103457
Dimer	Dimer 1 M1	55.201803	10.798020	44.403782	-10.798020
Dimer	Dimer 1 M2	52.955353	4.130205	48.825148	-4.130205
H2CO	O-H—Cat	52.776515	9.661618	43.114898	-9.661618
H2CO	N-H—Cat	52.596423	6.771980	45.824443	-6.771980
H2O	2Relay	26.919750	6.754410	20.165340	-6.754410
H2O	Cluster	32.228400	8.216485	24.011915	-8.216485
H2O	Dual H Bond	53.788673	7.964858	45.823815	-7.964858
H2O	Relay	34.532580	6.550473	27.982107	-6.550473
H2S	Dual H Bond	53.580970	9.010273	44.570697	-9.010273
H2S	Relay	28.735735	8.525843	20.209892	-8.525843
HCOOH	Relay	18.122828	6.170208	11.952620	-6.170208
HCOOH	N-H—Cat	49.717452	5.837633	43.879820	-5.837633
NH3	Cluster	36.201102	4.435798	31.765305	-4.435798
NH3	Dual H Bond	53.747885	8.124242	45.623642	-8.124242
NH3	N-H—Cat	53.076460	6.601928	46.474532	-6.601928
NH3	Relay	38.648352	6.366615	32.281738	-6.366615

A.4.2 Uncatalyzed Reaction

Table A.9: Cartesian coordinates for the uncatalyzed aminomethanol decomposition.

Species	Atom	X	Y	Z
Reactant Complex	C	0.000000	0.536659	0.000000
	N	1.214585	-0.210727	0.000000
	O	-1.131763	-0.333402	0.000000
	H	1.265147	-0.805348	0.817329
	H	1.265147	-0.805348	-0.817329
	H	-0.020220	1.171720	0.888494
	H	-0.020220	1.171720	-0.888494
	H	-1.937840	0.189608	0.000000
Transition State	C	0.346743	0.678673	0.007918
	N	1.071014	-0.444098	-0.157248
	O	-1.183106	-0.224361	0.128589
	H	1.459356	-0.747100	0.729963
	H	-0.212582	-0.877135	-0.186514
	H	0.359369	1.255239	0.929759
	H	0.112802	1.257753	-0.880991
	H	-1.831651	-0.057220	-0.567700
Product Complex	C	1.256152	-0.560066	0.019613
	N	0.901758	0.650937	0.002179
	O	-1.844905	-0.127670	-0.069527
	H	1.697725	1.283720	-0.050949
	H	-1.054567	0.433945	-0.031873
	H	2.295135	-0.890263	-0.016729
	H	0.483722	-1.324589	0.072403
	H	-2.511998	0.322383	0.450435

Table A.10: Computed rate constants for the uncatalyzed aminomethanol decomposition from 60 K to 1,000 K.

Temperature (K)	kTST (s-1)	kTST/W (s-1)	kTST/Eck (s-1)
60	2.69e-189	2.34e-187	5.89e-107
70	1.47e-160	9.47e-159	2.90e-92
80	5.36e-139	2.65e-137	3.18e-81
90	3.19e-122	1.25e-120	1.24e-72
100	8.42e-109	2.69e-107	8.48e-66
110	8.12e-98	2.16e-96	4.48e-60
120	1.16e-88	2.62e-87	2.07e-55
130	6.50e-81	1.26e-79	2.00e-51
140	2.85e-74	4.80e-73	5.85e-48
150	1.63e-68	2.41e-67	4.88e-45
160	1.79e-63	2.34e-62	2.03e-42
170	4.99e-59	5.86e-58	4.42e-40
180	4.48e-55	4.74e-54	4.57e-38
190	1.55e-51	1.48e-50	3.26e-36
200	2.36e-48	2.07e-47	1.64e-34
210	1.80e-45	1.44e-44	5.24e-33
220	7.51e-43	5.56e-42	1.31e-31
230	1.85e-40	1.27e-39	2.47e-30
240	2.90e-38	1.85e-37	3.65e-29
250	3.03e-36	1.80e-35	4.47e-28
260	2.21e-34	1.24e-33	4.73e-27
270	1.18e-32	6.18e-32	4.39e-26
280	4.73e-31	2.34e-30	3.48e-25
290	1.47e-29	6.89e-29	2.48e-24
300	3.64e-28	1.62e-27	1.63e-23
310	7.35e-27	3.10e-26	9.95e-23
320	1.23e-25	4.95e-25	5.64e-22

Continued on next page

Table A.10: Computed rate constants for the uncatalyzed aminomethanol decomposition from 60 K to 1,000 K.

Temperature (K)	kTST (s-1)	kTST/W (s-1)	kTST/Eck (s-1)
330	1.73e-24	6.66e-24	3.10e-21
340	2.09e-23	7.71e-23	1.59e-20
350	2.20e-22	7.75e-22	7.94e-20
360	2.02e-21	6.86e-21	3.83e-19
370	1.65e-20	5.39e-20	1.79e-18
380	1.21e-19	3.81e-19	8.14e-18
390	8.00e-19	2.43e-18	3.57e-17
400	4.82e-18	1.42e-17	1.51e-16
410	2.66e-17	7.56e-17	6.16e-16
420	1.35e-16	3.73e-16	2.41e-15
430	6.40e-16	1.71e-15	9.09e-15
440	2.82e-15	7.32e-15	3.29e-14
450	1.16e-14	2.94e-14	1.14e-13
460	4.50e-14	1.11e-13	3.79e-13
470	1.65e-13	3.97e-13	1.21e-12
480	5.73e-13	1.34e-12	3.73e-12
490	1.89e-12	4.33e-12	1.10e-11
500	5.96e-12	1.33e-11	3.15e-11
510	1.79e-11	3.93e-11	8.68e-11
520	5.18e-11	1.11e-10	2.31e-10
530	1.44e-10	3.02e-10	5.95e-10
540	3.84e-10	7.92e-10	1.48e-09
550	9.90e-10	2.00e-09	3.60e-09
560	2.47e-09	4.91e-09	8.46e-09
570	5.97e-09	1.17e-08	1.94e-08
580	1.40e-08	2.69e-08	4.32e-08
590	3.19e-08	6.03e-08	9.40e-08

Continued on next page

Table A.10: Computed rate constants for the uncatalyzed aminomethanol decomposition from 60 K to 1,000 K.

Temperature (K)	kTST (s-1)	kTST/W (s-1)	kTST/Eck (s-1)
600	7.07e-08	1.32e-07	2.00e-07
610	1.53e-07	2.80e-07	4.14e-07
620	3.22e-07	5.82e-07	8.40e-07
630	6.64e-07	1.18e-06	1.67e-06
640	1.34e-06	2.35e-06	3.25e-06
650	2.63e-06	4.57e-06	6.21e-06
660	5.09e-06	8.71e-06	1.16e-05
670	9.64e-06	1.63e-05	2.14e-05
680	1.79e-05	2.99e-05	3.88e-05
690	3.28e-05	5.41e-05	6.92e-05
700	5.88e-05	9.60e-05	1.21e-04
710	1.04e-04	1.68e-04	2.09e-04
720	1.81e-04	2.89e-04	3.57e-04
730	3.10e-04	4.90e-04	5.99e-04
740	5.23e-04	8.19e-04	9.91e-04
750	8.72e-04	1.35e-03	1.62e-03
760	1.43e-03	2.20e-03	2.62e-03
770	2.33e-03	3.54e-03	4.18e-03
780	3.73e-03	5.63e-03	6.59e-03
790	5.91e-03	8.84e-03	1.03e-02
800	9.26e-03	1.37e-02	1.59e-02
810	1.43e-02	2.11e-02	2.42e-02
820	2.20e-02	3.21e-02	3.66e-02
830	3.34e-02	4.84e-02	5.49e-02
840	5.02e-02	7.22e-02	8.15e-02
850	7.47e-02	1.07e-01	1.20e-01
860	1.10e-01	1.56e-01	1.75e-01

Continued on next page

Table A.10: Computed rate constants for the uncatalyzed aminomethanol decomposition from 60 K to 1,000 K.

Temperature (K)	kTST (s-1)	kTST/W (s-1)	kTST/Eck (s-1)
870	1.61e-01	2.27e-01	2.53e-01
880	2.34e-01	3.27e-01	3.62e-01
890	3.36e-01	4.67e-01	5.16e-01
900	4.79e-01	6.62e-01	7.28e-01
910	6.78e-01	9.32e-01	1.02e+00
920	9.53e-01	1.30e+00	1.42e+00
930	1.33e+00	1.81e+00	1.96e+00
940	1.84e+00	2.49e+00	2.70e+00
950	2.53e+00	3.40e+00	3.68e+00
960	3.46e+00	4.63e+00	4.99e+00
970	4.70e+00	6.25e+00	6.73e+00
980	6.35e+00	8.40e+00	9.01e+00
990	8.52e+00	1.12e+01	1.20e+01
1000	1.14e+01	1.49e+01	1.59e+01

A.4.3 Dimer Catalyzed Reactions

Cartesian Coordinates

Table A.11: Cartesian coordinates for the dimer 1 mechanism 1 catalyzed aminomethanol decomposition.

Species	Atom	X	Y	Z
Reactant Complex	C	1.906056	0.125263	-0.463503
	N	1.957074	-1.027177	0.401061
	O	1.336559	1.286690	0.107015
	H	1.013715	-1.319366	0.625138
	H	2.427729	-0.790067	1.265565
	H	2.922039	0.398395	-0.744284

Continued on next page

Table A.11: Cartesian coordinates for the dimer 1 mechanism 1 catalyzed aminomethanol decomposition.

Species	Atom	X	Y	Z
Reactant Complex	H	1.358121	-0.162952	-1.363488
	H	0.379103	1.153695	0.179197
	C	-2.133699	-0.289684	0.171960
	N	-1.654640	1.064284	0.072213
	O	-1.102862	-1.127294	-0.319018
	H	-1.791344	1.453711	-0.850944
	H	-2.080725	1.673585	0.755142
	H	-3.049446	-0.470748	-0.401289
	H	-2.332555	-0.501722	1.224839
	H	-1.467396	-1.982922	-0.557518
Transition State	C	1.859276	-0.191855	-0.541407
	N	1.874546	-0.826723	0.672984
	O	1.240220	1.258872	0.007439
	H	1.050298	-1.416937	0.740811
	H	1.428916	0.524142	0.883965
	H	2.815200	0.170056	-0.908916
	H	1.178083	-0.506353	-1.331450
	H	0.268283	1.260936	-0.161901
	C	-1.748205	-0.274611	0.450530
	N	-1.593028	1.069004	-0.071145
	O	-1.235001	-1.127325	-0.547168
	H	-2.155217	1.185731	-0.906200
	H	-1.891811	1.756215	0.610082
	H	-2.790219	-0.536724	0.666511
	H	-1.162539	-0.346031	1.372468
	H	-1.419804	-2.040574	-0.315148
Product Complex	C	-3.051846	-0.539047	0.312970

Continued on next page

Table A.11: Cartesian coordinates for the dimer 1 mechanism 1 catalyzed aminomethanol decomposition.

Species	Atom	X	Y	Z
Product Complex	N	-2.036895	0.069775	-0.117028
	O	0.067311	2.107959	-0.358074
	H	-1.187335	-0.494995	-0.038894
	H	-0.826889	1.766735	-0.486820
	H	-4.022311	-0.046216	0.287061
	H	-3.026194	-1.552033	0.721379
	H	0.424177	1.543433	0.339464
	C	1.883987	-0.527084	-0.371672
	N	1.907892	0.170844	0.889903
	O	0.745434	-1.375008	-0.337363
	H	2.162474	-0.447554	1.649236
	H	2.566265	0.938726	0.862231
	H	2.774914	-1.140420	-0.552684
	H	1.785713	0.220304	-1.160912
	H	0.757402	-1.939125	-1.114479

Table A.12: Cartesian coordinates for the dimer 1 mechanism 2 catalyzed aminomethanol decomposition.

Species	Atom	X	Y	Z
Reactant Complex	C	2.024098	0.049213	0.316880
	N	1.412270	1.340701	0.136520
	O	1.637895	-0.963157	-0.593467
	H	1.554513	1.678081	-0.806779
	H	0.416863	1.347152	0.322772
	H	3.098696	0.165425	0.190441
	H	1.837794	-0.274040	1.345133
	H	0.803799	-1.348737	-0.293887

Continued on next page

Table A.12: Cartesian coordinates for the dimer 1 mechanism 2 catalyzed aminomethanol decomposition.

Species	Atom	X	Y	Z
Reactant Complex	C	-1.607634	-0.260667	-0.490548
	N	-1.068658	-1.084280	0.568868
	O	-2.156351	0.969419	-0.057564
	H	-1.787074	-1.605187	1.054152
	H	-0.588683	-0.508722	1.252904
	H	-2.339708	-0.852583	-1.042107
	H	-0.802008	0.016243	-1.167911
	H	-2.950609	0.806045	0.457818
Transition State	C	-2.037421	-0.000655	-0.337390
	N	-1.560176	1.290408	0.100624
	O	-1.492596	-1.116739	0.330612
	H	-1.681831	1.392179	1.100357
	H	-0.579808	1.425154	-0.112445
	H	-3.112179	-0.037903	-0.166917
	H	-1.855300	-0.073716	-1.412446
	H	-0.617005	-1.302277	-0.052660
	C	1.644823	-0.395125	0.631661
	N	1.227362	-1.053958	-0.484236
	O	1.850115	1.117750	-0.173106
	H	1.970343	-1.619304	-0.880312
	H	1.450498	0.266973	-0.886830
	H	2.606207	-0.602558	1.098078
	H	0.869241	-0.073303	1.320533
	H	2.774955	1.336199	-0.347748
Product Complex	C	-1.963822	-0.640813	-0.144618
	N	-1.432307	-0.646957	1.190236
	O	-1.041174	-0.297625	-1.172713

Continued on next page

Table A.12: Cartesian coordinates for the dimer 1 mechanism 2 catalyzed aminomethanol decomposition.

Species	Atom	X	Y	Z
Product Complex	H	-0.664578	-1.300529	1.275529
	H	-1.091642	0.273572	1.442021
	H	-2.320551	-1.638848	-0.390404
	H	-2.809642	0.048422	-0.168550
	H	-0.819459	0.636017	-1.048310
	C	2.839105	-0.762259	0.062311
	N	1.779782	-0.098617	-0.091193
	O	-0.044632	2.031874	0.144555
	H	1.059786	-0.600842	-0.617496
	H	0.769347	1.494102	0.191625
	H	2.981712	-1.770688	-0.329110
	H	3.670020	-0.324798	0.611999
	H	0.227432	2.947057	0.058500

Table A.13: Cartesian coordinates for the dimer 2 mechanism 1 catalyzed aminomethanol decomposition.

Species	Atom	X	Y	Z
Reactant Complex	C	-1.994841	-0.094391	0.545985
	N	-1.858299	-1.306421	-0.229134
	O	-1.896754	1.105443	-0.185637
	H	-2.566317	-1.330877	-0.953221
	H	-0.960253	-1.323113	-0.697706
	H	-2.978277	-0.096390	1.012103
	H	-1.240550	-0.117211	1.338670
	H	-0.955267	1.236877	-0.374435
	C	1.562367	-0.332392	-0.121477
	N	1.066742	1.013676	-0.152926

Continued on next page

Table A.13: Cartesian coordinates for the dimer 2 mechanism 1 catalyzed aminomethanol decomposition.

Species	Atom	X	Y	Z
Reactant Complex	O	2.944424	-0.336500	0.200247
	H	1.578103	1.554005	-0.841195
	H	1.218229	1.456544	0.746567
	H	1.401754	-0.783367	-1.104558
	H	0.995855	-0.896216	0.624670
	H	3.261103	-1.241884	0.259595
Transition State	C	-1.968278	-0.138188	0.639052
	N	-1.805059	-1.227343	-0.185823
	O	-1.578854	1.010586	-0.453906
	H	-2.709946	-1.570300	-0.489371
	H	-1.518940	-0.006985	-0.956347
	H	-2.955791	0.157538	0.989088
	H	-1.204016	0.019783	1.403639
	H	-0.637034	1.266642	-0.258863
	C	1.394514	-0.279863	-0.198490
	N	1.125552	1.098282	0.143600
	O	2.747178	-0.579768	0.099055
	H	1.743141	1.707228	-0.382034
	H	1.332941	1.248907	1.125070
	H	1.191786	-0.413063	-1.263733
	H	0.710510	-0.925252	0.355262
	H	2.899889	-1.519307	-0.031713
Product Complex	C	-2.212645	1.025533	0.000005
	N	-2.402724	-0.223848	0.000013
	O	1.383507	2.155237	-0.000012
	H	-3.397533	-0.445081	-0.000050
	H	2.017784	2.873496	0.000031

Continued on next page

Table A.13: Cartesian coordinates for the dimer 2 mechanism 1 catalyzed aminomethanol decomposition.

Species	Atom	X	Y	Z
Product Complex	H	-3.023449	1.755970	-0.000059
	H	-1.196301	1.417669	0.000067
	H	1.903036	1.332834	-0.000009
	C	0.596417	-0.659910	0.000006
	N	2.037841	-0.670394	0.000009
	O	0.061431	-1.964235	-0.000014
	H	2.378356	-1.166685	-0.815020
	H	2.378350	-1.166749	0.815000
	H	0.264752	-0.111300	-0.885155
	H	0.264750	-0.111330	0.885183
	H	-0.897705	-1.840874	-0.000002

Table A.14: Cartesian coordinates for the dimer 2 mechanism 2 catalyzed aminomethanol decomposition.

Species	Atom	X	Y	Z
Reactant Complex	C	1.958946	-0.145489	-0.611129
	N	2.321714	-1.025072	0.474569
	O	1.602826	1.166668	-0.237414
	H	3.076883	-0.616997	1.012158
	H	1.539192	-1.150354	1.105252
	H	2.812836	-0.050516	-1.278988
	H	1.144292	-0.621637	-1.165307
	H	0.758776	1.111624	0.237186
	C	-1.604116	-0.221930	-0.283574
	N	-1.119135	0.616863	0.789498
	O	-3.008667	-0.347218	-0.360190
	H	-1.300045	0.206387	1.697387

Continued on next page

Table A.14: Cartesian coordinates for the dimer 2 mechanism 2 catalyzed aminomethanol decomposition.

Species	Atom	X	Y	Z
Reactant Complex	H	-1.581427	1.518663	0.762201
	H	-1.129505	-1.201540	-0.190869
	H	-1.299188	0.222950	-1.228709
	H	-3.322115	-0.912195	0.350274
Transition State	C	1.930581	-0.401365	0.475033
	N	2.687451	0.738993	0.018012
	O	1.161451	-1.051168	-0.510557
	H	3.280188	0.468572	-0.757558
	H	2.056399	1.455281	-0.321414
	H	2.620607	-1.146880	0.866521
	H	1.292017	-0.058339	1.296581
	H	0.476838	-0.416396	-0.787829
	C	-1.541421	0.229691	0.660743
	N	-1.001628	0.784780	-0.465937
	O	-2.881069	-0.450754	-0.121124
	H	-1.217297	1.774260	-0.524171
	H	-2.165584	0.081653	-0.878047
	H	-1.954925	0.843337	1.459618
	H	-1.085824	-0.695359	1.002214
	H	-3.681202	0.072881	0.018347
Product Complex	C	1.455513	0.426407	-0.375099
	N	2.490046	-0.566846	-0.314526
	O	0.654296	0.534713	0.796874
	H	3.083058	-0.415265	0.491566
	H	2.094072	-1.495316	-0.240810
	H	1.908052	1.405778	-0.516583
	H	0.820894	0.208011	-1.237112

Continued on next page

Table A.14: Cartesian coordinates for the dimer 2 mechanism 2 catalyzed aminomethanol decomposition.

Species	Atom	X	Y	Z
Product Complex	H	0.144217	-0.294808	0.863693
	C	-2.016703	-1.172025	-0.323580
	N	-1.048966	-1.685077	0.308437
	O	-1.460097	2.058747	-0.154258
	H	-1.151348	-2.692413	0.416077
	H	-0.692971	1.686949	0.316526
	H	-2.855704	-1.755303	-0.705602
	H	-2.028872	-0.096691	-0.494215
	H	-1.595408	2.938549	0.200225

Rate Constants

Table A.15: Computed rate constants for the Dimer 1 Mechanism 1 catalyzed aminomethanol decomposition from 60 K to 1,000 K.

Temperature (K)	kTST (s-1)	kTST/W (s-1)	kTST/Eck (s-1)
60	9.97e-190	6.33e-188	1.88e-120
70	4.71e-161	2.21e-159	6.19e-104
80	1.51e-139	5.47e-138	1.72e-91
90	8.12e-123	2.34e-121	7.66e-82
100	1.97e-109	4.63e-108	4.29e-74
110	1.76e-98	3.46e-97	9.18e-68
120	2.37e-89	3.94e-88	1.70e-62
130	1.26e-81	1.80e-80	5.07e-58
140	5.26e-75	6.56e-74	3.27e-54
150	2.88e-69	3.17e-68	7.13e-51
160	3.04e-64	2.97e-63	7.13e-48
170	8.21e-60	7.22e-59	2.47e-45

Continued on next page

Table A.15: Computed rate constants for the Dimer 1 Mechanism 1 catalyzed aminomethanol decomposition from 60 K to 1,000 K.

Temperature (K)	kTST (s-1)	kTST/W (s-1)	kTST/Eck (s-1)
180	7.15e-56	5.68e-55	5.47e-43
190	2.40e-52	1.74e-51	5.87e-41
200	3.58e-49	2.37e-48	4.52e-39
210	2.66e-46	1.62e-45	2.44e-37
220	1.09e-43	6.13e-43	8.41e-36
230	2.63e-41	1.38e-40	2.45e-34
240	4.03e-39	1.98e-38	5.02e-33
250	4.13e-37	1.90e-36	9.26e-32
260	2.97e-35	1.29e-34	1.37e-30
270	1.56e-33	6.36e-33	1.77e-29
280	6.15e-32	2.38e-31	2.02e-28
290	1.88e-30	6.93e-30	2.14e-27
300	4.60e-29	1.61e-28	2.05e-26
310	9.15e-28	3.06e-27	1.82e-25
320	1.51e-26	4.83e-26	1.55e-24
330	2.10e-25	6.44e-25	1.23e-23
340	2.51e-24	7.39e-24	9.23e-23
350	2.60e-23	7.37e-23	6.50e-22
360	2.36e-22	6.47e-22	4.29e-21
370	1.91e-21	5.05e-21	2.65e-20
380	1.38e-20	3.54e-20	1.52e-19
390	9.05e-20	2.24e-19	8.19e-19
400	5.39e-19	1.30e-18	4.12e-18
410	2.94e-18	6.89e-18	1.94e-17
420	1.48e-17	3.38e-17	8.59e-17
430	6.94e-17	1.54e-16	3.58e-16
440	3.03e-16	6.54e-16	1.41e-15

Continued on next page

Table A.15: Computed rate constants for the Dimer 1 Mechanism 1 catalyzed aminomethanol decomposition from 60 K to 1,000 K.

Temperature (K)	kTST (s-1)	kTST/W (s-1)	kTST/Eck (s-1)
450	1.24e-15	2.61e-15	5.25e-15
460	4.75e-15	9.81e-15	1.86e-14
470	1.73e-14	3.48e-14	6.26e-14
480	5.94e-14	1.17e-13	2.01e-13
490	1.94e-13	3.77e-13	6.19e-13
500	6.07e-13	1.15e-12	1.83e-12
510	1.81e-12	3.38e-12	5.17e-12
520	5.19e-12	9.51e-12	1.41e-11
530	1.43e-11	2.57e-11	3.71e-11
540	3.79e-11	6.72e-11	9.45e-11
550	9.70e-11	1.69e-10	2.33e-10
560	2.40e-10	4.13e-10	5.56e-10
570	5.77e-10	9.76e-10	1.29e-09
580	1.34e-09	2.24e-09	2.91e-09
590	3.04e-09	5.00e-09	6.39e-09
600	6.69e-09	1.09e-08	1.37e-08
610	1.44e-08	2.30e-08	2.86e-08
620	3.01e-08	4.77e-08	5.85e-08
630	6.16e-08	9.65e-08	1.17e-07
640	1.23e-07	1.91e-07	2.29e-07
650	2.41e-07	3.70e-07	4.39e-07
660	4.64e-07	7.03e-07	8.26e-07
670	8.73e-07	1.31e-06	1.53e-06
680	1.61e-06	2.40e-06	2.77e-06
690	2.93e-06	4.32e-06	4.96e-06
700	5.24e-06	7.64e-06	8.71e-06
710	9.20e-06	1.33e-05	1.51e-05

Continued on next page

Table A.15: Computed rate constants for the Dimer 1 Mechanism 1 catalyzed aminomethanol decomposition from 60 K to 1,000 K.

Temperature (K)	kTST (s-1)	kTST/W (s-1)	kTST/Eck (s-1)
720	1.59e-05	2.28e-05	2.57e-05
730	2.71e-05	3.86e-05	4.32e-05
740	4.56e-05	6.44e-05	7.16e-05
750	7.56e-05	1.06e-04	1.17e-04
760	1.24e-04	1.72e-04	1.89e-04
770	2.00e-04	2.76e-04	3.02e-04
780	3.19e-04	4.37e-04	4.77e-04
790	5.03e-04	6.84e-04	7.45e-04
800	7.84e-04	1.06e-03	1.15e-03
810	1.21e-03	1.62e-03	1.76e-03
820	1.85e-03	2.46e-03	2.65e-03
830	2.79e-03	3.70e-03	3.98e-03
840	4.18e-03	5.51e-03	5.90e-03
850	6.19e-03	8.12e-03	8.67e-03
860	9.09e-03	1.19e-02	1.26e-02
870	1.32e-02	1.72e-02	1.83e-02
880	1.91e-02	2.47e-02	2.62e-02
890	2.74e-02	3.52e-02	3.72e-02
900	3.89e-02	4.97e-02	5.25e-02
910	5.49e-02	6.98e-02	7.36e-02
920	7.69e-02	9.73e-02	1.02e-01
930	1.07e-01	1.35e-01	1.41e-01
940	1.47e-01	1.85e-01	1.94e-01
950	2.02e-01	2.53e-01	2.64e-01
960	2.75e-01	3.43e-01	3.58e-01
970	3.73e-01	4.62e-01	4.82e-01
980	5.02e-01	6.19e-01	6.45e-01

Continued on next page

Table A.15: Computed rate constants for the Dimer 1 Mechanism 1 catalyzed aminomethanol decomposition from 60 K to 1,000 K.

Temperature (K)	kTST (s-1)	kTST/W (s-1)	kTST/Eck (s-1)
990	6.71e-01	8.25e-01	8.58e-01
1000	8.92e-01	1.09e+00	1.14e+00

Table A.16: Computed rate constants for the Dimer 1 Mechanism 2 catalyzed aminomethanol decomposition from 60 K to 1,000 K.

Temperature (K)	kTST (s-1)	kTST/W (s-1)	kTST/Eck (s-1)
60	4.01e-181	3.02e-179	2.52e-104
70	1.46e-153	8.12e-152	5.68e-90
80	6.99e-133	2.99e-131	3.16e-79
90	8.62e-117	2.94e-115	6.16e-71
100	6.51e-104	1.81e-102	3.56e-64
110	2.26e-93	5.23e-92	1.09e-58
120	1.38e-84	2.71e-83	4.31e-54
130	3.77e-77	6.35e-76	3.01e-50
140	8.95e-71	1.31e-69	7.85e-47
150	3.01e-65	3.89e-64	5.76e-44
160	2.07e-60	2.37e-59	1.89e-41
170	3.84e-56	3.94e-55	3.87e-39
180	2.40e-52	2.22e-51	3.65e-37
190	5.97e-49	5.02e-48	2.24e-35
200	6.81e-46	5.24e-45	9.48e-34
210	3.98e-43	2.81e-42	3.15e-32
220	1.30e-40	8.51e-40	6.83e-31
230	2.58e-38	1.57e-37	1.26e-29
240	3.30e-36	1.86e-35	1.90e-28
250	2.86e-34	1.51e-33	2.15e-27
260	1.76e-32	8.73e-32	2.27e-26

Continued on next page

Table A.16: Computed rate constants for the Dimer 1 Mechanism 2 catalyzed aminomethanol decomposition from 60 K to 1,000 K.

Temperature (K)	kTST (s-1)	kTST/W (s-1)	kTST/Eck (s-1)
270	7.99e-31	3.73e-30	2.04e-25
280	2.76e-29	1.22e-28	1.64e-24
290	7.49e-28	3.14e-27	1.20e-23
300	1.63e-26	6.49e-26	8.00e-23
310	2.91e-25	1.10e-24	5.05e-22
320	4.35e-24	1.57e-23	3.04e-21
330	5.51e-23	1.91e-22	1.74e-20
340	6.02e-22	2.00e-21	9.62e-20
350	5.74e-21	1.83e-20	5.14e-19
360	4.83e-20	1.48e-19	2.65e-18
370	3.63e-19	1.07e-18	1.32e-17
380	2.45e-18	6.99e-18	6.26e-17
390	1.50e-17	4.14e-17	2.85e-16
400	8.40e-17	2.25e-16	1.24e-15
410	4.32e-16	1.12e-15	5.11e-15
420	2.06e-15	5.19e-15	2.02e-14
430	9.13e-15	2.24e-14	7.58e-14
440	3.78e-14	9.02e-14	2.72e-13
450	1.47e-13	3.42e-13	9.30e-13
460	5.40e-13	1.22e-12	3.04e-12
470	1.88e-12	4.15e-12	9.54e-12
480	6.19e-12	1.34e-11	2.87e-11
490	1.95e-11	4.11e-11	8.29e-11
500	5.84e-11	1.21e-10	2.31e-10
510	1.68e-10	3.41e-10	6.19e-10
520	4.64e-10	9.24e-10	1.61e-09
530	1.24e-09	2.41e-09	4.03e-09

Continued on next page

Table A.16: Computed rate constants for the Dimer 1 Mechanism 2 catalyzed aminomethanol decomposition from 60 K to 1,000 K.

Temperature (K)	kTST (s-1)	kTST/W (s-1)	kTST/Eck (s-1)
540	3.17e-09	6.08e-09	9.79e-09
550	7.86e-09	1.48e-08	2.31e-08
560	1.89e-08	3.50e-08	5.29e-08
570	4.40e-08	8.03e-08	1.18e-07
580	9.96e-08	1.79e-07	2.57e-07
590	2.19e-07	3.88e-07	5.44e-07
600	4.70e-07	8.20e-07	1.13e-06
610	9.84e-07	1.69e-06	2.28e-06
620	2.01e-06	3.41e-06	4.52e-06
630	4.02e-06	6.73e-06	8.77e-06
640	7.86e-06	1.30e-05	1.67e-05
650	1.51e-05	2.46e-05	3.12e-05
660	2.83e-05	4.57e-05	5.71e-05
670	5.22e-05	8.34e-05	1.03e-04
680	9.47e-05	1.50e-04	1.83e-04
690	1.69e-04	2.64e-04	3.18e-04
700	2.96e-04	4.57e-04	5.47e-04
710	5.10e-04	7.81e-04	9.26e-04
720	8.67e-04	1.31e-03	1.55e-03
730	1.45e-03	2.18e-03	2.54e-03
740	2.40e-03	3.57e-03	4.14e-03
750	3.91e-03	5.77e-03	6.64e-03
760	6.30e-03	9.22e-03	1.05e-02
770	1.00e-02	1.45e-02	1.65e-02
780	1.57e-02	2.27e-02	2.56e-02
790	2.45e-02	3.50e-02	3.93e-02
800	3.76e-02	5.34e-02	5.96e-02

Continued on next page

Table A.16: Computed rate constants for the Dimer 1 Mechanism 2 catalyzed aminomethanol decomposition from 60 K to 1,000 K.

Temperature (K)	kTST (s-1)	kTST/W (s-1)	kTST/Eck (s-1)
810	5.72e-02	8.06e-02	8.96e-02
820	8.62e-02	1.20e-01	1.33e-01
830	1.29e-01	1.78e-01	1.97e-01
840	1.90e-01	2.62e-01	2.88e-01
850	2.78e-01	3.81e-01	4.17e-01
860	4.03e-01	5.49e-01	5.99e-01
870	5.80e-01	7.86e-01	8.53e-01
880	8.28e-01	1.12e+00	1.21e+00
890	1.17e+00	1.57e+00	1.69e+00
900	1.65e+00	2.19e+00	2.36e+00
910	2.30e+00	3.04e+00	3.27e+00
920	3.19e+00	4.19e+00	4.49e+00
930	4.38e+00	5.74e+00	6.13e+00
940	5.99e+00	7.80e+00	8.31e+00
950	8.13e+00	1.05e+01	1.12e+01
960	1.10e+01	1.41e+01	1.50e+01
970	1.47e+01	1.89e+01	2.00e+01
980	1.96e+01	2.51e+01	2.65e+01
990	2.60e+01	3.31e+01	3.49e+01
1000	3.42e+01	4.34e+01	4.57e+01

Table A.17: Computed rate constants for the Dimer 2 Mechanism 1 catalyzed aminomethanol decomposition from 60 K to 1,000 K.

Temperature (K)	kTST (s-1)	kTST/W (s-1)	kTST/Eck (s-1)
60	2.21e-180	1.14e-178	2.94e-118
70	5.40e-153	2.06e-151	4.62e-102
80	1.89e-132	5.55e-131	8.09e-90

Continued on next page

Table A.17: Computed rate constants for the Dimer 2 Mechanism 1 catalyzed aminomethanol decomposition from 60 K to 1,000 K.

Temperature (K)	kTST (s-1)	kTST/W (s-1)	kTST/Eck (s-1)
90	1.80e-116	4.23e-115	2.43e-80
100	1.10e-103	2.11e-102	8.98e-73
110	3.19e-93	5.12e-92	1.48e-66
120	1.67e-84	2.28e-83	2.71e-61
130	4.01e-77	4.71e-76	6.81e-57
140	8.48e-71	8.71e-70	4.06e-53
150	2.58e-65	2.34e-64	8.44e-50
160	1.62e-60	1.31e-59	6.43e-47
170	2.77e-56	2.02e-55	2.15e-44
180	1.61e-52	1.06e-51	4.45e-42
190	3.75e-49	2.26e-48	5.02e-40
200	4.03e-46	2.23e-45	3.81e-38
210	2.23e-43	1.14e-42	1.83e-36
220	6.94e-41	3.30e-40	6.90e-35
230	1.31e-38	5.83e-38	1.97e-33
240	1.61e-36	6.68e-36	4.39e-32
250	1.34e-34	5.23e-34	8.15e-31
260	7.94e-33	2.93e-32	1.36e-29
270	3.48e-31	1.22e-30	1.96e-28
280	1.17e-29	3.87e-29	2.60e-27
290	3.07e-28	9.69e-28	3.17e-26
300	6.48e-27	1.96e-26	3.59e-25
310	1.13e-25	3.26e-25	3.75e-24
320	1.64e-24	4.55e-24	3.61e-23
330	2.03e-23	5.41e-23	3.19e-22
340	2.16e-22	5.57e-22	2.58e-21
350	2.02e-21	5.01e-21	1.91e-20

Continued on next page

Table A.17: Computed rate constants for the Dimer 2 Mechanism 1 catalyzed aminomethanol decomposition from 60 K to 1,000 K.

Temperature (K)	kTST (s-1)	kTST/W (s-1)	kTST/Eck (s-1)
360	1.66e-20	3.99e-20	1.29e-19
370	1.22e-19	2.85e-19	8.04e-19
380	8.09e-19	1.83e-18	4.61e-18
390	4.87e-18	1.07e-17	2.44e-17
400	2.67e-17	5.72e-17	1.20e-16
410	1.35e-16	2.82e-16	5.51e-16
420	6.34e-16	1.29e-15	2.37e-15
430	2.77e-15	5.49e-15	9.54e-15
440	1.13e-14	2.19e-14	3.63e-14
450	4.33e-14	8.21e-14	1.30e-13
460	1.57e-13	2.91e-13	4.45e-13
470	5.36e-13	9.78e-13	1.44e-12
480	1.74e-12	3.12e-12	4.47e-12
490	5.41e-12	9.51e-12	1.33e-11
500	1.61e-11	2.77e-11	3.77e-11
510	4.56e-11	7.75e-11	1.03e-10
520	1.25e-10	2.08e-10	2.72e-10
530	3.28e-10	5.40e-10	6.91e-10
540	8.31e-10	1.35e-09	1.70e-09
550	2.04e-09	3.27e-09	4.05e-09
560	4.85e-09	7.66e-09	9.36e-09
570	1.12e-08	1.74e-08	2.10e-08
580	2.50e-08	3.86e-08	4.60e-08
590	5.46e-08	8.31e-08	9.81e-08
600	1.16e-07	1.75e-07	2.04e-07
610	2.41e-07	3.58e-07	4.15e-07
620	4.87e-07	7.18e-07	8.24e-07

Continued on next page

Table A.17: Computed rate constants for the Dimer 2 Mechanism 1 catalyzed aminomethanol decomposition from 60 K to 1,000 K.

Temperature (K)	kTST (s-1)	kTST/W (s-1)	kTST/Eck (s-1)
630	9.65e-07	1.41e-06	1.60e-06
640	1.87e-06	2.70e-06	3.06e-06
650	3.56e-06	5.09e-06	5.72e-06
660	6.63e-06	9.40e-06	1.05e-05
670	1.21e-05	1.71e-05	1.89e-05
680	2.18e-05	3.04e-05	3.36e-05
690	3.86e-05	5.33e-05	5.86e-05
700	6.71e-05	9.20e-05	1.01e-04
710	1.15e-04	1.56e-04	1.70e-04
720	1.94e-04	2.62e-04	2.84e-04
730	3.23e-04	4.33e-04	4.67e-04
740	5.30e-04	7.05e-04	7.59e-04
750	8.58e-04	1.14e-03	1.22e-03
760	1.37e-03	1.80e-03	1.93e-03
770	2.17e-03	2.83e-03	3.02e-03
780	3.39e-03	4.40e-03	4.68e-03
790	5.23e-03	6.76e-03	7.16e-03
800	7.99e-03	1.03e-02	1.09e-02
810	1.21e-02	1.54e-02	1.63e-02
820	1.81e-02	2.30e-02	2.42e-02
830	2.68e-02	3.39e-02	3.56e-02
840	3.94e-02	4.96e-02	5.20e-02
850	5.74e-02	7.19e-02	7.52e-02
860	8.29e-02	1.03e-01	1.08e-01
870	1.19e-01	1.47e-01	1.54e-01
880	1.69e-01	2.08e-01	2.17e-01
890	2.37e-01	2.92e-01	3.04e-01

Continued on next page

Table A.17: Computed rate constants for the Dimer 2 Mechanism 1 catalyzed aminomethanol decomposition from 60 K to 1,000 K.

Temperature (K)	kTST (s-1)	kTST/W (s-1)	kTST/Eck (s-1)
900	3.32e-01	4.07e-01	4.22e-01
910	4.61e-01	5.62e-01	5.83e-01
920	6.36e-01	7.72e-01	8.00e-01
930	8.70e-01	1.05e+00	1.09e+00
940	1.18e+00	1.43e+00	1.47e+00
950	1.60e+00	1.92e+00	1.98e+00
960	2.15e+00	2.57e+00	2.65e+00
970	2.87e+00	3.42e+00	3.52e+00
980	3.81e+00	4.53e+00	4.66e+00
990	5.02e+00	5.96e+00	6.12e+00
1000	6.59e+00	7.79e+00	8.00e+00

Table A.18: Computed rate constants for the Dimer 2 Mechanism 1 catalyzed aminomethanol decomposition from 60 K to 1,000 K.

Temperature (K)	kTST (s-1)	kTST/W (s-1)	kTST/Eck (s-1)
60	1.06e-186	7.29e-185	7.85e-113
70	2.00e-158	1.02e-156	2.03e-97
80	3.27e-137	1.28e-135	8.51e-86
90	1.04e-120	3.23e-119	8.93e-77
100	1.66e-107	4.21e-106	1.45e-69
110	1.06e-96	2.23e-95	1.13e-63
120	1.07e-87	1.92e-86	1.05e-58
130	4.46e-80	6.88e-79	1.70e-54
140	1.52e-73	2.04e-72	6.44e-51
150	6.97e-68	8.25e-67	7.51e-48
160	6.28e-63	6.61e-62	4.30e-45
170	1.48e-58	1.40e-57	1.20e-42

Continued on next page

Table A.18: Computed rate constants for the Dimer 2 Mechanism 1 catalyzed aminomethanol decomposition from 60 K to 1,000 K.

Temperature (K)	kTST (s-1)	kTST/W (s-1)	kTST/Eck (s-1)
180	1.14e-54	9.72e-54	1.71e-40
190	3.42e-51	2.66e-50	1.43e-38
200	4.62e-48	3.28e-47	8.05e-37
210	3.14e-45	2.05e-44	3.32e-35
220	1.18e-42	7.14e-42	9.62e-34
230	2.65e-40	1.49e-39	2.20e-32
240	3.80e-38	1.99e-37	3.71e-31
250	3.66e-36	1.80e-35	5.51e-30
260	2.48e-34	1.14e-33	6.64e-29
270	1.23e-32	5.36e-32	6.98e-28
280	4.64e-31	1.91e-30	6.87e-27
290	1.36e-29	5.30e-29	5.78e-26
300	3.18e-28	1.18e-27	4.65e-25
310	6.07e-27	2.15e-26	3.48e-24
320	9.64e-26	3.26e-25	2.46e-23
330	1.30e-24	4.20e-24	1.66e-22
340	1.50e-23	4.66e-23	1.08e-21
350	1.50e-22	4.50e-22	6.69e-21
360	1.33e-21	3.83e-21	3.95e-20
370	1.05e-20	2.91e-20	2.22e-19
380	7.38e-20	1.99e-19	1.18e-18
390	4.71e-19	1.23e-18	5.90e-18
400	2.75e-18	6.93e-18	2.79e-17
410	1.47e-17	3.60e-17	1.25e-16
420	7.25e-17	1.73e-16	5.28e-16
430	3.32e-16	7.71e-16	2.11e-15
440	1.42e-15	3.22e-15	8.01e-15

Continued on next page

Table A.18: Computed rate constants for the Dimer 2 Mechanism 1 catalyzed aminomethanol decomposition from 60 K to 1,000 K.

Temperature (K)	kTST (s-1)	kTST/W (s-1)	kTST/Eck (s-1)
450	5.71e-15	1.26e-14	2.89e-14
460	2.16e-14	4.65e-14	9.91e-14
470	7.72e-14	1.62e-13	3.25e-13
480	2.62e-13	5.39e-13	1.02e-12
490	8.44e-13	1.70e-12	3.05e-12
500	2.60e-12	5.14e-12	8.81e-12
510	7.66e-12	1.48e-11	2.45e-11
520	2.17e-11	4.12e-11	6.54e-11
530	5.89e-11	1.10e-10	1.69e-10
540	1.54e-10	2.84e-10	4.23e-10
550	3.91e-10	7.07e-10	1.03e-09
560	9.58e-10	1.70e-09	2.41e-09
570	2.28e-09	3.98e-09	5.51e-09
580	5.25e-09	9.05e-09	1.23e-08
590	1.18e-08	2.00e-08	2.66e-08
600	2.57e-08	4.31e-08	5.63e-08
610	5.46e-08	9.04e-08	1.16e-07
620	1.13e-07	1.85e-07	2.35e-07
630	2.30e-07	3.72e-07	4.65e-07
640	4.57e-07	7.30e-07	9.01e-07
650	8.89e-07	1.40e-06	1.71e-06
660	1.70e-06	2.64e-06	3.19e-06
670	3.17e-06	4.89e-06	5.85e-06
680	5.82e-06	8.89e-06	1.05e-05
690	1.05e-05	1.59e-05	1.86e-05
700	1.86e-05	2.79e-05	3.25e-05
710	3.26e-05	4.83e-05	5.58e-05

Continued on next page

Table A.18: Computed rate constants for the Dimer 2 Mechanism 1 catalyzed aminomethanol decomposition from 60 K to 1,000 K.

Temperature (K)	kTST (s-1)	kTST/W (s-1)	kTST/Eck (s-1)
720	5.60e-05	8.24e-05	9.45e-05
730	9.49e-05	1.38e-04	1.58e-04
740	1.59e-04	2.29e-04	2.60e-04
750	2.62e-04	3.75e-04	4.22e-04
760	4.26e-04	6.05e-04	6.77e-04
770	6.84e-04	9.65e-04	1.07e-03
780	1.09e-03	1.52e-03	1.69e-03
790	1.70e-03	2.37e-03	2.61e-03
800	2.64e-03	3.65e-03	4.01e-03
810	4.06e-03	5.57e-03	6.09e-03
820	6.17e-03	8.41e-03	9.17e-03
830	9.29e-03	1.26e-02	1.37e-02
840	1.38e-02	1.86e-02	2.02e-02
850	2.04e-02	2.73e-02	2.95e-02
860	2.99e-02	3.98e-02	4.28e-02
870	4.34e-02	5.74e-02	6.15e-02
880	6.24e-02	8.21e-02	8.78e-02
890	8.90e-02	1.16e-01	1.24e-01
900	1.26e-01	1.64e-01	1.75e-01
910	1.77e-01	2.29e-01	2.44e-01
920	2.47e-01	3.18e-01	3.37e-01
930	3.42e-01	4.39e-01	4.64e-01
940	4.71e-01	6.01e-01	6.34e-01
950	6.44e-01	8.18e-01	8.61e-01
960	8.74e-01	1.11e+00	1.16e+00
970	1.18e+00	1.49e+00	1.56e+00
980	1.58e+00	1.98e+00	2.08e+00

Continued on next page

Table A.18: Computed rate constants for the Dimer 2 Mechanism 1 catalyzed aminomethanol decomposition from 60 K to 1,000 K.

Temperature (K)	kTST (s-1)	kTST/W (s-1)	kTST/Eck (s-1)
990	2.11e+00	2.64e+00	2.76e+00
1000	2.80e+00	3.48e+00	3.64e+00

A.4.4 CH_3NH_2 Catalyzed Reactions

Cartesian Coordinates

Table A.19: Cartesian coordinates for the CH_3NH_2 NH—Cat catalyzed aminomethanol decomposition.

Species	Atom	X	Y	Z
Reactant Complex	C	-1.575977	-0.170454	0.454636
	N	-1.344476	1.196534	0.147179
	O	-1.029708	-1.034500	-0.557842
	H	-0.349920	1.372527	0.032990
	H	-1.813991	1.457997	-0.709839
	H	-1.106053	-0.401784	1.413604
	H	-2.650294	-0.347772	0.536306
	H	-1.262694	-1.945225	-0.358030
	N	1.638154	0.474558	-0.575406
	H	2.404145	0.735368	-1.181684
	H	0.990148	-0.090103	-1.112652
	C	2.120358	-0.289731	0.571622
	H	2.672873	-1.198706	0.313919
	H	2.764547	0.338662	1.185088
	H	1.266876	-0.581496	1.183084
Transition State	C	-1.549474	-0.853303	-0.585987
	N	-1.268604	-0.785813	0.656055
	O	-1.026604	1.447940	-0.164326

Continued on next page

Table A.19: Cartesian coordinates for the CH_3NH_2 NH—Cat catalyzed aminomethanol decomposition.

Species	Atom	X	Y	Z
Transition State	H	-0.343640	-1.099380	0.965976
	H	-1.579555	0.113323	1.061160
	H	-0.983983	-1.517782	-1.227734
	H	-2.374137	-0.277329	-0.971263
	H	-1.057838	2.377914	-0.397249
	N	1.375424	0.055400	0.656509
	H	1.943470	0.423921	1.408525
	H	0.666196	0.766101	0.413224
	C	2.206916	-0.209176	-0.515750
	H	2.772318	0.659488	-0.865533
	H	2.911345	-1.015330	-0.310727
	H	1.566269	-0.526687	-1.339294
Product Complex	C	-1.959573	0.549377	-0.250102
	N	-1.994850	-0.611691	0.248875
	O	1.085497	1.951913	-0.068656
	H	-2.922099	-1.026042	0.167167
	H	1.667984	2.536656	0.417679
	H	-2.825029	1.032944	-0.708025
	H	-1.028477	1.114481	-0.230091
	H	1.177723	1.062556	0.341265
	C	1.322235	-1.301549	-0.634504
	N	1.028226	-0.738937	0.685289
	H	0.048015	-0.900998	0.904625
	H	1.585738	-1.188024	1.399713
	H	0.707038	-0.791675	-1.374385
	H	2.364124	-1.112886	-0.888643
	H	1.131400	-2.374882	-0.711575

Table A.20: Cartesian coordinates for the CH_3NH_2 OH—Cat catalyzed aminomethanol decomposition.

Species	Atom	X	Y	Z
Reactant Complex	C	1.508657	-0.155875	0.484979
	N	1.614489	1.138384	-0.150299
	O	1.037807	-1.198269	-0.335460
	H	2.214161	1.070835	-0.963834
	H	0.706445	1.445502	-0.477393
	H	2.500998	-0.446950	0.825487
	H	0.865275	-0.043936	1.363570
	H	0.068096	-1.122156	-0.366438
	C	-1.990533	0.799184	0.037248
	N	-1.796069	-0.651484	-0.011816
	H	-2.035816	-1.073891	0.876322
	H	-2.402271	-1.069908	-0.705922
	H	-1.325097	1.223936	0.788277
	H	-1.719877	1.227019	-0.927162
	H	-3.012057	1.107542	0.272215
Transition State	C	1.502222	-0.185453	0.599778
	N	1.662358	0.996366	-0.088342
	O	0.757886	-1.019504	-0.577972
	H	2.619323	1.078790	-0.414054
	H	0.980269	0.023302	-0.964969
	H	2.360544	-0.802416	0.861444
	H	0.746669	-0.191578	1.389653
	H	-0.217145	-1.045617	-0.341854
	C	-1.789672	0.871832	-0.105545
	N	-1.809019	-0.568810	0.200684
	H	-1.915102	-0.717812	1.196809
	H	-2.597325	-1.021305	-0.244925

Continued on next page

Table A.20: Cartesian coordinates for the CH_3NH_2 OH—Cat catalyzed aminomethanol decomposition.

Species	Atom	X	Y	Z
Transition State	H	-0.881926	1.316130	0.301781
	H	-1.745810	0.998219	-1.185646
	H	-2.661256	1.407156	0.273746
Product Complex	C	-1.959573	0.549377	-0.250102
	N	-1.994850	-0.611691	0.248875
	O	1.085497	1.951913	-0.068656
	H	-2.922099	-1.026042	0.167167
	H	1.667984	2.536656	0.417679
	H	-2.825029	1.032944	-0.708025
	H	-1.028477	1.114481	-0.230091
	H	1.177723	1.062556	0.341265
	C	1.322235	-1.301549	-0.634504
	N	1.028226	-0.738937	0.685289
	H	0.048015	-0.900998	0.904625
	H	1.585738	-1.188024	1.399713
	H	0.707038	-0.791675	-1.374385
	H	2.364124	-1.112886	-0.888643
	H	1.131400	-2.374882	-0.711575

Table A.21: Cartesian coordinates for the CH_3NH_2 dual hydrogen bond catalyzed aminomethanol decomposition.

Species	Atom	X	Y	Z
Reactant Complex	C	1.753625	-0.221891	0.187025
	N	1.276518	1.127436	-0.123242
	O	0.879671	-1.177857	-0.323787
	H	1.870655	1.824015	0.310829
	H	1.316207	1.276460	-1.125150

Continued on next page

Table A.21: Cartesian coordinates for the CH_3NH_2 dual hydrogen bond catalyzed aminomethanol decomposition.

Species	Atom	X	Y	Z
Reactant Complex	H	2.732684	-0.442194	-0.246166
	H	1.838729	-0.287299	1.277631
	H	0.011780	-1.035212	0.103871
	C	-2.254037	0.137909	-0.501681
	H	-1.552249	0.236017	-1.328923
	H	-2.869238	-0.740034	-0.691372
	H	-2.901271	1.018812	-0.492803
	N	-1.490796	-0.057501	0.731433
	H	-0.879466	0.738566	0.882458
	H	-2.102784	-0.151928	1.530522
Transition State	C	1.722554	-0.072795	0.442846
	N	1.396588	1.082943	-0.242960
	O	0.851521	-1.098338	-0.452564
	H	2.196090	1.422704	-0.764572
	H	0.815374	-0.093006	-0.955786
	H	2.733834	-0.473655	0.396998
	H	1.282859	-0.211567	1.432769
	H	-0.032406	-1.065650	0.014473
	C	-2.345834	0.162192	-0.395988
	H	-1.819025	0.320008	-1.336086
	H	-2.950286	-0.737532	-0.494565
	H	-3.010107	1.013148	-0.233382
	N	-1.356276	-0.023858	0.670236
	H	-0.760112	0.801482	0.722054
	H	-1.810892	-0.139200	1.566530
Product Complex	C	-1.959452	0.549577	-0.250150
	N	-1.994940	-0.611422	0.248968

Continued on next page

Table A.21: Cartesian coordinates for the CH_3NH_2 dual hydrogen bond catalyzed aminomethanol decomposition.

Species	Atom	X	Y	Z
Product Complex	O	1.085901	1.951737	-0.068681
	H	-2.922246	-1.025644	0.167256
	H	1.668012	2.536514	0.418063
	H	-2.824804	1.033223	-0.708186
	H	-1.028266	1.114533	-0.230150
	H	1.177917	1.062379	0.341288
	C	1.321917	-1.301646	-0.634559
	H	0.706677	-0.791671	-1.374335
	H	2.363792	-1.113075	-0.888822
	H	1.130960	-2.374956	-0.711666
	N	1.028133	-0.739076	0.685300
	H	0.047931	-0.901034	0.904747
	H	1.585681	-1.188265	1.399633

Rate Constants

Table A.22: Computed rate constants for the CH_3NH_2 NH—Cat catalyzed aminomethanol decomposition from 60 K to 1,000 K.

Temperature (K)	kTST (s-1)	kTST/W (s-1)	kTST/Eck (s-1)
60	2.92e-181	1.49e-180	2.89e-172
70	1.01e-153	4.05e-153	4.42e-148
80	4.57e-133	1.51e-132	9.45e-130
90	5.35e-117	1.51e-116	3.59e-115
100	3.85e-104	9.54e-104	4.95e-103
110	1.28e-93	2.84e-93	7.67e-93
120	7.50e-85	1.52e-84	2.96e-84
130	1.98e-77	3.71e-77	5.96e-77

Continued on next page

Table A.22: Computed rate constants for the CH_3NH_2 NH—Cat catalyzed aminomethanol decomposition from 60 K to 1,000 K.

Temperature (K)	kTST (s-1)	kTST/W (s-1)	kTST/Eck (s-1)
140	4.56e-71	8.01e-71	1.14e-70
150	1.49e-65	2.48e-65	3.23e-65
160	1.00e-60	1.58e-60	1.95e-60
170	1.83e-56	2.76e-56	3.25e-56
180	1.12e-52	1.63e-52	1.86e-52
190	2.75e-49	3.89e-49	4.32e-49
200	3.11e-46	4.26e-46	4.65e-46
210	1.80e-43	2.40e-43	2.58e-43
220	5.85e-41	7.64e-41	8.12e-41
230	1.15e-38	1.47e-38	1.55e-38
240	1.46e-36	1.84e-36	1.92e-36
250	1.26e-34	1.56e-34	1.62e-34
260	7.76e-33	9.47e-33	9.78e-33
270	3.52e-31	4.24e-31	4.36e-31
280	1.22e-29	1.45e-29	1.48e-29
290	3.30e-28	3.88e-28	3.97e-28
300	7.19e-27	8.37e-27	8.53e-27
310	1.28e-25	1.48e-25	1.51e-25
320	1.92e-24	2.20e-24	2.23e-24
330	2.44e-23	2.77e-23	2.81e-23
340	2.67e-22	3.01e-22	3.05e-22
350	2.55e-21	2.86e-21	2.89e-21
360	2.15e-20	2.40e-20	2.42e-20
370	1.62e-19	1.80e-19	1.81e-19
380	1.10e-18	1.21e-18	1.22e-18
390	6.74e-18	7.39e-18	7.45e-18
400	3.78e-17	4.13e-17	4.16e-17

Continued on next page

Table A.22: Computed rate constants for the CH_3NH_2 NH—Cat catalyzed aminomethanol decomposition from 60 K to 1,000 K.

Temperature (K)	kTST (s-1)	kTST/W (s-1)	kTST/Eck (s-1)
410	1.95e-16	2.13e-16	2.14e-16
420	9.33e-16	1.01e-15	1.02e-15
430	4.15e-15	4.48e-15	4.51e-15
440	1.72e-14	1.86e-14	1.87e-14
450	6.73e-14	7.22e-14	7.26e-14
460	2.48e-13	2.65e-13	2.66e-13
470	8.63e-13	9.21e-13	9.25e-13
480	2.85e-12	3.04e-12	3.05e-12
490	9.00e-12	9.55e-12	9.59e-12
500	2.71e-11	2.87e-11	2.88e-11
510	7.81e-11	8.26e-11	8.29e-11
520	2.17e-10	2.28e-10	2.29e-10
530	5.77e-10	6.08e-10	6.10e-10
540	1.49e-09	1.56e-09	1.56e-09
550	3.69e-09	3.87e-09	3.88e-09
560	8.89e-09	9.31e-09	9.33e-09
570	2.07e-08	2.17e-08	2.17e-08
580	4.71e-08	4.91e-08	4.92e-08
590	1.04e-07	1.08e-07	1.08e-07
600	2.23e-07	2.32e-07	2.33e-07
610	4.68e-07	4.86e-07	4.87e-07
620	9.58e-07	9.94e-07	9.97e-07
630	1.92e-06	1.99e-06	1.99e-06
640	3.75e-06	3.89e-06	3.90e-06
650	7.20e-06	7.46e-06	7.47e-06
660	1.36e-05	1.40e-05	1.40e-05
670	2.50e-05	2.59e-05	2.59e-05

Continued on next page

Table A.22: Computed rate constants for the CH_3NH_2 NH—Cat catalyzed aminomethanol decomposition from 60 K to 1,000 K.

Temperature (K)	kTST (s-1)	kTST/W (s-1)	kTST/Eck (s-1)
680	4.54e-05	4.69e-05	4.70e-05
690	8.10e-05	8.35e-05	8.36e-05
700	1.42e-04	1.46e-04	1.47e-04
710	2.45e-04	2.53e-04	2.53e-04
720	4.17e-04	4.29e-04	4.30e-04
730	7.00e-04	7.19e-04	7.21e-04
740	1.16e-03	1.19e-03	1.19e-03
750	1.89e-03	1.94e-03	1.94e-03
760	3.04e-03	3.12e-03	3.12e-03
770	4.84e-03	4.96e-03	4.97e-03
780	7.61e-03	7.80e-03	7.80e-03
790	1.18e-02	1.21e-02	1.21e-02
800	1.82e-02	1.86e-02	1.86e-02
810	2.77e-02	2.83e-02	2.84e-02
820	4.17e-02	4.26e-02	4.27e-02
830	6.22e-02	6.36e-02	6.37e-02
840	9.19e-02	9.39e-02	9.41e-02
850	1.35e-01	1.37e-01	1.38e-01
860	1.95e-01	1.99e-01	2.00e-01
870	2.81e-01	2.87e-01	2.87e-01
880	4.01e-01	4.09e-01	4.10e-01
890	5.68e-01	5.79e-01	5.78e-01
900	7.98e-01	8.13e-01	8.12e-01
910	1.11e+00	1.13e+00	1.14e+00
920	1.54e+00	1.57e+00	1.57e+00
930	2.12e+00	2.16e+00	2.15e+00
940	2.90e+00	2.94e+00	2.95e+00

Continued on next page

Table A.22: Computed rate constants for the CH_3NH_2 NH—Cat catalyzed aminomethanol decomposition from 60 K to 1,000 K.

Temperature (K)	kTST (s-1)	kTST/W (s-1)	kTST/Eck (s-1)
950	3.93e+00	3.99e+00	3.99e+00
960	5.30e+00	5.38e+00	5.38e+00
970	7.10e+00	7.21e+00	7.24e+00
980	9.46e+00	9.61e+00	9.58e+00
990	1.25e+01	1.27e+01	1.28e+01
1000	1.65e+01	1.68e+01	1.68e+01

Table A.23: Computed rate constants for the CH_3NH_2 OH—Cat catalyzed aminomethanol decomposition from 60 K to 1,000 K.

Temperature (K)	kTST (s-1)	kTST/W (s-1)	kTST/Eck (s-1)
60	4.62e-181	2.33e-179	1.50e-119
70	1.33e-153	4.95e-152	3.61e-103
80	5.21e-133	1.50e-131	7.75e-91
90	5.44e-117	1.25e-115	2.81e-81
100	3.55e-104	6.66e-103	1.36e-73
110	1.09e-93	1.70e-92	2.31e-67
120	5.95e-85	7.93e-84	4.11e-62
130	1.48e-77	1.70e-76	1.16e-57
140	3.22e-71	3.24e-70	8.63e-54
150	1.00e-65	8.92e-65	1.72e-50
160	6.43e-61	5.11e-60	1.27e-47
170	1.12e-56	8.02e-56	5.07e-45
180	6.62e-53	4.29e-52	1.01e-42
190	1.57e-49	9.28e-49	1.28e-40
200	1.71e-46	9.28e-46	9.75e-39
210	9.55e-44	4.80e-43	4.94e-37
220	3.01e-41	1.40e-40	1.80e-35

Continued on next page

Table A.23: Computed rate constants for the CH_3NH_2 OH—Cat catalyzed aminomethanol decomposition from 60 K to 1,000 K.

Temperature (K)	kTST (s-1)	kTST/W (s-1)	kTST/Eck (s-1)
230	5.74e-39	2.50e-38	5.44e-34
240	7.09e-37	2.89e-36	1.31e-32
250	5.95e-35	2.29e-34	2.55e-31
260	3.55e-33	1.29e-32	4.35e-30
270	1.57e-31	5.39e-31	6.62e-29
280	5.29e-30	1.73e-29	9.17e-28
290	1.40e-28	4.35e-28	1.16e-26
300	2.97e-27	8.84e-27	1.37e-25
310	5.19e-26	1.48e-25	1.48e-24
320	7.58e-25	2.07e-24	1.46e-23
330	9.42e-24	2.48e-23	1.32e-22
340	1.01e-22	2.56e-22	1.09e-21
350	9.45e-22	2.31e-21	8.21e-21
360	7.81e-21	1.85e-20	5.64e-20
370	5.76e-20	1.32e-19	3.55e-19
380	3.83e-19	8.53e-19	2.05e-18
390	2.31e-18	5.00e-18	1.10e-17
400	1.27e-17	2.68e-17	5.45e-17
410	6.45e-17	1.33e-16	2.52e-16
420	3.03e-16	6.08e-16	1.09e-15
430	1.33e-15	2.60e-15	4.40e-15
440	5.42e-15	1.04e-14	1.68e-14
450	2.08e-14	3.91e-14	6.07e-14
460	7.54e-14	1.39e-13	2.08e-13
470	2.59e-13	4.67e-13	6.78e-13
480	8.44e-13	1.49e-12	2.11e-12
490	2.62e-12	4.56e-12	6.27e-12

Continued on next page

Table A.23: Computed rate constants for the CH_3NH_2 OH—Cat catalyzed aminomethanol decomposition from 60 K to 1,000 K.

Temperature (K)	kTST (s-1)	kTST/W (s-1)	kTST/Eck (s-1)
500	7.79e-12	1.33e-11	1.79e-11
510	2.22e-11	3.73e-11	4.90e-11
520	6.07e-11	1.01e-10	1.30e-10
530	1.60e-10	2.61e-10	3.30e-10
540	4.06e-10	6.53e-10	8.14e-10
550	9.97e-10	1.58e-09	1.94e-09
560	2.37e-09	3.72e-09	4.51e-09
570	5.48e-09	8.47e-09	1.01e-08
580	1.23e-08	1.88e-08	2.22e-08
590	2.68e-08	4.05e-08	4.75e-08
600	5.71e-08	8.52e-08	9.89e-08
610	1.18e-07	1.75e-07	2.01e-07
620	2.40e-07	3.51e-07	4.01e-07
630	4.76e-07	6.89e-07	7.81e-07
640	9.24e-07	1.33e-06	1.49e-06
650	1.76e-06	2.50e-06	2.79e-06
660	3.28e-06	4.62e-06	5.13e-06
670	6.01e-06	8.39e-06	9.27e-06
680	1.08e-05	1.50e-05	1.65e-05
690	1.91e-05	2.63e-05	2.87e-05
700	3.33e-05	4.54e-05	4.94e-05
710	5.71e-05	7.72e-05	8.37e-05
720	9.64e-05	1.29e-04	1.40e-04
730	1.61e-04	2.14e-04	2.30e-04
740	2.64e-04	3.49e-04	3.75e-04
750	4.27e-04	5.62e-04	6.01e-04
760	6.84e-04	8.94e-04	9.53e-04

Continued on next page

Table A.23: Computed rate constants for the CH_3NH_2 OH—Cat catalyzed aminomethanol decomposition from 60 K to 1,000 K.

Temperature (K)	kTST (s-1)	kTST/W (s-1)	kTST/Eck (s-1)
770	1.08e-03	1.41e-03	1.49e-03
780	1.69e-03	2.18e-03	2.32e-03
790	2.61e-03	3.36e-03	3.55e-03
800	3.99e-03	5.10e-03	5.38e-03
810	6.04e-03	7.68e-03	8.09e-03
820	9.06e-03	1.14e-02	1.20e-02
830	1.34e-02	1.69e-02	1.77e-02
840	1.98e-02	2.47e-02	2.59e-02
850	2.88e-02	3.58e-02	3.74e-02
860	4.16e-02	5.15e-02	5.37e-02
870	5.95e-02	7.35e-02	7.65e-02
880	8.46e-02	1.04e-01	1.08e-01
890	1.19e-01	1.46e-01	1.52e-01
900	1.67e-01	2.03e-01	2.11e-01
910	2.32e-01	2.81e-01	2.91e-01
920	3.20e-01	3.87e-01	4.00e-01
930	4.38e-01	5.28e-01	5.45e-01
940	5.96e-01	7.15e-01	7.38e-01
950	8.05e-01	9.64e-01	9.93e-01
960	1.08e+00	1.29e+00	1.33e+00
970	1.44e+00	1.72e+00	1.77e+00
980	1.92e+00	2.27e+00	2.34e+00
990	2.53e+00	2.99e+00	3.07e+00
1000	3.33e+00	3.92e+00	4.02e+00

Table A.24: Computed rate constants for the CH_3NH_2 dual hydrogen bond catalyzed aminomethanol decomposition from 60 K to 1,000 K.

Temperature (K)	kTST (s-1)	kTST/W (s-1)	kTST/Eck (s-1)
60	1.01e-183	4.52e-182	1.55e-126
70	8.24e-156	2.72e-154	5.00e-109
80	7.13e-135	1.82e-133	7.09e-96
90	1.38e-118	2.81e-117	1.20e-85
100	1.49e-105	2.48e-104	1.63e-77
110	6.86e-95	9.58e-94	9.44e-71
120	5.30e-86	6.31e-85	3.88e-65
130	1.76e-78	1.81e-77	2.20e-60
140	4.94e-72	4.45e-71	2.54e-56
150	1.92e-66	1.53e-65	9.03e-53
160	1.49e-61	1.06e-60	1.14e-49
170	3.09e-57	1.99e-56	6.20e-47
180	2.12e-53	1.24e-52	1.76e-44
190	5.76e-50	3.08e-49	3.05e-42
200	7.10e-47	3.50e-46	3.05e-40
210	4.44e-44	2.03e-43	2.14e-38
220	1.55e-41	6.58e-41	1.07e-36
230	3.26e-39	1.29e-38	4.02e-35
240	4.38e-37	1.63e-36	1.25e-33
250	3.99e-35	1.40e-34	3.17e-32
260	2.56e-33	8.52e-33	7.04e-31
270	1.21e-31	3.82e-31	1.40e-29
280	4.36e-30	1.31e-29	2.49e-28
290	1.22e-28	3.51e-28	4.01e-27
300	2.75e-27	7.55e-27	5.79e-26
310	5.07e-26	1.33e-25	7.47e-25
320	7.78e-25	1.97e-24	8.59e-24

Continued on next page

Table A.24: Computed rate constants for the CH_3NH_2 dual hydrogen bond catalyzed aminomethanol decomposition from 60 K to 1,000 K.

Temperature (K)	kTST (s-1)	kTST/W (s-1)	kTST/Eck (s-1)
330	1.01e-23	2.47e-23	8.83e-23
340	1.13e-22	2.67e-22	8.11e-22
350	1.11e-21	2.53e-21	6.69e-21
360	9.52e-21	2.11e-20	4.98e-20
370	7.29e-20	1.57e-19	3.37e-19
380	5.02e-19	1.05e-18	2.08e-18
390	3.13e-18	6.37e-18	1.18e-17
400	1.78e-17	3.53e-17	6.16e-17
410	9.33e-17	1.81e-16	2.99e-16
420	4.52e-16	8.54e-16	1.35e-15
430	2.03e-15	3.76e-15	5.70e-15
440	8.53e-15	1.55e-14	2.26e-14
450	3.36e-14	5.97e-14	8.47e-14
460	1.25e-13	2.18e-13	3.00e-13
470	4.39e-13	7.51e-13	1.01e-12
480	1.47e-12	2.46e-12	3.24e-12
490	4.65e-12	7.70e-12	9.91e-12
500	1.41e-11	2.30e-11	2.91e-11
510	4.10e-11	6.58e-11	8.18e-11
520	1.14e-10	1.81e-10	2.21e-10
530	3.07e-10	4.79e-10	5.78e-10
540	7.95e-10	1.22e-09	1.46e-09
550	1.99e-09	3.02e-09	3.56e-09
560	4.81e-09	7.22e-09	8.42e-09
570	1.13e-08	1.67e-08	1.93e-08
580	2.57e-08	3.77e-08	4.32e-08
590	5.70e-08	8.27e-08	9.39e-08

Continued on next page

Table A.24: Computed rate constants for the CH_3NH_2 dual hydrogen bond catalyzed aminomethanol decomposition from 60 K to 1,000 K.

Temperature (K)	kTST (s-1)	kTST/W (s-1)	kTST/Eck (s-1)
600	1.23e-07	1.77e-07	1.99e-07
610	2.59e-07	3.69e-07	4.12e-07
620	5.33e-07	7.51e-07	8.35e-07
630	1.07e-06	1.49e-06	1.65e-06
640	2.11e-06	2.91e-06	3.20e-06
650	4.06e-06	5.57e-06	6.09e-06
660	7.67e-06	1.04e-05	1.13e-05
670	1.42e-05	1.92e-05	2.08e-05
680	2.59e-05	3.46e-05	3.74e-05
690	4.63e-05	6.15e-05	6.62e-05
700	8.15e-05	1.08e-04	1.15e-04
710	1.41e-04	1.85e-04	1.98e-04
720	2.41e-04	3.14e-04	3.34e-04
730	4.05e-04	5.24e-04	5.56e-04
740	6.72e-04	8.64e-04	9.14e-04
750	1.10e-03	1.41e-03	1.48e-03
760	1.78e-03	2.26e-03	2.38e-03
770	2.83e-03	3.58e-03	3.76e-03
780	4.47e-03	5.62e-03	5.89e-03
790	6.97e-03	8.72e-03	9.12e-03
800	1.07e-02	1.34e-02	1.40e-02
810	1.64e-02	2.03e-02	2.12e-02
820	2.47e-02	3.05e-02	3.18e-02
830	3.70e-02	4.54e-02	4.72e-02
840	5.48e-02	6.70e-02	6.95e-02
850	8.05e-02	9.79e-02	1.01e-01
860	1.17e-01	1.42e-01	1.47e-01

Continued on next page

Table A.24: Computed rate constants for the CH_3NH_2 dual hydrogen bond catalyzed aminomethanol decomposition from 60 K to 1,000 K.

Temperature (K)	kTST (s-1)	kTST/W (s-1)	kTST/Eck (s-1)
870	1.69e-01	2.04e-01	2.11e-01
880	2.42e-01	2.91e-01	3.00e-01
890	3.43e-01	4.11e-01	4.23e-01
900	4.83e-01	5.76e-01	5.93e-01
910	6.75e-01	8.03e-01	8.26e-01
920	9.37e-01	1.11e+00	1.14e+00
930	1.29e+00	1.53e+00	1.57e+00
940	1.77e+00	2.08e+00	2.13e+00
950	2.40e+00	2.82e+00	2.89e+00
960	3.25e+00	3.80e+00	3.89e+00
970	4.36e+00	5.09e+00	5.21e+00
980	5.83e+00	6.78e+00	6.93e+00
990	7.73e+00	8.97e+00	9.17e+00
1000	1.02e+01	1.18e+01	1.21e+01

A.4.5 H_2CO Catalyzed Reactions

Cartesian Coordinates

Table A.25: Cartesian coordinates for the H_2CO NH—Cat catalyzed aminomethanol decomposition.

Species	Atom	X	Y	Z
Reactant Complex	C	1.659970	-0.126575	0.321494
	N	0.965524	-1.202469	-0.289761
	O	1.149288	1.144807	-0.115807
	H	-0.014916	-1.216575	-0.031060
	H	1.046803	-1.172931	-1.296900
	H	1.547518	-0.206728	1.404466

Continued on next page

Table A.25: Cartesian coordinates for the H_2CO NH—Cat catalyzed aminomethanol decomposition.

Species	Atom	X	Y	Z
Reactant Complex	H	2.720077	-0.189476	0.067220
	H	1.689846	1.846979	0.256404
	C	-2.063772	0.539860	-0.184148
	H	-2.992544	1.133623	-0.214297
	H	-1.157558	0.983530	-0.622619
	O	-2.046173	-0.549912	0.320937
Transition State	C	1.328633	-0.896186	0.585382
	N	0.789176	-0.948052	-0.571134
	O	1.253410	1.363343	-0.099436
	H	-0.193099	-1.214940	-0.647242
	H	1.148423	-0.209201	-1.194430
	H	0.818598	-1.350761	1.426620
	H	2.299941	-0.445858	0.692879
	H	1.582765	2.261657	-0.026793
	C	-1.735445	0.646363	0.172482
	H	-2.583096	1.279242	0.485133
	H	-0.725638	1.101254	0.095949
	O	-1.932316	-0.524104	-0.073234
Product Complex	C	-2.353964	-0.932479	-0.006224
	N	-1.269382	-0.292691	0.007653
	O	-0.002640	2.261299	-0.014795
	H	-0.452708	-0.909071	0.016717
	H	-0.617030	1.503859	-0.001679
	H	-2.411760	-2.022195	-0.007668
	H	-3.297279	-0.389709	-0.017810
	H	-0.536367	3.048255	0.101363
	C	2.136197	-0.256901	-0.004620

Continued on next page

Table A.25: Cartesian coordinates for the H_2CO NH—Cat catalyzed aminomethanol decomposition.

Species	Atom	X	Y	Z
Product Complex	H	3.236485	-0.189398	-0.023785
	H	1.572072	0.687455	0.003246
	O	1.589999	-1.329308	0.007434

Table A.26: Cartesian coordinates for the H_2CO OH—Cat catalyzed aminomethanol decomposition.

Species	Atom	X	Y	Z
Reactant Complex	C	1.548530	-0.185410	0.368498
	N	1.190639	1.147904	-0.110784
	O	0.904228	-1.165854	-0.384554
	H	1.562570	1.859819	0.506661
	H	1.594848	1.298514	-1.027997
	H	2.616465	-0.400601	0.283737
	H	1.268880	-0.234915	1.425661
	H	-0.048453	-1.087650	-0.227435
	C	-2.091598	0.567316	-0.080177
	H	-1.291277	1.234131	-0.431044
	H	-3.109314	0.976287	0.023638
	O	-1.862950	-0.580690	0.196096
Transition State	C	-1.326737	-0.058984	0.647362
	N	-1.313560	-1.050750	-0.303559
	O	-0.858361	1.169675	-0.350294
	H	-2.258787	-1.262197	-0.603311
	H	-0.927977	0.195546	-0.948443
	H	-2.262399	0.299345	1.071257
	H	-0.515595	-0.058438	1.376218
	H	0.094747	1.313619	-0.188303

Continued on next page

Table A.26: Cartesian coordinates for the H_2CO OH—Cat catalyzed aminomethanol decomposition.

Species	Atom	X	Y	Z
Transition State	C	1.888805	-0.663584	-0.030544
	H	0.982449	-1.259125	-0.227464
	H	2.852445	-1.188622	0.059876
	O	1.840565	0.536642	0.085816
Product Complex	C	-1.662336	-0.261901	0.428065
	N	-1.574405	-1.301716	-0.282678
	O	-0.224347	2.122023	-0.124552
	H	-2.335633	-1.348609	-0.958676
	H	0.193210	2.962497	-0.319925
	H	-2.442648	0.491924	0.332288
	H	-0.907767	-0.073612	1.189762
	H	0.490232	1.469351	-0.125252
	C	1.686173	-1.140864	0.006515
	H	0.704721	-1.624260	-0.107293
	H	2.576517	-1.784249	0.095456
	O	1.799244	0.057422	0.032665

Rate Constants

Table A.27: Computed rate constants for the H_2CO NH—Cat catalyzed aminomethanol decomposition from 60 K to 1,000 K.

Temperature (K)	kTST (s-1)	kTST/W (s-1)	kTST/Eck (s-1)
60	2.22e-180	1.10e-179	8.34e-172
70	4.72e-153	1.85e-152	8.88e-148
80	1.46e-132	4.71e-132	1.52e-129
90	1.25e-116	3.45e-116	5.59e-115
100	6.92e-104	1.68e-103	7.29e-103

Continued on next page

Table A.27: Computed rate constants for the H_2CO NH—Cat catalyzed aminomethanol decomposition from 60 K to 1,000 K.

Temperature (K)	kTST (s-1)	kTST/W (s-1)	kTST/Eck (s-1)
110	1.83e-93	3.99e-93	9.86e-93
120	8.89e-85	1.77e-84	3.25e-84
130	1.98e-77	3.65e-77	5.64e-77
140	3.93e-71	6.79e-71	9.37e-71
150	1.13e-65	1.84e-65	2.36e-65
160	6.74e-61	1.05e-60	1.27e-60
170	1.10e-56	1.65e-56	1.92e-56
180	6.16e-53	8.87e-53	1.00e-52
190	1.39e-49	1.94e-49	2.14e-49
200	1.45e-46	1.96e-46	2.13e-46
210	7.79e-44	1.03e-43	1.10e-43
220	2.37e-41	3.07e-41	3.25e-41
230	4.40e-39	5.59e-39	5.86e-39
240	5.29e-37	6.60e-37	6.87e-37
250	4.34e-35	5.33e-35	5.52e-35
260	2.54e-33	3.08e-33	3.17e-33
270	1.10e-31	1.32e-31	1.35e-31
280	3.65e-30	4.32e-30	4.42e-30
290	9.53e-29	1.11e-28	1.14e-28
300	2.00e-27	2.32e-27	2.36e-27
310	3.46e-26	3.97e-26	4.04e-26
320	5.01e-25	5.71e-25	5.79e-25
330	6.18e-24	6.98e-24	7.07e-24
340	6.57e-23	7.38e-23	7.47e-23
350	6.12e-22	6.83e-22	6.90e-22
360	5.03e-21	5.59e-21	5.64e-21
370	3.70e-20	4.08e-20	4.12e-20

Continued on next page

Table A.27: Computed rate constants for the H_2CO NH—Cat catalyzed aminomethanol decomposition from 60 K to 1,000 K.

Temperature (K)	kTST (s-1)	kTST/W (s-1)	kTST/Eck (s-1)
380	2.45e-19	2.69e-19	2.71e-19
390	1.47e-18	1.61e-18	1.62e-18
400	8.11e-18	8.83e-18	8.88e-18
410	4.11e-17	4.45e-17	4.48e-17
420	1.93e-16	2.08e-16	2.09e-16
430	8.42e-16	9.07e-16	9.11e-16
440	3.44e-15	3.69e-15	3.71e-15
450	1.32e-14	1.41e-14	1.42e-14
460	4.79e-14	5.11e-14	5.14e-14
470	1.65e-13	1.75e-13	1.76e-13
480	5.37e-13	5.70e-13	5.72e-13
490	1.67e-12	1.77e-12	1.77e-12
500	4.96e-12	5.25e-12	5.27e-12
510	1.42e-11	1.49e-11	1.50e-11
520	3.87e-11	4.08e-11	4.09e-11
530	1.02e-10	1.07e-10	1.08e-10
540	2.60e-10	2.73e-10	2.73e-10
550	6.40e-10	6.70e-10	6.71e-10
560	1.52e-09	1.59e-09	1.60e-09
570	3.53e-09	3.68e-09	3.69e-09
580	7.92e-09	8.26e-09	8.28e-09
590	1.73e-08	1.80e-08	1.81e-08
600	3.69e-08	3.84e-08	3.84e-08
610	7.67e-08	7.97e-08	7.98e-08
620	1.56e-07	1.62e-07	1.62e-07
630	3.10e-07	3.21e-07	3.21e-07
640	6.02e-07	6.23e-07	6.24e-07

Continued on next page

Table A.27: Computed rate constants for the H_2CO NH—Cat catalyzed aminomethanol decomposition from 60 K to 1,000 K.

Temperature (K)	kTST (s-1)	kTST/W (s-1)	kTST/Eck (s-1)
650	1.15e-06	1.19e-06	1.19e-06
660	2.14e-06	2.21e-06	2.22e-06
670	3.93e-06	4.06e-06	4.06e-06
680	7.08e-06	7.30e-06	7.32e-06
690	1.26e-05	1.29e-05	1.29e-05
700	2.19e-05	2.25e-05	2.26e-05
710	3.76e-05	3.86e-05	3.87e-05
720	6.35e-05	6.53e-05	6.54e-05
730	1.06e-04	1.09e-04	1.09e-04
740	1.74e-04	1.79e-04	1.79e-04
750	2.83e-04	2.90e-04	2.90e-04
760	4.53e-04	4.64e-04	4.64e-04
770	7.17e-04	7.35e-04	7.35e-04
780	1.12e-03	1.15e-03	1.15e-03
790	1.74e-03	1.78e-03	1.78e-03
800	2.66e-03	2.72e-03	2.72e-03
810	4.03e-03	4.11e-03	4.12e-03
820	6.04e-03	6.17e-03	6.17e-03
830	8.97e-03	9.16e-03	9.17e-03
840	1.32e-02	1.35e-02	1.35e-02
850	1.92e-02	1.96e-02	1.97e-02
860	2.78e-02	2.84e-02	2.83e-02
870	3.99e-02	4.06e-02	4.07e-02
880	5.67e-02	5.77e-02	5.79e-02
890	8.00e-02	8.14e-02	8.13e-02
900	1.12e-01	1.14e-01	1.14e-01
910	1.56e-01	1.58e-01	1.59e-01

Continued on next page

Table A.27: Computed rate constants for the H_2CO NH—Cat catalyzed aminomethanol decomposition from 60 K to 1,000 K.

Temperature (K)	kTST (s-1)	kTST/W (s-1)	kTST/Eck (s-1)
920	2.15e-01	2.18e-01	2.18e-01
930	2.94e-01	2.99e-01	2.99e-01
940	4.01e-01	4.07e-01	4.09e-01
950	5.42e-01	5.50e-01	5.49e-01
960	7.28e-01	7.40e-01	7.40e-01
970	9.73e-01	9.88e-01	9.91e-01
980	1.29e+00	1.31e+00	1.31e+00
990	1.71e+00	1.73e+00	1.74e+00
1000	2.24e+00	2.27e+00	2.27e+00

Table A.28: Computed rate constants for the H_2CO OH—Cat catalyzed decomposition from 60 K to 1,000 K.

Temperature (K)	kTST (s-1)	kTST/W (s-1)	kTST/Eck (s-1)
60	9.22e-181	5.19e-179	1.49e-115
70	2.42e-153	1.01e-151	9.33e-100
80	8.88e-133	2.85e-131	7.61e-88
90	8.76e-117	2.24e-115	1.35e-78
100	5.47e-104	1.14e-102	3.10e-71
110	1.61e-93	2.81e-92	3.90e-65
120	8.53e-85	1.27e-83	4.69e-60
130	2.06e-77	2.63e-76	7.67e-56
140	4.38e-71	4.89e-70	4.00e-52
150	1.34e-65	1.32e-64	6.47e-49
160	8.41e-61	7.38e-60	4.26e-46
170	1.45e-56	1.14e-55	1.24e-43
180	8.41e-53	6.00e-52	1.90e-41
190	1.96e-49	1.28e-48	2.03e-39

Continued on next page

Table A.28: Computed rate constants for the H_2CO OH—Cat catalyzed decomposition from 60 K to 1,000 K.

Temperature (K)	kTST (s-1)	kTST/W (s-1)	kTST/Eck (s-1)
200	2.12e-46	1.26e-45	1.25e-37
210	1.17e-43	6.47e-43	5.74e-36
220	3.66e-41	1.87e-40	1.88e-34
230	6.95e-39	3.31e-38	4.72e-33
240	8.52e-37	3.79e-36	9.81e-32
250	7.11e-35	2.98e-34	1.64e-30
260	4.23e-33	1.67e-32	2.40e-29
270	1.86e-31	6.93e-31	3.13e-28
280	6.24e-30	2.21e-29	3.68e-27
290	1.65e-28	5.54e-28	3.97e-26
300	3.49e-27	1.12e-26	4.00e-25
310	6.08e-26	1.87e-25	3.77e-24
320	8.87e-25	2.61e-24	3.33e-23
330	1.10e-23	3.11e-23	2.73e-22
340	1.18e-22	3.21e-22	2.08e-21
350	1.10e-21	2.89e-21	1.47e-20
360	9.11e-21	2.31e-20	9.56e-20
370	6.72e-20	1.65e-19	5.77e-19
380	4.46e-19	1.06e-18	3.22e-18
390	2.69e-18	6.21e-18	1.67e-17
400	1.48e-17	3.33e-17	8.10e-17
410	7.53e-17	1.65e-16	3.67e-16
420	3.54e-16	7.54e-16	1.56e-15
430	1.55e-15	3.22e-15	6.21e-15
440	6.34e-15	1.29e-14	2.34e-14
450	2.44e-14	4.84e-14	8.36e-14
460	8.85e-14	1.72e-13	2.84e-13

Continued on next page

Table A.28: Computed rate constants for the H_2CO OH—Cat catalyzed decomposition from 60 K to 1,000 K.

Temperature (K)	kTST (s-1)	kTST/W (s-1)	kTST/Eck (s-1)
470	3.04e-13	5.78e-13	9.17e-13
480	9.92e-13	1.85e-12	2.83e-12
490	3.09e-12	5.65e-12	8.36e-12
500	9.18e-12	1.65e-11	2.37e-11
510	2.62e-11	4.62e-11	6.47e-11
520	7.17e-11	1.24e-10	1.70e-10
530	1.89e-10	3.23e-10	4.32e-10
540	4.81e-10	8.10e-10	1.06e-09
550	1.18e-09	1.96e-09	2.53e-09
560	2.82e-09	4.61e-09	5.85e-09
570	6.52e-09	1.05e-08	1.31e-08
580	1.47e-08	2.33e-08	2.87e-08
590	3.20e-08	5.04e-08	6.12e-08
600	6.83e-08	1.06e-07	1.27e-07
610	1.42e-07	2.18e-07	2.59e-07
620	2.88e-07	4.37e-07	5.15e-07
630	5.72e-07	8.59e-07	1.00e-06
640	1.11e-06	1.65e-06	1.91e-06
650	2.12e-06	3.12e-06	3.58e-06
660	3.96e-06	5.77e-06	6.57e-06
670	7.27e-06	1.05e-05	1.19e-05
680	1.31e-05	1.87e-05	2.10e-05
690	2.32e-05	3.29e-05	3.68e-05
700	4.05e-05	5.69e-05	6.32e-05
710	6.95e-05	9.69e-05	1.07e-04
720	1.17e-04	1.63e-04	1.79e-04
730	1.96e-04	2.69e-04	2.94e-04

Continued on next page

Table A.28: Computed rate constants for the H_2CO OH—Cat catalyzed decomposition from 60 K to 1,000 K.

Temperature (K)	kTST (s-1)	kTST/W (s-1)	kTST/Eck (s-1)
740	3.22e-04	4.39e-04	4.79e-04
750	5.23e-04	7.08e-04	7.69e-04
760	8.38e-04	1.13e-03	1.22e-03
770	1.33e-03	1.77e-03	1.91e-03
780	2.08e-03	2.76e-03	2.96e-03
790	3.22e-03	4.24e-03	4.54e-03
800	4.92e-03	6.45e-03	6.89e-03
810	7.46e-03	9.72e-03	1.04e-02
820	1.12e-02	1.45e-02	1.54e-02
830	1.66e-02	2.14e-02	2.27e-02
840	2.45e-02	3.14e-02	3.32e-02
850	3.57e-02	4.55e-02	4.80e-02
860	5.16e-02	6.55e-02	6.89e-02
870	7.40e-02	9.35e-02	9.82e-02
880	1.05e-01	1.32e-01	1.39e-01
890	1.49e-01	1.86e-01	1.95e-01
900	2.08e-01	2.59e-01	2.71e-01
910	2.89e-01	3.59e-01	3.75e-01
920	4.00e-01	4.94e-01	5.14e-01
930	5.48e-01	6.74e-01	7.01e-01
940	7.46e-01	9.15e-01	9.50e-01
950	1.01e+00	1.23e+00	1.28e+00
960	1.36e+00	1.65e+00	1.71e+00
970	1.82e+00	2.20e+00	2.28e+00
980	2.41e+00	2.92e+00	3.01e+00
990	3.19e+00	3.84e+00	3.96e+00
1000	4.19e+00	5.03e+00	5.19e+00

A.4.6 NH_3 Catalyzed Reactions

Cartesian Coordinates

Table A.29: Cartesian coordinates for the NH_3 NH—Cat catalyzed aminomethanol decomposition.

Species	Atom	X	Y	Z
Reactant Complex	C	1.141512	0.001749	0.429268
	N	0.755574	-1.238815	-0.142040
	O	0.657308	1.113694	-0.348597
	H	-0.255842	-1.321831	-0.150346
	H	1.106308	-1.331253	-1.085927
	H	0.727854	0.063655	1.438140
	H	2.230459	0.057044	0.485294
	H	1.060815	1.924469	-0.027078
	N	-2.178614	-0.062401	0.071987
	H	-2.673028	0.255858	0.895714
	H	-2.853246	-0.103227	-0.681456
	H	-1.489575	0.643749	-0.170803
Transition State	C	1.359191	-0.614047	0.484497
	N	0.728868	-0.804041	-0.608050
	O	0.323905	1.475665	-0.027326
	H	-0.155857	-1.313799	-0.575544
	H	0.723022	0.054136	-1.187416
	H	1.135922	-1.231267	1.346107
	H	2.134726	0.132272	0.520696
	H	0.247486	2.427319	0.065823
	N	-1.938159	-0.350421	0.111898
	H	-2.389498	-0.442276	1.013760
	H	-2.671968	-0.133463	-0.551650
	H	-1.305189	0.467279	0.152916

Continued on next page

Table A.29: Cartesian coordinates for the NH_3 NH—Cat catalyzed aminomethanol decomposition.

Species	Atom	X	Y	Z
Product Complex	C	2.351621	-0.185298	0.001335
	N	1.129551	0.114355	-0.005064
	O	-1.310284	1.560056	0.027301
	H	0.512418	-0.705768	-0.006915
	H	-0.362693	1.336238	0.008630
	H	2.721409	-1.212859	0.004326
Product Complex	H	3.100664	0.604956	0.004375
	H	-1.375708	2.496487	-0.162731
	N	-1.501359	-1.477237	-0.004315
	H	-1.904003	-1.893244	0.825979
	H	-1.912511	-1.948038	-0.800389
	H	-1.804365	-0.506257	-0.034037

Table A.30: Cartesian coordinates for the NH_3 dual hydrogen bond catalyzed aminomethanol decomposition.

Species	Atom	X	Y	Z
Reactant Complex	C	1.141512	0.001749	0.429268
	N	0.755574	-1.238815	-0.142040
	O	0.657308	1.113694	-0.348597
	H	-0.255842	-1.321831	-0.150346
	H	1.106308	-1.331253	-1.085927
	H	0.727854	0.063655	1.438140
	H	2.230459	0.057044	0.485294
	H	1.060815	1.924469	-0.027078
	N	-2.178614	-0.062401	0.071987
	H	-2.673028	0.255858	0.895714
	H	-2.853246	-0.103227	-0.681456

Continued on next page

Table A.30: Cartesian coordinates for the NH_3 dual hydrogen bond catalyzed aminomethanol decomposition.

Species	Atom	X	Y	Z
	H	-1.489575	0.643749	-0.170803
Transition State	C	-1.034486	-0.011456	0.613161
	N	-0.977341	-1.009387	-0.336704
	O	-0.401108	1.179472	-0.307486
	H	-1.905971	-1.223521	-0.681366
	H	-0.536303	0.257778	-0.952906
	H	-1.992121	0.392719	0.936182
	H	-0.315994	-0.056668	1.432615
	H	0.564188	1.115271	-0.110760
	N	1.991107	-0.181178	0.058110
	H	2.483264	-0.388659	0.918138
	H	2.679438	-0.181532	-0.684560
	H	1.342919	-0.948475	-0.126269
Product Complex	C	2.351621	-0.185298	0.001335
	N	1.129551	0.114355	-0.005064
	O	-1.310284	1.560056	0.027301
	H	0.512418	-0.705768	-0.006915
	H	-0.362693	1.336238	0.008630
	H	2.721409	-1.212859	0.004326
	H	3.100664	0.604956	0.004375
	H	-1.375708	2.496487	-0.162731
	N	-1.501359	-1.477237	-0.004315
	H	-1.904003	-1.893244	0.825979
	H	-1.912511	-1.948038	-0.800389
	H	-1.804365	-0.506257	-0.034037

Table A.31: Cartesian coordinates for the NH_3 cluster catalyzed aminomethanol decomposition.

Species	Atom	X	Y	Z
Reactant Complex	C	0.000001	1.248427	0.064252
	N	-0.000011	0.500028	1.261074
	O	0.000018	0.391046	-1.111394
	H	-0.835982	-0.067004	1.339940
	H	-0.891294	1.877738	0.027366
	H	0.891294	1.877742	0.027391
	H	-0.000032	0.943359	-1.898753
	H	1.879258	-0.683856	-0.634232
	N	2.606044	-0.897029	0.042621
	H	0.835984	-0.066963	1.339982
	H	3.468022	-0.479083	-0.283707
	H	2.742645	-1.899874	0.040738
	N	-2.606034	-0.897044	0.042613
	H	-3.467876	-0.478783	-0.283669
	H	-2.742972	-1.899842	0.040662
	H	-1.879190	-0.684054	-0.634234
Transition State	C	-0.051329	1.136377	0.791209
	N	-0.276551	1.309217	-0.468759
	O	-0.122587	-0.955471	1.004243
	H	0.583436	1.244997	-1.008355
	H	0.947225	1.205114	1.205667
	H	-0.880123	1.205550	1.484270
	H	-0.209329	-1.324168	1.886291
	H	-1.284768	-0.953359	0.106424
	N	-1.942962	-0.562402	-0.705117
	H	-1.280238	0.507925	-0.791274
	H	-2.910303	-0.466677	-0.424193

Continued on next page

Table A.31: Cartesian coordinates for the NH_3 cluster catalyzed aminomethanol decomposition.

Species	Atom	X	Y	Z
Transition State	H	-1.896670	-1.140425	-1.534321
	N	2.346723	-0.365280	-0.585355
	H	3.197144	-0.344496	-0.036003
	H	2.519517	-1.003270	-1.352392
	H	1.612301	-0.776429	-0.002692
Product Complex	C	2.726705	-0.500429	0.000031
	N	1.470751	-0.588368	-0.000051
	O	-2.301627	0.622518	0.000042
	H	1.049067	0.350153	-0.000041
	H	3.259700	0.454252	0.000092
	H	3.336763	-1.403200	0.000046
	H	-3.259386	0.624252	-0.000119
	H	-2.026383	-0.322537	0.000020
	N	-1.274565	-2.004872	-0.000006
	H	-0.282112	-1.763548	-0.000025
	H	-1.451990	-2.578457	-0.814906
	H	-1.451972	-2.578414	0.814930
	N	0.226964	2.257905	-0.000015
	H	0.318856	2.852405	-0.813915
	H	0.318847	2.852361	0.813920
	H	-0.720656	1.882504	-0.000030

Table A.32: Cartesian coordinates for the NH_3 relay catalyzed aminomethanol decomposition.

Species	Atom	X	Y	Z
Reactant Complex	C	-1.141476	0.001724	0.429280
	N	-0.755529	-1.238821	-0.142064

Continued on next page

Table A.32: Cartesian coordinates for the NH_3 relay catalyzed aminomethanol decomposition.

Species	Atom	X	Y	Z
Reactant Complex	O	-0.657352	1.113693	-0.348590
	H	-1.106316	-1.331256	-1.085934
	H	-2.230423	0.056978	0.485368
	H	-0.727768	0.063626	1.438133
	H	-1.060878	1.924448	-0.027044
	H	1.489639	0.643793	-0.171061
	N	2.178581	-0.062379	0.071942
	H	0.255892	-1.321792	-0.150441
	H	2.672528	0.255734	0.896007
	H	2.853630	-0.103022	-0.681137
Transition State	C	-1.236547	-0.100611	0.282420
	N	-0.665810	-1.222662	-0.110677
	O	-0.184838	1.338120	-0.261686
	H	-0.966273	-1.476814	-1.045430
	H	-2.145833	0.260542	-0.188157
	H	-1.148399	0.143181	1.337881
	H	-0.379683	2.123422	0.257106
	H	1.017848	0.681429	-0.033455
	N	1.693884	-0.239336	0.080119
	H	0.786396	-0.953261	0.039617
	H	2.213557	-0.282762	0.947239
	H	2.323855	-0.363043	-0.701924
Product Complex	C	1.568837	-0.817185	-0.000428
	N	1.837426	0.418293	-0.000215
	O	-1.702768	-1.265299	0.001828
	H	2.842792	0.583282	0.001097
	H	2.333740	-1.596516	0.000668

Continued on next page

Table A.32: Cartesian coordinates for the NH_3 relay catalyzed aminomethanol decomposition.

Species	Atom	X	Y	Z
Product Complex	H	0.529407	-1.140227	-0.001777
	H	-2.639850	-1.463274	-0.011096
	H	-1.626214	-0.287995	0.000333
	N	-1.060838	1.501872	-0.000106
	H	-0.045945	1.393514	-0.000286
	H	-1.310430	2.046710	0.815607
	H	-1.310490	2.048851	-0.814360

Rate Constants

Table A.33: Computed rate constants for the NH_3 NH—Cat catalyzed aminomethanol decomposition from 60 K to 1,000 K.

Temperature (K)	kTST (s-1)	kTST/W (s-1)	kTST/Eck (s-1)
60	8.62e-182	4.67e-181	5.75e-172
70	3.57e-154	1.51e-153	8.12e-148
80	1.84e-133	6.40e-133	1.28e-129
90	2.35e-117	6.97e-117	3.66e-115
100	1.81e-104	4.68e-104	3.52e-103
110	6.29e-94	1.46e-93	4.74e-93
120	3.83e-85	8.05e-85	1.75e-84
130	1.04e-77	2.01e-77	3.48e-77
140	2.44e-71	4.41e-71	6.60e-71
150	8.10e-66	1.38e-65	1.87e-65
160	5.50e-61	8.91e-61	1.13e-60
170	1.01e-56	1.56e-56	1.88e-56
180	6.22e-53	9.28e-53	1.08e-52
190	1.53e-49	2.21e-49	2.50e-49

Continued on next page

Table A.33: Computed rate constants for the NH_3 NH—Cat catalyzed aminomethanol decomposition from 60 K to 1,000 K.

Temperature (K)	kTST (s-1)	kTST/W (s-1)	kTST/Eck (s-1)
200	1.73e-46	2.42e-46	2.68e-46
210	1.00e-43	1.37e-43	1.49e-43
220	3.27e-41	4.34e-41	4.66e-41
230	6.44e-39	8.37e-39	8.88e-39
240	8.17e-37	1.04e-36	1.10e-36
250	7.05e-35	8.85e-35	9.24e-35
260	4.33e-33	5.34e-33	5.55e-33
270	1.96e-31	2.38e-31	2.46e-31
280	6.76e-30	8.12e-30	8.36e-30
290	1.83e-28	2.17e-28	2.23e-28
300	3.97e-27	4.68e-27	4.78e-27
310	7.09e-26	8.26e-26	8.43e-26
320	1.06e-24	1.22e-24	1.24e-24
330	1.34e-23	1.54e-23	1.56e-23
340	1.46e-22	1.67e-22	1.69e-22
350	1.40e-21	1.58e-21	1.60e-21
360	1.18e-20	1.32e-20	1.34e-20
370	8.83e-20	9.86e-20	9.96e-20
380	5.97e-19	6.63e-19	6.69e-19
390	3.66e-18	4.04e-18	4.08e-18
400	2.05e-17	2.25e-17	2.27e-17
410	1.06e-16	1.16e-16	1.17e-16
420	5.04e-16	5.50e-16	5.53e-16
430	2.24e-15	2.43e-15	2.45e-15
440	9.28e-15	1.00e-14	1.01e-14
450	3.62e-14	3.90e-14	3.92e-14
460	1.33e-13	1.43e-13	1.44e-13

Continued on next page

Table A.33: Computed rate constants for the NH_3 NH—Cat catalyzed aminomethanol decomposition from 60 K to 1,000 K.

Temperature (K)	kTST (s-1)	kTST/W (s-1)	kTST/Eck (s-1)
470	4.62e-13	4.96e-13	4.98e-13
480	1.53e-12	1.63e-12	1.64e-12
490	4.81e-12	5.12e-12	5.15e-12
500	1.45e-11	1.54e-11	1.54e-11
510	4.16e-11	4.42e-11	4.43e-11
520	1.15e-10	1.22e-10	1.22e-10
530	3.07e-10	3.24e-10	3.25e-10
540	7.88e-10	8.31e-10	8.34e-10
550	1.96e-09	2.06e-09	2.07e-09
560	4.71e-09	4.94e-09	4.96e-09
570	1.10e-08	1.15e-08	1.15e-08
580	2.49e-08	2.60e-08	2.61e-08
590	5.48e-08	5.73e-08	5.74e-08
600	1.18e-07	1.23e-07	1.23e-07
610	2.46e-07	2.57e-07	2.57e-07
620	5.04e-07	5.25e-07	5.26e-07
630	1.01e-06	1.05e-06	1.05e-06
640	1.97e-06	2.05e-06	2.05e-06
650	3.78e-06	3.92e-06	3.93e-06
660	7.11e-06	7.37e-06	7.38e-06
670	1.31e-05	1.36e-05	1.36e-05
680	2.38e-05	2.46e-05	2.46e-05
690	4.24e-05	4.38e-05	4.38e-05
700	7.43e-05	7.67e-05	7.68e-05
710	1.28e-04	1.32e-04	1.32e-04
720	2.18e-04	2.25e-04	2.25e-04
730	3.65e-04	3.76e-04	3.76e-04

Continued on next page

Table A.33: Computed rate constants for the NH_3 NH—Cat catalyzed aminomethanol decomposition from 60 K to 1,000 K.

Temperature (K)	kTST (s-1)	kTST/W (s-1)	kTST/Eck (s-1)
740	6.03e-04	6.21e-04	6.21e-04
750	9.83e-04	1.01e-03	1.01e-03
760	1.58e-03	1.63e-03	1.63e-03
770	2.52e-03	2.59e-03	2.59e-03
780	3.96e-03	4.06e-03	4.06e-03
790	6.15e-03	6.30e-03	6.31e-03
800	9.45e-03	9.68e-03	9.69e-03
810	1.44e-02	1.47e-02	1.47e-02
820	2.16e-02	2.21e-02	2.21e-02
830	3.22e-02	3.30e-02	3.30e-02
840	4.76e-02	4.87e-02	4.88e-02
850	6.97e-02	7.12e-02	7.14e-02
860	1.01e-01	1.03e-01	1.03e-01
870	1.45e-01	1.48e-01	1.49e-01
880	2.07e-01	2.12e-01	2.12e-01
890	2.94e-01	2.99e-01	2.99e-01
900	4.12e-01	4.20e-01	4.20e-01
910	5.75e-01	5.86e-01	5.87e-01
920	7.95e-01	8.10e-01	8.11e-01
930	1.09e+00	1.11e+00	1.11e+00
940	1.49e+00	1.52e+00	1.52e+00
950	2.02e+00	2.06e+00	2.06e+00
960	2.73e+00	2.78e+00	2.77e+00
970	3.66e+00	3.72e+00	3.73e+00
980	4.87e+00	4.95e+00	4.94e+00
990	6.45e+00	6.55e+00	6.56e+00
1000	8.49e+00	8.62e+00	8.65e+00

Table A.34: Computed rate constants for the NH_3 dual hydrogen bond catalyzed aminomethanol decomposition from 60 K to 1,000 K.

Temperature (K)	kTST (s-1)	kTST/W (s-1)	kTST/Eck (s-1)
60	4.39e-184	2.16e-182	6.12e-123
70	4.00e-156	1.46e-154	5.35e-106
80	3.75e-135	1.06e-133	2.66e-93
90	7.70e-119	1.73e-117	2.35e-83
100	8.67e-106	1.59e-104	1.86e-75
110	4.14e-95	6.36e-94	5.79e-69
120	3.28e-86	4.30e-85	1.70e-63
130	1.11e-78	1.26e-77	5.90e-59
140	3.18e-72	3.14e-71	5.76e-55
150	1.25e-66	1.09e-65	1.41e-51
160	9.83e-62	7.66e-61	1.50e-48
170	2.05e-57	1.44e-56	6.41e-46
180	1.42e-53	9.04e-53	1.66e-43
190	3.88e-50	2.26e-49	2.31e-41
200	4.80e-47	2.57e-46	1.90e-39
210	3.02e-44	1.49e-43	1.12e-37
220	1.06e-41	4.85e-41	4.83e-36
230	2.22e-39	9.54e-39	1.62e-34
240	3.00e-37	1.21e-36	4.28e-33
250	2.74e-35	1.04e-34	9.20e-32
260	1.76e-33	6.30e-33	1.73e-30
270	8.36e-32	2.83e-31	2.89e-29
280	3.01e-30	9.68e-30	4.36e-28
290	8.46e-29	2.59e-28	6.04e-27
300	1.90e-27	5.59e-27	7.68e-26
310	3.51e-26	9.87e-26	8.94e-25
320	5.40e-25	1.46e-24	9.47e-24

Continued on next page

Table A.34: Computed rate constants for the NH_3 dual hydrogen bond catalyzed aminomethanol decomposition from 60 K to 1,000 K.

Temperature (K)	kTST (s-1)	kTST/W (s-1)	kTST/Eck (s-1)
330	7.03e-24	1.83e-23	9.10e-23
340	7.89e-23	1.98e-22	7.94e-22
350	7.70e-22	1.86e-21	6.28e-21
360	6.63e-21	1.55e-20	4.53e-20
370	5.09e-20	1.15e-19	2.98e-19
380	3.50e-19	7.73e-19	1.80e-18
390	2.19e-18	4.69e-18	1.00e-17
400	1.25e-17	2.60e-17	5.14e-17
410	6.53e-17	1.33e-16	2.46e-16
420	3.16e-16	6.28e-16	1.10e-15
430	1.42e-15	2.76e-15	4.59e-15
440	5.99e-15	1.14e-14	1.81e-14
450	2.36e-14	4.39e-14	6.72e-14
460	8.78e-14	1.60e-13	2.36e-13
470	3.09e-13	5.52e-13	7.91e-13
480	1.03e-12	1.81e-12	2.52e-12
490	3.28e-12	5.65e-12	7.68e-12
500	9.96e-12	1.69e-11	2.24e-11
510	2.89e-11	4.83e-11	6.28e-11
520	8.08e-11	1.33e-10	1.70e-10
530	2.17e-10	3.51e-10	4.41e-10
540	5.62e-10	8.97e-10	1.11e-09
550	1.41e-09	2.21e-09	2.70e-09
560	3.41e-09	5.30e-09	6.37e-09
570	8.00e-09	1.23e-08	1.46e-08
580	1.82e-08	2.77e-08	3.26e-08
590	4.05e-08	6.07e-08	7.07e-08

Continued on next page

Table A.34: Computed rate constants for the NH_3 dual hydrogen bond catalyzed aminomethanol decomposition from 60 K to 1,000 K.

Temperature (K)	kTST (s-1)	kTST/W (s-1)	kTST/Eck (s-1)
600	8.75e-08	1.30e-07	1.50e-07
610	1.84e-07	2.70e-07	3.10e-07
620	3.79e-07	5.51e-07	6.26e-07
630	7.63e-07	1.10e-06	1.24e-06
640	1.50e-06	2.14e-06	2.40e-06
650	2.89e-06	4.08e-06	4.55e-06
660	5.47e-06	7.65e-06	8.47e-06
670	1.01e-05	1.41e-05	1.55e-05
680	1.85e-05	2.54e-05	2.79e-05
690	3.31e-05	4.52e-05	4.93e-05
700	5.83e-05	7.89e-05	8.57e-05
710	1.01e-04	1.36e-04	1.47e-04
720	1.72e-04	2.30e-04	2.48e-04
730	2.90e-04	3.85e-04	4.13e-04
740	4.82e-04	6.35e-04	6.79e-04
750	7.89e-04	1.03e-03	1.10e-03
760	1.27e-03	1.66e-03	1.76e-03
770	2.04e-03	2.63e-03	2.79e-03
780	3.21e-03	4.13e-03	4.37e-03
790	5.01e-03	6.41e-03	6.76e-03
800	7.73e-03	9.83e-03	1.04e-02
810	1.18e-02	1.49e-02	1.57e-02
820	1.78e-02	2.24e-02	2.35e-02
830	2.67e-02	3.34e-02	3.50e-02
840	3.95e-02	4.93e-02	5.15e-02
850	5.81e-02	7.20e-02	7.51e-02
860	8.45e-02	1.04e-01	1.09e-01

Continued on next page

Table A.34: Computed rate constants for the NH_3 dual hydrogen bond catalyzed aminomethanol decomposition from 60 K to 1,000 K.

Temperature (K)	kTST (s-1)	kTST/W (s-1)	kTST/Eck (s-1)
870	1.22e-01	1.50e-01	1.56e-01
880	1.75e-01	2.14e-01	2.22e-01
890	2.48e-01	3.02e-01	3.13e-01
900	3.49e-01	4.24e-01	4.39e-01
910	4.89e-01	5.91e-01	6.11e-01
920	6.78e-01	8.18e-01	8.45e-01
930	9.35e-01	1.12e+00	1.16e+00
940	1.28e+00	1.53e+00	1.58e+00
950	1.74e+00	2.08e+00	2.14e+00
960	2.36e+00	2.80e+00	2.88e+00
970	3.17e+00	3.75e+00	3.86e+00
980	4.23e+00	5.00e+00	5.13e+00
990	5.62e+00	6.61e+00	6.79e+00
1000	7.42e+00	8.71e+00	8.93e+00

Table A.35: Computed rate constants for the NH_3 cluster catalyzed aminomethanol decomposition from 60 K to 1,000 K.

Temperature (K)	kTST (s-1)	kTST/W (s-1)	kTST/Eck (s-1)
60	1.32e-120	4.47e-119	6.00e-75
70	7.25e-102	1.82e-100	5.02e-65
80	7.93e-88	1.54e-86	1.81e-57
90	6.39e-77	9.96e-76	1.15e-51
100	3.31e-68	4.24e-67	4.67e-47
110	4.38e-61	4.71e-60	3.32e-43
120	3.70e-55	3.41e-54	4.64e-40
130	3.78e-50	3.02e-49	2.25e-37
140	7.35e-46	5.17e-45	5.18e-35

Continued on next page

Table A.35: Computed rate constants for the NH_3 cluster catalyzed aminomethanol decomposition from 60 K to 1,000 K.

Temperature (K)	kTST (s-1)	kTST/W (s-1)	kTST/Eck (s-1)
150	3.80e-42	2.37e-41	5.61e-33
160	6.69e-39	3.76e-38	3.54e-31
170	4.86e-36	2.47e-35	1.30e-29
180	1.69e-33	7.85e-33	4.00e-28
190	3.16e-31	1.35e-30	8.69e-27
200	3.49e-29	1.38e-28	1.54e-25
210	2.46e-27	9.05e-27	2.40e-24
220	1.17e-25	4.04e-25	3.43e-23
230	3.99e-24	1.29e-23	4.41e-22
240	1.01e-22	3.09e-22	5.25e-21
250	1.98e-21	5.71e-21	5.70e-20
260	3.07e-20	8.44e-20	5.61e-19
270	3.89e-19	1.02e-18	4.95e-18
280	4.11e-18	1.03e-17	3.91e-17
290	3.68e-17	8.86e-17	2.77e-16
300	2.85e-16	6.60e-16	1.77e-15
310	1.94e-15	4.32e-15	1.02e-14
320	1.17e-14	2.51e-14	5.32e-14
330	6.30e-14	1.31e-13	2.55e-13
340	3.08e-13	6.23e-13	1.12e-12
350	1.38e-12	2.70e-12	4.56e-12
360	5.65e-12	1.08e-11	1.73e-11
370	2.15e-11	4.01e-11	6.11e-11
380	7.64e-11	1.39e-10	2.03e-10
390	2.54e-10	4.51e-10	6.37e-10
400	7.96e-10	1.38e-09	1.89e-09
410	2.36e-09	4.02e-09	5.34e-09

Continued on next page

Table A.35: Computed rate constants for the NH_3 cluster catalyzed aminomethanol decomposition from 60 K to 1,000 K.

Temperature (K)	kTST (s-1)	kTST/W (s-1)	kTST/Eck (s-1)
420	6.63e-09	1.11e-08	1.44e-08
430	1.78e-08	2.92e-08	3.70e-08
440	4.56e-08	7.35e-08	9.16e-08
450	1.12e-07	1.78e-07	2.18e-07
460	2.66e-07	4.14e-07	4.99e-07
470	6.06e-07	9.30e-07	1.11e-06
480	1.34e-06	2.02e-06	2.37e-06
490	2.85e-06	4.26e-06	4.94e-06
500	5.91e-06	8.70e-06	9.98e-06
510	1.19e-05	1.73e-05	1.97e-05
520	2.33e-05	3.35e-05	3.78e-05
530	4.46e-05	6.33e-05	7.08e-05
540	8.32e-05	1.17e-04	1.30e-04
550	1.52e-04	2.11e-04	2.33e-04
560	2.71e-04	3.73e-04	4.09e-04
570	4.75e-04	6.47e-04	7.06e-04
580	8.15e-04	1.10e-03	1.20e-03
590	1.37e-03	1.84e-03	1.99e-03
600	2.28e-03	3.03e-03	3.25e-03
610	3.72e-03	4.90e-03	5.24e-03
620	5.97e-03	7.80e-03	8.32e-03
630	9.44e-03	1.22e-02	1.30e-02
640	1.47e-02	1.90e-02	2.01e-02
650	2.26e-02	2.90e-02	3.06e-02
660	3.44e-02	4.37e-02	4.61e-02
670	5.16e-02	6.52e-02	6.85e-02
680	7.65e-02	9.61e-02	1.01e-01

Continued on next page

Table A.35: Computed rate constants for the NH_3 cluster catalyzed aminomethanol decomposition from 60 K to 1,000 K.

Temperature (K)	kTST (s-1)	kTST/W (s-1)	kTST/Eck (s-1)
690	1.12e-01	1.40e-01	1.46e-01
700	1.63e-01	2.02e-01	2.11e-01
710	2.34e-01	2.88e-01	3.00e-01
720	3.32e-01	4.08e-01	4.24e-01
730	4.67e-01	5.71e-01	5.93e-01
740	6.52e-01	7.93e-01	8.22e-01
750	9.02e-01	1.09e+00	1.13e+00
760	1.24e+00	1.49e+00	1.54e+00
770	1.68e+00	2.02e+00	2.08e+00
780	2.27e+00	2.71e+00	2.80e+00
790	3.04e+00	3.62e+00	3.73e+00
800	4.05e+00	4.80e+00	4.93e+00
810	5.35e+00	6.31e+00	6.48e+00
820	7.02e+00	8.25e+00	8.47e+00
830	9.15e+00	1.07e+01	1.10e+01
840	1.19e+01	1.38e+01	1.42e+01
850	1.53e+01	1.78e+01	1.82e+01
860	1.96e+01	2.27e+01	2.32e+01
870	2.49e+01	2.88e+01	2.94e+01
880	3.16e+01	3.64e+01	3.72e+01
890	3.98e+01	4.57e+01	4.67e+01
900	4.99e+01	5.72e+01	5.83e+01
910	6.22e+01	7.11e+01	7.25e+01
920	7.73e+01	8.81e+01	8.97e+01
930	9.56e+01	1.09e+02	1.11e+02
940	1.18e+02	1.33e+02	1.36e+02
950	1.44e+02	1.63e+02	1.66e+02

Continued on next page

Table A.35: Computed rate constants for the NH_3 cluster catalyzed aminomethanol decomposition from 60 K to 1,000 K.

Temperature (K)	kTST (s-1)	kTST/W (s-1)	kTST/Eck (s-1)
960	1.76e+02	1.98e+02	2.02e+02
970	2.14e+02	2.41e+02	2.45e+02
980	2.59e+02	2.91e+02	2.95e+02
990	3.12e+02	3.50e+02	3.55e+02
1000	3.75e+02	4.20e+02	4.26e+02

Table A.36: Computed rate constants for the NH_3 relay catalyzed aminomethanol decomposition from 60 K to 1,000 K.

Temperature (K)	kTST (s-1)	kTST/W (s-1)	kTST/Eck (s-1)
60	3.20e-129	8.18e-128	3.01e-90
70	3.65e-109	6.95e-108	5.43e-78
80	3.93e-94	5.83e-93	7.92e-69
90	1.89e-82	2.26e-81	1.01e-61
100	4.12e-73	4.06e-72	5.22e-56
110	1.77e-65	1.47e-64	2.81e-51
120	3.98e-59	2.85e-58	2.50e-47
130	9.35e-54	5.83e-53	4.73e-44
140	3.71e-49	2.05e-48	3.91e-41
150	3.56e-45	1.75e-44	1.26e-38
160	1.07e-41	4.79e-41	2.21e-36
170	1.26e-38	5.11e-38	2.28e-34
180	6.67e-36	2.49e-35	1.65e-32
190	1.82e-33	6.28e-33	8.92e-31
200	2.82e-31	9.06e-31	3.94e-29
210	2.69e-29	8.10e-29	1.47e-27
220	1.70e-27	4.80e-27	4.60e-26
230	7.43e-26	1.99e-25	1.20e-24

Continued on next page

Table A.36: Computed rate constants for the NH_3 relay catalyzed aminomethanol decomposition from 60 K to 1,000 K.

Temperature (K)	kTST (s-1)	kTST/W (s-1)	kTST/Eck (s-1)
240	2.37e-24	6.01e-24	2.59e-23
250	5.72e-23	1.38e-22	4.62e-22
260	1.08e-21	2.49e-21	6.85e-21
270	1.64e-20	3.62e-20	8.54e-20
280	2.04e-19	4.34e-19	9.07e-19
290	2.14e-18	4.38e-18	8.28e-18
300	1.91e-17	3.79e-17	6.60e-17
310	1.48e-16	2.85e-16	4.63e-16
320	1.01e-15	1.89e-15	2.90e-15
330	6.14e-15	1.11e-14	1.63e-14
340	3.35e-14	5.92e-14	8.31e-14
350	1.66e-13	2.86e-13	3.87e-13
360	7.52e-13	1.26e-12	1.66e-12
370	3.14e-12	5.16e-12	6.61e-12
380	1.21e-11	1.96e-11	2.45e-11
390	4.38e-11	6.93e-11	8.49e-11
400	1.48e-10	2.30e-10	2.77e-10
410	4.73e-10	7.22e-10	8.55e-10
420	1.43e-09	2.15e-09	2.50e-09
430	4.10e-09	6.06e-09	6.97e-09
440	1.12e-08	1.63e-08	1.86e-08
450	2.93e-08	4.20e-08	4.74e-08
460	7.33e-08	1.04e-07	1.16e-07
470	1.77e-07	2.48e-07	2.74e-07
480	4.11e-07	5.69e-07	6.25e-07
490	9.23e-07	1.26e-06	1.38e-06
500	2.01e-06	2.72e-06	2.95e-06

Continued on next page

Table A.36: Computed rate constants for the NH_3 relay catalyzed aminomethanol decomposition from 60 K to 1,000 K.

Temperature (K)	kTST (s-1)	kTST/W (s-1)	kTST/Eck (s-1)
510	4.23e-06	5.67e-06	6.12e-06
520	8.67e-06	1.15e-05	1.24e-05
530	1.73e-05	2.28e-05	2.43e-05
540	3.37e-05	4.39e-05	4.67e-05
550	6.39e-05	8.26e-05	8.76e-05
560	1.19e-04	1.52e-04	1.61e-04
570	2.15e-04	2.74e-04	2.89e-04
580	3.83e-04	4.84e-04	5.08e-04
590	6.69e-04	8.39e-04	8.78e-04
600	1.15e-03	1.43e-03	1.49e-03
610	1.93e-03	2.39e-03	2.49e-03
620	3.19e-03	3.93e-03	4.09e-03
630	5.21e-03	6.37e-03	6.61e-03
640	8.36e-03	1.02e-02	1.05e-02
650	1.32e-02	1.60e-02	1.65e-02
660	2.06e-02	2.48e-02	2.56e-02
670	3.18e-02	3.81e-02	3.92e-02
680	4.83e-02	5.76e-02	5.93e-02
690	7.26e-02	8.61e-02	8.85e-02
700	1.08e-01	1.27e-01	1.31e-01
710	1.59e-01	1.86e-01	1.91e-01
720	2.31e-01	2.70e-01	2.76e-01
730	3.32e-01	3.87e-01	3.96e-01
740	4.73e-01	5.49e-01	5.62e-01
750	6.68e-01	7.73e-01	7.89e-01
760	9.35e-01	1.08e+00	1.10e+00
770	1.30e+00	1.49e+00	1.52e+00

Continued on next page

Table A.36: Computed rate constants for the NH_3 relay catalyzed aminomethanol decomposition from 60 K to 1,000 K.

Temperature (K)	kTST (s-1)	kTST/W (s-1)	kTST/Eck (s-1)
780	1.78e+00	2.04e+00	2.08e+00
790	2.44e+00	2.78e+00	2.83e+00
800	3.30e+00	3.76e+00	3.82e+00
810	4.44e+00	5.04e+00	5.12e+00
820	5.92e+00	6.70e+00	6.81e+00
830	7.86e+00	8.87e+00	9.01e+00
840	1.04e+01	1.16e+01	1.18e+01
850	1.35e+01	1.52e+01	1.54e+01
860	1.76e+01	1.97e+01	2.00e+01
870	2.28e+01	2.55e+01	2.58e+01
880	2.93e+01	3.27e+01	3.31e+01
890	3.75e+01	4.17e+01	4.22e+01
900	4.77e+01	5.29e+01	5.35e+01
910	6.03e+01	6.68e+01	6.76e+01
920	7.60e+01	8.39e+01	8.49e+01
930	9.52e+01	1.05e+02	1.06e+02
940	1.19e+02	1.31e+02	1.32e+02
950	1.47e+02	1.62e+02	1.64e+02
960	1.82e+02	2.00e+02	2.02e+02
970	2.24e+02	2.45e+02	2.48e+02
980	2.75e+02	3.00e+02	3.03e+02
990	3.35e+02	3.65e+02	3.69e+02
1000	4.08e+02	4.44e+02	4.48e+02

A.4.7 H_2O Catalyzed Reactions

Cartesian Coordinates

Table A.37: Cartesian coordinates for the H_2O dual hydrogen bond catalyzed aminomethanol decomposition.

Species	Atom	X	Y	Z
Reactant Complex	C	1.075289	-0.109034	0.393329
	N	0.591656	1.132395	-0.221792
	O	0.581176	-1.215068	-0.296347
	H	0.871936	1.937188	0.326185
	H	0.991580	1.232766	-1.147709
	H	2.162804	-0.198809	0.368477
	H	0.745772	-0.098274	1.436302
	H	-0.384080	-1.201110	-0.220533
	O	-1.952080	-0.005925	0.158100
	H	-1.279880	0.655136	-0.096658
	H	-2.734225	0.168489	-0.367514
Transition State	C	-0.975933	-0.135315	0.606849
	N	-0.623560	-1.080241	-0.333916
	O	-0.609362	1.181034	-0.308892
	H	-1.441427	-1.519583	-0.737493
	H	-0.452706	0.238994	-0.935529
	H	-2.020512	0.019231	0.866563
	H	-0.303050	-0.003361	1.451913
	H	0.295430	1.437369	-0.057644
	O	1.873475	-0.015263	0.075126
	H	1.272038	-0.749030	-0.164512
	H	2.757833	-0.376209	0.143152
Product Complex	C	1.514535	-0.887672	0.037581
	N	1.670420	0.364535	-0.038813
	O	-1.760045	-1.127971	0.063906
	H	2.651233	0.630324	-0.098987
	H	-2.490181	-1.321231	-0.525742

Continued on next page

Table A.37: Cartesian coordinates for the H_2O dual hydrogen bond catalyzed aminomethanol decomposition.

Species	Atom	X	Y	Z
Product Complex	H	2.347927	-1.591680	0.039346
	H	0.505370	-1.290925	0.099889
	H	-1.613074	-0.167733	0.000403
	O	-0.891204	1.520702	-0.074761
	H	0.060334	1.284115	-0.065973
	H	-1.031771	2.089568	0.684119

Table A.38: Cartesian coordinates for the H_2O cluster catalyzed aminomethanol decomposition.

Species	Atom	X	Y	Z
Reactant Complex	C	-1.209104	-0.769421	-0.199243
	N	-2.056920	0.340526	-0.484511
	O	-0.376954	-0.535252	0.950293
	H	-2.664695	0.552712	0.295179
	H	-1.519490	1.166275	-0.716778
	H	-1.827632	-1.646592	-0.007048
	H	-0.569031	-0.961198	-1.061062
	H	0.437719	-1.045187	0.837465
	O	0.954803	1.652517	0.001151
	H	0.411165	1.058683	0.554723
	H	1.200155	2.400495	0.548456
	O	2.076588	-0.895338	-0.308845
	H	2.003118	0.069784	-0.375381
	H	2.946261	-1.137543	-0.629316
Transition State	C	-1.135189	-0.773241	-0.543415
	N	-1.679714	0.407164	-0.558156
	O	-0.147691	-0.823444	1.222541

Continued on next page

Table A.38: Cartesian coordinates for the H_2O cluster catalyzed aminomethanol decomposition.

Species	Atom	X	Y	Z
Transition State	H	-2.587820	0.508739	-0.130312
	H	-0.918098	1.174537	-0.380599
	H	-1.741052	-1.651153	-0.366859
	H	-0.177236	-0.888806	-1.032884
	H	0.683546	-1.289197	1.059782
	O	0.404939	1.444663	0.298711
	H	0.119967	0.166435	1.073427
	H	0.636508	2.274478	0.713898
	O	2.006040	-0.454029	-0.581748
	H	1.587459	0.407084	-0.319947
	H	2.859551	-0.250332	-0.964953
Product Complex	C	-1.613024	-0.748530	-0.644391
	N	-1.969450	0.316848	-0.066184
	O	0.866030	-1.300348	1.297850
	H	-2.950896	0.307006	0.201160
	H	-0.550993	1.300453	0.369034
	H	-2.291360	-1.579675	-0.836819
	H	-0.580937	-0.855806	-0.967356
	H	1.381635	-1.239845	0.484653
	O	0.378825	1.576112	0.559385
	H	0.713543	-0.377037	1.525495
	H	0.361413	2.512205	0.764358
	O	1.693188	-0.103899	-1.213526
	H	1.387645	0.658416	-0.691768
	H	2.489901	0.172619	-1.668793

Table A.39: Cartesian coordinates for the H_2O relay catalyzed aminomethanol decomposition.

Species	Atom	X	Y	Z
Reactant Complex	C	-1.070139	0.092481	0.423024
	N	-0.869994	-1.186235	-0.155343
	O	-0.414633	1.125485	-0.348711
	H	-1.227927	-1.226742	-1.099934
	H	0.112766	-1.432692	-0.159371
	H	-2.137362	0.314643	0.463937
	H	-0.657643	0.090922	1.432963
	H	-0.620739	1.984485	0.030987
	O	2.016143	-0.182552	0.143298
	H	1.378284	0.466191	-0.190080
	H	2.851329	0.008490	-0.285941
Transition State	C	-1.213742	-0.016276	0.337959
	N	-0.724083	-1.122515	-0.156132
	O	0.012551	1.356499	-0.276915
	H	-1.040157	-1.340338	-1.091642
	H	0.458326	-1.087187	0.012302
	H	-2.115415	0.426897	-0.064972
	H	-0.981468	0.206327	1.371427
	H	0.086795	2.128896	0.290955
	O	1.596318	-0.423119	0.012697
	H	0.898819	0.666829	-0.111055
	H	2.173183	-0.513199	0.771897
Product Complex	C	1.514490	-0.887704	0.037582
	N	1.670459	0.364492	-0.038819
	O	-1.760098	-1.127923	0.063894
	H	2.651292	0.630214	-0.098968
	H	0.060408	1.284142	-0.065969

Continued on next page

Table A.39: Cartesian coordinates for the H_2O relay catalyzed aminomethanol decomposition.

Species	Atom	X	Y	Z
Product Complex	H	2.347834	-1.591767	0.039372
	H	0.505298	-1.290893	0.099866
	H	-2.490327	-1.321134	-0.525654
	O	-0.891135	1.520713	-0.074758
	H	-1.613082	-0.167694	0.000390
	H	-1.031708	2.089591	0.684112

Table A.40: Cartesian coordinates for the H_2O double relay catalyzed aminomethanol decomposition.

Species	Atom	X	Y	Z
Reactant Complex	C	1.673239	-0.250266	-0.331965
	N	1.096363	-1.171373	0.566356
	O	1.153237	1.091916	-0.139864
	H	1.246919	-0.922074	1.532942
	H	0.113657	-1.344353	0.382377
	H	2.753869	-0.209508	-0.186148
	H	1.454399	-0.566017	-1.352612
	H	1.600841	1.697225	-0.738253
	O	-1.837414	-1.296571	-0.230266
	H	-0.611732	1.367240	0.096558
	H	-2.418427	-1.574038	-0.939603
	O	-1.582868	1.430332	0.162087
	H	-1.947086	-0.333995	-0.138147
	H	-1.770050	1.781312	1.034529
Transition State	C	-1.205285	-0.826865	0.506641
	N	-0.432141	-1.492394	-0.279641
	O	-1.472904	1.032863	-0.308939

Continued on next page

Table A.40: Cartesian coordinates for the H_2O double relay catalyzed aminomethanol decomposition.

Species	Atom	X	Y	Z
Transition State	H	-0.844581	-1.975724	-1.063026
	H	0.669630	-1.276902	-0.213883
	H	-2.273624	-0.982836	0.498758
	H	-0.749947	-0.368704	1.373910
	H	-2.010934	1.644432	0.201864
	O	1.915910	-0.640885	-0.079048
	H	-0.442595	1.332377	-0.167930
	H	2.495345	-0.871354	0.647749
	O	0.882970	1.515709	0.137690
	H	1.501731	0.454777	0.038852
	H	1.303866	2.190394	-0.396272
Product Complex	C	0.041618	-1.658550	0.400905
	N	1.054743	-1.576445	-0.348937
	O	-2.345530	-0.262399	-0.099064
	H	1.091257	-2.326690	-1.035154
	H	1.862106	0.018065	-0.154235
	H	-0.713252	-2.438163	0.329118
	H	-0.112010	-0.899589	1.163570
	H	-3.201567	0.037875	0.209969
	O	2.012342	0.973831	0.032108
	H	-1.771140	0.524162	-0.085443
	H	2.654997	1.024858	0.741160
	O	-0.567213	1.899522	0.007326
	H	0.373480	1.638499	0.067755
	H	-0.613574	2.519774	-0.722581

Rate Constants

Table A.41: Computed rate constants for the H_2O dual hydrogen bond catalyzed aminomethanol decomposition from 60 K to 1,000 K.

Temperature (K)	kTST (s-1)	kTST/W (s-1)	kTST/Eck (s-1)
60	4.22e-184	2.27e-182	5.72e-120
70	4.22e-156	1.68e-154	2.33e-103
80	4.30e-135	1.32e-133	5.85e-91
90	9.52e-119	2.33e-117	2.71e-81
100	1.15e-105	2.29e-104	1.61e-73
110	5.82e-95	9.71e-94	3.63e-67
120	4.88e-86	6.93e-85	7.33e-62
130	1.74e-78	2.13e-77	2.17e-57
140	5.21e-72	5.57e-71	1.66e-53
150	2.14e-66	2.02e-65	3.86e-50
160	1.75e-61	1.47e-60	3.50e-47
170	3.79e-57	2.87e-56	1.44e-44
180	2.71e-53	1.86e-52	2.89e-42
190	7.64e-50	4.78e-49	3.81e-40
200	9.74e-47	5.60e-46	2.91e-38
210	6.30e-44	3.34e-43	1.52e-36
220	2.26e-41	1.11e-40	6.18e-35
230	4.88e-39	2.24e-38	1.86e-33
240	6.73e-37	2.89e-36	4.29e-32
250	6.27e-35	2.53e-34	8.31e-31
260	4.12e-33	1.57e-32	1.41e-29
270	1.99e-31	7.18e-31	2.08e-28
280	7.30e-30	2.50e-29	2.76e-27
290	2.09e-28	6.80e-28	3.41e-26
300	4.78e-27	1.49e-26	3.88e-25
310	8.96e-26	2.67e-25	4.10e-24
320	1.40e-24	3.99e-24	4.03e-23

Continued on next page

Table A.41: Computed rate constants for the H_2O dual hydrogen bond catalyzed aminomethanol decomposition from 60 K to 1,000 K.

Temperature (K)	kTST (s-1)	kTST/W (s-1)	kTST/Eck (s-1)
330	1.85e-23	5.07e-23	3.65e-22
340	2.10e-22	5.55e-22	3.04e-21
350	2.08e-21	5.30e-21	2.32e-20
360	1.81e-20	4.47e-20	1.63e-19
370	1.41e-19	3.36e-19	1.05e-18
380	9.81e-19	2.27e-18	6.26e-18
390	6.19e-18	1.39e-17	3.45e-17
400	3.57e-17	7.81e-17	1.76e-16
410	1.89e-16	4.02e-16	8.38e-16
420	9.24e-16	1.92e-15	3.73e-15
430	4.20e-15	8.51e-15	1.56e-14
440	1.78e-14	3.53e-14	6.12e-14
450	7.10e-14	1.38e-13	2.27e-13
460	2.66e-13	5.05e-13	8.02e-13
470	9.45e-13	1.76e-12	2.69e-12
480	3.18e-12	5.80e-12	8.58e-12
490	1.02e-11	1.83e-11	2.62e-11
500	3.12e-11	5.49e-11	7.67e-11
510	9.14e-11	1.58e-10	2.16e-10
520	2.57e-10	4.38e-10	5.84e-10
530	6.96e-10	1.17e-09	1.52e-09
540	1.81e-09	3.00e-09	3.84e-09
550	4.57e-09	7.44e-09	9.39e-09
560	1.11e-08	1.79e-08	2.22e-08
570	2.63e-08	4.17e-08	5.12e-08
580	6.05e-08	9.46e-08	1.15e-07
590	1.35e-07	2.09e-07	2.50e-07

Continued on next page

Table A.41: Computed rate constants for the H_2O dual hydrogen bond catalyzed aminomethanol decomposition from 60 K to 1,000 K.

Temperature (K)	kTST (s-1)	kTST/W (s-1)	kTST/Eck (s-1)
600	2.93e-07	4.48e-07	5.31e-07
610	6.22e-07	9.39e-07	1.10e-06
620	1.29e-06	1.92e-06	2.23e-06
630	2.60e-06	3.85e-06	4.43e-06
640	5.15e-06	7.54e-06	8.61e-06
650	9.98e-06	1.45e-05	1.64e-05
660	1.90e-05	2.72e-05	3.07e-05
670	3.54e-05	5.03e-05	5.63e-05
680	6.47e-05	9.13e-05	1.02e-04
690	1.16e-04	1.63e-04	1.80e-04
700	2.06e-04	2.86e-04	3.15e-04
710	3.59e-04	4.94e-04	5.42e-04
720	6.16e-04	8.41e-04	9.18e-04
730	1.04e-03	1.41e-03	1.53e-03
740	1.73e-03	2.34e-03	2.53e-03
750	2.85e-03	3.82e-03	4.11e-03
760	4.63e-03	6.15e-03	6.61e-03
770	7.42e-03	9.80e-03	1.05e-02
780	1.18e-02	1.54e-02	1.65e-02
790	1.84e-02	2.40e-02	2.56e-02
800	2.85e-02	3.70e-02	3.93e-02
810	4.37e-02	5.64e-02	5.97e-02
820	6.63e-02	8.50e-02	8.98e-02
830	9.95e-02	1.27e-01	1.34e-01
840	1.48e-01	1.88e-01	1.98e-01
850	2.18e-01	2.75e-01	2.89e-01
860	3.19e-01	4.00e-01	4.20e-01

Continued on next page

Table A.41: Computed rate constants for the H_2O dual hydrogen bond catalyzed aminomethanol decomposition from 60 K to 1,000 K.

Temperature (K)	kTST (s-1)	kTST/W (s-1)	kTST/Eck (s-1)
870	4.61e-01	5.77e-01	6.04e-01
880	6.62e-01	8.25e-01	8.62e-01
890	9.44e-01	1.17e+00	1.22e+00
900	1.33e+00	1.65e+00	1.71e+00
910	1.87e+00	2.30e+00	2.39e+00
920	2.61e+00	3.19e+00	3.31e+00
930	3.60e+00	4.40e+00	4.56e+00
940	4.95e+00	6.02e+00	6.23e+00
950	6.76e+00	8.18e+00	8.46e+00
960	9.16e+00	1.10e+01	1.14e+01
970	1.23e+01	1.48e+01	1.53e+01
980	1.65e+01	1.98e+01	2.04e+01
990	2.20e+01	2.63e+01	2.71e+01
1000	2.92e+01	3.47e+01	3.57e+01

Table A.42: Computed rate constants for the H_2O cluster catalyzed aminomethanol decomposition from 60 K to 1,000 K.

Temperature (K)	kTST (s-1)	kTST/W (s-1)	kTST/Eck (s-1)
60	3.85e-106	2.38e-105	2.74e-95
70	2.00e-89	9.59e-89	3.55e-82
80	6.73e-77	2.63e-76	2.82e-72
90	3.67e-67	1.21e-66	2.33e-64
100	2.23e-59	6.39e-59	1.09e-57
110	5.16e-53	1.31e-52	6.81e-52
120	1.03e-47	2.36e-47	6.83e-47
130	3.11e-43	6.53e-43	1.37e-42
140	2.14e-39	4.17e-39	7.17e-39

Continued on next page

Table A.42: Computed rate constants for the H_2O cluster catalyzed aminomethanol decomposition from 60 K to 1,000 K.

Temperature (K)	kTST (s-1)	kTST/W (s-1)	kTST/Eck (s-1)
150	4.51e-36	8.24e-36	1.24e-35
160	3.63e-33	6.27e-33	8.61e-33
170	1.33e-30	2.18e-30	2.80e-30
180	2.50e-28	3.94e-28	4.82e-28
190	2.72e-26	4.12e-26	4.85e-26
200	1.84e-24	2.70e-24	3.09e-24
210	8.32e-23	1.18e-22	1.32e-22
220	2.66e-21	3.68e-21	4.04e-21
230	6.26e-20	8.47e-20	9.18e-20
240	1.13e-18	1.50e-18	1.61e-18
250	1.62e-17	2.11e-17	2.24e-17
260	1.90e-16	2.42e-16	2.55e-16
270	1.84e-15	2.31e-15	2.42e-15
280	1.52e-14	1.88e-14	1.96e-14
290	1.08e-13	1.32e-13	1.37e-13
300	6.78e-13	8.18e-13	8.43e-13
310	3.76e-12	4.49e-12	4.61e-12
320	1.87e-11	2.22e-11	2.27e-11
330	8.47e-11	9.92e-11	1.01e-10
340	3.50e-10	4.07e-10	4.15e-10
350	1.34e-09	1.54e-09	1.57e-09
360	4.72e-09	5.40e-09	5.49e-09
370	1.56e-08	1.77e-08	1.80e-08
380	4.84e-08	5.46e-08	5.54e-08
390	1.42e-07	1.59e-07	1.61e-07
400	3.92e-07	4.38e-07	4.43e-07
410	1.03e-06	1.15e-06	1.16e-06

Continued on next page

Table A.42: Computed rate constants for the H_2O cluster catalyzed aminomethanol decomposition from 60 K to 1,000 K.

Temperature (K)	kTST (s-1)	kTST/W (s-1)	kTST/Eck (s-1)
420	2.61e-06	2.88e-06	2.91e-06
430	6.28e-06	6.92e-06	6.98e-06
440	1.46e-05	1.60e-05	1.61e-05
450	3.25e-05	3.55e-05	3.58e-05
460	7.00e-05	7.62e-05	7.67e-05
470	1.46e-04	1.58e-04	1.59e-04
480	2.95e-04	3.19e-04	3.21e-04
490	5.80e-04	6.25e-04	6.29e-04
500	1.11e-03	1.19e-03	1.20e-03
510	2.07e-03	2.22e-03	2.23e-03
520	3.77e-03	4.03e-03	4.05e-03
530	6.70e-03	7.15e-03	7.18e-03
540	1.17e-02	1.24e-02	1.25e-02
550	1.99e-02	2.12e-02	2.13e-02
560	3.34e-02	3.54e-02	3.55e-02
570	5.49e-02	5.81e-02	5.83e-02
580	8.88e-02	9.37e-02	9.41e-02
590	1.41e-01	1.49e-01	1.49e-01
600	2.21e-01	2.33e-01	2.34e-01
610	3.41e-01	3.58e-01	3.60e-01
620	5.20e-01	5.45e-01	5.47e-01
630	7.80e-01	8.17e-01	8.20e-01
640	1.16e+00	1.21e+00	1.21e+00
650	1.70e+00	1.77e+00	1.78e+00
660	2.46e+00	2.56e+00	2.57e+00
670	3.52e+00	3.66e+00	3.67e+00
680	4.99e+00	5.19e+00	5.20e+00

Continued on next page

Table A.42: Computed rate constants for the H_2O cluster catalyzed aminomethanol decomposition from 60 K to 1,000 K.

Temperature (K)	kTST (s-1)	kTST/W (s-1)	kTST/Eck (s-1)
690	7.00e+00	7.27e+00	7.29e+00
700	9.72e+00	1.01e+01	1.01e+01
710	1.34e+01	1.39e+01	1.39e+01
720	1.83e+01	1.89e+01	1.90e+01
730	2.47e+01	2.56e+01	2.57e+01
740	3.32e+01	3.43e+01	3.44e+01
750	4.42e+01	4.57e+01	4.58e+01
760	5.85e+01	6.03e+01	6.05e+01
770	7.67e+01	7.91e+01	7.94e+01
780	1.00e+02	1.03e+02	1.03e+02
790	1.29e+02	1.33e+02	1.34e+02
800	1.67e+02	1.71e+02	1.72e+02
810	2.13e+02	2.19e+02	2.20e+02
820	2.71e+02	2.78e+02	2.79e+02
830	3.42e+02	3.51e+02	3.52e+02
840	4.30e+02	4.41e+02	4.42e+02
850	5.37e+02	5.51e+02	5.53e+02
860	6.68e+02	6.85e+02	6.87e+02
870	8.27e+02	8.48e+02	8.48e+02
880	1.02e+03	1.04e+03	1.05e+03
890	1.25e+03	1.28e+03	1.28e+03
900	1.52e+03	1.56e+03	1.56e+03
910	1.85e+03	1.89e+03	1.89e+03
920	2.24e+03	2.29e+03	2.29e+03
930	2.70e+03	2.76e+03	2.77e+03
940	3.24e+03	3.31e+03	3.32e+03
950	3.88e+03	3.96e+03	3.96e+03

Continued on next page

Table A.42: Computed rate constants for the H_2O cluster catalyzed aminomethanol decomposition from 60 K to 1,000 K.

Temperature (K)	kTST (s-1)	kTST/W (s-1)	kTST/Eck (s-1)
960	4.62e+03	4.71e+03	4.73e+03
970	5.49e+03	5.59e+03	5.61e+03
980	6.49e+03	6.62e+03	6.61e+03
990	7.65e+03	7.80e+03	7.82e+03
1000	9.00e+03	9.16e+03	9.19e+03

Table A.43: Computed rate constants for the H_2O relay catalyzed aminomethanol decomposition from 60 K to 1,000 K.

Temperature (K)	kTST (s-1)	kTST/W (s-1)	kTST/Eck (s-1)
60	4.06e-114	1.55e-112	3.33e-66
70	3.37e-96	9.53e-95	2.39e-57
80	9.12e-83	2.00e-81	9.51e-51
90	2.52e-72	4.41e-71	1.22e-45
100	5.60e-64	8.04e-63	1.80e-41
110	3.74e-57	4.50e-56	3.63e-38
120	1.80e-51	1.85e-50	2.46e-35
130	1.15e-46	1.02e-45	6.58e-33
140	1.49e-42	1.17e-41	7.90e-31
150	5.46e-39	3.79e-38	4.83e-29
160	7.13e-36	4.43e-35	2.05e-27
170	3.98e-33	2.24e-32	5.78e-26
180	1.09e-30	5.61e-30	1.14e-24
190	1.66e-28	7.80e-28	1.86e-23
200	1.52e-26	6.60e-26	2.48e-22
210	9.02e-25	3.64e-24	2.94e-21
220	3.69e-23	1.39e-22	3.13e-20
230	1.09e-21	3.84e-21	3.08e-19

Continued on next page

Table A.43: Computed rate constants for the H_2O relay catalyzed aminomethanol decomposition from 60 K to 1,000 K.

Temperature (K)	kTST (s-1)	kTST/W (s-1)	kTST/Eck (s-1)
240	2.42e-20	8.04e-20	2.82e-18
250	4.20e-19	1.32e-18	2.41e-17
260	5.83e-18	1.74e-17	1.91e-16
270	6.66e-17	1.89e-16	1.40e-15
280	6.38e-16	1.73e-15	9.35e-15
290	5.23e-15	1.35e-14	5.72e-14
300	3.72e-14	9.25e-14	3.20e-13
310	2.33e-13	5.58e-13	1.64e-12
320	1.30e-12	3.00e-12	7.70e-12
330	6.56e-12	1.46e-11	3.34e-11
340	3.00e-11	6.46e-11	1.35e-10
350	1.26e-10	2.63e-10	5.05e-10
360	4.86e-10	9.87e-10	1.77e-09
370	1.75e-09	3.45e-09	5.84e-09
380	5.87e-09	1.13e-08	1.82e-08
390	1.85e-08	3.48e-08	5.35e-08
400	5.53e-08	1.01e-07	1.50e-07
410	1.56e-07	2.80e-07	4.00e-07
420	4.20e-07	7.39e-07	1.02e-06
430	1.08e-06	1.86e-06	2.50e-06
440	2.66e-06	4.49e-06	5.90e-06
450	6.28e-06	1.04e-05	1.34e-05
460	1.43e-05	2.33e-05	2.94e-05
470	3.14e-05	5.05e-05	6.25e-05
480	6.69e-05	1.06e-04	1.29e-04
490	1.38e-04	2.15e-04	2.58e-04
500	2.77e-04	4.25e-04	5.04e-04

Continued on next page

Table A.43: Computed rate constants for the H_2O relay catalyzed aminomethanol decomposition from 60 K to 1,000 K.

Temperature (K)	kTST (s-1)	kTST/W (s-1)	kTST/Eck (s-1)
510	5.40e-04	8.18e-04	9.59e-04
520	1.03e-03	1.54e-03	1.78e-03
530	1.91e-03	2.81e-03	3.23e-03
540	3.46e-03	5.05e-03	5.75e-03
550	6.15e-03	8.86e-03	1.00e-02
560	1.07e-02	1.53e-02	1.71e-02
570	1.83e-02	2.58e-02	2.87e-02
580	3.06e-02	4.27e-02	4.73e-02
590	5.04e-02	6.97e-02	7.67e-02
600	8.16e-02	1.12e-01	1.22e-01
610	1.30e-01	1.77e-01	1.93e-01
620	2.04e-01	2.76e-01	2.99e-01
630	3.17e-01	4.23e-01	4.57e-01
640	4.84e-01	6.42e-01	6.90e-01
650	7.30e-01	9.61e-01	1.03e+00
660	1.09e+00	1.42e+00	1.52e+00
670	1.60e+00	2.08e+00	2.21e+00
680	2.33e+00	3.01e+00	3.19e+00
690	3.36e+00	4.30e+00	4.55e+00
700	4.79e+00	6.10e+00	6.43e+00
710	6.76e+00	8.56e+00	9.01e+00
720	9.46e+00	1.19e+01	1.25e+01
730	1.31e+01	1.64e+01	1.72e+01
740	1.80e+01	2.24e+01	2.34e+01
750	2.45e+01	3.04e+01	3.17e+01
760	3.32e+01	4.09e+01	4.26e+01
770	4.45e+01	5.45e+01	5.67e+01

Continued on next page

Table A.43: Computed rate constants for the H_2O relay catalyzed aminomethanol decomposition from 60 K to 1,000 K.

Temperature (K)	kTST (s-1)	kTST/W (s-1)	kTST/Eck (s-1)
780	5.93e+01	7.23e+01	7.50e+01
790	7.83e+01	9.51e+01	9.86e+01
800	1.03e+02	1.24e+02	1.29e+02
810	1.34e+02	1.61e+02	1.67e+02
820	1.74e+02	2.08e+02	2.15e+02
830	2.24e+02	2.67e+02	2.76e+02
840	2.87e+02	3.41e+02	3.52e+02
850	3.65e+02	4.33e+02	4.45e+02
860	4.62e+02	5.46e+02	5.61e+02
870	5.82e+02	6.85e+02	7.04e+02
880	7.30e+02	8.56e+02	8.78e+02
890	9.10e+02	1.06e+03	1.09e+03
900	1.13e+03	1.32e+03	1.35e+03
910	1.39e+03	1.62e+03	1.66e+03
920	1.72e+03	1.99e+03	2.03e+03
930	2.10e+03	2.42e+03	2.48e+03
940	2.56e+03	2.95e+03	3.01e+03
950	3.11e+03	3.57e+03	3.65e+03
960	3.76e+03	4.31e+03	4.39e+03
970	4.53e+03	5.17e+03	5.28e+03
980	5.44e+03	6.20e+03	6.32e+03
990	6.51e+03	7.39e+03	7.53e+03
1000	7.75e+03	8.79e+03	8.95e+03

Table A.44: Computed rate constants for the H_2O double relay catalyzed aminomethanol decomposition from 60 K to 1,000 K.

Temperature (K)	kTST (s-1)	kTST/W (s-1)	kTST/Eck (s-1)
60	1.33e-86	2.76e-85	3.91e-56
70	1.12e-72	1.72e-71	8.82e-49
80	3.03e-62	3.65e-61	2.95e-43
90	3.86e-54	3.76e-53	6.23e-39
100	1.16e-47	9.34e-47	1.87e-35
110	2.27e-42	1.55e-41	1.36e-32
120	5.74e-38	3.39e-37	3.69e-30
130	3.02e-34	1.56e-33	4.69e-28
140	4.61e-31	2.12e-30	3.40e-26
150	2.62e-28	1.09e-27	1.67e-24
160	6.70e-26	2.52e-25	6.08e-23
170	8.85e-24	3.05e-23	1.84e-21
180	6.75e-22	2.15e-21	4.72e-20
190	3.24e-20	9.59e-20	1.03e-18
200	1.05e-18	2.91e-18	1.86e-17
210	2.44e-17	6.36e-17	2.79e-16
220	4.24e-16	1.04e-15	3.48e-15
230	5.73e-15	1.34e-14	3.62e-14
240	6.22e-14	1.39e-13	3.19e-13
250	5.56e-13	1.18e-12	2.40e-12
260	4.19e-12	8.57e-12	1.57e-11
270	2.71e-11	5.34e-11	8.99e-11
280	1.53e-10	2.92e-10	4.59e-10
290	7.69e-10	1.42e-09	2.10e-09
300	3.46e-09	6.17e-09	8.74e-09
310	1.41e-08	2.44e-08	3.33e-08
320	5.25e-08	8.88e-08	1.17e-07

Continued on next page

Table A.44: Computed rate constants for the H_2O double relay catalyzed aminomethanol decomposition from 60 K to 1,000 K.

Temperature (K)	kTST (s-1)	kTST/W (s-1)	kTST/Eck (s-1)
330	1.81e-07	2.98e-07	3.80e-07
340	5.77e-07	9.30e-07	1.16e-06
350	1.72e-06	2.72e-06	3.31e-06
360	4.84e-06	7.48e-06	8.94e-06
370	1.29e-05	1.95e-05	2.29e-05
380	3.24e-05	4.83e-05	5.59e-05
390	7.79e-05	1.14e-04	1.30e-04
400	1.79e-04	2.58e-04	2.92e-04
410	3.95e-04	5.61e-04	6.28e-04
420	8.39e-04	1.18e-03	1.30e-03
430	1.72e-03	2.38e-03	2.62e-03
440	3.41e-03	4.66e-03	5.09e-03
450	6.57e-03	8.87e-03	9.61e-03
460	1.23e-02	1.64e-02	1.77e-02
470	2.24e-02	2.95e-02	3.17e-02
480	3.97e-02	5.19e-02	5.54e-02
490	6.89e-02	8.92e-02	9.47e-02
500	1.17e-01	1.50e-01	1.59e-01
510	1.94e-01	2.47e-01	2.60e-01
520	3.16e-01	3.99e-01	4.19e-01
530	5.06e-01	6.33e-01	6.63e-01
540	7.95e-01	9.88e-01	1.03e+00
550	1.23e+00	1.52e+00	1.58e+00
560	1.87e+00	2.29e+00	2.39e+00
570	2.81e+00	3.42e+00	3.55e+00
580	4.15e+00	5.03e+00	5.21e+00
590	6.06e+00	7.29e+00	7.54e+00

Continued on next page

Table A.44: Computed rate constants for the H_2O double relay catalyzed aminomethanol decomposition from 60 K to 1,000 K.

Temperature (K)	kTST (s-1)	kTST/W (s-1)	kTST/Eck (s-1)
600	8.74e+00	1.05e+01	1.08e+01
610	1.25e+01	1.48e+01	1.53e+01
620	1.75e+01	2.08e+01	2.14e+01
630	2.44e+01	2.88e+01	2.96e+01
640	3.37e+01	3.95e+01	4.06e+01
650	4.60e+01	5.37e+01	5.51e+01
660	6.23e+01	7.24e+01	7.41e+01
670	8.35e+01	9.67e+01	9.89e+01
680	1.11e+02	1.28e+02	1.31e+02
690	1.46e+02	1.68e+02	1.72e+02
700	1.92e+02	2.19e+02	2.24e+02
710	2.49e+02	2.84e+02	2.89e+02
720	3.21e+02	3.65e+02	3.72e+02
730	4.11e+02	4.66e+02	4.74e+02
740	5.23e+02	5.91e+02	6.01e+02
750	6.61e+02	7.45e+02	7.57e+02
760	8.31e+02	9.33e+02	9.48e+02
770	1.04e+03	1.16e+03	1.18e+03
780	1.29e+03	1.44e+03	1.46e+03
790	1.59e+03	1.78e+03	1.80e+03
800	1.96e+03	2.18e+03	2.21e+03
810	2.40e+03	2.66e+03	2.69e+03
820	2.92e+03	3.23e+03	3.27e+03
830	3.54e+03	3.90e+03	3.95e+03
840	4.27e+03	4.70e+03	4.76e+03
850	5.13e+03	5.63e+03	5.70e+03
860	6.14e+03	6.73e+03	6.81e+03

Continued on next page

Table A.44: Computed rate constants for the H_2O double relay catalyzed aminomethanol decomposition from 60 K to 1,000 K.

Temperature (K)	kTST (s-1)	kTST/W (s-1)	kTST/Eck (s-1)
870	7.32e+03	8.00e+03	8.09e+03
880	8.68e+03	9.48e+03	9.58e+03
890	1.03e+04	1.12e+04	1.13e+04
900	1.21e+04	1.32e+04	1.33e+04
910	1.42e+04	1.54e+04	1.56e+04
920	1.66e+04	1.80e+04	1.82e+04
930	1.94e+04	2.10e+04	2.12e+04
940	2.25e+04	2.44e+04	2.46e+04
950	2.61e+04	2.82e+04	2.85e+04
960	3.02e+04	3.25e+04	3.28e+04
970	3.48e+04	3.74e+04	3.78e+04
980	4.00e+04	4.30e+04	4.33e+04
990	4.59e+04	4.92e+04	4.96e+04
1000	5.24e+04	5.61e+04	5.66e+04

A.4.8 CH_3OH Catalyzed Reactions

Cartesian Coordinates

Table A.45: Cartesian coordinates for the CH_3OH NH—Cat catalyzed aminomethanol decomposition.

Species	Atom	X	Y	Z
Reactant Complex	C	1.726606	0.127296	0.406908
	N	1.545800	-1.159876	-0.158506
	O	0.998362	1.133727	-0.334159
	H	0.573767	-1.443564	-0.116899
	H	1.859894	-1.190565	-1.118952
	H	1.363369	0.114438	1.435517

Continued on next page

Table A.45: Cartesian coordinates for the CH_3OH NH—Cat catalyzed aminomethanol decomposition.

Species	Atom	X	Y	Z
Reactant Complex	H	2.785859	0.388148	0.396360
	H	1.203364	2.002395	0.023181
	H	-0.761224	0.371036	-0.154104
	C	-2.697510	0.051568	-0.019015
	H	-2.941254	0.246165	-1.066592
	H	-3.319210	-0.769966	0.330406
	H	-2.941053	0.939992	0.569621
	O	-1.350698	-0.335244	0.144614
Transition State	C	1.789915	-0.502951	0.607285
	N	1.465366	-0.689566	-0.608359
	O	0.546041	1.500512	-0.053260
	H	0.722997	-1.351564	-0.818808
	H	1.495233	0.159154	-1.185245
	H	1.474752	-1.218086	1.355330
	H	2.383188	0.359918	0.862250
	H	0.213125	2.393211	0.046155
	H	-0.498790	0.437104	0.009157
	C	-2.409709	-0.168677	0.068146
	H	-2.733642	0.444183	-0.780239
	H	-2.972842	-1.102765	0.042544
	H	-2.679591	0.361394	0.988114
	O	-1.038944	-0.453739	0.014093
Product Complex	C	1.802487	-1.202075	-0.051354
	N	2.310638	-0.061424	0.145938
	O	0.215359	1.805345	0.046287
	H	3.313080	-0.107621	0.316866
	H	1.052245	1.297389	0.105697

Continued on next page

Table A.45: Cartesian coordinates for the CH_3OH NH—Cat catalyzed aminomethanol decomposition.

Species	Atom	X	Y	Z
Product Complex	H	2.386578	-2.123406	-0.038309
	H	0.732628	-1.278476	-0.238412
	H	0.344338	2.453773	-0.648037
	H	-0.932267	0.409163	-0.261200
	C	-2.628102	-0.422475	0.246189
	H	-3.295390	0.307874	-0.219768
	H	-3.075953	-1.408954	0.139763
	H	-2.550807	-0.191936	1.312193
	O	-1.364762	-0.452912	-0.378708

Table A.46: Cartesian coordinates for the CH_3OH OH—Cat catalyzed aminomethanol decomposition.

Species	Atom	X	Y	Z
Reactant Complex	C	-1.363516	-0.137797	0.539618
	N	-1.148349	-1.187174	-0.424858
	O	-1.409850	1.172062	0.007791
	H	-1.913959	-1.211620	-1.087029
	H	-0.304245	-0.996766	-0.953496
	H	-2.322164	-0.301495	1.027445
	H	-0.577241	-0.201482	1.296256
	H	-0.518046	1.366046	-0.300574
	C	2.096974	-0.388122	0.406641
	O	1.464050	0.521705	-0.486072
	H	2.342143	0.090892	1.355964
	H	3.002183	-0.809889	-0.032147
	H	2.103891	1.175643	-0.774575
	H	1.391535	-1.195737	0.590858

Continued on next page

Table A.46: Cartesian coordinates for the CH_3OH OH—Cat catalyzed aminomethanol decomposition.

Species	Atom	X	Y	Z
Transition State	C	1.427311	0.014464	0.660972
	N	1.576574	1.012068	-0.266675
	O	0.898990	-1.149846	-0.402619
	H	2.553371	1.105866	-0.523282
	H	1.076593	-0.155121	-0.954721
	H	2.289342	-0.448106	1.137538
	H	0.566692	0.083561	1.326728
	H	-0.064770	-1.251890	-0.270342
	C	-1.852471	0.816048	-0.071558
	O	-1.737440	-0.595146	0.119659
	H	-2.265987	1.295401	0.816567
	H	-2.478587	1.044003	-0.934750
	H	-2.605560	-0.981118	0.246648
	H	-0.848552	1.199796	-0.250466
Product Complex	C	1.742022	-0.910862	-0.439319
	N	2.021435	-0.064977	0.455186
	O	-0.061261	1.980901	-0.127646
	H	2.922873	-0.253928	0.890443
	H	0.694443	1.491357	0.226348
	H	2.390654	-1.746028	-0.709046
	H	0.799666	-0.815490	-0.976979
	H	-0.590371	1.309142	-0.570279
	C	-1.694244	-0.598043	0.757824
	O	-1.576251	-0.496927	-0.658287
	H	-2.174680	-1.533624	1.048482
	H	-2.243752	0.247666	1.172490
	H	-2.452166	-0.489145	-1.049225

Continued on next page

Table A.46: Cartesian coordinates for the CH_3OH OH—Cat catalyzed aminomethanol decomposition.

Species	Atom	X	Y	Z
Product Complex	H	-0.683279	-0.573466	1.157906

Table A.47: Cartesian coordinates for the CH_3OH dual hydrogen bond catalyzed aminomethanol decomposition.

Species	Atom	X	Y	Z
Reactant Complex	C	1.726606	0.127296	0.406908
	N	1.545800	-1.159876	-0.158506
	O	0.998362	1.133727	-0.334159
	H	0.573767	-1.443564	-0.116899
	H	1.859894	-1.190565	-1.118952
	H	1.363369	0.114438	1.435517
	H	2.785859	0.388148	0.396360
	H	1.203364	2.002395	0.023181
	H	-0.761224	0.371036	-0.154104
	C	-2.697510	0.051568	-0.019015
	H	-2.941254	0.246165	-1.066592
	H	-3.319210	-0.769966	0.330406
	H	-2.941053	0.939992	0.569621
	O	-1.350698	-0.335244	0.144614
Transition State	C	-1.558199	-0.211024	0.624447
	N	-1.149762	-1.108723	-0.341235
	O	-1.351780	1.141639	-0.279876
	H	-1.933982	-1.628586	-0.714759
	H	-1.141335	0.231389	-0.932784
	H	-2.603305	-0.162264	0.921305
	H	-0.873974	-0.025556	1.450424
	H	-0.456275	1.461168	-0.065532

Continued on next page

Table A.47: Cartesian coordinates for the CH_3OH dual hydrogen bond catalyzed aminomethanol decomposition.

Species	Atom	X	Y	Z
Transition State	O	1.239311	0.221444	-0.019892
	H	0.705829	-0.565769	-0.244188
	C	2.609549	-0.108007	0.061006
	H	2.990756	-0.478703	-0.893109
	H	3.153984	0.797397	0.320809
	H	2.798287	-0.858494	0.831903
Product Complex	C	1.802487	-1.202075	-0.051354
	N	2.310638	-0.061424	0.145938
	O	0.215359	1.805345	0.046287
	H	3.313080	-0.107621	0.316866
	H	1.052245	1.297389	0.105697
	H	2.386578	-2.123406	-0.038309
	H	0.732628	-1.278476	-0.238412
	H	0.344338	2.453773	-0.648037
	H	-0.932267	0.409163	-0.261200
	C	-2.628102	-0.422475	0.246189
	H	-3.295390	0.307874	-0.219768
	H	-3.075953	-1.408954	0.139763
	H	-2.550807	-0.191936	1.312193
	O	-1.364762	-0.452912	-0.378708

Table A.48: Cartesian coordinates for the CH_3OH cluster catalyzed aminomethanol decomposition.

Species	Atom	X	Y	Z
Reactant Complex	C	-1.504251	-1.485447	-0.048539
	N	-2.512820	-0.705321	-0.689845
	O	-0.877997	-0.788606	1.040241

Continued on next page

Table A.48: Cartesian coordinates for the CH_3OH cluster catalyzed aminomethanol decomposition.

Species	Atom	X	Y	Z
Reactant Complex	H	-3.245145	-0.443592	-0.043607
	H	-2.124081	0.133204	-1.102981
	H	-1.960277	-2.396354	0.340189
	H	-0.740090	-1.749364	-0.780310
	H	0.056949	-1.040784	1.058297
	O	-0.044733	1.461463	-0.296411
	H	-0.494253	0.862029	0.326610
	C	-0.133064	2.797977	0.158541
	H	-1.171958	3.125988	0.233957
	H	0.348728	2.927107	1.130230
	H	0.375004	3.427992	-0.568033
	C	3.073625	-0.845980	-0.252702
	O	1.700805	-0.694265	0.045027
	H	3.260293	-0.783659	-1.326863
	H	3.377354	-1.831140	0.093627
	H	1.382283	0.174375	-0.244772
	H	3.682467	-0.096582	0.257922
Transition State	C	-1.563814	-1.340713	-0.410856
	N	-2.089471	-0.262859	-0.915559
	O	-0.935235	-0.760819	1.413939
	H	-3.062267	-0.082074	-0.717484
	H	-1.374060	0.566417	-0.860724
	H	-2.197464	-2.147283	-0.068869
	H	-0.531895	-1.556268	-0.655344
	H	-0.085142	-1.198113	1.560638
	O	-0.220789	1.134814	-0.070788
	H	-0.648036	0.147744	1.005906

Continued on next page

Table A.48: Cartesian coordinates for the CH_3OH cluster catalyzed aminomethanol decomposition.

Species	Atom	X	Y	Z
Transition State	C	0.078523	2.484573	0.121528
	H	-0.769803	3.039099	0.541950
	H	0.920642	2.615435	0.811974
	H	0.353629	2.973987	-0.819958
	C	2.870028	-0.649467	-0.357631
	O	1.527595	-0.830936	0.027354
	H	2.954775	-0.351265	-1.406377
	H	3.392737	-1.596157	-0.229367
	H	1.021386	0.014209	-0.093287
	H	3.370801	0.103451	0.257564
Product Complex	C	-2.645857	0.963857	-0.383154
	N	-2.728005	-0.294406	-0.296722
	O	2.487878	-0.821762	-1.236005
	H	-3.688457	-0.627418	-0.347852
	H	-1.102064	-1.106310	-0.210055
	H	-3.515228	1.611906	-0.497830
	H	-1.664364	1.434410	-0.343566
	H	2.291336	0.101919	-1.418941
	O	-0.137365	-1.249652	-0.098816
	H	1.617918	-1.217531	-1.103500
	C	0.128251	-1.588018	1.252697
	H	-0.231618	-2.590666	1.488996
	H	1.208041	-1.559478	1.391459
	H	-0.334414	-0.873315	1.938437
	C	1.570337	1.669999	0.862633
	O	0.691058	1.430491	-0.220720
	H	1.064243	1.562568	1.826479

Continued on next page

Table A.48: Cartesian coordinates for the CH_3OH cluster catalyzed aminomethanol decomposition.

Species	Atom	X	Y	Z
	H	1.929681	2.693428	0.776802
	H	0.444149	0.490910	-0.210005
Product Complex	H	2.427861	0.992782	0.837900

Table A.49: Cartesian coordinates for the CH_3OH relay catalyzed aminomethanol decomposition.

Species	Atom	X	Y	Z
Reactant Complex	C	-1.513867	0.198174	0.518950
	N	-1.551207	-1.130875	0.027769
	O	-0.935423	1.101215	-0.449868
	H	-2.096654	-1.199557	-0.820563
	H	-0.615978	-1.480733	-0.145036
	H	-2.525977	0.534614	0.748017
	H	-0.910148	0.220165	1.428147
	H	-1.038810	2.007994	-0.148061
	O	1.415449	-0.469333	-0.476782
	H	0.758722	0.207742	-0.689545
	C	2.411027	0.107102	0.340075
	H	1.986106	0.571271	1.235456
	H	3.081974	-0.689411	0.654597
	H	2.996042	0.857331	-0.198352
Transition State	C	-1.532584	-0.211825	0.541954
	N	-1.049441	-1.200933	-0.167399
	O	-0.769901	1.364499	-0.263199
	H	-1.603061	-1.428724	-0.982967
	H	0.124760	-0.926473	-0.375707
	H	-2.569430	0.087879	0.454677

Continued on next page

Table A.49: Cartesian coordinates for the CH_3OH relay catalyzed aminomethanol decomposition.

Species	Atom	X	Y	Z
Transition State	H	-1.049963	-0.002705	1.488905
	H	-0.643815	2.110842	0.329784
	O	1.083033	-0.109541	-0.599265
	H	0.233334	0.812069	-0.458059
	C	2.078080	-0.112205	0.393107
	H	1.720670	0.327087	1.334243
	H	2.408920	-1.131397	0.605332
	H	2.946642	0.462463	0.064934
Product Complex	C	-2.078677	0.244636	0.275935
	N	-1.688116	-0.850070	-0.221310
	O	0.636322	2.058985	0.061411
	H	-2.435781	-1.538432	-0.279970
	H	0.120845	-0.797772	-0.664438
	H	-3.105132	0.418038	0.602214
	H	-1.365766	1.060501	0.382676
	H	1.149308	2.733032	-0.386312
	O	1.070851	-0.566296	-0.666864
	H	0.912901	1.205520	-0.321352
	C	1.649771	-1.123764	0.498239
	H	1.178409	-0.735898	1.405444
	H	1.575923	-2.213362	0.498116
	H	2.702159	-0.847885	0.511375

Table A.50: Cartesian coordinates for the CH_3OH double relay catalyzed aminomethanol decomposition.

Species	Atom	X	Y	Z
Reactant Complex	C	2.231979	-0.731846	-0.416050

Continued on next page

Table A.50: Cartesian coordinates for the CH_3OH double relay catalyzed aminomethanol decomposition.

Species	Atom	X	Y	Z
Reactant Complex	N	1.506637	-1.633238	0.391322
	O	2.007041	0.645769	-0.019358
	H	1.737397	-1.549052	1.370859
	H	0.503140	-1.574835	0.250443
	H	3.301748	-0.930795	-0.332883
	H	1.917400	-0.852912	-1.453137
	H	2.590564	1.224455	-0.518020
	O	-1.387646	-0.974215	-0.232900
	H	0.370409	1.186733	0.622938
	O	-0.554627	1.463108	0.736792
	H	-1.258461	-0.112017	0.199590
	C	-2.730371	-1.385431	-0.096557
	H	-2.831387	-2.354044	-0.581896
	H	-3.018985	-1.492923	0.952093
	H	-3.418518	-0.686141	-0.579029
	C	-0.853520	2.384401	-0.296245
	H	-1.890303	2.691417	-0.175833
	H	-0.221117	3.272573	-0.233895
	H	-0.735013	1.930168	-1.283642
Transition State	C	-1.508196	-1.310358	0.612629
	N	-0.469871	-1.915594	0.148597
	O	-2.049285	0.088795	-0.776998
	H	-0.614095	-2.688382	-0.483449
	H	0.516710	-1.368088	0.235884
	H	-2.488394	-1.758920	0.549558
	H	-1.340338	-0.526138	1.337830
	H	-2.813980	0.648496	-0.617208

Continued on next page

Table A.50: Cartesian coordinates for the CH_3OH double relay catalyzed aminomethanol decomposition.

Species	Atom	X	Y	Z
Transition State	O	1.489599	-0.379980	0.382614
	H	-1.148369	0.700920	-0.678848
	O	0.017653	1.324885	-0.417397
	H	0.831421	0.488555	-0.012179
	C	2.674176	-0.509636	-0.363204
	H	3.548815	-0.429666	0.286347
	H	2.721136	-1.479627	-0.870183
	H	2.741173	0.269957	-1.127192
	C	-0.132344	2.368527	0.505227
	H	0.571404	2.263733	1.337939
	H	0.043396	3.340872	0.036516
	H	-1.145333	2.386648	0.931147
Product Complex	C	0.739372	1.872916	0.664883
	N	-0.390862	2.192119	0.199818
	O	2.699774	0.393982	-0.684089
	H	-0.402965	3.139803	-0.169921
	H	-1.431509	0.723195	0.122501
	H	1.607791	2.527688	0.673079
	H	0.876469	0.876286	1.077519
	H	3.277692	0.185594	-1.419477
	O	-1.729601	-0.213245	0.103402
	H	1.977879	-0.261991	-0.715395
	O	0.641912	-1.416100	-0.419289
	H	-0.265466	-1.057561	-0.378004
	C	-3.032940	-0.293229	-0.435265
	H	-3.316329	-1.343057	-0.471946
	H	-3.753602	0.237446	0.190570

Continued on next page

Table A.50: Cartesian coordinates for the CH_3OH double relay catalyzed aminomethanol decomposition.

Species	Atom	X	Y	Z
Product Complex	H	-3.077459	0.113340	-1.448413
	C	0.875777	-2.164858	0.758500
	H	0.483164	-1.653908	1.641013
	H	0.418340	-3.154628	0.697189
	H	1.952097	-2.283106	0.873660

Rate Constants

Table A.51: Computed rate constants for the CH_3OH NH—Cat catalyzed aminomethanol decomposition from 60 K to 1,000 K.

Temperature (K)	kTST (s-1)	kTST/W (s-1)	kTST/Eck (s-1)
60	6.69e-160	2.58e-159	8.93e-155
70	1.93e-135	5.97e-135	8.09e-133
80	4.30e-117	1.12e-116	9.20e-116
90	8.09e-103	1.83e-102	5.45e-102
100	2.14e-91	4.33e-91	8.43e-91
110	4.76e-82	8.79e-82	1.37e-81
120	2.94e-74	5.04e-74	6.89e-74
130	1.16e-67	1.86e-67	2.33e-67
140	5.21e-62	7.95e-62	9.42e-62
150	4.15e-57	6.05e-57	6.90e-57
160	8.10e-53	1.14e-52	1.26e-52
170	4.96e-49	6.72e-49	7.29e-49
180	1.15e-45	1.52e-45	1.62e-45
190	1.19e-42	1.53e-42	1.61e-42
200	6.14e-40	7.72e-40	8.07e-40
210	1.75e-37	2.16e-37	2.24e-37

Continued on next page

Table A.51: Computed rate constants for the CH_3OH NH—Cat catalyzed aminomethanol decomposition from 60 K to 1,000 K.

Temperature (K)	kTST (s-1)	kTST/W (s-1)	kTST/Eck (s-1)
220	3.00e-35	3.63e-35	3.75e-35
230	3.28e-33	3.92e-33	4.02e-33
240	2.43e-31	2.87e-31	2.93e-31
250	1.28e-29	1.49e-29	1.52e-29
260	4.98e-28	5.73e-28	5.83e-28
270	1.48e-26	1.68e-26	1.71e-26
280	3.44e-25	3.89e-25	3.94e-25
290	6.46e-24	7.25e-24	7.33e-24
300	9.98e-23	1.11e-22	1.12e-22
310	1.29e-21	1.43e-21	1.45e-21
320	1.43e-20	1.57e-20	1.59e-20
330	1.37e-19	1.50e-19	1.51e-19
340	1.15e-18	1.25e-18	1.26e-18
350	8.52e-18	9.24e-18	9.29e-18
360	5.67e-17	6.12e-17	6.15e-17
370	3.40e-16	3.66e-16	3.68e-16
380	1.86e-15	1.99e-15	2.00e-15
390	9.33e-15	9.96e-15	1.00e-14
400	4.32e-14	4.59e-14	4.61e-14
410	1.85e-13	1.97e-13	1.97e-13
420	7.44e-13	7.87e-13	7.90e-13
430	2.80e-12	2.95e-12	2.96e-12
440	9.90e-12	1.04e-11	1.05e-11
450	3.32e-11	3.49e-11	3.50e-11
460	1.05e-10	1.11e-10	1.11e-10
470	3.19e-10	3.34e-10	3.35e-10
480	9.23e-10	9.64e-10	9.66e-10

Continued on next page

Table A.51: Computed rate constants for the CH_3OH NH—Cat catalyzed aminomethanol decomposition from 60 K to 1,000 K.

Temperature (K)	kTST (s-1)	kTST/W (s-1)	kTST/Eck (s-1)
490	2.56e-09	2.67e-09	2.67e-09
500	6.80e-09	7.08e-09	7.09e-09
510	1.74e-08	1.81e-08	1.81e-08
520	4.30e-08	4.46e-08	4.47e-08
530	1.03e-07	1.06e-07	1.07e-07
540	2.37e-07	2.46e-07	2.46e-07
550	5.32e-07	5.50e-07	5.51e-07
560	1.16e-06	1.20e-06	1.20e-06
570	2.46e-06	2.54e-06	2.54e-06
580	5.09e-06	5.24e-06	5.24e-06
590	1.03e-05	1.06e-05	1.06e-05
600	2.02e-05	2.08e-05	2.08e-05
610	3.90e-05	4.00e-05	4.01e-05
620	7.36e-05	7.55e-05	7.57e-05
630	1.36e-04	1.40e-04	1.40e-04
640	2.47e-04	2.53e-04	2.53e-04
650	4.40e-04	4.51e-04	4.52e-04
660	7.71e-04	7.89e-04	7.91e-04
670	1.33e-03	1.36e-03	1.36e-03
680	2.25e-03	2.30e-03	2.30e-03
690	3.76e-03	3.84e-03	3.84e-03
700	6.19e-03	6.32e-03	6.34e-03
710	1.00e-02	1.03e-02	1.02e-02
720	1.61e-02	1.64e-02	1.65e-02
730	2.54e-02	2.59e-02	2.59e-02
740	3.97e-02	4.05e-02	4.04e-02
750	6.13e-02	6.25e-02	6.24e-02

Continued on next page

Table A.51: Computed rate constants for the CH_3OH NH—Cat catalyzed aminomethanol decomposition from 60 K to 1,000 K.

Temperature (K)	kTST (s-1)	kTST/W (s-1)	kTST/Eck (s-1)
760	9.36e-02	9.53e-02	9.53e-02
770	1.41e-01	1.44e-01	1.44e-01
780	2.11e-01	2.15e-01	2.15e-01
790	3.12e-01	3.17e-01	3.18e-01
800	4.57e-01	4.64e-01	4.63e-01
810	6.63e-01	6.73e-01	6.72e-01
820	9.53e-01	9.68e-01	9.70e-01
830	1.36e+00	1.38e+00	1.38e+00
840	1.92e+00	1.95e+00	1.94e+00
850	2.69e+00	2.73e+00	2.73e+00
860	3.75e+00	3.80e+00	3.81e+00
870	5.17e+00	5.24e+00	5.24e+00
880	7.09e+00	7.18e+00	7.16e+00
890	9.65e+00	9.77e+00	9.82e+00
900	1.30e+01	1.32e+01	1.32e+01
910	1.75e+01	1.77e+01	1.77e+01
920	2.34e+01	2.37e+01	2.38e+01
930	3.10e+01	3.14e+01	3.12e+01
940	4.09e+01	4.13e+01	4.16e+01
950	5.36e+01	5.42e+01	5.40e+01
960	6.98e+01	7.06e+01	7.08e+01
970	9.05e+01	9.15e+01	9.16e+01
980	1.17e+02	1.18e+02	1.18e+02
990	1.50e+02	1.51e+02	1.52e+02
1000	1.91e+02	1.93e+02	1.93e+02

Table A.52: Computed rate constants for the CH_3OH OH—Cat catalyzed aminomethanol decomposition from 60 K to 1,000 K.

Temperature (K)	kTST (s-1)	kTST/W (s-1)	kTST/Eck (s-1)
60	1.52e-182	9.19e-181	2.17e-115
70	8.60e-155	3.84e-153	1.79e-99
80	5.67e-134	1.95e-132	1.65e-87
90	8.91e-118	2.44e-116	3.25e-78
100	8.13e-105	1.82e-103	8.16e-71
110	3.28e-94	6.12e-93	1.11e-64
120	2.27e-85	3.60e-84	1.43e-59
130	6.89e-78	9.41e-77	3.05e-55
140	1.79e-71	2.13e-70	1.33e-51
150	6.50e-66	6.83e-65	2.65e-48
160	4.78e-61	4.46e-60	1.79e-45
170	9.41e-57	7.90e-56	5.19e-43
180	6.18e-53	4.70e-52	8.89e-41
190	1.61e-49	1.12e-48	9.72e-39
200	1.92e-46	1.22e-45	6.03e-37
210	1.16e-43	6.81e-43	2.75e-35
220	3.95e-41	2.14e-40	8.68e-34
230	8.07e-39	4.07e-38	2.29e-32
240	1.06e-36	4.99e-36	4.38e-31
250	9.44e-35	4.17e-34	7.59e-30
260	5.95e-33	2.48e-32	1.06e-28
270	2.76e-31	1.09e-30	1.31e-27
280	9.75e-30	3.63e-29	1.46e-26
290	2.69e-28	9.54e-28	1.48e-25
300	5.97e-27	2.01e-26	1.40e-24
310	1.08e-25	3.49e-25	1.25e-23
320	1.64e-24	5.07e-24	1.05e-22

Continued on next page

Table A.52: Computed rate constants for the CH_3OH OH—Cat catalyzed aminomethanol decomposition from 60 K to 1,000 K.

Temperature (K)	kTST (s-1)	kTST/W (s-1)	kTST/Eck (s-1)
330	2.11e-23	6.25e-23	8.26e-22
340	2.34e-22	6.66e-22	6.10e-21
350	2.26e-21	6.19e-21	4.21e-20
360	1.92e-20	5.09e-20	2.70e-19
370	1.46e-19	3.73e-19	1.62e-18
380	9.94e-19	2.47e-18	9.02e-18
390	6.15e-18	1.48e-17	4.69e-17
400	3.47e-17	8.11e-17	2.28e-16
410	1.80e-16	4.10e-16	1.04e-15
420	8.66e-16	1.92e-15	4.42e-15
430	3.87e-15	8.34e-15	1.78e-14
440	1.61e-14	3.40e-14	6.78e-14
450	6.33e-14	1.30e-13	2.44e-13
460	2.34e-13	4.70e-13	8.36e-13
470	8.17e-13	1.61e-12	2.73e-12
480	2.71e-12	5.22e-12	8.50e-12
490	8.56e-12	1.62e-11	2.54e-11
500	2.59e-11	4.80e-11	7.27e-11
510	7.48e-11	1.36e-10	2.00e-10
520	2.08e-10	3.72e-10	5.31e-10
530	5.55e-10	9.77e-10	1.36e-09
540	1.43e-09	2.48e-09	3.38e-09
550	3.56e-09	6.08e-09	8.11e-09
560	8.59e-09	1.44e-08	1.89e-08
570	2.01e-08	3.33e-08	4.29e-08
580	4.56e-08	7.46e-08	9.45e-08
590	1.01e-07	1.63e-07	2.03e-07

Continued on next page

Table A.52: Computed rate constants for the CH_3OH OH—Cat catalyzed aminomethanol decomposition from 60 K to 1,000 K.

Temperature (K)	kTST (s-1)	kTST/W (s-1)	kTST/Eck (s-1)
600	2.17e-07	3.46e-07	4.26e-07
610	4.55e-07	7.17e-07	8.73e-07
620	9.34e-07	1.45e-06	1.75e-06
630	1.87e-06	2.88e-06	3.43e-06
640	3.67e-06	5.59e-06	6.59e-06
650	7.05e-06	1.06e-05	1.24e-05
660	1.33e-05	1.98e-05	2.30e-05
670	2.46e-05	3.63e-05	4.17e-05
680	4.46e-05	6.53e-05	7.45e-05
690	7.97e-05	1.15e-04	1.31e-04
700	1.40e-04	2.01e-04	2.26e-04
710	2.42e-04	3.45e-04	3.86e-04
720	4.12e-04	5.82e-04	6.48e-04
730	6.92e-04	9.69e-04	1.07e-03
740	1.15e-03	1.59e-03	1.76e-03
750	1.87e-03	2.58e-03	2.83e-03
760	3.02e-03	4.14e-03	4.52e-03
770	4.81e-03	6.54e-03	7.12e-03
780	7.57e-03	1.02e-02	1.11e-02
790	1.18e-02	1.58e-02	1.71e-02
800	1.81e-02	2.42e-02	2.61e-02
810	2.76e-02	3.67e-02	3.94e-02
820	4.17e-02	5.49e-02	5.88e-02
830	6.23e-02	8.16e-02	8.71e-02
840	9.21e-02	1.20e-01	1.28e-01
850	1.35e-01	1.75e-01	1.86e-01
860	1.96e-01	2.53e-01	2.68e-01

Continued on next page

Table A.52: Computed rate constants for the CH_3OH OH—Cat catalyzed aminomethanol decomposition from 60 K to 1,000 K.

Temperature (K)	kTST (s-1)	kTST/W (s-1)	kTST/Eck (s-1)
870	2.83e-01	3.63e-01	3.83e-01
880	4.04e-01	5.16e-01	5.44e-01
890	5.73e-01	7.27e-01	7.66e-01
900	8.06e-01	1.02e+00	1.07e+00
910	1.13e+00	1.42e+00	1.49e+00
920	1.56e+00	1.95e+00	2.05e+00
930	2.15e+00	2.68e+00	2.80e+00
940	2.94e+00	3.65e+00	3.81e+00
950	3.99e+00	4.94e+00	5.15e+00
960	5.39e+00	6.64e+00	6.91e+00
970	7.24e+00	8.88e+00	9.23e+00
980	9.65e+00	1.18e+01	1.23e+01
990	1.28e+01	1.56e+01	1.62e+01
1000	1.69e+01	2.05e+01	2.12e+01

Table A.53: Computed rate constants for the CH_3OH dual hydrogen bond catalyzed aminomethanol decomposition from 60 K to 1,000 K.

Temperature (K)	kTST (s-1)	kTST/W (s-1)	kTST/Eck (s-1)
60	2.20e-184	1.15e-182	6.02e-121
70	2.25e-156	8.73e-155	2.88e-104
80	2.33e-135	6.95e-134	9.54e-92
90	5.18e-119	1.23e-117	5.06e-82
100	6.24e-106	1.22e-104	3.35e-74
110	3.16e-95	5.14e-94	8.25e-68
120	2.65e-86	3.66e-85	1.60e-62
130	9.42e-79	1.12e-77	5.74e-58
140	2.80e-72	2.92e-71	4.05e-54

Continued on next page

Table A.53: Computed rate constants for the CH_3OH dual hydrogen bond catalyzed aminomethanol decomposition from 60 K to 1,000 K.

Temperature (K)	kTST (s-1)	kTST/W (s-1)	kTST/Eck (s-1)
150	1.15e-66	1.06e-65	1.07e-50
160	9.35e-62	7.68e-61	1.01e-47
170	2.02e-57	1.49e-56	3.87e-45
180	1.44e-53	9.66e-53	8.50e-43
190	4.05e-50	2.48e-49	1.09e-40
200	5.15e-47	2.89e-46	8.60e-39
210	3.32e-44	1.72e-43	4.91e-37
220	1.19e-41	5.73e-41	2.01e-35
230	2.56e-39	1.15e-38	6.14e-34
240	3.53e-37	1.48e-36	1.48e-32
250	3.28e-35	1.30e-34	2.95e-31
260	2.15e-33	8.04e-33	5.10e-30
270	1.04e-31	3.67e-31	7.77e-29
280	3.80e-30	1.28e-29	1.07e-27
290	1.09e-28	3.47e-28	1.37e-26
300	2.48e-27	7.58e-27	1.61e-25
310	4.65e-26	1.36e-25	1.76e-24
320	7.24e-25	2.03e-24	1.78e-23
330	9.57e-24	2.58e-23	1.65e-22
340	1.09e-22	2.82e-22	1.40e-21
350	1.07e-21	2.69e-21	1.08e-20
360	9.36e-21	2.27e-20	7.69e-20
370	7.26e-20	1.70e-19	5.01e-19
380	5.05e-19	1.15e-18	3.00e-18
390	3.19e-18	7.06e-18	1.66e-17
400	1.84e-17	3.96e-17	8.54e-17
410	9.71e-17	2.04e-16	4.08e-16

Continued on next page

Table A.53: Computed rate constants for the CH_3OH dual hydrogen bond catalyzed aminomethanol decomposition from 60 K to 1,000 K.

Temperature (K)	kTST (s-1)	kTST/W (s-1)	kTST/Eck (s-1)
420	4.75e-16	9.72e-16	1.82e-15
430	2.16e-15	4.31e-15	7.64e-15
440	9.15e-15	1.79e-14	3.01e-14
450	3.64e-14	6.96e-14	1.12e-13
460	1.36e-13	2.56e-13	3.96e-13
470	4.84e-13	8.88e-13	1.33e-12
480	1.63e-12	2.93e-12	4.25e-12
490	5.21e-12	9.23e-12	1.30e-11
500	1.59e-11	2.77e-11	3.81e-11
510	4.67e-11	7.99e-11	1.07e-10
520	1.31e-10	2.21e-10	2.90e-10
530	3.55e-10	5.88e-10	7.59e-10
540	9.25e-10	1.51e-09	1.92e-09
550	2.33e-09	3.75e-09	4.68e-09
560	5.68e-09	9.02e-09	1.11e-08
570	1.34e-08	2.10e-08	2.55e-08
580	3.08e-08	4.77e-08	5.72e-08
590	6.87e-08	1.05e-07	1.25e-07
600	1.49e-07	2.26e-07	2.65e-07
610	3.16e-07	4.73e-07	5.50e-07
620	6.54e-07	9.68e-07	1.12e-06
630	1.32e-06	1.94e-06	2.21e-06
640	2.61e-06	3.79e-06	4.30e-06
650	5.06e-06	7.28e-06	8.20e-06
660	9.62e-06	1.37e-05	1.53e-05
670	1.79e-05	2.53e-05	2.82e-05
680	3.28e-05	4.59e-05	5.08e-05

Continued on next page

Table A.53: Computed rate constants for the CH_3OH dual hydrogen bond catalyzed aminomethanol decomposition from 60 K to 1,000 K.

Temperature (K)	kTST (s-1)	kTST/W (s-1)	kTST/Eck (s-1)
690	5.90e-05	8.19e-05	9.02e-05
700	1.04e-04	1.44e-04	1.57e-04
710	1.82e-04	2.48e-04	2.71e-04
720	3.11e-04	4.22e-04	4.59e-04
730	5.26e-04	7.09e-04	7.67e-04
740	8.77e-04	1.17e-03	1.26e-03
750	1.44e-03	1.91e-03	2.06e-03
760	2.34e-03	3.09e-03	3.31e-03
770	3.75e-03	4.92e-03	5.25e-03
780	5.94e-03	7.74e-03	8.24e-03
790	9.29e-03	1.20e-02	1.28e-02
800	1.44e-02	1.85e-02	1.96e-02
810	2.20e-02	2.82e-02	2.98e-02
820	3.34e-02	4.26e-02	4.49e-02
830	5.01e-02	6.36e-02	6.69e-02
840	7.46e-02	9.41e-02	9.88e-02
850	1.10e-01	1.38e-01	1.45e-01
860	1.60e-01	2.00e-01	2.10e-01
870	2.32e-01	2.89e-01	3.02e-01
880	3.33e-01	4.13e-01	4.30e-01
890	4.75e-01	5.85e-01	6.09e-01
900	6.71e-01	8.24e-01	8.56e-01
910	9.41e-01	1.15e+00	1.19e+00
920	1.31e+00	1.60e+00	1.65e+00
930	1.81e+00	2.20e+00	2.28e+00
940	2.49e+00	3.01e+00	3.11e+00
950	3.39e+00	4.09e+00	4.22e+00

Continued on next page

Table A.53: Computed rate constants for the CH_3OH dual hydrogen bond catalyzed aminomethanol decomposition from 60 K to 1,000 K.

Temperature (K)	kTST (s-1)	kTST/W (s-1)	kTST/Eck (s-1)
960	4.60e+00	5.52e+00	5.70e+00
970	6.20e+00	7.41e+00	7.64e+00
980	8.30e+00	9.89e+00	1.02e+01
990	1.10e+01	1.31e+01	1.35e+01
1000	1.46e+01	1.73e+01	1.78e+01

Table A.54: Computed rate constants for the CH_3OH cluster catalyzed aminomethanol decomposition from 60 K to 1,000 K.

Temperature (K)	kTST (s-1)	kTST/W (s-1)	kTST/Eck (s-1)
60	8.43e-106	4.52e-105	7.19e-97
70	3.69e-89	1.55e-88	1.54e-83
80	1.10e-76	3.81e-76	2.38e-73
90	5.52e-67	1.62e-66	4.27e-65
100	3.15e-59	8.11e-59	4.72e-58
110	6.96e-53	1.60e-52	4.72e-52
120	1.34e-47	2.81e-47	5.81e-47
130	3.97e-43	7.65e-43	1.29e-42
140	2.69e-39	4.84e-39	7.11e-39
150	5.61e-36	9.53e-36	1.28e-35
160	4.50e-33	7.26e-33	9.12e-33
170	1.64e-30	2.53e-30	3.03e-30
180	3.10e-28	4.61e-28	5.33e-28
190	3.38e-26	4.85e-26	5.46e-26
200	2.30e-24	3.20e-24	3.54e-24
210	1.05e-22	1.42e-22	1.54e-22
220	3.37e-21	4.47e-21	4.78e-21
230	8.02e-20	1.04e-19	1.10e-19

Continued on next page

Table A.54: Computed rate constants for the CH_3OH cluster catalyzed aminomethanol decomposition from 60 K to 1,000 K.

Temperature (K)	kTST (s-1)	kTST/W (s-1)	kTST/Eck (s-1)
240	1.46e-18	1.86e-18	1.96e-18
250	2.12e-17	2.65e-17	2.77e-17
260	2.50e-16	3.08e-16	3.20e-16
270	2.45e-15	2.98e-15	3.08e-15
280	2.04e-14	2.45e-14	2.53e-14
290	1.47e-13	1.75e-13	1.79e-13
300	9.29e-13	1.09e-12	1.12e-12
310	5.21e-12	6.06e-12	6.19e-12
320	2.62e-11	3.02e-11	3.08e-11
330	1.20e-10	1.37e-10	1.39e-10
340	4.99e-10	5.67e-10	5.76e-10
350	1.92e-09	2.17e-09	2.20e-09
360	6.85e-09	7.69e-09	7.78e-09
370	2.28e-08	2.55e-08	2.57e-08
380	7.14e-08	7.92e-08	8.00e-08
390	2.11e-07	2.32e-07	2.35e-07
400	5.89e-07	6.46e-07	6.52e-07
410	1.56e-06	1.71e-06	1.72e-06
420	3.97e-06	4.32e-06	4.35e-06
430	9.64e-06	1.05e-05	1.05e-05
440	2.25e-05	2.43e-05	2.45e-05
450	5.05e-05	5.44e-05	5.48e-05
460	1.10e-04	1.18e-04	1.18e-04
470	2.30e-04	2.46e-04	2.48e-04
480	4.68e-04	5.00e-04	5.03e-04
490	9.25e-04	9.86e-04	9.91e-04
500	1.78e-03	1.89e-03	1.90e-03

Continued on next page

Table A.54: Computed rate constants for the CH_3OH cluster catalyzed aminomethanol decomposition from 60 K to 1,000 K.

Temperature (K)	kTST (s-1)	kTST/W (s-1)	kTST/Eck (s-1)
510	3.34e-03	3.54e-03	3.55e-03
520	6.11e-03	6.46e-03	6.49e-03
530	1.09e-02	1.15e-02	1.16e-02
540	1.91e-02	2.02e-02	2.02e-02
550	3.28e-02	3.45e-02	3.46e-02
560	5.52e-02	5.80e-02	5.82e-02
570	9.12e-02	9.57e-02	9.60e-02
580	1.48e-01	1.55e-01	1.56e-01
590	2.37e-01	2.47e-01	2.48e-01
600	3.72e-01	3.89e-01	3.90e-01
610	5.77e-01	6.02e-01	6.03e-01
620	8.82e-01	9.18e-01	9.20e-01
630	1.33e+00	1.38e+00	1.39e+00
640	1.98e+00	2.06e+00	2.06e+00
650	2.91e+00	3.02e+00	3.03e+00
660	4.23e+00	4.38e+00	4.39e+00
670	6.08e+00	6.29e+00	6.31e+00
680	8.65e+00	8.94e+00	8.96e+00
690	1.22e+01	1.26e+01	1.26e+01
700	1.70e+01	1.75e+01	1.76e+01
710	2.34e+01	2.42e+01	2.42e+01
720	3.21e+01	3.31e+01	3.31e+01
730	4.36e+01	4.48e+01	4.49e+01
740	5.86e+01	6.03e+01	6.05e+01
750	7.83e+01	8.05e+01	8.06e+01
760	1.04e+02	1.07e+02	1.07e+02
770	1.37e+02	1.40e+02	1.40e+02

Continued on next page

Table A.54: Computed rate constants for the CH_3OH cluster catalyzed aminomethanol decomposition from 60 K to 1,000 K.

Temperature (K)	kTST (s-1)	kTST/W (s-1)	kTST/Eck (s-1)
780	1.79e+02	1.83e+02	1.84e+02
790	2.32e+02	2.38e+02	2.38e+02
800	2.99e+02	3.06e+02	3.07e+02
810	3.83e+02	3.92e+02	3.92e+02
820	4.88e+02	4.99e+02	5.00e+02
830	6.18e+02	6.32e+02	6.33e+02
840	7.78e+02	7.96e+02	7.96e+02
850	9.75e+02	9.96e+02	9.97e+02
860	1.22e+03	1.24e+03	1.24e+03
870	1.51e+03	1.54e+03	1.54e+03
880	1.86e+03	1.90e+03	1.90e+03
890	2.28e+03	2.33e+03	2.33e+03
900	2.79e+03	2.85e+03	2.85e+03
910	3.40e+03	3.47e+03	3.46e+03
920	4.12e+03	4.20e+03	4.22e+03
930	4.98e+03	5.07e+03	5.09e+03
940	5.99e+03	6.09e+03	6.10e+03
950	7.17e+03	7.30e+03	7.30e+03
960	8.56e+03	8.71e+03	8.74e+03
970	1.02e+04	1.04e+04	1.03e+04
980	1.21e+04	1.23e+04	1.23e+04
990	1.43e+04	1.45e+04	1.45e+04
1000	1.68e+04	1.70e+04	1.70e+04

Table A.55: Computed rate constants for the CH_3OH relay catalyzed aminomethanol decomposition from 60 K to 1,000 K.

Temperature (K)	kTST (s-1)	kTST/W (s-1)	kTST/Eck (s-1)
60	1.29e-109	6.27e-108	1.29e-55
70	2.12e-92	7.65e-91	1.82e-48
80	1.71e-79	4.77e-78	5.10e-43
90	1.85e-69	4.12e-68	9.95e-39
100	1.96e-61	3.56e-60	2.13e-35
110	7.13e-55	1.09e-53	1.58e-32
120	2.08e-49	2.70e-48	2.93e-30
130	8.73e-45	9.76e-44	2.89e-28
140	7.96e-41	7.79e-40	1.60e-26
150	2.15e-37	1.86e-36	4.44e-25
160	2.15e-34	1.66e-33	9.96e-24
170	9.52e-32	6.62e-31	1.58e-22
180	2.14e-29	1.35e-28	1.84e-21
190	2.71e-27	1.56e-26	1.80e-20
200	2.12e-25	1.12e-24	1.53e-19
210	1.09e-23	5.34e-23	1.11e-18
220	3.92e-22	1.78e-21	7.45e-18
230	1.03e-20	4.38e-20	4.64e-17
240	2.06e-19	8.22e-19	2.74e-16
250	3.25e-18	1.22e-17	1.54e-15
260	4.13e-17	1.47e-16	8.32e-15
270	4.36e-16	1.46e-15	4.33e-14
280	3.88e-15	1.24e-14	2.15e-13
290	2.97e-14	9.06e-14	1.02e-12
300	1.99e-13	5.79e-13	4.60e-12
310	1.18e-12	3.28e-12	1.96e-11
320	6.23e-12	1.67e-11	7.88e-11

Continued on next page

Table A.55: Computed rate constants for the CH_3OH relay catalyzed aminomethanol decomposition from 60 K to 1,000 K.

Temperature (K)	kTST (s-1)	kTST/W (s-1)	kTST/Eck (s-1)
330	2.98e-11	7.69e-11	2.99e-10
340	1.30e-10	3.24e-10	1.07e-09
350	5.22e-10	1.26e-09	3.62e-09
360	1.94e-09	4.51e-09	1.16e-08
370	6.71e-09	1.51e-08	3.52e-08
380	2.18e-08	4.77e-08	1.02e-07
390	6.64e-08	1.42e-07	2.81e-07
400	1.92e-07	3.98e-07	7.40e-07
410	5.26e-07	1.06e-06	1.87e-06
420	1.37e-06	2.72e-06	4.54e-06
430	3.44e-06	6.64e-06	1.06e-05
440	8.25e-06	1.56e-05	2.40e-05
450	1.90e-05	3.52e-05	5.23e-05
460	4.24e-05	7.68e-05	1.11e-04
470	9.11e-05	1.62e-04	2.27e-04
480	1.90e-04	3.32e-04	4.53e-04
490	3.84e-04	6.60e-04	8.80e-04
500	7.56e-04	1.28e-03	1.67e-03
510	1.45e-03	2.41e-03	3.09e-03
520	2.71e-03	4.43e-03	5.59e-03
530	4.94e-03	7.97e-03	9.90e-03
540	8.83e-03	1.40e-02	1.72e-02
550	1.54e-02	2.42e-02	2.93e-02
560	2.65e-02	4.10e-02	4.90e-02
570	4.45e-02	6.81e-02	8.06e-02
580	7.36e-02	1.11e-01	1.30e-01
590	1.20e-01	1.79e-01	2.07e-01

Continued on next page

Table A.55: Computed rate constants for the CH_3OH relay catalyzed aminomethanol decomposition from 60 K to 1,000 K.

Temperature (K)	kTST (s-1)	kTST/W (s-1)	kTST/Eck (s-1)
600	1.92e-01	2.83e-01	3.26e-01
610	3.02e-01	4.41e-01	5.04e-01
620	4.69e-01	6.78e-01	7.68e-01
630	7.18e-01	1.03e+00	1.16e+00
640	1.08e+00	1.54e+00	1.72e+00
650	1.62e+00	2.28e+00	2.53e+00
660	2.39e+00	3.33e+00	3.69e+00
670	3.48e+00	4.82e+00	5.30e+00
680	5.03e+00	6.90e+00	7.55e+00
690	7.17e+00	9.77e+00	1.06e+01
700	1.01e+01	1.37e+01	1.49e+01
710	1.42e+01	1.90e+01	2.06e+01
720	1.97e+01	2.62e+01	2.83e+01
730	2.71e+01	3.58e+01	3.85e+01
740	3.69e+01	4.85e+01	5.19e+01
750	4.99e+01	6.51e+01	6.96e+01
760	6.69e+01	8.69e+01	9.25e+01
770	8.91e+01	1.15e+02	1.22e+02
780	1.18e+02	1.51e+02	1.60e+02
790	1.55e+02	1.97e+02	2.09e+02
800	2.02e+02	2.56e+02	2.70e+02
810	2.62e+02	3.30e+02	3.48e+02
820	3.37e+02	4.23e+02	4.45e+02
830	4.31e+02	5.39e+02	5.65e+02
840	5.49e+02	6.83e+02	7.15e+02
850	6.95e+02	8.61e+02	9.00e+02
860	8.75e+02	1.08e+03	1.13e+03

Continued on next page

Table A.55: Computed rate constants for the CH_3OH relay catalyzed aminomethanol decomposition from 60 K to 1,000 K.

Temperature (K)	kTST (s-1)	kTST/W (s-1)	kTST/Eck (s-1)
870	1.10e+03	1.35e+03	1.40e+03
880	1.37e+03	1.67e+03	1.74e+03
890	1.70e+03	2.06e+03	2.14e+03
900	2.09e+03	2.54e+03	2.63e+03
910	2.57e+03	3.11e+03	3.22e+03
920	3.15e+03	3.79e+03	3.92e+03
930	3.84e+03	4.60e+03	4.76e+03
940	4.66e+03	5.56e+03	5.75e+03
950	5.63e+03	6.70e+03	6.92e+03
960	6.78e+03	8.04e+03	8.29e+03
970	8.13e+03	9.62e+03	9.91e+03
980	9.72e+03	1.15e+04	1.18e+04
990	1.16e+04	1.36e+04	1.40e+04
1000	1.37e+04	1.61e+04	1.66e+04

Table A.56: Computed rate constants for the CH_3OH double relay catalyzed aminomethanol decomposition from 60 K to 1,000 K.

Temperature (K)	kTST (s-1)	kTST/W (s-1)	kTST/Eck (s-1)
60	3.12e-82	5.81e-81	8.40e-54
70	5.33e-69	7.43e-68	7.56e-47
80	4.39e-59	4.80e-58	1.38e-41
90	2.23e-51	1.97e-50	1.72e-37
100	3.22e-45	2.37e-44	3.43e-34
110	3.49e-40	2.18e-39	1.85e-31
120	5.44e-36	2.94e-35	3.81e-29
130	1.91e-32	9.06e-32	3.88e-27
140	2.07e-29	8.77e-29	2.55e-25

Continued on next page

Table A.56: Computed rate constants for the CH_3OH double relay catalyzed aminomethanol decomposition from 60 K to 1,000 K.

Temperature (K)	kTST (s-1)	kTST/W (s-1)	kTST/Eck (s-1)
150	8.81e-27	3.36e-26	1.20e-23
160	1.75e-24	6.10e-24	4.57e-22
170	1.86e-22	5.96e-22	1.44e-20
180	1.18e-20	3.49e-20	3.83e-19
190	4.80e-19	1.33e-18	8.40e-18
200	1.35e-17	3.49e-17	1.50e-16
210	2.75e-16	6.72e-16	2.17e-15
220	4.27e-15	9.87e-15	2.58e-14
230	5.21e-14	1.15e-13	2.55e-13
240	5.16e-13	1.08e-12	2.12e-12
250	4.24e-12	8.55e-12	1.51e-11
260	2.97e-11	5.76e-11	9.40e-11
270	1.80e-10	3.36e-10	5.14e-10
280	9.56e-10	1.73e-09	2.50e-09
290	4.53e-09	7.95e-09	1.10e-08
300	1.93e-08	3.30e-08	4.39e-08
310	7.52e-08	1.25e-07	1.61e-07
320	2.68e-07	4.35e-07	5.44e-07
330	8.87e-07	1.40e-06	1.72e-06
340	2.73e-06	4.23e-06	5.06e-06
350	7.89e-06	1.20e-05	1.41e-05
360	2.15e-05	3.20e-05	3.70e-05
370	5.53e-05	8.10e-05	9.25e-05
380	1.36e-04	1.95e-04	2.20e-04
390	3.18e-04	4.50e-04	5.03e-04
400	7.13e-04	9.96e-04	1.10e-03
410	1.54e-03	2.12e-03	2.32e-03

Continued on next page

Table A.56: Computed rate constants for the CH_3OH double relay catalyzed aminomethanol decomposition from 60 K to 1,000 K.

Temperature (K)	kTST (s-1)	kTST/W (s-1)	kTST/Eck (s-1)
420	3.20e-03	4.35e-03	4.74e-03
430	6.43e-03	8.64e-03	9.34e-03
440	1.25e-02	1.66e-02	1.79e-02
450	2.37e-02	3.11e-02	3.32e-02
460	4.35e-02	5.66e-02	6.02e-02
470	7.80e-02	1.00e-01	1.06e-01
480	1.36e-01	1.74e-01	1.84e-01
490	2.33e-01	2.95e-01	3.10e-01
500	3.90e-01	4.89e-01	5.13e-01
510	6.40e-01	7.96e-01	8.32e-01
520	1.03e+00	1.27e+00	1.33e+00
530	1.63e+00	2.00e+00	2.08e+00
540	2.53e+00	3.08e+00	3.20e+00
550	3.87e+00	4.68e+00	4.85e+00
560	5.83e+00	7.01e+00	7.25e+00
570	8.67e+00	1.04e+01	1.07e+01
580	1.27e+01	1.51e+01	1.56e+01
590	1.84e+01	2.17e+01	2.23e+01
600	2.63e+01	3.09e+01	3.17e+01
610	3.71e+01	4.34e+01	4.46e+01
620	5.19e+01	6.04e+01	6.19e+01
630	7.17e+01	8.32e+01	8.51e+01
640	9.82e+01	1.13e+02	1.16e+02
650	1.33e+02	1.53e+02	1.56e+02
660	1.79e+02	2.05e+02	2.09e+02
670	2.38e+02	2.72e+02	2.77e+02
680	3.15e+02	3.58e+02	3.65e+02

Continued on next page

Table A.56: Computed rate constants for the CH_3OH double relay catalyzed aminomethanol decomposition from 60 K to 1,000 K.

Temperature (K)	kTST (s-1)	kTST/W (s-1)	kTST/Eck (s-1)
690	4.13e+02	4.68e+02	4.76e+02
700	5.37e+02	6.07e+02	6.17e+02
710	6.94e+02	7.81e+02	7.94e+02
720	8.90e+02	9.99e+02	1.01e+03
730	1.13e+03	1.27e+03	1.29e+03
740	1.44e+03	1.60e+03	1.63e+03
750	1.81e+03	2.01e+03	2.04e+03
760	2.26e+03	2.51e+03	2.54e+03
770	2.81e+03	3.11e+03	3.15e+03
780	3.47e+03	3.84e+03	3.89e+03
790	4.28e+03	4.71e+03	4.77e+03
800	5.23e+03	5.75e+03	5.82e+03
810	6.38e+03	6.99e+03	7.08e+03
820	7.73e+03	8.46e+03	8.56e+03
830	9.34e+03	1.02e+04	1.03e+04
840	1.12e+04	1.22e+04	1.24e+04
850	1.34e+04	1.46e+04	1.48e+04
860	1.60e+04	1.74e+04	1.76e+04
870	1.90e+04	2.06e+04	2.08e+04
880	2.25e+04	2.43e+04	2.46e+04
890	2.65e+04	2.86e+04	2.89e+04
900	3.11e+04	3.36e+04	3.39e+04
910	3.65e+04	3.93e+04	3.96e+04
920	4.25e+04	4.57e+04	4.61e+04
930	4.95e+04	5.31e+04	5.36e+04
940	5.74e+04	6.15e+04	6.20e+04
950	6.63e+04	7.10e+04	7.16e+04

Continued on next page

Table A.56: Computed rate constants for the CH_3OH double relay catalyzed aminomethanol decomposition from 60 K to 1,000 K.

Temperature (K)	kTST (s-1)	kTST/W (s-1)	kTST/Eck (s-1)
960	7.64e+04	8.17e+04	8.24e+04
970	8.79e+04	9.38e+04	9.45e+04
980	1.01e+05	1.07e+05	1.08e+05
990	1.15e+05	1.23e+05	1.24e+05
1000	1.31e+05	1.40e+05	1.41e+05

A.4.9 H_2S Catalyzed Reactions

Cartesian Coordinates

Table A.57: Cartesian coordinates for the H_2S dual hydrogen bond catalyzed aminomethanol decomposition.

Species	Atom	X	Y	Z
Reactant Complex	C	1.641306	-0.113806	0.429674
	N	1.255518	1.123034	-0.243489
	O	1.180152	-1.221997	-0.286318
	H	1.526178	1.931470	0.303814
	H	1.721818	1.185516	-1.141029
	H	2.722419	-0.246291	0.508934
	H	1.221369	-0.080692	1.439960
	H	0.214921	-1.216216	-0.263395
	H	-0.934802	0.786713	-0.156869
	H	-2.304591	-0.147188	-1.177316
	S	-2.015312	0.024016	0.118926
Transition State	C	-1.483460	-0.197143	0.637179
	N	-1.230449	-1.067383	-0.384838
	O	-1.243245	1.201948	-0.277057
	H	-2.094334	-1.444316	-0.758137

Continued on next page

Table A.57: Cartesian coordinates for the H_2S dual hydrogen bond catalyzed aminomethanol decomposition.

Species	Atom	X	Y	Z
Transition State	H	-1.061224	0.245501	-0.909979
	H	-2.486688	-0.065302	1.034972
	H	-0.705989	-0.069737	1.389419
	H	-0.375487	1.572237	-0.048046
	H	0.935365	-0.877422	-0.229762
	H	2.262230	0.199620	-1.166787
	S	1.936624	-0.032602	0.110973
Product Complex	C	2.389523	-0.514965	-0.424499
	N	1.559465	-0.790740	0.486984
	O	0.477077	1.930995	0.102581
	H	1.801276	-1.651689	0.974948
	H	0.654626	1.080707	0.525867
	H	3.258547	-1.131041	-0.658084
	H	2.236731	0.390574	-1.007870
	H	-0.426773	1.851430	-0.214630
	H	-0.802865	-0.705018	0.080170
	H	-2.310317	-0.076477	1.121738
	S	-2.092577	-0.411342	-0.156542

Table A.58: Cartesian coordinates for the H_2S relay catalyzed aminomethanol decomposition.

Species	Atom	X	Y	Z
Reactant Complex	C	-1.591219	0.039206	0.479578
	N	-1.410597	-1.221567	-0.150320
	O	-1.160745	1.115383	-0.369656
	H	-1.908117	-1.266625	-1.029672
	H	-0.429684	-1.408395	-0.319056

Continued on next page

Table A.58: Cartesian coordinates for the H_2S relay catalyzed aminomethanol decomposition.

Species	Atom	X	Y	Z
Reactant Complex	H	-2.646804	0.175321	0.721301
	H	-1.010059	0.051802	1.404839
	H	-1.454338	1.952645	0.000329
	H	0.992844	0.690516	-0.313734
	H	1.930970	0.100305	1.283426
	S	2.077040	-0.056432	-0.038463
Transition State	C	-1.552262	-0.269704	0.509916
	N	-1.118870	-1.202063	-0.273839
	O	-0.816617	1.430221	-0.302506
	H	-1.633446	-1.446895	-1.105967
	H	-0.076929	-1.333574	-0.247114
	H	-2.583279	0.044936	0.458575
	H	-0.972194	-0.073875	1.398997
	H	-0.817232	2.245633	0.210696
	H	0.151952	1.068866	-0.253938
	H	1.843849	-0.093666	1.306638
	S	1.735367	-0.113783	-0.030654
Product Complex	C	-2.178954	0.181211	0.024539
	N	-1.813462	-1.026784	-0.033814
	O	0.451526	2.282497	0.040918
	H	-2.607675	-1.664970	-0.032842
	H	0.261543	-1.139035	-0.074847
	H	-3.224750	0.490942	0.070321
	H	-1.426369	0.967815	0.028733
	H	1.005096	2.970675	-0.332671
	H	0.964738	1.465621	-0.030621
	H	1.670121	-0.946315	1.265284

Continued on next page

Table A.58: Cartesian coordinates for the H_2S relay catalyzed aminomethanol decomposition.

Species	Atom	X	Y	Z
Product Complex	S	1.594566	-0.894030	-0.070702

Rate Constants

Table A.59: Computed rate constants for the H_2S dual hydrogen bond catalyzed aminomethanol decomposition from 60 K to 1,000 K.

Temperature (K)	kTST (s-1)	kTST/W (s-1)	kTST/Eck (s-1)
60	1.86e-183	1.23e-181	2.98e-112
70	1.36e-155	6.62e-154	6.93e-97
80	1.08e-134	4.08e-133	2.67e-85
90	1.98e-118	5.91e-117	2.64e-76
100	2.03e-105	4.95e-104	4.55e-69
110	9.00e-95	1.83e-93	3.77e-63
120	6.74e-86	1.16e-84	3.59e-58
130	2.18e-78	3.24e-77	4.93e-54
140	5.99e-72	7.76e-71	2.15e-50
150	2.28e-66	2.60e-65	2.47e-47
160	1.75e-61	1.77e-60	1.43e-44
170	3.57e-57	3.25e-56	3.84e-42
180	2.43e-53	2.00e-52	5.47e-40
190	6.52e-50	4.88e-49	4.44e-38
200	7.96e-47	5.46e-46	2.52e-36
210	4.95e-44	3.12e-43	1.04e-34
220	1.72e-41	1.00e-40	3.13e-33
230	3.58e-39	1.94e-38	7.15e-32
240	4.80e-37	2.43e-36	1.29e-30
250	4.35e-35	2.06e-34	1.93e-29

Continued on next page

Table A.59: Computed rate constants for the H_2S dual hydrogen bond catalyzed aminomethanol decomposition from 60 K to 1,000 K.

Temperature (K)	kTST (s-1)	kTST/W (s-1)	kTST/Eck (s-1)
260	2.79e-33	1.24e-32	2.43e-28
270	1.31e-31	5.53e-31	2.73e-27
280	4.71e-30	1.88e-29	2.66e-26
290	1.32e-28	4.99e-28	2.41e-25
300	2.96e-27	1.07e-26	2.04e-24
310	5.45e-26	1.87e-25	1.61e-23
320	8.35e-25	2.75e-24	1.21e-22
330	1.09e-23	3.42e-23	8.64e-22
340	1.22e-22	3.68e-22	5.84e-21
350	1.19e-21	3.46e-21	3.74e-20
360	1.02e-20	2.87e-20	2.26e-19
370	7.82e-20	2.12e-19	1.29e-18
380	5.39e-19	1.41e-18	6.93e-18
390	3.36e-18	8.54e-18	3.49e-17
400	1.92e-17	4.72e-17	1.66e-16
410	1.00e-16	2.40e-16	7.39e-16
420	4.86e-16	1.13e-15	3.11e-15
430	2.19e-15	4.96e-15	1.24e-14
440	9.21e-15	2.03e-14	4.67e-14
450	3.64e-14	7.84e-14	1.67e-13
460	1.35e-13	2.85e-13	5.68e-13
470	4.76e-13	9.81e-13	1.85e-12
480	1.59e-12	3.21e-12	5.74e-12
490	5.06e-12	1.00e-11	1.71e-11
500	1.54e-11	2.98e-11	4.89e-11
510	4.48e-11	8.50e-11	1.34e-10
520	1.25e-10	2.33e-10	3.57e-10

Continued on next page

Table A.59: Computed rate constants for the H_2S dual hydrogen bond catalyzed aminomethanol decomposition from 60 K to 1,000 K.

Temperature (K)	kTST (s-1)	kTST/W (s-1)	kTST/Eck (s-1)
530	3.36e-10	6.16e-10	9.15e-10
540	8.72e-10	1.57e-09	2.27e-09
550	2.18e-09	3.87e-09	5.46e-09
560	5.29e-09	9.25e-09	1.27e-08
570	1.24e-08	2.14e-08	2.89e-08
580	2.84e-08	4.82e-08	6.38e-08
590	6.31e-08	1.06e-07	1.37e-07
600	1.37e-07	2.25e-07	2.89e-07
610	2.88e-07	4.69e-07	5.92e-07
620	5.94e-07	9.55e-07	1.19e-06
630	1.20e-06	1.90e-06	2.34e-06
640	2.36e-06	3.70e-06	4.50e-06
650	4.55e-06	7.07e-06	8.49e-06
660	8.60e-06	1.32e-05	1.57e-05
670	1.60e-05	2.43e-05	2.87e-05
680	2.91e-05	4.39e-05	5.13e-05
690	5.22e-05	7.79e-05	9.04e-05
700	9.21e-05	1.36e-04	1.57e-04
710	1.60e-04	2.34e-04	2.68e-04
720	2.73e-04	3.97e-04	4.51e-04
730	4.61e-04	6.63e-04	7.48e-04
740	7.66e-04	1.09e-03	1.23e-03
750	1.26e-03	1.78e-03	1.98e-03
760	2.03e-03	2.85e-03	3.17e-03
770	3.25e-03	4.53e-03	5.01e-03
780	5.13e-03	7.11e-03	7.82e-03
790	8.01e-03	1.10e-02	1.21e-02

Continued on next page

Table A.59: Computed rate constants for the H_2S dual hydrogen bond catalyzed aminomethanol decomposition from 60 K to 1,000 K.

Temperature (K)	kTST (s-1)	kTST/W (s-1)	kTST/Eck (s-1)
800	1.24e-02	1.69e-02	1.84e-02
810	1.89e-02	2.57e-02	2.79e-02
820	2.86e-02	3.86e-02	4.18e-02
830	4.29e-02	5.74e-02	6.20e-02
840	6.36e-02	8.47e-02	9.12e-02
850	9.35e-02	1.24e-01	1.33e-01
860	1.36e-01	1.79e-01	1.92e-01
870	1.97e-01	2.58e-01	2.75e-01
880	2.82e-01	3.68e-01	3.91e-01
890	4.01e-01	5.20e-01	5.52e-01
900	5.66e-01	7.30e-01	7.73e-01
910	7.92e-01	1.02e+00	1.07e+00
920	1.10e+00	1.41e+00	1.48e+00
930	1.52e+00	1.93e+00	2.04e+00
940	2.08e+00	2.64e+00	2.77e+00
950	2.84e+00	3.58e+00	3.75e+00
960	3.84e+00	4.82e+00	5.05e+00
970	5.17e+00	6.46e+00	6.76e+00
980	6.91e+00	8.60e+00	8.98e+00
990	9.19e+00	1.14e+01	1.19e+01
1000	1.22e+01	1.50e+01	1.56e+01

Table A.60: Computed rate constants for the H_2S relay catalyzed aminomethanol decomposition from 60 K to 1,000 K.

Temperature (K)	kTST (s-1)	kTST/W (s-1)	kTST/Eck (s-1)
60	1.82e-93	5.37e-93	1.89e-91
70	1.64e-78	3.98e-78	1.65e-77

Continued on next page

Table A.60: Computed rate constants for the H_2S relay catalyzed aminomethanol decomposition from 60 K to 1,000 K.

Temperature (K)	kTST (s-1)	kTST/W (s-1)	kTST/Eck (s-1)
80	2.63e-67	5.51e-67	1.16e-66
90	1.34e-58	2.51e-58	3.95e-58
100	1.23e-51	2.09e-51	2.82e-51
110	6.04e-46	9.53e-46	1.17e-45
120	3.31e-41	4.92e-41	5.70e-41
130	3.36e-37	4.75e-37	5.30e-37
140	9.08e-34	1.23e-33	1.34e-33
150	8.52e-31	1.12e-30	1.19e-30
160	3.39e-28	4.31e-28	4.53e-28
170	6.63e-26	8.24e-26	8.57e-26
180	7.21e-24	8.77e-24	9.06e-24
190	4.78e-22	5.70e-22	5.86e-22
200	2.08e-20	2.44e-20	2.49e-20
210	6.30e-19	7.29e-19	7.43e-19
220	1.40e-17	1.60e-17	1.63e-17
230	2.37e-16	2.68e-16	2.72e-16
240	3.17e-15	3.55e-15	3.60e-15
250	3.44e-14	3.83e-14	3.87e-14
260	3.11e-13	3.43e-13	3.47e-13
270	2.39e-12	2.62e-12	2.64e-12
280	1.58e-11	1.73e-11	1.74e-11
290	9.23e-11	1.00e-10	1.01e-10
300	4.78e-10	5.15e-10	5.18e-10
310	2.22e-09	2.38e-09	2.40e-09
320	9.40e-09	1.00e-08	1.01e-08
330	3.64e-08	3.87e-08	3.89e-08
340	1.30e-07	1.38e-07	1.39e-07

Continued on next page

Table A.60: Computed rate constants for the H_2S relay catalyzed aminomethanol decomposition from 60 K to 1,000 K.

Temperature (K)	kTST (s-1)	kTST/W (s-1)	kTST/Eck (s-1)
350	4.33e-07	4.58e-07	4.59e-07
360	1.35e-06	1.42e-06	1.42e-06
370	3.94e-06	4.14e-06	4.16e-06
380	1.09e-05	1.14e-05	1.15e-05
390	2.86e-05	2.99e-05	3.00e-05
400	7.15e-05	7.47e-05	7.49e-05
410	1.71e-04	1.78e-04	1.79e-04
420	3.93e-04	4.08e-04	4.09e-04
430	8.67e-04	9.00e-04	9.02e-04
440	1.85e-03	1.91e-03	1.92e-03
450	3.80e-03	3.93e-03	3.94e-03
460	7.59e-03	7.84e-03	7.86e-03
470	1.47e-02	1.52e-02	1.52e-02
480	2.77e-02	2.86e-02	2.86e-02
490	5.10e-02	5.24e-02	5.25e-02
500	9.14e-02	9.39e-02	9.40e-02
510	1.60e-01	1.64e-01	1.65e-01
520	2.75e-01	2.82e-01	2.82e-01
530	4.62e-01	4.73e-01	4.74e-01
540	7.61e-01	7.80e-01	7.81e-01
550	1.23e+00	1.26e+00	1.26e+00
560	1.96e+00	2.01e+00	2.01e+00
570	3.07e+00	3.14e+00	3.15e+00
580	4.74e+00	4.84e+00	4.83e+00
590	7.20e+00	7.35e+00	7.36e+00
600	1.08e+01	1.10e+01	1.10e+01
610	1.60e+01	1.63e+01	1.62e+01

Continued on next page

Table A.60: Computed rate constants for the H_2S relay catalyzed aminomethanol decomposition from 60 K to 1,000 K.

Temperature (K)	kTST (s-1)	kTST/W (s-1)	kTST/Eck (s-1)
620	2.33e+01	2.37e+01	2.37e+01
630	3.36e+01	3.42e+01	3.43e+01
640	4.80e+01	4.88e+01	4.87e+01
650	6.77e+01	6.88e+01	6.89e+01
660	9.45e+01	9.60e+01	9.62e+01
670	1.31e+02	1.33e+02	1.33e+02
680	1.79e+02	1.82e+02	1.82e+02
690	2.43e+02	2.46e+02	2.46e+02
700	3.27e+02	3.31e+02	3.32e+02
710	4.36e+02	4.42e+02	4.41e+02
720	5.77e+02	5.85e+02	5.88e+02
730	7.58e+02	7.68e+02	7.65e+02
740	9.89e+02	1.00e+03	1.01e+03
750	1.28e+03	1.30e+03	1.29e+03
760	1.65e+03	1.67e+03	1.67e+03
770	2.10e+03	2.13e+03	2.13e+03
780	2.67e+03	2.70e+03	2.70e+03
790	3.37e+03	3.41e+03	3.42e+03
800	4.23e+03	4.27e+03	4.28e+03
810	5.28e+03	5.33e+03	5.35e+03
820	6.55e+03	6.62e+03	6.58e+03
830	8.08e+03	8.17e+03	8.23e+03
840	9.93e+03	1.00e+04	1.01e+04
850	1.21e+04	1.23e+04	1.22e+04
860	1.48e+04	1.49e+04	1.50e+04
870	1.79e+04	1.81e+04	1.82e+04
880	2.16e+04	2.18e+04	2.17e+04

Continued on next page

Table A.60: Computed rate constants for the H_2S relay catalyzed aminomethanol decomposition from 60 K to 1,000 K.

Temperature (K)	kTST (s-1)	kTST/W (s-1)	kTST/Eck (s-1)
890	2.59e+04	2.62e+04	2.61e+04
900	3.10e+04	3.13e+04	3.16e+04
910	3.70e+04	3.73e+04	3.70e+04
920	4.39e+04	4.42e+04	4.46e+04
930	5.19e+04	5.23e+04	5.28e+04
940	6.12e+04	6.16e+04	6.11e+04
950	7.18e+04	7.24e+04	7.17e+04
960	8.41e+04	8.47e+04	8.51e+04
970	9.81e+04	9.88e+04	9.97e+04
980	1.14e+05	1.15e+05	1.14e+05
990	1.32e+05	1.33e+05	1.32e+05
1000	1.53e+05	1.54e+05	1.55e+05

A.4.10 HCOOH Catalyzed Reactions

Cartesian Coordinates

Table A.61: Cartesian coordinates for the HCOOH NH—Cat catalyzed aminomethanol decomposition.

Species	Atom	X	Y	Z
Reactant Complex	C	2.194411	0.080560	0.289047
	N	1.704337	-1.089061	-0.342420
	O	1.421236	1.243865	-0.070932
	H	0.763316	-1.325297	-0.048104
	H	1.736260	-1.016335	-1.349804
	H	2.148111	-0.057284	1.370715
	H	3.232199	0.245696	-0.006730
	H	1.846456	2.026517	0.290416

Continued on next page

Table A.61: Cartesian coordinates for the HCOOH NH—Cat catalyzed aminomethanol decomposition.

Species	Atom	X	Y	Z
Reactant Complex	O	-1.368446	-1.122757	0.318331
	C	-1.559624	0.001839	-0.031179
	H	-0.753933	0.689345	-0.323704
	O	-2.796791	0.520479	-0.084515
	H	-2.759487	1.433698	-0.386130
Transition State	C	1.969576	-0.497699	0.693133
	N	1.570564	-0.800875	-0.478964
	O	1.171072	1.584587	-0.189996
	H	0.740321	-1.388210	-0.586580
	H	1.732432	-0.051550	-1.162861
	H	1.575548	-1.045874	1.540616
	H	2.712758	0.271695	0.813304
	H	1.207668	2.543236	-0.189626
	O	-1.149060	-1.232736	-0.170612
	C	-1.304324	-0.043004	-0.037731
	H	-0.480967	0.707031	-0.103918
	O	-2.523109	0.448955	0.213110
	H	-2.464441	1.407566	0.289380
Product Complex	C	-2.913640	-0.870408	-0.041819
	N	-1.797884	-0.288897	0.013570
	O	-0.501013	2.241498	-0.014094
	H	-1.015062	-0.946787	0.054929
	H	-1.126041	1.490456	0.000764
	H	-3.028007	-1.955381	-0.043245
	H	-3.825741	-0.278786	-0.092093
	H	-1.003817	3.022275	0.221207
	O	1.034039	-1.375058	0.058561

Continued on next page

Table A.61: Cartesian coordinates for the HCOOH NH—Cat catalyzed aminomethanol decomposition.

Species	Atom	X	Y	Z
Product Complex	C	1.515803	-0.281140	0.025510
	H	0.935250	0.650256	0.061337
	O	2.841236	-0.102642	-0.059406
	H	3.041536	0.839155	-0.080523

Table A.62: Cartesian coordinates for the HCOOH relay catalyzed aminomethanol decomposition.

Species	Atom	X	Y	Z
Reactant Complex	C	1.757262	-0.035888	-0.433780
	N	1.609740	-1.056403	0.528908
	O	1.081967	1.186661	-0.021813
	H	1.946463	-0.784197	1.441239
	H	0.652956	-1.382008	0.576731
	H	2.811641	0.204411	-0.572862
	H	1.322712	-0.373111	-1.373972
	H	1.318450	1.902752	-0.619224
	O	-1.568019	0.983646	0.351546
	H	-0.581774	1.039484	0.240105
	C	-1.991763	-0.206090	-0.023469
	H	-3.080721	-0.287447	0.070429
	O	-1.295311	-1.104456	-0.419897
Transition State	C	-1.622238	-0.462185	0.514695
	N	-1.062156	-1.305376	-0.291087
	O	-1.329653	1.315468	-0.285744
	H	-1.573781	-1.639631	-1.092108
	H	0.015420	-1.348432	-0.243754
	H	-2.695432	-0.345269	0.524637

Continued on next page

Table A.62: Cartesian coordinates for the HCOOH relay catalyzed aminomethanol decomposition.

Species	Atom	X	Y	Z
Transition State	H	-1.060794	-0.190872	1.398073
	H	-1.589353	2.091300	0.221636
	O	1.131762	1.144682	0.002145
	H	-0.282827	1.254949	-0.220439
	C	1.852464	0.117954	0.052984
	H	2.936237	0.298603	0.141864
	O	1.485923	-1.074852	0.021301
Product Complex	C	1.439147	1.125541	0.552484
	N	0.635171	1.642813	-0.271788
	O	1.935534	-1.420522	-0.311253
	H	1.090479	2.245923	-0.951754
	H	-0.909075	1.108904	-0.255347
	H	2.511274	1.306079	0.543932
	H	1.052349	0.447877	1.307589
	H	2.197127	-2.342320	-0.339152
	O	-0.848371	-1.222768	0.261821
	H	0.974885	-1.424625	-0.181687
	C	-1.834666	-0.549152	0.065502
	H	-2.844657	-0.973799	0.104983
	O	-1.855346	0.727532	-0.204813

Rate Constants

Table A.63: Computed rate constants for the HCOOH NH—Cat catalyzed aminomethanol decomposition from 60 K to 1,000 K.

Temperature (K)	kTST (s-1)	kTST/W (s-1)	kTST/Eck (s-1)
60	7.18e-170	3.05e-169	1.68e-163

Continued on next page

Table A.63: Computed rate constants for the HCOOH NH—Cat catalyzed aminomethanol decomposition from 60 K to 1,000 K.

Temperature (K)	kTST (s-1)	kTST/W (s-1)	kTST/Eck (s-1)
70	4.87e-144	1.65e-143	1.71e-140
80	1.14e-124	3.22e-124	7.63e-123
90	1.32e-109	3.22e-109	1.49e-108
100	1.48e-97	3.20e-97	7.79e-97
110	1.06e-87	2.09e-87	3.73e-87
120	1.74e-79	3.15e-79	4.72e-79
130	1.56e-72	2.63e-72	3.52e-72
140	1.41e-66	2.25e-66	2.81e-66
150	2.06e-61	3.14e-61	3.71e-61
160	6.83e-57	9.95e-57	1.13e-56
170	6.66e-53	9.35e-53	1.04e-52
180	2.34e-49	3.19e-49	3.46e-49
190	3.50e-46	4.63e-46	4.95e-46
200	2.52e-43	3.25e-43	3.44e-43
210	9.71e-41	1.23e-40	1.29e-40
220	2.18e-38	2.71e-38	2.82e-38
230	3.07e-36	3.75e-36	3.88e-36
240	2.87e-34	3.45e-34	3.55e-34
250	1.86e-32	2.21e-32	2.27e-32
260	8.80e-31	1.03e-30	1.05e-30
270	3.13e-29	3.63e-29	3.70e-29
280	8.63e-28	9.92e-28	1.01e-27
290	1.90e-26	2.16e-26	2.19e-26
300	3.40e-25	3.84e-25	3.88e-25
310	5.05e-24	5.67e-24	5.73e-24
320	6.36e-23	7.08e-23	7.15e-23
330	6.87e-22	7.61e-22	7.68e-22

Continued on next page

Table A.63: Computed rate constants for the HCOOH NH—Cat catalyzed aminomethanol decomposition from 60 K to 1,000 K.

Temperature (K)	kTST (s-1)	kTST/W (s-1)	kTST/Eck (s-1)
340	6.46e-21	7.11e-21	7.17e-21
350	5.35e-20	5.86e-20	5.90e-20
360	3.94e-19	4.30e-19	4.33e-19
370	2.61e-18	2.83e-18	2.85e-18
380	1.57e-17	1.69e-17	1.70e-17
390	8.57e-17	9.23e-17	9.28e-17
400	4.31e-16	4.63e-16	4.65e-16
410	2.01e-15	2.15e-15	2.16e-15
420	8.69e-15	9.26e-15	9.30e-15
430	3.51e-14	3.74e-14	3.75e-14
440	1.33e-13	1.42e-13	1.42e-13
450	4.78e-13	5.06e-13	5.07e-13
460	1.62e-12	1.71e-12	1.71e-12
470	5.22e-12	5.49e-12	5.51e-12
480	1.60e-11	1.68e-11	1.69e-11
490	4.69e-11	4.92e-11	4.93e-11
500	1.32e-10	1.38e-10	1.38e-10
510	3.55e-10	3.71e-10	3.72e-10
520	9.23e-10	9.63e-10	9.65e-10
530	2.31e-09	2.41e-09	2.42e-09
540	5.61e-09	5.83e-09	5.85e-09
550	1.32e-08	1.37e-08	1.37e-08
560	3.00e-08	3.11e-08	3.12e-08
570	6.64e-08	6.88e-08	6.89e-08
580	1.43e-07	1.48e-07	1.48e-07
590	3.00e-07	3.10e-07	3.11e-07
600	6.15e-07	6.35e-07	6.36e-07

Continued on next page

Table A.63: Computed rate constants for the HCOOH NH—Cat catalyzed aminomethanol decomposition from 60 K to 1,000 K.

Temperature (K)	kTST (s-1)	kTST/W (s-1)	kTST/Eck (s-1)
610	1.23e-06	1.27e-06	1.27e-06
620	2.41e-06	2.48e-06	2.48e-06
630	4.61e-06	4.75e-06	4.75e-06
640	8.66e-06	8.91e-06	8.93e-06
650	1.60e-05	1.64e-05	1.64e-05
660	2.89e-05	2.96e-05	2.97e-05
670	5.13e-05	5.26e-05	5.27e-05
680	8.97e-05	9.19e-05	9.21e-05
690	1.54e-04	1.58e-04	1.58e-04
700	2.61e-04	2.67e-04	2.68e-04
710	4.36e-04	4.46e-04	4.46e-04
720	7.17e-04	7.33e-04	7.33e-04
730	1.16e-03	1.19e-03	1.19e-03
740	1.87e-03	1.90e-03	1.91e-03
750	2.95e-03	3.01e-03	3.01e-03
760	4.62e-03	4.71e-03	4.71e-03
770	7.13e-03	7.27e-03	7.27e-03
780	1.09e-02	1.11e-02	1.11e-02
790	1.65e-02	1.68e-02	1.68e-02
800	2.47e-02	2.51e-02	2.51e-02
810	3.66e-02	3.73e-02	3.73e-02
820	5.37e-02	5.47e-02	5.46e-02
830	7.82e-02	7.95e-02	7.97e-02
840	1.13e-01	1.15e-01	1.14e-01
850	1.61e-01	1.64e-01	1.64e-01
860	2.29e-01	2.32e-01	2.33e-01
870	3.21e-01	3.26e-01	3.27e-01

Continued on next page

Table A.63: Computed rate constants for the HCOOH NH—Cat catalyzed aminomethanol decomposition from 60 K to 1,000 K.

Temperature (K)	kTST (s-1)	kTST/W (s-1)	kTST/Eck (s-1)
880	4.49e-01	4.55e-01	4.54e-01
890	6.22e-01	6.31e-01	6.31e-01
900	8.55e-01	8.68e-01	8.71e-01
910	1.17e+00	1.18e+00	1.18e+00
920	1.59e+00	1.61e+00	1.61e+00
930	2.14e+00	2.17e+00	2.18e+00
940	2.86e+00	2.90e+00	2.89e+00
950	3.81e+00	3.86e+00	3.87e+00
960	5.05e+00	5.11e+00	5.12e+00
970	6.64e+00	6.72e+00	6.70e+00
980	8.69e+00	8.80e+00	8.85e+00
990	1.13e+01	1.14e+01	1.14e+01
1000	1.46e+01	1.48e+01	1.48e+01

Table A.64: Computed rate constants for the HCOOH relay catalyzed aminomethanol decomposition from 60 K to 1,000 K.

Temperature (K)	kTST (s-1)	kTST/W (s-1)	kTST/Eck (s-1)
60	1.38e-54	4.61e-54	6.82e-52
70	3.60e-45	9.80e-45	7.99e-44
80	4.15e-38	9.63e-38	2.82e-37
90	1.29e-32	2.63e-32	5.00e-32
100	3.19e-28	5.87e-28	8.92e-28
110	1.25e-24	2.12e-24	2.83e-24
120	1.23e-21	1.95e-21	2.40e-21
130	4.20e-19	6.29e-19	7.34e-19
140	6.22e-17	8.89e-17	9.99e-17
150	4.72e-15	6.49e-15	7.11e-15

Continued on next page

Table A.64: Computed rate constants for the HCOOH relay catalyzed aminomethanol decomposition from 60 K to 1,000 K.

Temperature (K)	kTST (s-1)	kTST/W (s-1)	kTST/Eck (s-1)
160	2.09e-13	2.78e-13	2.98e-13
170	5.90e-12	7.63e-12	8.08e-12
180	1.15e-10	1.45e-10	1.52e-10
190	1.64e-09	2.03e-09	2.11e-09
200	1.80e-08	2.18e-08	2.25e-08
210	1.56e-07	1.86e-07	1.92e-07
220	1.12e-06	1.31e-06	1.35e-06
230	6.75e-06	7.83e-06	7.99e-06
240	3.50e-05	4.02e-05	4.09e-05
250	1.59e-04	1.81e-04	1.84e-04
260	6.46e-04	7.27e-04	7.37e-04
270	2.36e-03	2.63e-03	2.67e-03
280	7.86e-03	8.70e-03	8.80e-03
290	2.41e-02	2.65e-02	2.68e-02
300	6.86e-02	7.50e-02	7.57e-02
310	1.82e-01	1.98e-01	2.00e-01
320	4.56e-01	4.94e-01	4.98e-01
330	1.08e+00	1.16e+00	1.17e+00
340	2.43e+00	2.61e+00	2.63e+00
350	5.23e+00	5.59e+00	5.62e+00
360	1.08e+01	1.15e+01	1.15e+01
370	2.13e+01	2.27e+01	2.28e+01
380	4.08e+01	4.32e+01	4.34e+01
390	7.54e+01	7.96e+01	8.00e+01
400	1.35e+02	1.42e+02	1.43e+02
410	2.36e+02	2.48e+02	2.49e+02
420	4.00e+02	4.20e+02	4.21e+02

Continued on next page

Table A.64: Computed rate constants for the HCOOH relay catalyzed aminomethanol decomposition from 60 K to 1,000 K.

Temperature (K)	kTST (s-1)	kTST/W (s-1)	kTST/Eck (s-1)
430	6.63e+02	6.94e+02	6.96e+02
440	1.07e+03	1.12e+03	1.13e+03
450	1.70e+03	1.77e+03	1.78e+03
460	2.65e+03	2.75e+03	2.76e+03
470	4.03e+03	4.19e+03	4.20e+03
480	6.04e+03	6.27e+03	6.29e+03
490	8.91e+03	9.22e+03	9.25e+03
500	1.29e+04	1.34e+04	1.34e+04
510	1.85e+04	1.91e+04	1.92e+04
520	2.61e+04	2.69e+04	2.70e+04
530	3.64e+04	3.75e+04	3.76e+04
540	5.00e+04	5.15e+04	5.16e+04
550	6.81e+04	7.00e+04	7.02e+04
560	9.16e+04	9.40e+04	9.42e+04
570	1.22e+05	1.25e+05	1.26e+05
580	1.61e+05	1.65e+05	1.65e+05
590	2.10e+05	2.15e+05	2.16e+05
600	2.72e+05	2.78e+05	2.79e+05
610	3.49e+05	3.57e+05	3.58e+05
620	4.45e+05	4.55e+05	4.56e+05
630	5.62e+05	5.74e+05	5.74e+05
640	7.06e+05	7.20e+05	7.22e+05
650	8.79e+05	8.97e+05	8.99e+05
660	1.09e+06	1.11e+06	1.11e+06
670	1.34e+06	1.36e+06	1.37e+06
680	1.64e+06	1.67e+06	1.67e+06
690	1.99e+06	2.03e+06	2.03e+06

Continued on next page

Table A.64: Computed rate constants for the HCOOH relay catalyzed aminomethanol decomposition from 60 K to 1,000 K.

Temperature (K)	kTST (s-1)	kTST/W (s-1)	kTST/Eck (s-1)
700	2.41e+06	2.45e+06	2.46e+06
710	2.90e+06	2.94e+06	2.96e+06
720	3.47e+06	3.52e+06	3.52e+06
730	4.13e+06	4.19e+06	4.20e+06
740	4.89e+06	4.97e+06	4.99e+06
750	5.77e+06	5.86e+06	5.87e+06
760	6.78e+06	6.88e+06	6.87e+06
770	7.94e+06	8.05e+06	8.07e+06
780	9.25e+06	9.38e+06	9.43e+06
790	1.07e+07	1.09e+07	1.09e+07
800	1.24e+07	1.26e+07	1.26e+07
810	1.43e+07	1.45e+07	1.45e+07
820	1.65e+07	1.67e+07	1.68e+07
830	1.88e+07	1.91e+07	1.91e+07
840	2.15e+07	2.18e+07	2.17e+07
850	2.45e+07	2.48e+07	2.47e+07
860	2.78e+07	2.81e+07	2.82e+07
870	3.14e+07	3.18e+07	3.20e+07
880	3.54e+07	3.58e+07	3.59e+07
890	3.99e+07	4.03e+07	4.01e+07
900	4.47e+07	4.52e+07	4.50e+07
910	5.01e+07	5.06e+07	5.07e+07
920	5.59e+07	5.65e+07	5.70e+07
930	6.23e+07	6.29e+07	6.33e+07
940	6.93e+07	6.99e+07	6.99e+07
950	7.69e+07	7.76e+07	7.71e+07
960	8.51e+07	8.59e+07	8.55e+07

Continued on next page

Table A.64: Computed rate constants for the HCOOH relay catalyzed aminomethanol decomposition from 60 K to 1,000 K.

Temperature (K)	kTST (s-1)	kTST/W (s-1)	kTST/Eck (s-1)
970	9.40e+07	9.48e+07	9.52e+07
980	1.04e+08	1.05e+08	1.06e+08
990	1.14e+08	1.15e+08	1.16e+08
1000	1.25e+08	1.26e+08	1.26e+08

References

(1) Gibb, E. L.; Whittet, D. C. B.; Boogert, A. C. A.; Tielens, A. G. G. M. Interstellar Ice: The Infrared Space Observatory Legacy. *Astrophys. J. Suppl.* **2004**, *151*, 35.

(2) Jeffery, C. S.; Werner, K.; Kilkenny, D.; Miszalski, B.; Monageng, I.; Snowdon, E. J. Hot White Dwarfs and Pre-White Dwarfs Discovered with SALT. *Mon. Not. R. Astron. Soc.* **2023**, *519*, 2321–2330.

(3) Herbst, E.; Van Dishoeck, E. F. Complex Organic Interstellar Molecules. *Annu. Rev. Astron. Astrophys.* **2009**, *47*, 427–480.

(4) Balucani, N. Elementary Reactions and Their Role in Gas-Phase Prebiotic Chemistry. *Int. J. Mol. Sci.* **2009**, *10*, 2304–2335.

(5) Ziurys, L. M.; Adande, G. R.; Edwards, J. L.; Schmidt, D. R.; Halfen, D. T.; Woolf, N. J. Prebiotic Chemical Evolution in the Astrophysical Context. *Origins Life Evol. Biospheres* **2015**, *45*, 275–288.

(6) Nuth, J. A.; Charnley, S. B.; Johnson, N. M., *Chemical Processes in the Interstellar Medium: Source of the Gas and Dust in the Primitive Solar Nebula*; The University of Arizona Press: Tuscon, AZ, 2006, pp 147–167.

(7) Puzzarini, C. Gas-phase Chemistry in the Interstellar Medium: The Role of Laboratory Astrochemistry. *Front. Astron. Space Sci.* **2022**, *8*, DOI: `https://doi.org/10.3389/fspas.2021.811342`.

(8) Öberg, K. I.; Boogert, A. C.; Pontoppidan, K. M.; Van Den Broek, S.; Van Dishoeck, E. F.; Bottinelli, S.; Blake, G. A.; Evans, N. J. The Spitzer Ice Legacy: Ice Evolution From Cores to Protostars. *Astrophys. J.* **2011**, *740*, 109.

(9) Herbst, E. Unusual Chemical Processes in Interstellar Chemistry: Past and Present. *Front. Astron. Space Sci.* **2021**, *8*, DOI: https://doi.org/10.3389/fspas.2021.776942.

(10) Oba, Y.; Takano, Y.; Watanabe, N.; Kouchi, A. Deuterium Fractionation During Amino Acid Formation by Photolysis of Interstellar Ice Analogs Containing Deuterated Methanol. *Astrophys. J. Lett.* **2016**, *827*, DOI: https://doi.org/10.3847/2041-8205/827/1/L18.

(11) Charnley, S. B., Interstellar Organic Chemistry. In *The Bridge between the Big Bang and Biology*, Consiglio Nazionale delle Ricerche, Italy, F. Giovannelli, Ed.; 2001; 139.

(12) Charnley, S. B.; Rogers, S. D.; Butner, H. M.; Ehrenfreund, P. Chemical Processes in Cometary Comae. *Earth Moon Planets* **2002**, *90*, 349–360.

(13) Woon, D. E. Ab Initio Quantum Chemical Studies of Reactions in Astrophysical Ices: 1. Aminolysis, Hydrolysis, and Polymerization in $H_2CO/NH_3/H_2O$ Ices. *Icarus* **1999**, *142*, 550–556.

(14) Chen, L.; Woon, D. E. A Theoretical Investigation of the Plausibility of Reactions between Ammonia and Carbonyl Species (Formaldehyde, Acetaldehyde, and Acetone) in Interstellar Ice Analogs at Ultracold Temperatures. *J. Phys. Chem. A* **2011**, *115*, 5166–5183.

(15) Bovolenta, G. M.; Silva-Vera, G.; Bovino, S.; Molpeceres, G.; Kästner, J.; Vogt-Geisse, S. In-depth Exploration of Catalytic Sites on Amorphous Solid Water: I. The Astrosynthesis of Aminomethanol. *Phys. Chem. Chem. Phys.* **2024**, *26*, 18692–18706.

(16) Widicus, S. L.; Drouin, B. J.; Dyl, K. A.; Blake, G. A. Millimeter Wavelength Measurements of the Rotational Spectrum of 2-Aminoethanol. *J. Mol. Spec* **2003**, *217*, 278–281.

(17) Rivilla, V. M.; Jiménez-Serra, I.; Martín-Pintado, J.; Briones, C.; Rodríguez-Almeida, L. F.; Rico-Villas, F.; Tercero, B.; Zeng, S.; Colzi, L.; de Vicente, P.; Martín, S.; Requena-Torres, M. A. Discovery in Space of Ethanolamine, the Simplest Phospholipid Head Group. *Proc. Natl. Acad. Sci.* **2021**, *118*, e2101314118.

(18) Bunn, H. A.; Schultz, C. P.; Jernigan, C. M.; Widicus Weaver, S. L. Laser-Induced Chemistry Observed during 248 nm Vacuum Ultraviolet Photolysis of an O_3 and CH_3NH_2 Mixture. *J. Phys. Chem. A* **2020**, *124*, PMID: 33307703, 10838–10848.

(19) Gordy, W.; Cook, R., *Microwave Molecular Spectra*; John Wiley & Sons, Inc.: New York, 1984.

(20) Widicus Weaver, S. L. Millimeter-Wave and Submillimeter-Wave Laboratory Spectroscopy in Support of Observational Astronomy. *Ann. Rev. Astron. Astrophys.* **2018**, *57*, 79–112.

(21) Bernath, P., *Spectra of Atoms and Molecules*; Oxford University Press: New York, 2005.

(22) Pickett, H. M. The Fitting and Prediction of Vibration-Rotation Spectra with Spin Interactions. *J. Mol. Spectrosc.* **1991**, *148*, 371–377.

(23) Hays, B. M.; McCabe, M. N.; Shipman, S. T.; Widicus Weaver, S. L. Fast Sweep Direct Absorption (Sub)millimeter-wave Spectroscopy. *Rev. Sci. Instrum.* **2016**, *87*, 113109.

(24) Zou, L.; Hays, B. M.; Weaver, S. L. Weakly Bound Clusters in Astrochemistry? Millimeter and Submillimeter Spectroscopy of trans-HO_3 and Comparison to Astronomical Observations. *J. Phys. Chem. A* **2016**, *120*, 657–667.

(25) Zou, L. Astrochemistry in Star-Forming Regions: Laboratory Millimeter-Submillimeter Spectroscopy and Broadband Astronomical Line Surveys, English, Ph.D. Thesis, Emory University, 2017, p 162.

(26) Schrödinger, E. An Undulatory Theory of the Mechanics of Atoms and Molecules. *Phys. Rev.* **1926**, *28*, 1049–1070.

(27) Levine, I. N. In *Quantum Chemistry*; Prentice-Hall Inc.: 2000; Chapter 13, pp 366–451.

(28) Born, M.; Oppenheimer, R. Zur Quantentheorie der Molekeln. *Ann. Phys.* **1927**, *389*, 457–484.

(29) Hartree, D. R. The Wave Mechanics of an Atom with a Non-Coulomb Central Field. Part II. Some Results and Discussion. *Math. Proc. Cambridge Philos. Soc.* **1928**, *24*, 111–132.

(30) Fock, V. Näherungsmethode zur Lösung des Quantenmechanischen Mehrkörperproblems. *Zeitschrift für Physik* **1930**, *61*, 126–148.

(31) Slater, J. C. Note on Hartree's Method. *Phys. Rev.* **1930**, *35*, 210–211.

(32) Hartree, D. R.; Hartree, W. Self-Consistent Field, with Exchange, for Beryllium. *Proc. R. Soc. London, Ser. A* **1935**, *150*, 9–33.

(33) Slater, J. C. A Simplification of the Hartree-Fock Method. *Phys. Rev.* **1951**, *81*, 385–390.

(34) Roothaan, C. C. J. New Developments in Molecular Orbital Theory. *Rev. Mod. Phys.* **1951**, *23*, 69–89.

(35) Møller, C.; Plesset, M. S. Note on an Approximation Treatment for Many-Electron Systems. *Phys. Rev.* **1934**, *46*, 618–622.

(36) Krishnan, R.; Pople, J. A. Approximate Fourth-Order Perturbation Theory of the Electron Correlation Energy. *Int. J. Quantum Chem.* **1978**, *14*, 91–100.

(37) Bartlett, R. J.; Purvis, G. D. Many-Body Perturbation Theory, Coupled-Pair Many-Electron Theory, and the Importance of Quadruple Excitations for the Correlation Problem. *Int. J. Quantum Chem.* **1978**, *14*, 561–581.

(38) Pople, J. A.; Krishnan, R.; Schlegel, H. B.; Binkley, J. S. Electron Correlation Theories and Their Application to the Study of Simple Reaction Potential Surfaces. *Int. J. Quantum Chem.* **1978**, *14*, 545–560.

(39) III, G. D. P.; Bartlett, R. J. A Full Coupled-Cluster Singles and Doubles Model: The Inclusion of Disconnected Triples. *J. Chem. Phys.* **1982**, *76*, 1910–1918.

(40) Raghavachari, K.; Trucks, G. W.; Pople, J. A.; Head-Gordon, M. A Fifth-Order Perturbation Comparison of Electron Correlation Theories. *Chem. Phys. Lett.* **1989**, *157*, 479–483.

(41) Foresman, J. B.; Head-Gordon, M.; Pople, J. A.; Frisch, M. J. Toward a Systematic Molecular Orbital Theory for Excited States. *J. Phys. Chem.* **1992**, *96*, 135–149.

(42) Head-Gordon, M.; Rico, R. J.; Oumi, M.; Lee, T. J. A Doubles Correction to Electronic Excited States from Configuration Interaction in the Space of Single Substitutions. *Chem. Phys. Lett.* **1994**, *219*, 21–29.

(43) Nyden, M. R.; Petersson, G. A. Complete Basis Set Correlation Energies. I. The Asymptotic Convergence of Pair Natural Orbital Expansions. *J. Chem. Phys.* **1981**, *75*, 1843–1862.

(44) Curtiss, L. A.; Raghavachari, K.; Trucks, G. W.; Pople, J. A. Gaussian-2 Theory for Molecular Energies of First- and Second-row compounds. *J. Chem. Phys.* **1991**, *94*, 7221–7230.

(45) Curtiss, L. A.; Raghavachari, K.; Redfern, P. C.; Rassolov, V.; Pople, J. A. Gaussian-3 (G3) Theory for Molecules Containing First and Second-Row Atoms. *J. Chem. Phys.* **1998**, *109*, 7764–7776.

(46) Tajti, A.; Szalay, P. G.; Császár, A. G.; Kállay, M.; Gauss, J.; Valeev, E. F.; Flowers, B. A.; Vázquez, J.; Stanton, J. F. HEAT: High Accuracy Extrapolated ab initio Thermochemistry. *J. Chem. Phys.* **2004**, *121*, 11599–11613.

(47) Hohenberg, P.; Kohn, W. Inhomogeneous Electron Gas. *Phys. Rev.* **1964**, *136*, B864–B871.

(48) Kohn, W.; Sham, L. J. Self-Consistent Equations Including Exchange and Correlation Effects. *Phys. Rev.* **1965**, *140*, A1133–A1138.

(49) Parr, R. G. Density Functional Theory. *Annu. Rev. of Phys. Chem.* **1983**, *34*, 631–656.

(50) Levine, I. N. In *Quantum Chemistry*; Prentice-Hall Inc.: 2000; Chapter 15.20, pp 573–591.

(51) Levy, M. Universal Variational Functionals of Electron Densities, First-Order Density Matrices, and Natural Spin-Orbitals and Solution of the v-Representability Problem. *Proc. Natl. Acad. Sci.* **1979**, *76*, 6062–6065.

(52) Von Barth, U.; Hedin, L. A Local Exchange-Correlation Potential for the Spin Polarized Case. i. *J. of Phys. C: Solid State Phys.* **1972**, *5*, 1629.

(53) Gunnarsson, O.; Lundqvist, B. I. Exchange and Correlation in Atoms, Molecules, and Solids By the Spin-Density-Functional Formalism. *Phys. Rev. B* **1976**, *13*, 4274–4298.

(54) Langreth, D. C.; Mehl, M. J. Beyond the Local-Density Approximation in Calculations of Ground-State Electronic Properties. *Phys. Rev. B* **1983**, *28*, 1809–1834.

(55) Becke, A. D. Density-Functional Exchange-Energy Approximation with Correct Asymptotic Behavior. *Phys. Rev. A* **1988**, *38*, 3098–3100.

(56) Perdew, J. P.; Chevary, J. A.; Vosko, S. H.; Jackson, K. A.; Pederson, M. R.; Singh, D. J.; Fiolhais, C. Atoms, Molecules, Solids, and Surfaces: Applications of the Generalized Gradient Approximation for Exchange and Correlation. *Phys. Rev. B* **1992**, *46*, 6671–6687.

(57) Perdew, J. P.; Kurth, S.; Zupan, A. š.; Blaha, P. Accurate Density Functional with Correct Formal Properties: A Step Beyond the Generalized Gradient Approximation. *Phys. Rev. Lett.* **1999**, *82*, 2544–2547.

(58) Becke, A. D. A New Mixing of Hartree–Fock and Local Density-Functional Theories. *J. Chem. Phys.* **1993**, *98*, 1372–1377.

(59) Sinanoğlu, O. Many-Electron Theory of Atoms and Molecules. I. Shells, Electron Pairs vs Many-Electron Correlations. *J. Chem. Phys.* **1962**, *36*, 706–717.

(60) Čížek, J. On the Correlation Problem in Atomic and Molecular Systems. Calculation of Wavefunction Components in Ursell-Type Expansion Using Quantum-Field Theoretical Methods. *J. Chem. Phys.* **1966**, *45*, 4256–4266.

(61) Čížek, J.; Paldus, J. Coupled Cluster Approach. *Phys. Scr.* **1980**, *21*, 251.

(62) Levine, I. N. In *Quantum Chemistry*, and references therein; Prentice-Hall Inc.: 2000; Chapter 15.19, pp 573–591.

(63) Arrhenius, S. Über die Dissociationswärme und den Einfluss der Temperatur auf den Dissociationsgrad der Elektrolyte. *Z. Phys. Chem.* **1889**, *4U*, 96–116.

(64) Wigner, E. On the Quantum Correction for Thermodynamic Equilibrium. *Phys. Rev.* **1932**, *40*, 749–759.

(65) Eyring, H. The Activated Complex in Chemical Reactions. *J. Chem. Phys.* **1935**, *3*, 107–115.

(66) Wigner, E. The Transition State Method. *Trans. Faraday Soc.* **1938**, *34*, 29–41.

(67) Eckart, C. The Penetration of a Potential Barrier by Electrons. *Phys. Rev.* **1930**, *35*, 1303–1309.

(68) Canneaux, S.; Bohr, F.; Henon, E. KiSThelP: A Program to Predict Thermodynamic Properties and Rate Constants from Quantum Chemistry Results. *J. Comput. Chem.* **2014**, *35*, 82–93.

(69) Keck, J. C. In *Adv. Chem. Phys.* John Wiley & Sons, Ltd: 1967, pp 85–121.

(70) Garrett, B. C.; Truhlar, D. G. Criterion of Minimum State Density in the Transition State theory of Bimolecular Reactions. *J. Chem. Phys.* **1979**, *70*, 1593–1598.

(71) Miller, W. H. Quantum Mechanical Transition State Theory and a New Semiclassical Model for Reaction Rate Constants. *J. Chem. Phys.* **1974**, *61*, 1823–1834.

(72) Jaffe, R. L.; Henry, J. M.; Anderson, J. B. Variational Theory of Reaction Rates: Application to $F + H_2 \rightleftarrows HF + H$. *J. Chem. Phys.* **1973**, *59*, 1128–1141.

(73) Keck, J. C. Variational Theory of Chemical Reaction Rates Applied to Three-Body Recombinations. *J. Chem. Phys.* **1960**, *32*, 1035–1050.

(74) Fernandez-Ramos, A.; Ellingson, B. A.; Garrett, B. C.; Truhlar, D. G. In *Rev. Comp. Chem.* John Wiley & Sons, Ltd: 2007; Chapter 3, pp 125–232.

(75) Fernández-Ramos, A.; Ellingson, B. A.; Meana-Pañeda, R.; Marques, J. M. C.; Truhlar, D. G. Symmetry Numbers and Chemical Reaction Rates. *Theor. Chem. Account.* **2007**, *118*, 813–826.

(76) Zhang, F.; Dibble, T. S. Impact of Tunneling on Hydrogen-Migration of the n-propylperoxy Radical. *Phys. Chem. Chem. Phys.* **2011**, *13*, 17969–17977.

(77) Bao, J. L.; Truhlar, D. G. Variational Transition State Theory: Theoretical Framework and Recent Developments. *Chem. Soc. Rev.* **2017**, *46*, 7548–7596.

(78) Truhlar, D. G.; Kuppermann, A. Exact Tunneling Calculations. *J. Am. Chem. Soc.* **1971**, *93*, 1840–1851.

(79) Liu, Y. P.; Lynch, G. C.; Truong, T. N.; Lu, D. H.; Truhlar, D. G.; Garrett, B. C. Molecular Modeling of the Kinetic Isotope Effect for the [1,5]-Sigmatropic Rearrangement of cis-1,3-Pentadiene. *J. Am. Chem. Soc.* **1993**, *115*, 2408–2415.

(80) Fernandez-Ramos, A.; Truhlar, D. G. Improved Algorithm for Corner-Cutting Tunneling Calculations. *J. Chem. Phys.* **2001**, *114*, 1491–1496.

(81) Liu, Y. P.; Lu, D. H.; Gonzalez-Lafont, A.; Truhlar, D. G.; Garrett, B. C. Direct Dynamics Calculation of the Kinetic Isotope Effect for an Organic Hydrogen-Transfer Reaction, Including Corner-Cutting Tunneling in 21 Dimensions. *J. Am. Chem. Soc.* **1993**, *115*, 7806–7817.

(82) Hays, B. M. Rotational Spectroscopy of O(^1D) Insertion Products, English, Ph.D. Thesis, Emory University, 2015, p 152.

(83) Hays, B. M.; Widicus Weaver, S. L. Theoretical Examination of O(^{1}D Insertion Reactions to Form Methanediol, Methoxymethanol, and Aminomethanol. *J. Phys. Chem. A* **2013**, *117*, 7142–7148.

(84) Burkholder, J. B.; Sander, S. P.; Abbatt, J. P. D.; Barker, J. R.; Cappa, C.; Crounse, J. D.; Dibble, T. S.; Huie, R. E.; Kolb, C. E.; Kurylo, M. J.; Orkin, V. L.; Percival, C. J.; Wilmouth, D. M.; Wine, P. H. *Chemical Kinetics and Photochemical Data for Use in Atmospheric Studies Evaluation Number 19 NASA Panel for Data Evaluation*; tech. rep.; NASA Jet Propulsion Laboratory, 2020, pp 1–16100.

(85) Glarborg, P.; Andreasen, C. S.; Hashemi, H.; Qian, R.; Marshall, P. Oxidation of Methylamine. *Int. J. Chem. Kinet.* **2020**, *52*, 893–906.

(86) Valehi Reykandeh, S.; Vahedpour, M.; Douroudgari, H.; Razavizadeh, S. A.; Asgharzadeh, S. Computational Study of the Mechanism, Reaction Rate and Thermochemistry of Atmospheric Oxidation of Methylamine with Singlet Oxygen. *Phys. Chem. Res.* **2016**, *4*, 191–208.

(87) Felder, P.; Haas, B.-M.; Robert Huber, J. The Photoreaction $N_2O \longrightarrow O(^1D) + N_2(^1\Sigma)$ at 193 nm Studied by Photofragment Translational Spectroscopy. *Chem. Phys. Lett.* **1991**, *186*, 177–182.

(88) Wolfe, G. M.; Marvin, M. R.; Roberts, S. J.; Travis, K. R.; Liao, J. The Framework for 0-D Atmospheric Modeling (F0AM) v3.1. *Geosci. Model Dev.* **2016**, *9*, 3309–3319.

(89) Saunders, S. M.; Jenkin, M. E.; Derwent, R. G.; Pilling, M. J. Protocol for the Development of the Master Chemical Mechanism MCM v3 (Part A): Tropospheric Degradation of Non-Aromatic Volatile Organic Compounds. *Atmos. Chem. Phys.* **2003**, *3*, 161–180.

(90) Satyapal, S.; Park, J.; Bersohn, R.; Katz, B. Dissociation of Methanol and Ethanol Activated by a Chemical Reaction or By Light. *J. Chem. Phys.* **1989**, *91*, 6271.

(91) Nishida, S.; Takahashi, K.; Matsumi, Y.; Taniguchi, N.; Hayashida, S. Formation of $O(^3P)$ Atoms in the Photolysis of N_2O at 193 nm and $O(^3P) + N_2O$ Product Channel in the Reaction of $O(^1D) + N_2O$. *J. Phys. Chem. A* **2004**, *108*, 2451–2456.

(92) Carder, J. T.; Ochs, W.; Herbst, E. Modelling the Insertion of $O(^1D)$ into Methane on the Surface of Interstellar Ice Mantles. *Mon. Not. R. Astron. Soc.* **2021**, *508*, 1526–1532.

(93) Hays, B. M.; Wehres, N.; DePrince, B. A.; Roy, A. A.; Laas, J. C.; Widicus Weaver, S. L. Rotational Spectral Studies of $O(^1D)$ Insertion Reactions with Methane and Ethylene: Methanol and Vinyl Alcohol in a Supersonic Expansion. *Chem. Phys. Lett.* **2015**, *630*, 18–26.

(94) Konen, I. M.; Pollack, I. B.; Li, E. X.; Lester, M. I.; Varner, M. E.; Stanton, J. F. Infrared Overtone Spectroscopy and Unimolecular Decay Dynamics of Peroxynitrous Acid. *J. Chem. Phys* **2005**, *122*, DOI: 10.1063/1.1854094.

(95) DeMore, W. B.; Raper, O. F. Reaction of $O(^1D)$ with Methane. *The Journal of Chemical Physics* **1967**, *46*, 2500–2505.

(96) Bergner, J. B.; Öberg, K. I.; Rajappan, M. Methanol Formation via Oxygen Insertion Chemistry in Ices. *Astrophys. J.* **2017**, *845*, DOI: 10.3847/1538-4357/aa7d09.

(97) Bennett, C. J.; Chen, S.-H.; Sun, B.-J.; Chang, A. H. H.; Kaiser, R. I. Mechanistical Studies on the Irradiation of Methanol in Extraterrestrial Ices. *Astrophys. J.* **2007**, *660*, 1588–1608.

(98) Chang, A. H. H.; Lin, S. H. A Theoretical Study of the $O(^1D)$ + CH_4 Reaction I. *Chem. Phys. Lett.* **2002**, *363*, 175–181.

(99) Goldsmith, P. F.; Langer, W. D. Population Diagram Analysis of Molecular Line Emission. *Astrophys. J.* **1999**, *517*, 209–225.

(100) Laas, J. C.; Hays, B. M.; Widicus Weaver, S. L. Multipass Millimeter/Submillimeter Spectrometer to Probe Dissociative Reaction Dynamics. *J. Phys. Chem. A* **2013**, *117*, 9548–9554.

(101) Yocum, K. M.; Milam, S. N.; Gerakines, P. A.; Weaver, S. L. W. Sublimation of Laboratory Ices Millimeter/Submillimeter Experiment (SubLIME): Structure-specific Identifications of Products from UV-photolyzed Methanol Ice. *Astrophys. J.* **2021**, *913*, 61.

(102) Splatalogue Database for Astronomical Spectroscopy, `https://splatalogue.online/`, Accessed: 2023-11-15.

(103) Müller, H. S. P.; Thorwirth, S.; Roth, D. A.; Winnewisser, G. The Cologne Database for Molecular Spectroscopy, CDMS. *Astron. Astrophys.* **2001**, *370*, L49–L52.

(104) Müller, H. S.; Schlöder, F.; Stutzki, J.; Winnewisser, G. The Cologne Database for Molecular Spectroscopy, CDMS: a Useful Tool for Astronomers and Spectroscopists. *J. Mol. Struct.* **2005**, *742*, 215–227.

(105) Endres, C. P.; Schlemmer, S.; Schilke, P.; Stutzki, J.; Müller, H. S. The Cologne Database for Molecular Spectroscopy, CDMS, in the Virtual Atomic and Molecular Data Centre, VAMDC. *J. Mol. Spec.* **2016**, *327*, 95–104.

(106) Pickett, H.; Poynter, R.; Cohen, E.; Delitsky, M.; Pearson, J.; Müller, H. Submillimeter, Millimeter, and Microwave Spectral Line Catalog. *J. of Quant. Spectrosc. Radiat. Transfer* **1998**, *60*, 883–890.

(107) Pickett, H. M.; Cohen, E. A.; Drouin, B. J.; Pearson, J. C. *Submillimeter, Millimeter, and Microwave Spectral Line Catalog*; tech. rep.; Jet Propulsion Laboratory / National Aeronautics and Space Administration, 2003.

(108) Kondo, K.; Oka, T. Stark-Zeeman Effects on Asymmetric Top Molecules. Formaldehyde H_2CO. *J. Phys. Soc. Jpn.* **1960**, *15*, 307–314.

(109) Xu, L.-H.; Fisher, J.; Lees, R.; Shi, H.; Hougen, J.; Pearson, J.; Drouin, B.; Blake, G.; Braakman, R. Torsion–Rotation Global Analysis of the First Three Torsional States (νt=0, 1, 2) and Terahertz Database for Methanol. *J. Mol. Spec.* **2008**, *251*, 305–313.

(110) Chang, A.; Lin, S. A Theoretical Study of the $O(^1D)$+CH_4 Reaction II. *Chem. Phys. Lett.* **2004**, *384*, 229–235.

(111) Division, C. S. M. Corning HPFS 7979, 7980, 8655 Fused Silica Optical Materials Product Information, Accessed Feb. 24, 2026, 2015.

(112) Corp., N. I. PCI-5124 Specifications, `https://www.ni.com/docs/en-US/bundle/pci-5124-specs/page/specs.html`, Accessed March 12, 2026, 2023.

(113) Rigol Technologies, I. Rigol DS1000Z-E Series Data Sheet, `https://www.rigol.com/dam/global/downloads/brochures/en/data-sheet/oscilloscopes/DS1000Z-E_DataSheet_EN.pdf`, Accessed March 12, 2026.

(114) Kaur, D.; de Souza, A. M.; Wanna, J.; Hammad, S. A.; Mercorelli, L.; Perry, D. S. Multipass Cell for Molecular Beam Absorption Spectroscopy. *Appl. Opt.* **1990**, *29*, 119–124.

(115) Van Helden, J. H.; Peverall, R.; Ritchie, G. In *Cavity Ring-down Spectroscopy Techniques and Applications*, Berden, G., Engeln, R., Eds.; John Wiley & Sons, Ltd: 2009; Chapter 2, pp 27–32.

(116) Optics, E. Laser Resonator Modes, `https://www.edmundoptics.com/knowledge-center/application-notes/lasers/laser-resonator-modes/`, Accessed March 18, 2026.

(117) Rigol Technologies, I. Rigol DS1000Z-E Series User Guide, `https://f00.psgsm.net/product/894828/ds1000z-e-userguide-en.pdf`, Accessed March 19, 2026.

(118) Rigol Technologies, I. Rigol DS1000Z-E Series Programming Guide, `https://f00.psgsm.net/product/894828/ds1000z-e-programmingguide-en.pdf`, Accessed March 19, 2026.

(119) Grabow, J.-U.; Palmer, E. S.; McCarthy, M. C.; Thaddeus, P. Supersonic-jet Cryogenic-Resonator Coaxially Oriented Beam-Resonator Arrangement Fourier Transform Microwave Spectrometer. *Rev. Sci. Instrum.* **2005**, *76*, 093106.

(120) McCarthy, M. C.; Chen, W.; Travers, M. J.; Thaddeus, P. Microwave Spectra of 11 Polyyne Carbon Chains. *Astrophys. J. Suppl. Ser.* **2000**, *129*, 611.

(121) Lieberman, M. A.; Lichtenberg, A. J. In *Principles of Plasma Discharges and Materials Processing*; John Wiley & Sons, Ltd: 2005; Chapter 14, pp 535–569.

(122) Buenker, R. J.; Olbrich, G.; Schuchmann, H. P.; Schuermann, B. L.; Von Sonntag, C. Photolysis of Methanol at 185 nm. Quantum-Mechanical Calculations and Product Study. *J. Am. Chem. Soc.* **1984**, *106*, 4362–4368.

(123) Panajapo, P.; Siwawannapong, K.; Sagarik, K. Mechanisms of the Photodissociations of Single Isolated Methanol. *AIP Adv.* **2020**, *10*, 075124.

(124) Michael, J. V.; Noyes, W. A. The Photochemistry of Methylamine. *J. Am. Chem. Soc.* **1963**, *85*, 1228–1233.

(125) Mutunga, F. M.; Anderson, D. T. Infrared Spectroscopy and 193 nm Photochemistry of Methylamine Isolated in Solid Parahydrogen. *J. Phys. Chem. A* **2015**, *119*, 2420–2428.

(126) Strecker, A. Ueber die künstliche Bildung der Milchsäure und einen neuen, dem Glycocoll homologen Körper. *Liebigs Ann. Chem.* **1850**, *75*, 27–45.

(127) Miller, S. L. A Production of Amino Acids Under Possible Primitive Earth Conditions. *Science* **1953**, *117*, 528–529.

(128) Brack, A. From Interstellar Amino Acids to Prebiotic Catalytic Peptides: A Review. *Chem. Biodivers.* **2007**, *4*, 665–679.

(129) Magrino, T.; Pietrucci, F.; Saitta, A. M. Step by Step Strecker Amino Acid Synthesis from Ab Initio Prebiotic Chemistry. *J. Phys. Chem. Lett.* **2021**, *12*, 2630–2637.

(130) Rimola, A.; Sodupe, M.; Ugliengo, P. Deep-space Glycine Formation via Strecker-type Reactions Activated by Ice Water Dust Mantles. A Computational Approach. *Phys. Chem. Chem. Phys.* **2010**, *12*, 5285–5294.

(131) Feldmann, M. T.; Widicus, S. L.; Blake, G. A.; Kent David R., I.; Goddard William A., I. Aminomethanol Water Elimination: Theoretical examination. *J. Chem. Phys.* **2005**, *123*, 034304.

(132) Minyaev, R. M. Pathways of the Reaction of Nucleophilic Addition of Ammonia to Formaldehyde in the Gas Phase and in the Complex with Formic Acid:Ab Initio Calculations. *Russ. Chem. Bull.* **1998**, *47*, 8–16.

(133) Wang, L.-P.; Titov, A.; McGibbon, R.; Liu, F.; Pande, V. S.; Martínez, T. J. Discovering chemistry with an ab initio nanoreactor. *Nat. Chem.* **2014**, *6*, 1044–1048.

(134) Sarkar, S.; Monu; Bandyopadhyay, B. Aldehyde as a Potential Source of Aminol in the Troposphere: Influence of Water and Formic Acid Catalysis on Ammonolysis of Formaldehyde. *Atmos. Environ.* **2019**, *213*, 223–230.

(135) Li, X.-T.; Mi, S.; Xu, Y.; Li, B.-W.; Zhu, T.; Zhang, J. Z. H. Discovery of New Synthetic Routes of Amino Acids in Prebiotic Chemistry. *JACS Au* **2024**, *4*, 4757–4768.

(136) Riffet, V.; Frison, G.; Bouchoux, G. Quantum-Chemical Modeling of the First Steps of the Strecker Synthesis: From the Gas-Phase to Water Solvation. *J. Phys. Chem. A* **2018**, *122*, 1643–1657.

(137) Singh, K. K.; Tandon, P.; Kumar, R.; Misra, A.; Shivani; Yadav, M.; Ahmad, A.; Chaudhary, M. K. Formation of Aminomethanol in Ammonia-water Interstellar Ice. *Mon. Not. R. Astron. Soc.* **2021**, *506*, 2059–2065.

(138) Wolf, M. E.; Hoobler, P. R.; Turney, J. M.; Schaefer, H. F. Important Features of the Potential Energy Surface of the Methylamine plus O(^{1}D) Reaction. *Phys. Chem. Chem. Phys.* **2019**, *21*, 24194–24205.

(139) Danger, G.; Duvernay, F.; Theulé, P.; Borget, F.; Chiavassa, T. Hydroxyacetonitrile ($HOCH_2CN$) Formation in Astrophysical Conditions. Competition with the Aminomethanol, a Glycine Precursor. *Astrophys. J.* **2012**, *756*, 11.

(140) Schutte, W. A.; Allamandola, L. J.; Sandford, S. A. Formaldehyde and Organic Molecule Production in Astrophysical Ices at Cryogenic Temperatures. *Science* **1993**, *259*, 1143–1145.

(141) Schutte, W.; Allamandola, L.; Sandford, S. An Experimental Study of the Organic Molecules Produced in Cometary and Interstellar Ice Analogs by Thermal Formaldehyde Reactions. *Icarus* **1993**, *104*, 118–137.

(142) Bossa, J. B.; Theule, P.; Duvernay, F.; Chiavassa, T. NH_2CH_2OH Thermal Formation in Interstellar Ices Contribution to the 5–8-μm Region Toward Embedded Protostars. *Astrophys. J.* **2009**, *707*, 1524.

(143) Singh, S. K.; Zhu, C.; Jeunesse, J. L.; Fortenberry, R. C.; Kaiser, R. I. Experimental Identification of Aminomethanol (NH_2CH_2OH)—the Key Intermediate in the Strecker Synthesis. *Nat. Commun.* **2022**, *13*, 375.

(144) Redondo, P.; Barrientos, C.; Largo, A. Peptide Bond Formation Through Gas-Phase Reactions in the Interstellar Medium: Formamide and Acetamide as Prototypes. *Astrophys. J.* **2014**, *793*, 32.

(145) Redondo, P.; Largo, A.; Barrientos, C. Is the Reaction Between Formic Acid and Protonated Aminomethanol a Possible Source of Glycine Precursors in the Interstellar Medium? *Astron. Astrophys.* **2015**, *579*, A125.

(146) Courmier, D.; Gardebien, F.; Minot, C.; St-Amant, A. A Computational Study of the Water-Catalyzed Formation of NH_2CH_2OH. *Chem. Phys. Lett.* **2005**, *405*, 357–363.

(147) Walch, S. P.; Bakes, E. On the reaction $CH_2NH_2^+$+HCN/HNC→$NH_2CH_2CNH^+$. *Chem. Phys. Lett.* **2001**, *346*, 267–273.

(148) Frisch, M. J. et al. Gaussian˜16 Revision C.01, Gaussian Inc. Wallingford CT, 2016.

(149) Head-Gordon, M.; Pople, J. A.; Frisch, M. J. MP2 Energy Evaluation by Direct Methods. *Chem. Phys. Lett.* **1988**, *153*, 503–506.

(150) Sæbø, S.; Almlöf, J. Avoiding the Integral Storage Bottleneck in LCAO Calculations of Electron Correlation. *Chem. Phys. Lett.* **1989**, *154*, 83–89.

(151) Frisch, M. J.; Head-Gordon, M.; Pople, J. A. A Direct MP2 Gradient Method. *Chem. Phys. Lett.* **1990**, *166*, 275–280.

(152) Frisch, M. J.; Head-Gordon, M.; Pople, J. A. Semi-Direct Algorithms for the MP2 Energy and Gradient. *Chemical Physics Letters* **1990**, *166*, 281–289.

(153) Head-Gordon, M.; Head-Gordon, T. Analytic MP2 Frequencies Without Fifth-Order Storage. Theory and Application to Bifurcated Hydrogen Bonds in the Water Hexamer. *Chem. Phys. Lett.* **1994**, *220*, 122–128.

(154) Lee, C.; Yang, W.; Parr, R. G. Development of the Colle-Salvetti Correlation-Energy Formula into a Functional of the Electron Density. *Phys. Rev. B* **1988**, *37*, 785–789.

(155) Becke, A. D. Density-Functional Thermochemistry. III. The Role of Exact Exchange. *J. Chem. Phys.* **1993**, *98*, 5648–5652.

(156) Perdew, J. P.; Burke, K.; Ernzerhof, M. Generalized Gradient Approximation Made Simple. *Phys. Rev. Lett.* **1996**, *77*, 3865–3868.

(157) Perdew, J. P.; Burke, K.; Ernzerhof, M. Generalized Gradient Approximation Made Simple. *Phys. Rev. Lett.* **1997**, *78*, 1396–1396.

(158) Adamo, C.; Barone, V. Toward Reliable Density Functional Methods Without Adjustable Parameters: The PBE0 Model. *J. Chem. Phys.* **1999**, *110*, 6158–6170.

(159) Chai, J.-D.; Head-Gordon, M. Long-Range Corrected Hybrid Density Functionals with Damped Atom–Atom Dispersion Corrections. *Phys. Chem. Chem. Phys.* **2008**, *10*, 6615–6620.

(160) Zhao, Y.; Truhlar, D. G. A New Local Density Functional for Main-Group Thermochemistry, Transition Metal Bonding, Thermochemical Kinetics, and Noncovalent Interactions. *J. Chem. Phys.* **2006**, *125*, 194101.

(161) Yu, H. S.; He, X.; Truhlar, D. G. MN15-L: A New Local Exchange-Correlation Functional for Kohn–Sham Density Functional Theory with Broad Accuracy for Atoms, Molecules, and Solids. *J. Chem. Theory Comput.* **2016**, *12*, 1280–1293.

(162) Zhao, Y.; Truhlar, D. G. The M06 Suite of Density Functionals for Main Group Thermochemistry, Thermochemical Kinetics, Noncovalent Interactions, Excited States, and Transition Elements: Two New Functionals and Systematic Testing of Four M06-Class Functionals and 12 Other Functionals. *Theor. Chem. Acc.* **2008**, *120*, 215–241.

(163) Zhao, Y.; Truhlar, D. G. Exploring the Limit of Accuracy of the Global Hybrid Meta Density Functional for Main-Group Thermochemistry, Kinetics, and Noncovalent Interactions. *J. Chem. Theory Comput.* **2008**, *4*, 1849–1868.

(164) Yu, H. S.; He, X.; Li, S. L.; Truhlar, D. G. MN15: A Kohn–Sham Global-Hybrid Exchange–Correlation Density Functional with Broad Accuracy for Multi-Reference and Single-Reference Systems and Noncovalent Interactions. *Chem. Sci.* **2016**, *7*, 5032–5051.

(165) Van Voorhis, T.; Scuseria, G. E. A Novel Form for the Exchange-Correlation Energy Functional. *J. Chem. Phys.* **1998**, *109*, 400–410.

(166) Mardirossian, N.; Head-Gordon, M. How Accurate Are the Minnesota Density Functionals for Noncovalent Interactions, Isomerization Energies, Thermochemistry, and Barrier Heights Involving Molecules Composed of Main-Group Elements? *J. Chem. Theory Comput.* **2016**, *12*, 4303–4325.

(167) Dunning Thom H., J. Gaussian Basis Sets for Use in Correlated Molecular Calculations. I. The Atoms Boron Through Neon and Hydrogen. *J. Chem. Phys.* **1989**, *90*, 1007–1023.

(168) Kendall, R. A.; Dunning Thom H., J.; Harrison, R. J. Electron Affinities of the First-Row Atoms Revisited. Systematic Basis Sets and Wave Functions. *J. Chem. Phys.* **1992**, *96*, 6796–6806.

(169) Woon, D. E.; Dunning Thom H., J. Gaussian Basis Sets for Use in Correlated Molecular Calculations. III. The Atoms Aluminum Through Argon. *J. Chem. Phys.* **1993**, *98*, 1358–1371.

(170) Peterson, K. A.; Woon, D. E.; Dunning Thom H., J. Benchmark Calculations with Correlated Molecular Wave Functions. IV. The Classical Barrier Height of the H+H2→H2+H Reaction. *J. Chem. Phys.* **1994**, *100*, 7410–7415.

(171) Alecu, I. M.; Zheng, J.; Zhao, Y.; Truhlar, D. G. Computational Thermochemistry: Scale Factor Databases and Scale Factors for Vibrational Frequencies Obtained from Electronic Model Chemistries. *J. Chem. Theory Comput.* **2010**, *6*, 2872–2887.

(172) Johnson III, R. D. NIST Computational Chemistry Comparison and Benchmark Database NIST Standard Reference Database Number 101, Release 22, 2022.

(173) Fukui, K. The Path of Chemical Reactions - the IRC Approach. *Accounts Chm. Res.* **1981**, *14*, 363–368.

(174) Gonzalez, C.; Schlegel, H. B. Reaction Path Following in Mass-weighted Internal Coordinates. *J. Phys. Chem.* **1990**, *94*, 5523–5527.

(175) Stanton, J. F.; Gauss, J.; Cheng, L.; Harding, M. E.; Matthews, D. A.; Szalay, P. G. CFOUR, Coupled-Cluster techniques for Computational Chemistry, a quantum-chemical program package, With contributions from A. Asthana, A.A. Auer, R.J. Bartlett, U. Benedikt, C. Berger, D.E. Bernholdt, S. Blaschke, Y. J. Bomble, S. Burger, O. Christiansen, D. Datta, F. Engel, R. Faber, J. Greiner, M. Heckert, O. Heun, M. Hilgenberg, C. Huber, T.-C. Jagau, D. Jonsson, J. Jusélius, T. Kirsch, M.-P. Kitsaras, K. Klein, G.M. Kopper,

W.J. Lauderdale, F. Lipparini, J. Liu, T. Metzroth, L. Monzel, L.A. Mück, D.P. O'Neill, T. Nottoli, J. Oswald, D.R. Price, E. Prochnow, C. Puzzarini, K. Ruud, F. Schiffmann, W. Schwalbach, C. Simmons, S. Stopkowicz, A. Tajti, T. Uhlířová, J. Vázquez, F. Wang, J.D. Watts, P. Yergün. C. Zhang, X. Zheng, and the integral packages MOLECULE (J. Almlöf and P.R. Taylor), PROPS (P.R. Taylor), ABACUS (T. Helgaker, H.J. Aa. Jensen, P. Jørgensen, and J. Olsen), and ECP routines by A. V. Mitin and C. van Wüllen. For the current version, see http://www.cfour.de.

(176) Čížek, J. In *Adv. Chem. Phys.* John Wiley & Sons, Ltd: 1969, pp 35–89.

(177) Pople, J. A.; Head-Gordon, M.; Raghavachari, K. Quadratic Configuration Interaction. A General Technique for Determining Electron Correlation Energies. *J. Chem. Phys.* **1987**, *87*, 5968–5975.

(178) Scuseria, G. E.; Janssen, C. L.; Schaefer Henry F., I. An Efficient Reformulation of the Closed-Shell Coupled Cluster Single and Double Excitation (CCSD) Equations. *J. Chem. Phys.* **1988**, *89*, 7382–7387.

(179) Scuseria, G. E.; Schaefer Henry F., I. Is Coupled Cluster Singles and Doubles (CCSD) More Computationally Intensive than Quadratic Configuration Interaction (QCISD)? *J. Chem. Phys.* **1989**, *90*, 3700–3703.

(180) Zheng, J.; Bao, J. L.; Zhang, S.; Meana-Pañeda, R.; Chuang, Y.-Y.; Coitiño, E. L.; Ellingson, B. A.; Truhlar, D. G. Gaussrate 17, (University of Minnesota, Minneapolis, MN), 2017.

(181) Zheng, J. et al. Polyrate-version 2017-C, (University of Minnesota, Minneapolis, MN), 2017.

(182) Skodje, R. T.; Truhlar, D. G.; Garrett, B. C. A General Small-Curvature Approximation for Transition-State-Theory Transmission Coefficients. *J. Phys. Chem.* **1981**, *85*, 3019–3023.

(183) Yu, H. S.; Fiedler, L. J.; Alecu, I.; Truhlar, D. G. Computational Thermochemistry: Automated Generation of Scale Factors for Vibrational Frequencies Calculated by Electronic Structure Model Chemistries. *Comp. Phys. Commun.* **2017**, *210*, 132–138.

(184) Wang, J.; Zhang, C.; Li, Y.; Zhou, Y.; Shu, Y.; Liang, S.; Zhang, G.; Liu, Z.; Wang, Y. Performance of Minnesota Functionals on Vibrational Frequency. *Int. J. Quantum Chem.* **2024**, *124*, e27516.

(185) Konkoli, Z.; Cremer, D. A New Way of Analyzing Vibrational Spectra. I. Derivation of Adiabatic Internal Modes. *Int. J. Quantum Chem.* **1998**, *67*, 1–9.

(186) Konkoli, Z.; Larsson, J. A.; Cremer, D. A New Way of Analyzing Vibrational Spectra. II. Comparison of Internal Mode Frequencies. *Int. J. Quantum Chem.* **1998**, *67*, 11–27.

(187) Konkoli, Z.; Cremer, D. A New Way of Analyzing Vibrational Spectra. III. Characterization of Normal Vibrational Modes in Terms of Internal Vibrational Modes. *Int. J. Quantum Chem.* **1998**, *67*, 29–40.

(188) Konkoli, Z.; Larsson, J. A.; Cremer, D. A New Way of Analyzing Vibrational Spectra. IV. Application and Testing of Adiabatic Modes Within the Concept of the Characterization of Normal Modes. *Int. J. Quantum Chem.* **1998**, *67*, 41–55.

(189) Kraka, E.; Zou, W.; Tao, Y. Decoding Chemical Information from Vibrational Spectroscopy Data: Local Vibrational Mode Theory. *WIREs Comput. Mol. Sci.* **2020**, *10*, e1480.

(190) Pickett, H. M.; Poynter, R. L.; Cohen, E. A.; Delitsky, M. L.; Pearson, J.; Müller, H. Submillimeter, Millimeter, and Microwave Spectral Line Catalog. *J. Quant. Spectrosc. Ra.* **1998**, *60*, 883–890.

(191) Garrod, R. T.; Weaver, S. L. W.; Herbst, E. Complex Chemistry in Star-forming Regions: An Expanded Gas-Grain Warm-up Chemical Model. *Astrophys. J.* **2008**, *682*, 283.

(192) Öberg, K. I. Photochemistry and Astrochemistry: Photochemical Pathways to Interstellar Complex Organic Molecules. *Chem. Rev.* **2016**, *116*, 9631–9663.

(193) Bursch, M.; Mewes, J.-M.; Hansen, A.; Grimme, S. Best-Practice DFT Protocols for Basic Molecular Computational Chemistry. *Angew. Chem. Int. Edit.* **2022**, *61*, e202205735.

(194) Rocha, W. R. M. et al. Ice Inventory Towards the Protostar Ced 110 IRS4 Observed with the James Webb Space Telescope - Results from the Early Release Science Ice Age Program. *Astron. Astrophys.* **2025**, *693*, A288.

(195) McClure, M. K. et al. An Ice Age JWST Inventory of Dense Molecular Cloud Ices. *Nat. Astron.* **2023**, *7*, 431–443.

(196) Calmonte, U. et al. Sulphur-bearing Species in the Coma of Comet 67P/Churyumov–Gerasimenko. *Mon. Not. R. Astron. Soc.* **2016**, *462*, S253–S273.

(197) Santos, J. C.; Enrique-Romero, J.; Lamberts, T.; Linnartz, H.; Chuang, K.-J. Formation of S-Bearing Complex Organic Molecules in Interstellar Clouds via Ice Reactions with C_2H_2, HS, and Atomic H. *ACS Earth Space Chem.* **2024**, *8*, 1646–1660.

(198) Lim, D.-W.; Sadakiyo, M.; Kitagawa, H. Proton Transfer in Hydrogen-Bonded Degenerate Systems of Water and Ammonia in Metal–Organic Frameworks. *Chem. Sci.* **2019**, *10*, 16–33.

(199) Ohshimo, K.; Miyazaki, S.; Hattori, K.; Misaizu, F. Long-Distance Proton Transfer Induced by a Single Ammonia Molecule: Ion Mobility Mass Spectrometry of Protonated Benzocaine Reacted with NH_3. *Phys. Chem. Chem. Phys.* **2020**, *22*, 8164–8170.

(200) Chang, K.-H.; Peng, Y.-C.; Su, K.-H.; Lin, Y.-H.; Liu, J.-C.; Liu, Y.-H.; Hsu, C.-H.; Yang, H.-C.; Chou, P.-T. Long-Range Hydrogen-Bond Relay Catalyses the Excited-State Proton Transfer Reaction. *Chem. Sci.* **2023**, *14*, 7237–7247.

(201) Li, H.; Xin, C.; Cai, J.; Yuan, B.; Wei, Z.; Jin, G. Hydrogen Bond Capability Tunable Different "Relay-Race" Mechanisms of the Excited-State Proton Transfer Process for 4'-methoxy-3-hydroxyflavone. *Org. Elec.* **2020**, *81*, 105678.

(202) Bartmess, J. E. In *Reviews in Computational ChemistryNIST Chemistry WebBook, NIST Standard Reference Database Number 69, Eds. P.J. Linstrom and W.G. Mallard*; National Institue of Standards and Technology: 2025.

(203) Ervin, K. M.; DeTuri, V. F. Anchoring the Gas-Phase Acidity Scale. *J. Phys. Chem. A* **2002**, *106*, 9947–9956.

(204) Eyet, N.; Villano, S. M.; Bierbaum, V. M. Anchoring the Gas-Phase Acidity Scale: From Formic Acid to Methanethiol. *Int. J. of Mass Spec.* **2009**, *283*, A Collection of Invited Papers Dedicated to Michael T. Bowers on the Occasion of his 70th Birthday, 26–29.

(205) Theulé, P.; Duvernay, F.; Danger, G.; Borget, F.; Bossa, J.; Vinogradoff, V.; Mispelaer, F.; Chiavassa, T. Thermal Reactions in Interstellar Ice: A Step Towards Molecular Complexity in the Interstellar Medium. *Adv. Space Res.* **2013**, *52*, 1567–1579.

(206) Meisner, J.; Kamp, I.; Thi, W.-F.; Kästner, J. The Role of Atom Tunneling in Gas-Phase Reactions in Planet-Forming Disks. *Astron. Astrophys.* **2019**, *627*, A45.

(207) Schreiner, P. R. Quantum Mechanical Tunneling Is Essential to Understanding Chemical Reactivity. *Trends Chem.* **2020**, *2*, 980–989.

(208) Marks, J. H.; Nikolayev, A. A.; Evseev, M. M.; Wang, J.; Turner, A. M.; Kleimeier, N. F.; Kuznetsov, O. V.; McAnally, M.; Morozov, A. N.; Antonov, I. O.; Mebel, A. M.; Kaiser, R. I. Quantum-Tunneling-Mediated Synthesis of Prebiotic Chelation Agents in Interstellar Analog Ices. *Chem* **2023**, *9*, 3286–3303.

(209) Truhlar, D. G.; Kohen, A. Convex Arrhenius Plots and Their Interpretation. *Proc. Natl. Acad. Sci.* **2001**, *98*, 848–851.

(210) Aquilanti, V.; Coutinho, N. D.; Carvalho-Silva, V. H. Kinetics of Low-Temperature Transitions and a Reaction Rate Theory from Non-Equilibrium Distributions. *Phil. Trans. R. Soc. A* **2017**, *375*, 20160201.

(211) Yocum, K. M.; Smith, H. H.; Todd, E. W.; Mora, L.; Gerakines, P. A.; Milam, S. N.; Widicus Weaver, S. L. Millimeter/Submillimeter Spectroscopic Detection of Desorbed Ices: A New Technique in Laboratory Astrochemistry. *J. Phys. Chem. A* **2019**, *123*, 8702–8708.

(212) Keller-Rudek, H.; Moortgat, G. K.; Sander, R.; Sörensen, R. The MPI-Mainz UV/VIS Spectral Atlas of Gaseous Molecules of Atmospheric Interest. *Earth Syst. Sci. Data* **2013**, *5*, 365–373.

(213) Haak, H. K.; Stuhl, F. Argon Fluoride (193 nm) Laser Photolysis of HN_3, Methylamine (CH_3NH_2), and Hydrazine (N_2H_4): Formation of Excited Imidogen (NH) Radicals. *J. Phys. Chem.* **1984**, *88*, 3627–3633.

(214) Lange, E.; Lozano, A. I.; Jones, N. C.; Hoffmann, S. V.; Kumar, S.; Śmiałek, M. A.; Duflot, D.; Brunger, M. J.; Limão-Vieira, P. Absolute Photoabsorption Cross-Sections of Methanol for Terrestrial and Astrophysical Relevance. *J. Phys. Chem. A* **2020**, *124*, 8496–8508.

(215) Zavelovich, J.; Rothschild, M.; Gornik, W.; Rhodes, C. K. VUV Fluorescence Following Photodissociation of N_2O at 193 nm. *J. Chem. Phys.* **1981**, *74*, 6787–6791.

(216) Atkinson, R.; Baulch, D. L.; Cox, R. A.; Hampson R. F., J.; Kerr, J. A.; Rossi, M. J.; Troe, J. Evaluated Kinetic, Photochemical and Heterogeneous Data for Atmospheric Chemistry: Supplement V. IUPAC Subcommittee on Gas Kinetic Data Evaluation for Atmospheric Chemistry. *J. Phys. Chem. Ref. Data* **1997**, *26*, 521–1011.

(217) Yonehara, T.; Kato, S. Role of Isomerization Channel in Unimolecular Dissociation Reaction $H_2CO \longrightarrow H_2 + CO$: Ab Initio Global Potential Energy Surface and Classical Trajectory Analysis. *J. Chem. Phys.* **2002**, *117*, 11131–11138.

(218) Tuazon, E. C.; Atkinson, R.; Aschmann, S. M.; Arey, J. Kinetics and Products of the Gas-Phase Reactions of O_3 with Amines and Related Compounds. *Res. Chem. Intermed.* **1994**, *20*, 303–320.

(219) Atkinson, R.; Pitts J. N., J. Kinetics of the Reactions of O(^{3}P) Atoms with the Amines CH_3NH_2, $C_2H_5NH_2$, $(CH_3)_2NH$, and $(CH_3)_3N$ Over the Temperature Range 298–440 ^{o}K. *J. Chem. Phys.* **1978**, *68*, 911–915.

(220) Pantaleone, S.; Salvini, C.; Zamirri, L.; Signorile, M.; Bonino, F.; Ugliengo, P. A Quantum Mechanical Study of Dehydration vs. Decarbonylation of Formamide Catalysed by Amorphous Silica Surfaces. *Phys. Chem. Chem. Phys.* **2020**, *22*, 8353–8363.